Cold Atoms in Cavity QED for Quantum Information Processing

Thesis by

David W. Vernooy

In Partial Fulfillment of the Requirements

for the Degree of

Doctor of Philosophy

California Institute of Technology

Pasadena, California

2000

(Defended May 5, 2000)

ii

Acknowledgements

I would like to thank first and foremost Jeff Kimble for providing the kind of atmosphere and resources necessary to do world-class research in atomic and optical physics. Virtually everything I now know about doing science, from daily experimental "plumbing" techniques to assessment of long-term scientific goals, comes from him. His personal encouragement of, keen interest in, and contributions to every aspect of the work presented here have been much appreciated. His energy and enthusiasm have been infectious.

I am indebted to all those with whom I have had the pleasure of working during my tenure at Caltech, including Joe Buck, Akira Furusawa, Chris Fuchs, Nikos Georgiades, Christina Hood, Ron Legere, Theresa Lynn, Jason McKeever, Michael Nielsen, Dan Stamper-Kurn, Quentin Turchette and Steven van Enk. I would like to especially acknowledge Vladimir Ilchenko, Hideo Mabuchi, Christoph Nagerl, Sze Tan and Jun Ye for the myriad of experimental and theoretical tricks I have learned from them. Outside the lab, both Franklin Monzon and Bill Weber have been great roommates and have helped keep me abreast of scientific developments outside of quantum optics.

Finally, I want to recognize my parents for the continual encouragement of my endeavours and Stephanie for all of your love and support over the last few years.

Abstract

The new field of quantum information science has exploded into virtually every area of modern physics because of the promise it holds for understanding physical limits to communication, computation and more generally the processing of information. Remarkably, this has come concomitantly with stunning successes at integrating laser cooling and trapping techniques with high finesse microresonators. A regime where some of the new theoretical ideas may be experimentally tested in the particular setting of cavity quantum electrodynamics (QED) has now been reached.

This thesis contains three inter-related parts. First, work with microspheres as a possible next generation microcavity is presented, including both successful attempts to push the limits of their quality factors in the near infrared and first experimental results at atomic interaction with the mode of the sphere at the one-photon level. The unique properties of these resonators led to some theoretical investigations of the atom-field interaction emphasizing the quantization of the atomic center of mass degrees of freedom. This has been largely unexplored both theoretically and experimentally to this point, yet remains an extremely important aspect of most serious implementations of quantum information processing in the setting of optical cavity QED. Finally, the emphasis of the last part of this thesis is on an attempt at intra-cavity atomic localization in the laboratory. Results to date include the first ever trapping of single atoms inside a high finesse microresonator. The techniques and capabilities developed en route to this achievement should form the experimental backbone for future work in optical cavity QED.

Contents

List of Figures

List of Tables

Chapter 1   Introduction

The last five years have heralded in an extremely exciting new era in which physicists have begun to explore both theoretically and experimentally the fundamental physical limits to information science [1]. Perhaps not surprisingly, it has since become generally recognized that principles of quantum mechanics, such as superposition, can be used to extreme advantage in certain types of algorithms [2], communications [3, 4], cryptography [5] and teleportation protocols [6]. On the experimental side, there has been a tremendous push to implement some of these ideas using various forms of "hardware," including teleportation of quantum states of the electromagnetic field [7, 8], optical and microwave cavity QED [9, 10], ion traps [11, 12], NMR systems [13], and more recently an electronic and nuclear spin-based proposal [14].

The very simple fact that useful information systems usually have outputs (which might be inputs to other systems) means that any quantum mechanical information system must be open to the outside world ("the environment"). This would seem to compete with the requirement that such a system maintain coherence, since it has been shown that decoherence in an otherwise isolated system can arise from coupling to this external reservoir [15]. The study of such open quantum systems in the field of optical cavity QED has been steadily progressing towards the point at which these loss rates to the environment can be suppressed with respect to the system's internal clock, even when considering the interaction between individual quanta. This is known as the *strong coupling* requirement in the study of open quantum systems, and an appropriate set of criteria can be identified for each of the experimental paradigms mentioned above.

Strongly coupled atomic physics based systems have had some overwhelming recent successes, including creation of Fock states of the electromagnetic field [16] and QND measurement of intracavity photon number [17] in microwave cavity QED, the entanglement of four particles [18], studies of decoherence to engineered reservoirs [19]

and cooling to the motional ground state [20, 12] in ion trap work at the single ion level, and trapping of single atoms inside high finesse cavities [21, 22, 23] in optical cavity QED.

The generic optical cavity QED system of a single, two-level atom of excited state linewidth $\gamma_\parallel$, strongly coupled at the Rabi frequency g to a single photon inside of a high finesse optical resonator of linewidth κ, was among the first candidate systems to be identified and exploited for quantum information processing [24]. The quantum mechanical structure of this simple system has been studied extensively and is described by the well-known Jaynes-Cummings Hamiltonian. The strong coupling parameter in this idealized system is given by $g^2/\kappa\gamma_\parallel$ and experimentally can now reach values much greater than unity.

A "quantum mechanical processor" based on this atomic system will have a photon flux into the output field of g^2/κ for the atomic dwell time T, prompting the identification of the *optical information per atom* of $g^2 T/\kappa$ [25]. The push to increase T forces the system to be considered from the perspective of the atomic center of mass (c.m.). Even though this is not a fundamentally new idea, the possibility of cooling the atomic c.m. motion down to near its zero point [20, 27, 12] would add a whole new dimension to the traditional Jaynes-Cummings energy spectrum and would signify a revolution in the capabilities of such a system from a *quantum computational* perspective.

The fact that this system can even be considered as a possibility for experimental investigation is due to two recent major experimental advances. First, breakthroughs in mirror coating technology have allowed for microresonators to be constructed from mirrors with losses at the few ppm level, while maintaining a small mode volume for large electric fields even at the single photon level. Second, there have been stunning recent advances in atomic cooling and trapping techniques, which were pioneered in parallel by groups seeking more precision in atomic clocks [28] and those pursuing the Bose-Einstein phase transition [29, 30]. Hence, there has been the extremely fortuitous situation of simultaneous advances for g, κ and T.

With the majority of experiments in optical cavity QED having previously been

done with atomic beams and Fabry-Perot cavities ([31] and [24] represent the last of this era in the Kimble labs), my graduate work in 1994 started with investigations of microspheres as possible next-generation resonators. They promised to deliver ultra-high Q's for long photon storage times while maintaining a large coupling g due to the small mode volume.

As a first project, with initial help from Hideo Mabuchi who had first started building up serious microsphere capabilities in the lab, I spent about a year building an apparatus to reproducibly fabricate high quality spheres and measure their Q's at several different wavelengths. This work was done in collaboration with Vladimir Ilchenko, who had pioneered many of the techniques I was using and came for an intense two-week visit from Moscow to gauge my progress. An undergraduate, Erik Streed, also spent a summer working with an atomic force microscope to characterize the surface roughness of the spheres. I was successful at measuring a world-record for finesse for an optical resonator, eclipsing the mark held previously (also by our group) for a Fabry-Perot geometry.

Another year and a half was spent building a second apparatus to see some first indication of interaction of atoms with these microresonators. Initially, it was thought a magneto-optical trap (MOT) would be necessary for this, and Nikos Georgiades worked with me to incorporate a MOT into a chamber capable of housing a sphere coupling apparatus. After Nikos graduated, a visiting scientist from Nikon Corporation, Akira Furusawa, got acquainted with cavity QED basics by helping me continue this experiment, and Vladimir again was invaluable during a second two-week visit in helping this experiment finally see some initial evidence of atomic interaction. For about 3 months, Jeff and I worked very intensely to try to understand the experimental results. My experimental microsphere work is summarized in two papers [32], [33] and forms the first section of this thesis.

While this particular work was underway in the lab, I started a set of theoretical calculations with the help of visiting scientist Sze Tan. The hope was to look for possible c.m. effects in a far off-resonance trapping (FORT) potential Hideo and Jeff had earlier identified for microspheres. This led to a paper [34] discussing the

bound state structure of this potential, but for me the implications turned out to be profound. It was immediately noticeable that the c.m. wavefunctions for these bound states could have structure on the same spatial scale as the quantized optical field, forcing one far away from the situation where the atomic motion could be considered in a billiard ball model. This was studied in much more depth in a second paper [35] in which Jeff and I identified three separate regimes depending on the relevant energy scales in the problem. The addition of a confining external potential for the atomic c.m. turns out to have an impact on both the usual structure of the Jaynes-Cummings states (which we called the "well-dressed states," since the usual "dressed states" are impacted by the presence of an external potential well) and resulting dynamics.

A discussion of this theoretical work forms the second part of my thesis, and serves as a very nice introduction to the final part in which I discuss experimental work I have pursued (and continue to pursue) in the hopes of seeing some of these c.m. effects in the lab. I began working with Jun Ye, a post-doc in our group, in December 1997 with the ultimate goal then of trying to trap a single atom inside of one of these high-finesse resonators. The idea behind this effort is that it will become absolutely essential for many future experiments in quantum information science based on cavity QED to start with an initial condition of a single atom at rest in a known position inside the cavity.

We were able to build somewhat on Hideo's precision position measurement work [36], but much of the existing hardware had to be re-designed for the purposes of an atom trapping experiment. Jun and I were finally successful in the early summer of 1999 in trapping a single atom inside of a high finesse Fabry-Perot resonator using an intra-cavity FORT [21]. We hope that this result, and the experimental infrastructure which is now in place, will enable a whole new generation of experiments for which a single atom, localized inside a high finesse resonator, is merely the initial condition! Finally, I will discuss on-going work being done by myself, along with post-docs Christoph Nagerl and Dan Stamper-Kurn, and new graduate student Jason McKeever, with an emphasis presently being placed on an understanding of the technical limitations to the trap lifetime. The next major scientific goal is to try to cool the

c.m. degrees of freedom using the rich eigenvalue structure of the well-dressed states.

On an organizational note, the first two sections (five chapters) of this thesis, based on my early graduate career, are written in a rather terse fashion for the purpose of keeping the whole effort to a reasonable length. However, the final section (three chapters) based on the most recent 2 1/2 years of work is heavily loaded with detail in the hopes that it may be useful to those who are carrying on with this cavity QED experiment. To complement this overview, each of Parts I - III includes a somewhat self-contained introduction.

Part I

MICROSPHERES

Chapter 2 Microsphere Resonators in Cavity QED

2.1 The Motivation: Microspheres as a Future Direction for CQED Experiments

Small optical resonators with large quality factors Q have diverse technological and scientific applications, ranging from frequency stabilization of semiconductor diode lasers [37] to environmental sensing by trace absorption detection in compact, integrated structures [38]. Our own interest in such resonators arises within the realm of cavity quantum electrodynamics (QED) where it is necessary to simultaneously achieve small cavity mode volumes (for large electric fields per photon) *and* ultra-low resonator losses (for long photon storage times) [9]. In the optical domain, these conditions have previously been met only in small Fabry-Perot cavities. An attractive alternative are the WGMs of quartz microspheres, as was pointed out in the pioneering work of Ref. [39]. These modes can have both large coupling coefficients for the atom-cavity interaction (mode volume $V \approx 5 \times 10^3$ $\mu\mathrm{m}^3$) [40, 41] and extremely low losses [43, 44].

Fig. 2.1 is a famous plot from the Kimble group that chronicles the march over the last two decades to ever smaller parameters

$$m_0 = \frac{\gamma_\perp \gamma_\parallel}{4g^2} b, \, N_0 = \frac{2\kappa\gamma_\perp}{g^2} \tag{2.1}$$

where N_0 is the critical atom number necessary to significantly influence the intracavity field, and m_0 is the number of photons necessary to saturate a single atom. Note that for purely radiative decay, $\gamma_\perp = \gamma_\parallel/2$.

The data on this graph are for published experiments in the group. The points ($\blacktriangle$)
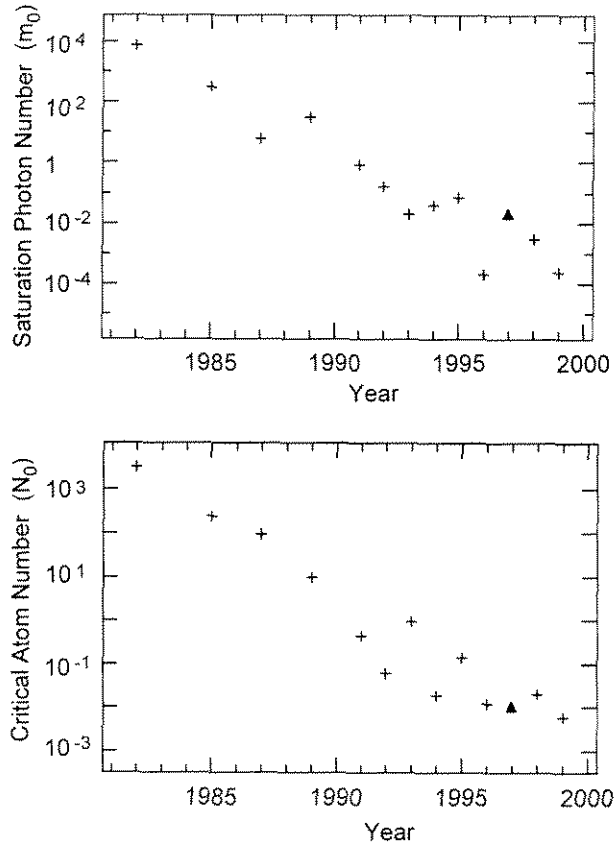
Figure 2.1: Progress in the critical numbers (m_0, N_0) of Eq. (2.1) for cavity QED experiments in the Kimble group over the last 15 years (data here are for published experiments). Though the overall trend has historically been determined by Fabry-Perot cavity technology and continues to be impressive, emphasized in this plot (▲) is the first report of atomic interaction with microspheres of Ref. [33]. The technology determining (m_0, N_0) is still far from reaching any fundamental physical or technical limits.

in 1997 correspond to the first published reports [33] of atomic interaction with the high Q sphere mode at the level of one atom in the mode volume, whereas all other experiments are done with Fabry-Perot cavities. Though the most recent Fabry-Perot data are the result of mirror superpolishing and ultra-low loss, ultra-high quality interference coatings, estimates of present experimental capabilities indicate that these numbers will reach something of an upper limit as the mirror gap approaches the order of a wavelength (present gaps allow 5 to 10 standing waves inside the Fabry-Perot microresonators [65]). In a Fabry-Perot cavity of length L, the coupling $g \propto L^{-3/4}$, and the linewidth $\kappa \propto L^{-1}$ so that the ratio $g/\kappa \propto L^{1/4}$ in fact favors longer cavities. However, the requirement of strong coupling, namely $g > \gamma_\perp, \kappa$ means that L must ultimately be kept as small as possible to continue to decrease (m_0, N_0).

On the other hand, for a microsphere of diameter D, $g \propto D^{-11/12}$, and the linewidth $\kappa \propto D^{-n}$, with $n = 0$ for absorption-limited losses and $n = 1/2$ for surface-scattering limited linewidths (radiative losses are ignored for $D/\lambda \gg 20$ at a wavelength λ). The data to be presented below suggest that $n < 1$, so that $g/\kappa \propto D^{-(11/12-n)}$ will *increase* with decreasing sphere sizes until radiative Q limitations are reached. This is also the same condition on D necessary for maximizing the coupling.

The Q factors for spheres used in actual reported cavity QED experiments (i.e., spheres coupled to a dipole) tend to be several orders of magnitude lower than the best Q factors yet measured for spheres on their own. In fact, m_0 can gain three orders of magnitude if a Q of 10^{10} could be maintained for a 100 μm diameter sphere, and even more spectacular progress could be made with smaller spheres. Actual experimental results reported in Refs. [45, 32] demonstrated beautifully that experimental Q factors can reach the intrinsic absorption limit of fused silica (at 633 nm, $Q = (8 \pm 1) \times 10^9$ was reported). For use in cavity QED and otherwise, the microsphere WGMs are thus worthy of immediate further investigation, especially with the possibility of even higher Q in the near infrared (NIR), as the bulk silica absorption coefficient falls more than five-fold moving from 600 nm to 1 μm.

With this motivation, I will first start with a very quick introduction to the so-

called Whispering Gallery Modes (WGMs), and will then document efforts which led to a series of high Q measurements for different wavelengths in the NIR and an attempt to understand the fundamental limits to these measurements.

2.2 Whispering Gallery Modes

2.2.1 Mode Functions

The solution of the classical electromagnetics problem for the resonant microsphere mode structure is well-known [46]. Two different polarizations are allowed, but the mode splittings in the small spheres considered here are large enough (~ 100 GHz) compared to the linewidths ($\lesssim 100$ MHz) to ensure that only one polarization is excited at any given time. The TM modes of *electric type* briefly considered here have a predominantly radial electric field vector. In polar coordinates, the TM electric field inside the sphere scales as

$$E_r\left(\mathbf{r} \right) \sim -l\left(l+1 \right) \frac{j_l\left(Kr \right)}{Kr} P_l{}^m \left(\cos\theta \right) e^{im\phi}, \tag{2.2}$$

where the $P_l{}^m$ are associated Legendre polynomials and the j_l are spherical Bessel functions. The field outside the sphere is given by the above expression with j_l replaced by the outgoing spherical Hankel function $h_l^{(1)}$. The wavevector K inside the sphere must also be replaced by $k = 2\pi/\lambda = K/n$, with n the sphere's refractive index.

Resonances in the Mie scattering coefficients are determined from the boundary conditions on Maxwell's equations. For a sphere of radius a, the following characteristic equation with $\rho = Ka$ applies to TM modes,

$$\frac{j_{l-1}\left(\rho \right)}{j_l\left(\rho \right)} - \frac{l}{\rho} = \frac{nh_{l-1}^{(1)}\left(\frac{\rho}{n} \right)}{h_l^{(1)}\left(\frac{\rho}{n} \right)} - \frac{n^2 l}{\rho}. \tag{2.3}$$

The solutions ρ_{ql} determine the resonant frequencies by $\omega_{ql} = \text{Re}\left(\frac{c\rho_{ql}}{na} \right)$. The mode indices q and m are, respectively, the number of field maxima inside the sphere and

the number of azimuthal maxima. The WGMs are highly confined to the sphere equator and have $l \approx m$, where $l \approx Ka$ for large l. For perfect spheres, the modes are degenerate in m, but a slight asphericity is enough to cause splittings (3% asphericity gives a 10 GHz splitting in a 100 μm diameter sphere). For visualization, Fig. 2.2 shows a numerical calculation of the field radial dependence.
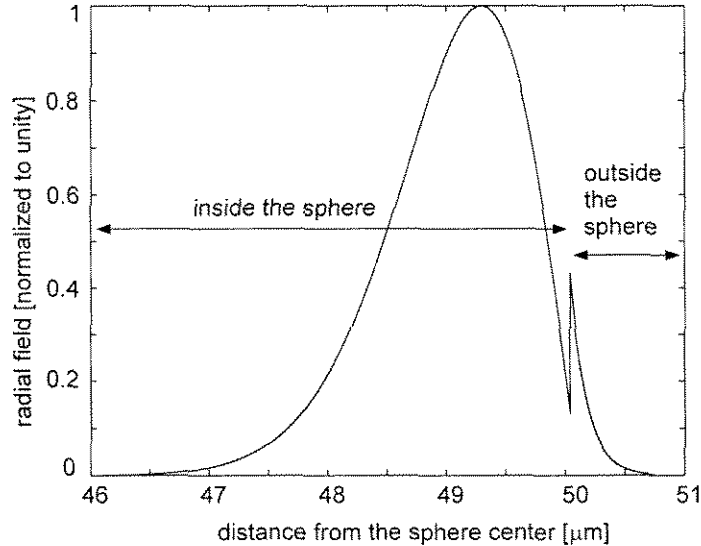
Figure 2.2: The radial field dependency for the WGM $(q, l, m) = (1, 521, 521)$ for a 50 μm radius sphere of index $n = 1.452$ at 852 nm $(ka = 456)$. The field maximum lies just inside the sphere and decays exponentially outside the sphere with $1/e$ length $\lambda/2\pi \sim 120$ nm at 850 nm.

2.2.2 Radiative Quality Factors

The cavity damping rate κ (note, $Q = \omega_{ql}/2\kappa$) can be a *very* small number and this is one of the main reasons why microsphere resonators are interesting for strongly-coupled cavity QED. This value can be predicted using the results of Ref. [47]. The intrinsic radiative Q_{rad} is found by considering the functional form of the Mie scattering coefficient b_l, given explicitly for TM modes by

$$b_l = \frac{j_l(\rho)\left[n\rho j_l(n\rho)\right]' - n^2 j_l(n\rho)\left[\rho j_l(\rho)\right]'}{n^2 j_l(n\rho)\left[\rho h_l^{(1)}(\rho)\right]' - h_l^{(1)}(\rho)\left[n\rho j_l(n\rho)\right]'}. \tag{2.4}$$

Numerical evaluation predicts Q_{rad} values $> 10^{20}$ for $\frac{2a}{\lambda} \geq 30$ (as is typically satisfied in our work) so that radiative losses are generally not the limiting factor in determining the ultimate Q experimentally, as was first shown by a measurement of $Q \sim 8 \times 10^9$ at 633 nm by the Moscow group [45].

Chapter 3   High Q Measurements for Fused Silica Microspheres in the NIR

3.1   Experimental Issues

3.1.1   Fabrication and Cleaning

The microspheres were fabricated using an ultrapure oxygen-hydrogen micro-torch apparatus [48], a sketch of which is provided in Fig. 3.1. It took considerable experience to be able to reproducibly make high quality, spherical microspheres of a given diameter and stem size. The most important factor was flame temperature control using the ratio of oxygen to hydrogen. The mixture was then "doped" by bubbling it through a 50% methanol/water mixture for further control of the flame properties. The silica rods (CeramOptec, Heraeus Amersil, Suprasil), of OH content < 20 ppm, were first cleaned to remove any surface contamination. This procedure typically included manual cleaning of these preforms with a detergent such as Alconox to get rid of inorganics, a very short 50% nitric acid (30 s) or 50% hydrofluoric acid (5 s) etch, and periods of ultrasonic cleaning interspersed with liberal rinsing with high purity solvents such as acetone, methanol and isopropyl alcohol. In this way, it was possible to eliminate virtually all visible surface scattering of diffuse light from particles on the surface of the rod before sphere fabrication. Anecdotally, it was my experience that when such scattering could be seen from the surface, high Q was never achieved.

Sphere fabrication begins with "preform" and "manipulator" rods of high quality silica. Material at the end of the preform rod was heated to the melting point such that, under surface tension, it formed a sphere naturally upon cooling. In time, spheres up to 1 mm and down to 20 μm diameter could be fabricated reliably with this method, with about 5% error in the target diameter. A high quality stereomicroscope

(Zeiss Stemi-SV11) with a fairly long working distance of 11 cm and typical 70X magnification was invaluable for this work.
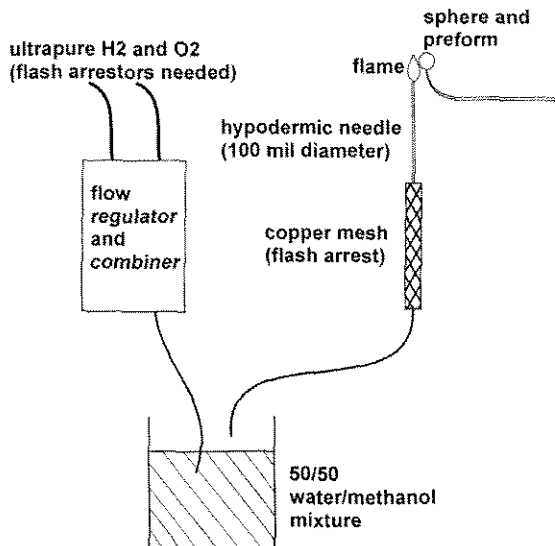
Figure 3.1: The basic apparatus for microsphere fabrication shows the oxygen-hydrogen microtorch and methanol doping mixture. Care had to be taken to ensure cleanliness and safety with this apparatus. In addition, the highest Q measurements had to be performed within 1.5 minutes of fabrication due to absorption by adsorbed water on the sphere surface.

3.1.2 Mode Coupling and Ringdown Measurements

Both to extend to the NIR the Moscow measurement at 633 nm mentioned above, and also to improve our own capabilities at microsphere fabrication with an eye towards an experimental cavity QED implementation, Q factors were measured at three additional wavelengths, namely 670 nm, 780 nm and 850 nm. For each of the wavelengths studied, the excitation source was a home-built external grating stabilized diode laser [42], with linewidth of a few hundred kHz.

The laser output was coupled into the microsphere using frustrated total internal reflection from a coupling prism [43], since WGM excitation is efficiently achieved experimentally by allowing the evanescent component of a focused Gaussian beam to meet the sphere at grazing incidence. To obtain an output beam free of any forward

scattering, the in-coupling beam was injected at an angle Θ to the sphere's equatorial plane and an angle Φ with respect to a tangent plane at the sphere surface in order to take advantage of the so-called precessing modes [49, 50]. The excitation geometry and apparatus are illustrated in Figs. 3.2 (a) and (b) for reference. This geometry, with $(\Theta, \Phi) \sim (10°, 10°)$ typically necessary for efficient excitation, can also be used for mode identification so that a 100 μm diameter sphere would have $(q, l, m) \sim (1, 400, 385)$. Note that q is primarily determined by the "depth" angle Φ and m via the off-axis "launch" angle Θ.

The spheres were mounted on a long silica rod which was glued to a magnetic base. This base could be manipulated into place quickly using a refrigerator magnet mounted to the micro-translation stage (Burleigh PZS-100) used to control the gap between the sphere and the coupling prism. The coupling lens, of focal length 5 mm, was a high numerical aperture aspheric lens of the sort typically used for diode laser collimation. The whole alignment procedure was monitored through the stereomicroscope system by learning to recognize the pattern of reflected spots on the prism.

Cavity lifetimes were determined by way of a "ringdown" measurement with the incident field gated by an acousto-optic modulator (AOM) used as a fast shutter. Two separate methods were typically used. In the first, an AOM was gated off by a preset threshold of the Lorentzian mode buildup in the sphere as the feedback grating was dithered to scan the laser frequency. The trigger output of a fast analog oscilloscope (Tektronix, 400 MHz) was used for this gating because it was very easy to set the trigger threshold. The exponential energy decay was detected by a photomultiplier tube (Hamamatsu) terminated in a small load (typically 200 Ω) for speed and recorded on a digital storage oscilloscope (LeCroy 9400) for later transfer to a PC. In a second method, the AOM was continually chopped with a 50% duty cycle at about 10 kHz. As the laser was scanned through a mode (asynchronous with respect to the chopping), a digital scope triggered on the chopping waveform could record the buildup and subsequent ringdown of light in the mode in much the same fashion as the first method.
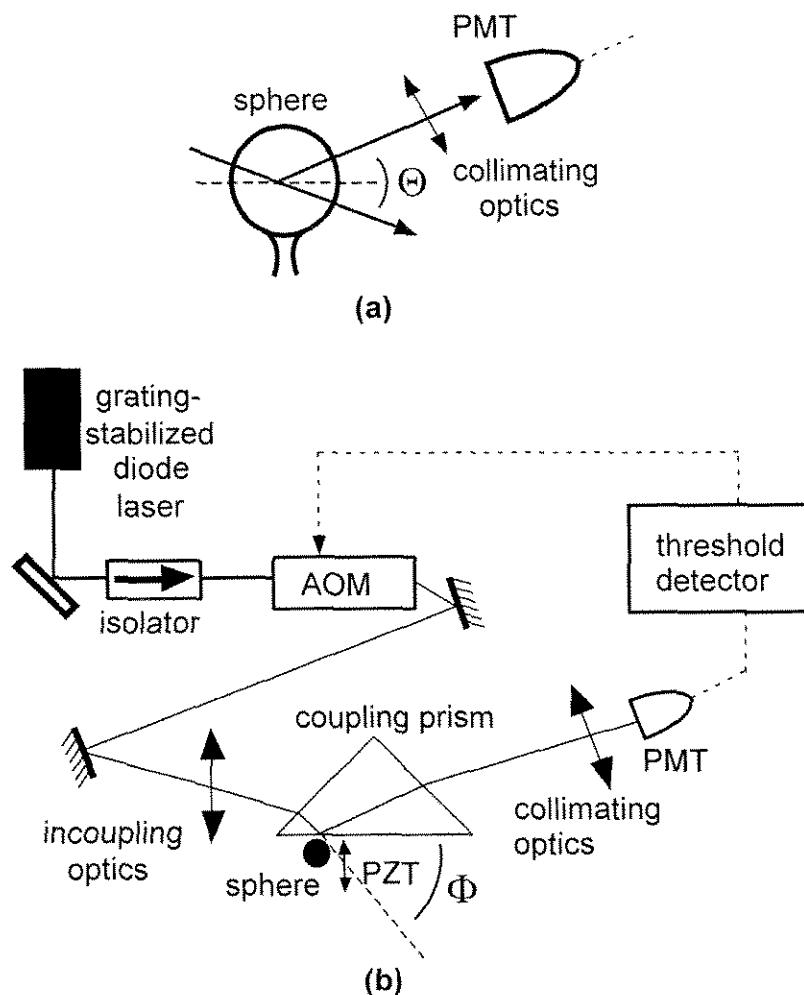
Figure 3.2: The incoupling excitation was at an angle Θ to the sphere equatorial plane in order to excite a precessing mode. The outcoupled light in (a) will give a typical "transmitted" intensity profile. Ringdown measurements in (b) used this Lorentzian buildup to gate off an acousto-optical modulator (AOM) as a fast shutter.

Another important issue with regard to mode coupling is the fact that the buildup of light in the sphere can cause thermal bistability if more than about 10 μW of power is allowed to circulate in a few hundred μm diameter sphere [48]. Furthermore, the Q of the sphere is "loaded" by the coupling prism, which causes severe line broadening, as will be discussed later. Fortunately, the solution to both of these problems is very simple. Moving the sphere away from the prism exponentially diminishes the loaded

Q contribution, and at the same time attenuates the circulating power, helping to overcome any thermal problems.

In Figs. 3.3 (a) - (c), the field energy as a function of time is plotted for the highest Q's recorded at the three wavelengths, corresponding to $(8 \pm 1) \times 10^9$ at 670 nm in a sphere of diameter $D = 750$ μm, $(7.5 \pm 1) \times 10^9$ at 780 nm with $D = 800$ μm and $(7.2 \pm 1) \times 10^9$ at 850 nm for $D = 680$ μm. In the case of the two NIR wavelengths, either the 670 nm laser or a 633 nm HeNe laser was overlapped for visual alignment of the incoupling beam spot on the prism with the equatorial plane of the sphere. Though mode splittings are seen for $Q \gtrsim 5 \times 10^8$, as reported in [51], the particular results reported here have an observed resonator energy decay well fit by $\exp -t/\tau = \exp -\omega t/Q$, corresponding to excitation of only one eigenmode when the light was gated off.

In each case, the ringdown time is on the order of a few μs, which is much longer than either the RC time constant of the PMT (typically ~ 100 ns) or the acoustic delay of the AOM (typically ~ 10 ns). These Q's were repeated in at least one other sphere for all three wavelengths. The high Q was never seen in instances where the sphere had contacted the coupling prism during the process of alignment. The highest Q's were also never seen in spheres below 500 μm. As documented in [45], we also see a time dependence of the Q due to water absorption on the surface as will be discussed in Sec. 3.2.2, and the data in Fig. 3.3 all correspond to measurements made within 1.5 minutes of fabrication of the sphere. It certainly took much practice and a considerable amount of manual dexterity to complete the whole process in this amount of time.

To make contact with other measurements of resonator loss, we use the cavity finesse, $\mathcal{F}$, for a free spectral range corresponding to an additional wavelength around the sphere's circumference [53]. For $(D, \lambda) = (345$ μm, 670 nm$)$, $\mathcal{F} = 2.3 \times 10^6$ which is the highest value yet reported for an optical interferometer, while for $(D, \lambda) = (680$ μm, 850 nm$)$, $\mathcal{F} = 2.2 \times 10^6$ (exceeding the value $\mathcal{F} = 1.9 \times 10^6$ at 850 nm in Ref. [54]).
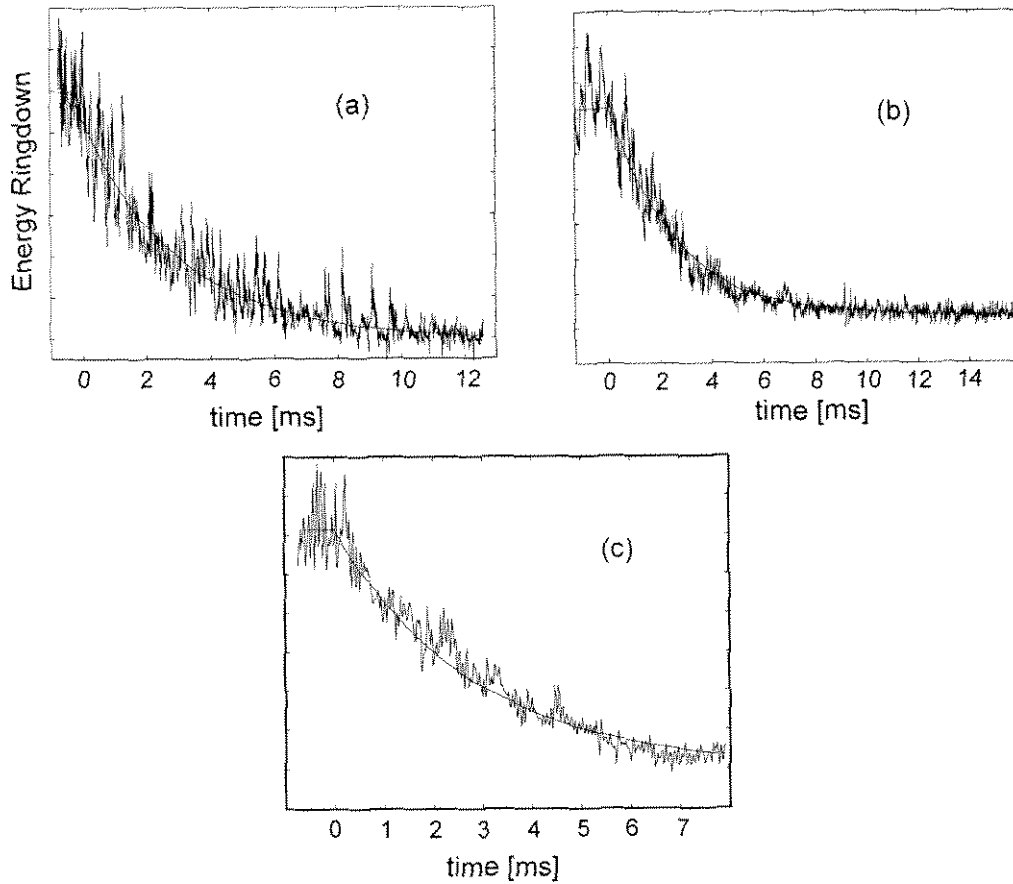
Figure 3.3: Microsphere ringdown measurements along with exponential fits. The corresponding Q's inferred via $Q = \omega\tau$ give $(8 \pm 1) \times 10^9$ at 670 nm with $D = 750$ μm (a), $(7.5 \pm 1) \times 10^9$ at 780 nm with $D = 800$ μm (b) and $(7.2 \pm 1) \times 10^9$ at 850 nm for $D = 680$ μm (c).

3.2   Measurements

3.2.1   Wavelength Dependence of the Q

In Fig. 3.4, the measurements above are plotted along with the point from Ref. [45] at 633 nm with $D = 750$ μm, which, taken together, are the highest Q's for WGMs in the optical domain achieved to date. Also shown in Fig. 3.4 is the expected variation for Q *if* bulk material absorption was the limit (i.e., $Q_{mat} = nk/\alpha_{mat}$, with refractive index $n = 1.452$, $k = 2\pi/\lambda$ and the absorption coefficient $\alpha_{mat}(\lambda)$ in very low-*OH* fibre-grade fused silica given in [55]). Although the two data points at (633, 670) nm approach Q_{mat}, the data at (780, 850) nm in the NIR fall substantially short.
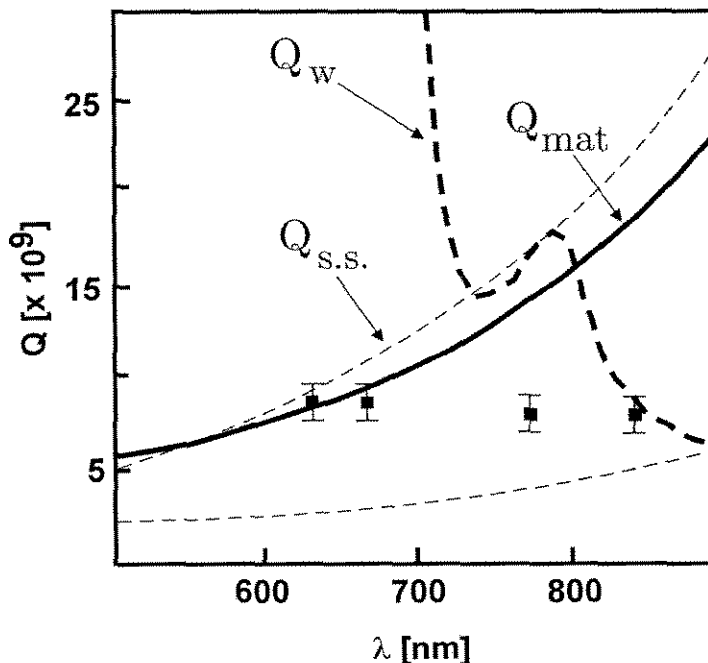
Figure 3.4: The highest Q values measured at 670, 780 and 850 nm are shown, along with the wavelength dependencies for Q_{mat} (thick, solid line) limited by intrinsic surface scattering, Q_{ss} for surface scattering (the region between the thin, dashed lines shows a bound due to AFM surface data) and Q_w for an adsorbed layer of water (thick, dashed curve). The point at 633 nm is from Ref. [45].

3.2.2 What is Limiting the Q?

Surface Roughness

One possible reason for reduced Q is surface contamination, although the cleaning procedure outlined in Sec. 3.1.1 was developed to eliminate virtually all diffuse scattering from particles on the preform surface. Furthermore, as described in Sec. 2.2.2, the limit set by radiative losses is irrelevant for these "large" spheres with $D \gg 20\lambda$.

In the absence of a more rigorous test of the cleaning procedure, scattering from surface inhomogeneities is now investigated as another candidate loss mechanism. The formation of the sphere surface is determined by the annealing history of the silica ball as it is withdrawn from the flame and cooled. Although scanning electron microscopy (SEM) was initially attempted, high resolution atomic force microscopy (AFM) proved to be much more fruitful in providing quantitative data on the surface quality of the microspheres. Surface morphology was measured in a 20 nm × 20 nm square grid of 256×256 points near the sphere equator, with a nominal vertical resolution of 0.01 nm. Features with curvature on this scale could reliably be reconstructed.

These data were organized as 256 line scans of 256 points each (i.e., heights $h_i(x)$, with $x(j) = 20j/256$ [nm], $i, j = \{1 \dots 256\}$ and $\langle h_i(x) \rangle_x = 0$), of which three typical line scans are shown in Fig. 3.5(a). Calculating the standard deviation $\sigma_i^2 = \langle h_i(x) h_i(x) \rangle_x$ of surface roughness from each line scan results in an average $\bar{\sigma} = (2.5 \pm 0.7)$ nm. Similarly, for each line scan $R_i(u) = \langle h_i(x) h_i(x + u) \rangle_x$ is calculated and an average correlation function $R(u) = \langle R_i(u) \rangle_i$ constructed, as in Fig. 3.5(b). A statistical correlation length of $B = (5 \pm 0.5)$ nm can be identified from this plot. The Fourier transform $P(k)$ of $R(u)$ is shown in Fig. 3.5(c) and gives the "power spectrum" of surface fluctuations in reciprocal space, which is correspondingly flat out to a spatial frequency $k_0 \sim 1/B$. Though no analytic model has been constructed, note that the functional form of $R(u)$ has characteristics of both $R_1(u) \sim \frac{\sin(u/B)}{u/B}$ $(P_1(k) \sim 1 - \theta(|k| - B)$, with $\theta(k)$ the step function) as for bandpass, additive white Gaussian noise and $R_2(u) \sim \exp(-|u|/B)$ $\left(\text{or } P_2(k) \sim \frac{1}{1+(kB)^2} \right)$, as for

a random telegraph signal, with the interpretation of B as the correlation length the same in both cases. It was verified that an increase in the scan region to 100 nm × 100 nm while accordingly decreasing the resolution (as set by the 256 point sample) did not affect the surface height distribution data, but did inhibit the extraction of B from surface correlations due to spatial undersampling.
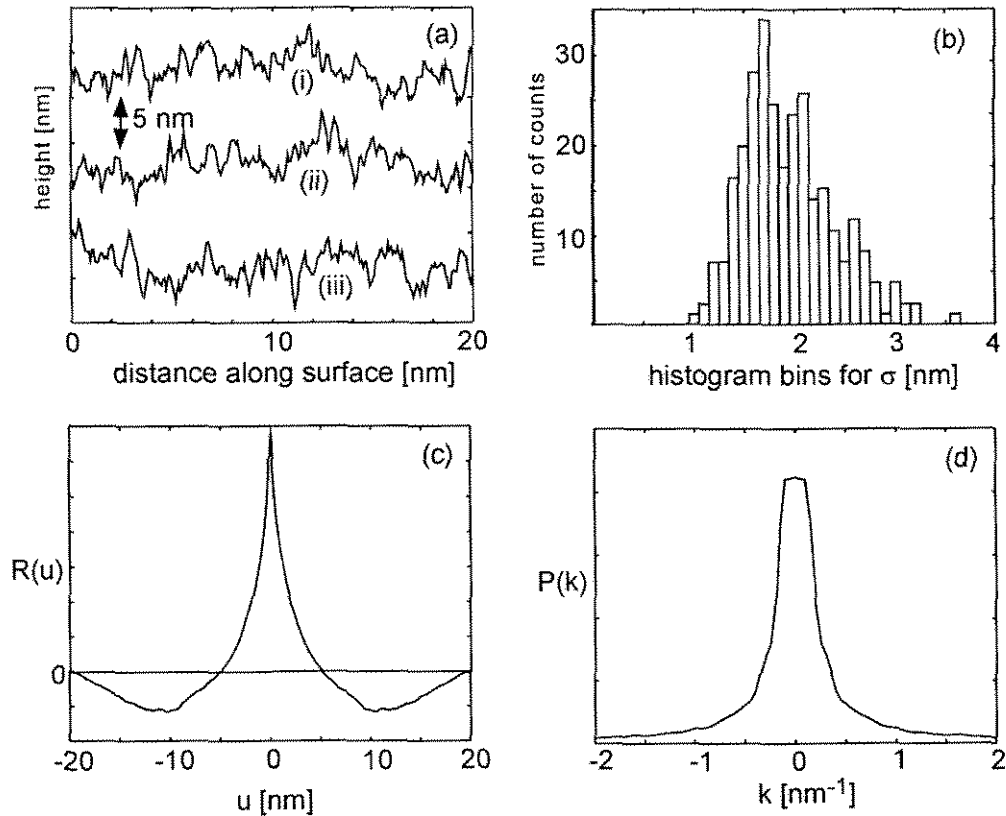
Figure 3.5: (a) Typical line scans of surface data showing features at nm resolution. In (b), the distribution of averaged surface roughness for 256 different line scans is shown, from which $\sigma = (1.7 \pm 0.5)$ nm. (c) Correlation function $R(u)$ and (d) estimate of its Fourier Transform, the power spectral density $P(k)$, shown after averaging over 256 scans of the type in (a) on a 20 nm square grid, as explained in the text. Both support the identification of the correlation length $B \sim 5$ nm.

Given (σ, B), the surface scattering limited $Q_{s.s.}$ must take into account precisely how the energy of the resonant mode field distribution is scattered into the complete set of modes pertinent to the spherical geometry. For example, surface scattering limits are expected to depend upon radial mode number q, but because the modes

excited here have $q \lesssim 3$, a simple estimate may be based upon scattering from particles of dielectric constant $\varepsilon = n^2$ and volume $\sigma B^2 \ll \lambda^3$. Such scatterers will have an absorption cross-section scaling as $(\text{volume})^2 / (\text{wavelength})^4$ and scattering density proportional to $(1/\text{volume})$, so the effective absorption coefficient for these scatterers is $\sim k^4 \sigma B^2$. Using the volumetric ratio $\sim \sigma / \sqrt{\lambda D}$ of a surface layer of such particles to that of the mode, one finds an effective absorption coefficient which scales as $k^4 (\sigma^2 B^2) / \left(\sqrt{\lambda D} \right)$ so that

$$Q_{\text{s.s.}} \sim \frac{3\varepsilon (\varepsilon + 2)^2}{(4\pi)^3 (\varepsilon - 1)^{5/2}} \frac{\lambda^{7/2} D^{1/2}}{\sigma^2 B^2}. \tag{3.1}$$

An equivalent expression can be derived using a different approach based on surface scattering from planar waveguides [56, 57, 58] by substituting the ratio of external to internal mode volumes of the sphere $\sim \sqrt{\lambda/D}$ for the ratio of external to internal guided power in the waveguide. Using (σ, B) from above and $(D, \lambda) = (800 \ \mu\text{m}, 800 \ \text{nm})$, we estimate $Q_{\text{s.s.}} \sim (7.5 \pm 5) \times 10^9$ which compares well to the measurements with $Q \sim 8 \times 10^9$.

Size Dependence of Q

In Fig. 3.6, the highest Q achieved as a function of D is plotted for my work with spheres at fixed $\lambda = 670$ nm with the caveat that the repeatability in obtaining the "highest" Q for a given D accounts for the considerable scatter in the data. Nevertheless, a fit $\propto D^{1/2}$ as suggested by Eq. (3.1) yields $\sigma B \sim 5$ nm^2, which coincides well with our analysis of the experimental AFM data. Though the trend in Fig. 3.6 argues for measurements with still larger spheres, our fabrication technology is not suited for D much in excess of 1 mm.

Water Absorption on the Surface

As in [45], a time dependent reduction in Q is seen, with the highest Q data measured within $\Delta t = 1.5$ minutes of fabrication. A simple mechanism for this process is based on the hydration of a "fresh" silica surface in air [59, 60]. When a sphere is first
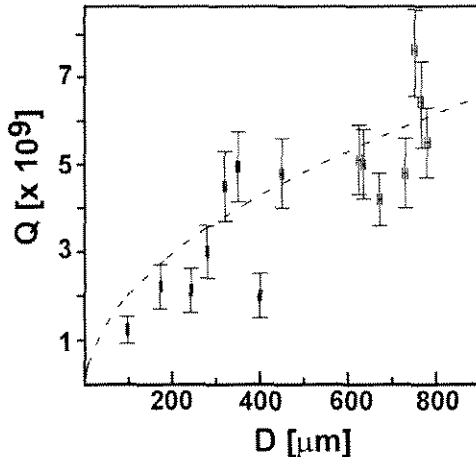
Figure 3.6: The highest Q values measured in spheres of diameter D at 670 nm. The dependence $Q_{ss} \propto D^{1/2}$ is suggested by Eq. 3.1.

formed from a rod of SiO_2, there are dangling surface silicon bonds, which then undergo changes to their chemistry depending upon the surrounding environment. In air, O_2 molecules see a potential minimum near the silica surface and are absorbed by a physical bond with a typical time scale of 10^{-7} s. Dissociation of O_2 can further reduce the surface energy in a process known as chemisorption, which has a time scale of 10 s (the competing desorption process has a 350 s time scale). Hydrogen, in the form of hydroxyl radicals, then forms a chemical bond with the oxygen with a characteristic time scale of $\tau_a \sim 50$ s, depending upon the presence of water in the air as a hydroxyl source. This surface water layer is assumed to cause the time dependent light absorption (and subsequent Q degradation) due to O-H bond resonances. In fact, for a water layer of width $\delta \ll \lambda/2\pi$ occupying a fraction of the total mode volume $\propto \delta/\sqrt{\lambda D}$, and absorption coefficient $\beta_w(\lambda)$, we estimate

$$Q_w \sim \sqrt{\frac{\pi}{8n^3}} \frac{D^{1/2}}{\delta \lambda^{1/2} \beta_w(\lambda)}, \tag{3.2}$$

which shows the same $D^{1/2}$ dependence as $Q_{s.s.}$. Though the exact chemistry of the surface adsorption process would seem to be very important in determining both $\beta_w(\lambda)$ and δ at the time Δt of our measurements, an estimate using β_w of bulk water

in the 500 nm to 900 nm range from Ref. [61] and $\delta \sim 0.2$ nm as appropriate for 1 to 2 monolayers gives $Q_{\mathrm{w}} \sim 7 \times 10^{10}$ for our data point at 670 nm with $D = 750$ μm (likewise, the data of Fig. 3.6 at 670 nm would predict δ about an order of magnitude too large). This estimate favors material absorption and surface scattering losses at long visible wavelengths and small Δt. However, there is a rapid decrease to $Q_{\mathrm{w}} \sim 8 \times 10^{9}$ at 850 nm (with $D = 680$ μm), strongly suggesting that water absorption plays a fundamental role further into the NIR. The dependence suggested by Eq. 3.2 is also shown in Fig. 3.4.

There is a real possibility that even higher Q could be recorded in a dry environment as $\Delta t \rightarrow 0$, as chemical changes in the surface due to oxygen alone should not cause the absorption. This immediately suggests drying of the air as an approach to maintaining high Q. At STP and a relative humidity of 50%, there is a water vapor partial pressure of $\frac{n_{water}}{n_{air}} \sim 11,500$ ppm in air. Hence, I next attempted to implement a dry glove box into the fabrication and measurement scheme, but dry nitrogen purging made it very difficult to light the torch. I then investigated an industrial laboratory gas dryer based on dehumidification of the Caltech compressed air line using a molecular sieve desiccant that can produce $\frac{n_{water}}{n_{air}} < 1$ ppm. This should translate into a lengthening of Q preservation in such an atmosphere from $100s$ to on the order of many hours. Such a system was installed, but further work was not pursued, since I now turned my attention to doing some atomic physics with these spheres.

Chapter 4   Cavity QED with High Q Whispering Gallery Modes

Cavity QED has proven to be a fertile arena in which to study coherent interactions between single atoms and photons [62]. In the optical domain, the cavities employed to achieve strong coupling have been Fabry-Perot microresonators with finesse $\mathcal{F} \sim 10^5$, as in the initial work of Ref. [63] and continuing to the recent demonstrations of real-time cavity QED with individual atoms [64, 65]. By contrast, the WGMs offer an alternative avenue to strong coupling with the potential to surpass Fabry-Perot cavities with respect to certain key parameters. For example, such resonators have the capability of achieving extremely long photon storage lifetimes while maintaining a strong dipole coupling to an atomic [40], ionic [66], or molecular [67] species via the small volume of a single mode, leading to the potential for ratios of coherent coupling to loss mechanisms in excess of 10^3.

Motivated by these prospects, I will now discuss measurements of the interaction of atoms with the external evanescent field of a WGM in a domain in which cavity QED effects become important. More specifically, there are significant modifications of cavity transmission due to the coupling of $\bar{N}_T \sim 1$ Cesium (Cs) atom in a thermal gas with a single resonant WGM at the level of a few photons in the mode. The possibility for sensitivity to $\bar{N}_T \sim 1$ atom in the microsphere's evanescent field in the face of Doppler broadening of roughly 100 times the natural linewidth is a consequence of the novel features of the microspheres used here, namely small size (with radius $a < 60$ μm and mode volume $V_m \sim 10^{-8}$ cm^3) and narrow linewidth (with $Q_1 = 5 \times 10^5 \leq Q \leq Q_2 = 5 \times 10^7$). Although it is clearly desirable to reduce the Doppler broadening by coupling to cold atoms, these experiments are an exciting initial step towards realizing the potential of WGMs for long-lived coherent dynamics in cavity QED.

4.1 UHV Sphere Apparatus and Data Acquisition

The actual setup is depicted in Fig. 4.1 and consists of a grating stabilized diode laser of a few hundred kHz linewidth coupled into a microsphere via frustrated total internal reflection from a prism [43]. The microspheres, of index $n = 1.452$, were fabricated using the procedure outline in 3.1.1 and then mounted inside the vacuum system.
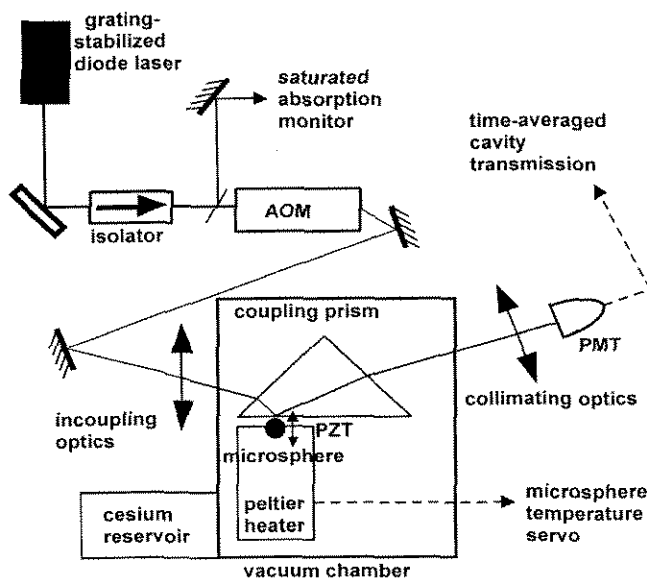
Figure 4.1: A simplified schematic of the experimental setup is shown along with a detailed discussion in the text. The microsphere (shown as a circle up against the prism) is surrounded by a dilute atomic vapor.

The main vacuum chamber is shown in Fig. 4.2 and consisted of a 5 inch square hollow piece of fused silica mated (by Glass Instruments, Pasadena) to a 4 1/2 inch glass to metal conflat flange on one side and a 1.33 inch glass to metal "quickflange" on the other. The microsphere coupling apparatus was mounted onto a matching 4 1/2 inch conflat flange with a port for electrical feedthroughs, and this was carefully screwed into the bottom of the main chamber every time a new sphere was made. The quickflange led to a six-way cross, from which there were ports for a turbo roughing pump, a cesium cold finger, a 20 l/s ion pump and a window on the top.
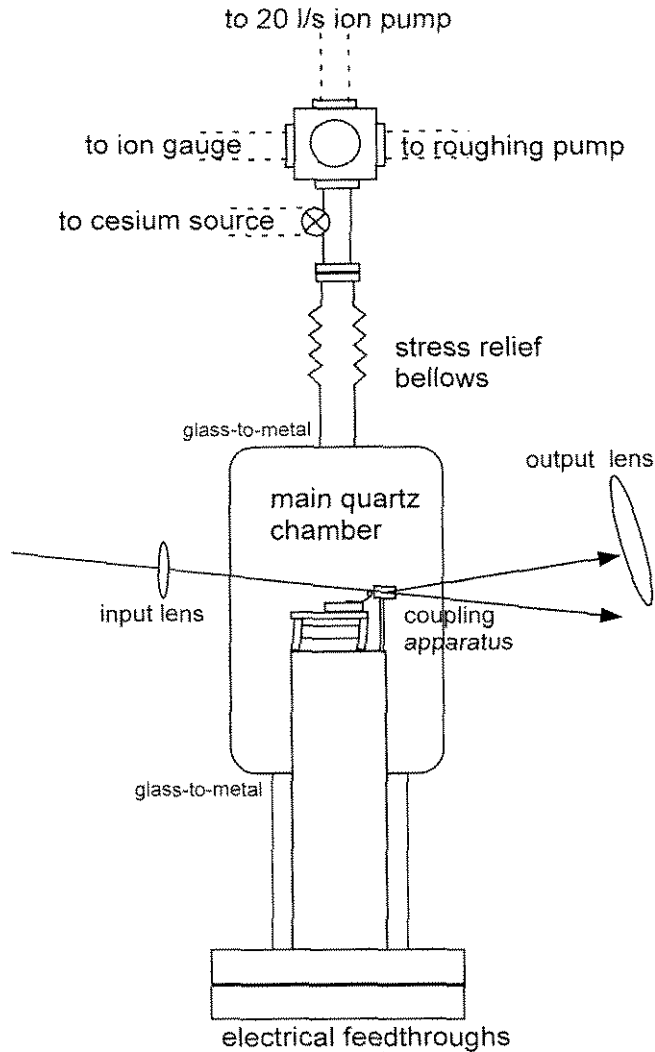
Figure 4.2: The vacuum chamber design for this experiment is shown schematically (not to scale). The chamber was fabricated by Glass Instruments (Pasadena, CA) from high grade quartz. Its optical properties were found to be adequate for this experiment, though sphere replacement was inconvenient.

The sphere was mounted close to the prism on a homemade micro-translation stage using a specially made vacuum-compatible piezo stack (EDO Corporation, Salt Lake City) that had 20 μm travel for 1 kV of bias. It turned out to be very difficult to maintain Q much higher than about 1×10^8 in these experiments for several reasons. First, the sphere was inevitably bumped against the prism during the process of pre-aligning the sphere on the translation stage and the subsequent bolting of the bottom flange to the main chamber. Second, the spheres usually were exposed to air for at least 30 minutes before the system could be initially pumped down. Finally, typical spheres in these experiments were 100 μm diameter or less (to keep the mode volumes small), which is much smaller than the sizes with which the highest Q results of Sec. 3.2.1 had been obtained.

In any case, the range $Q_1 \rightarrow Q_2$ discussed here was accessed by using different spheres and various modes of the same sphere, by loading the bare Q of any individual mode with the prism outcoupler, and by waiting for the gradual degradation of the Q due to repeated contact of the sphere with the prism during day-to-day process of optimizing the coupling in vacuo. In fact, it was necessary to couple to higher order WGM radial modes ($q \sim 3 - 4$) in order to maintain an acceptable coupling efficiency, as the incoupling lens was mounted outside the vacuum chamber. For this experiment, this lens was a doublet of focal length 14 cm. In addition, the light was injected off of the horizontal symmetry plane of the microsphere by an angle $\Theta \sim 10° - 15°$ to take advantage of the slight ellipticity of the spheres (typically ~ 3 %) and excite the so-called precessing modes as described in 3.1.2 allowing the direct emission from a WGM to be separated from the reflected exciting beam and collected onto a PMT. A single travelling-wave mode (q, l, m) was thus excited. It is degenerate *only* with the counter-rotating $(q, l, -m)$ mode, which for $Q \lesssim 5 \times 10^7$ is unexcited as evidenced by the absence of any resolved doublets in the transmitted intensity [51].

The microsphere assembly was thermally contacted to a Peltier element using indium solder, and the Peltier element was heat sunk to a copper block with temperature conductive epoxy. Temperature changes were monitored with a thermistor, compared to a manually set reference potentiometer and then fed back to the Peltier

element for active temperature control. The reference potentiometer was used to tune a given cavity resonance ω_{cavity} to the frequency ω_{atom} of the $F = 4 \longleftrightarrow F' = 5$ hyperfine transition of the Cs $D2$ line (lifetime $\tau = 1/2\gamma \simeq 32$ ns, see Fig. 6.1) at $\lambda_{\text{atom}} = 852$ nm, relying primarily upon the thermally induced change in the sphere's index of refraction. Because there was no active stabilization of the cavity to the atomic line *per se*, residual drifts of the mode $\sim \pm 500$ kHz over 10 minutes with respect to the atomic line were present, but could be compensated manually with very little trouble. The piezo-controlled translation stage allowed fine control of the prism-sphere distance. A picture of this completed system is shown in Fig. 4.3.
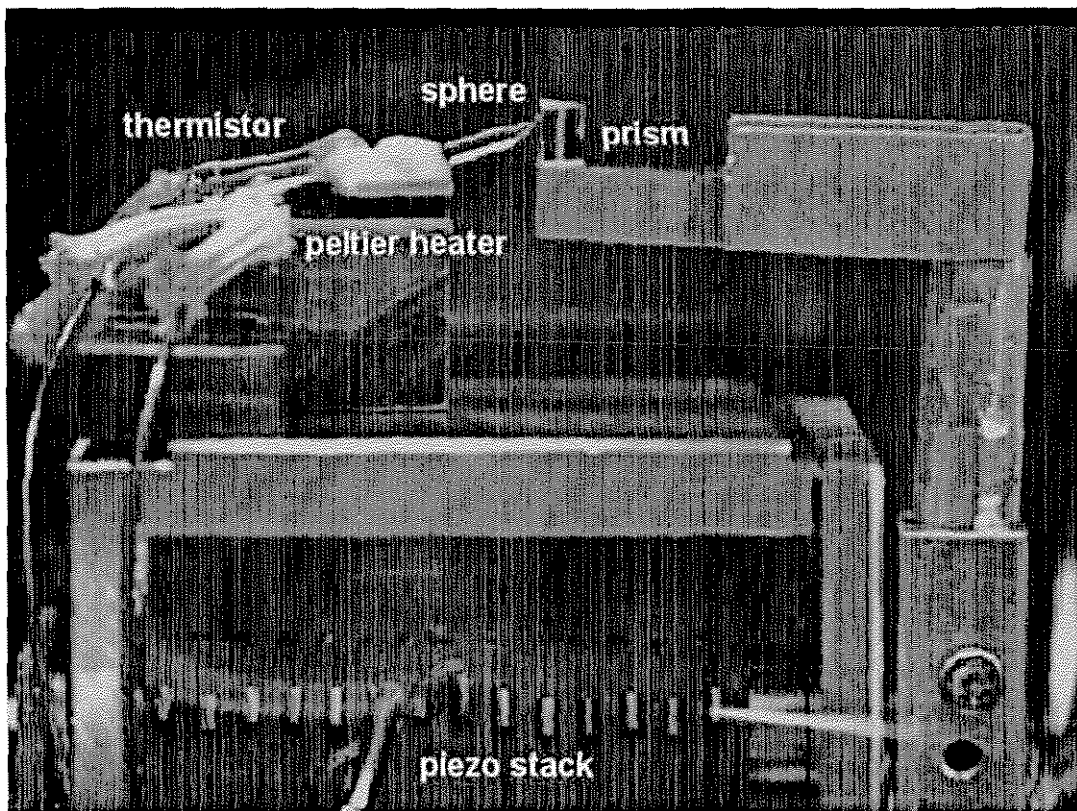
Figure 4.3: A close-up photograph through the quartz chamber at the micrsophere coupling apparatus. The peltier heater and thermistor for the sphere temperature tuning servo are obvious, along with the micropositioning system and optics.

The vacuum system itself was pumped to a background pressure of 10^{-8} torr and contained a thermal Cs reservoir, leading to an atomic density of typically 2×10^9

atoms/cm^3, as monitored by optical absorption in the vapor. Under the assumption that this background Cs density is a fair representation of the atomic density in the evanescent field, the total mode volume external to the sphere $V_m^e \sim 5 \times 10^{-10}$ cm^3 implying that $\bar{N}_T \sim 1$ atom in this dilute vapor interacts with the mode volume.

The procedure for data acquisition was to scan the frequency ω_L of the incident laser while recording the intensity transmitted by the microsphere, with averaging times of several minutes required to achieve an acceptable signal-to-noise ratio. A digital storage oscilloscope (Lecroy 9400) was used for the averaging and the resulting traces transferred to a PC for analysis. The frequency of the incident laser is independently monitored via saturated absorption spectroscopy in a separate Cs cell. For small frequency scans of ± 25 MHz, a second method consists of FM locking of the laser to the atomic line [52] and frequency scanning using a double-passed acousto-optic modulator.

4.2 Observations

As shown in Fig. 4.4 for the case of coincident cavity ω_{cavity} and atomic ω_{atom} resonance frequencies, sub-Doppler features are clearly observed as "absorption dips" in the transmission spectrum $T(\omega_L)$ obtained upon averaging the transmitted cavity intensity for several minutes. Other scans demonstrate that when ω_{cavity} is tuned away from ω_{atom}, the absorptive feature in $T(\omega_L)$ does not similarly shift. It was impossible to remove the atoms completely for further verification of this effect, as this would have involved either tuning the sphere resonance $\gtrsim 500$ MHz off of the Doppler line or pumping the atoms from the vicinity of the sphere. With the present set-up, it would be impossible to maintain a constant sphere/prism gap (and hence, the cavity transmission) during either of these procedures.

4.2.1 Q Dependency

From data as in Fig. 4.4 over a range $Q_1 \leq Q \leq Q_2$, Fig. 4.5 shows the width $\Delta \nu$ of the narrow absorption feature versus the *inverse width* $\Delta \Omega^{-1}$ of the broad
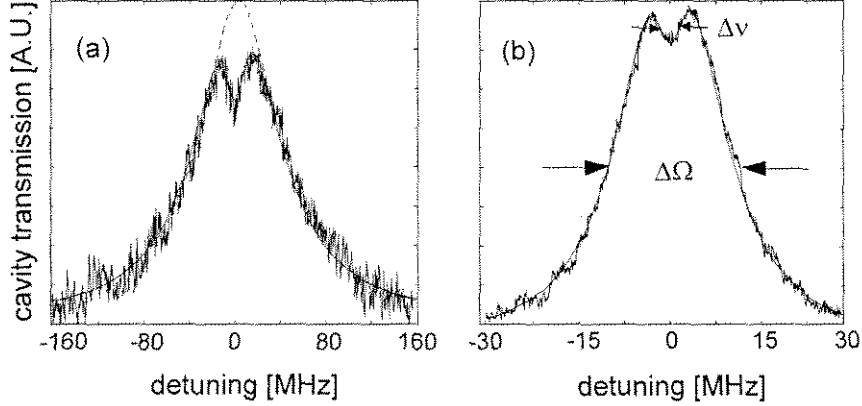
Figure 4.4: The transmitted intensity $T(\omega_L)$ for single WGMs is shown for (a) $Q = 1.5 \times 10^6$ and (b) $Q = 4 \times 10^7$. For the data of (a), we infer from a phenomenological model [solid line, see Eq. (4.4)] that the dip width is driven by a set of atoms selected by the cavity geometry. As the Q increases (b), the width of the absorptive feature narrows, suggestive of a class of atoms with small velocity. Zero detuning corresponds to the common atom-cavity resonance ($\omega_L = \omega_{\text{atom}} = \omega_{\text{cavity}}$). The inferred empty cavity transmission is indicated in (a) (dashed line).

transmission function, with ($\Delta\nu$, $\Delta\Omega$) defined in Fig. 4.4. Note that $\Delta\Omega$ serves as an indirect measure of the linewidth of the empty cavity and hence of Q^{-1} via $q \equiv \omega_{\text{cavity}}/\Delta\Omega$. Given that the Doppler HWHM in the Cesium vapor is $\Delta\omega_d\sqrt{\ln 2}/2\pi \sim 190$ MHz and that the data in Fig. 4.5 are taken in a linear regime, it is perhaps surprising that $\Delta\nu \ll \Delta\omega_d$. This will be discussed extensively in Sec. 4.3.

4.2.2 Intracavity Photon Number Calibration

The important issue of how to calculate the efficiency with which light was collected immediately arises in order to estimate the mean number of photons in the cavity, and so calibrate the transmitted intensity axes in Fig. 4.4. The WGM linewidth proper (HWHM) $\kappa = \kappa_i + \kappa_p(d)$ is a sum of the intrinsic linewidth κ_i (due to absorption in the bulk silica, scattering by surface inhomogeneities, contamination, etc.) and the loaded linewidth due to the prism $\kappa_p(d)$ which depends exponentially on the distance d between the sphere and the prism as $\kappa_p(d) = \kappa_p(0) \exp(-4\pi d/\lambda)$. By monitoring both the cavity transmission and the mode linewidth as a function of d, it is found
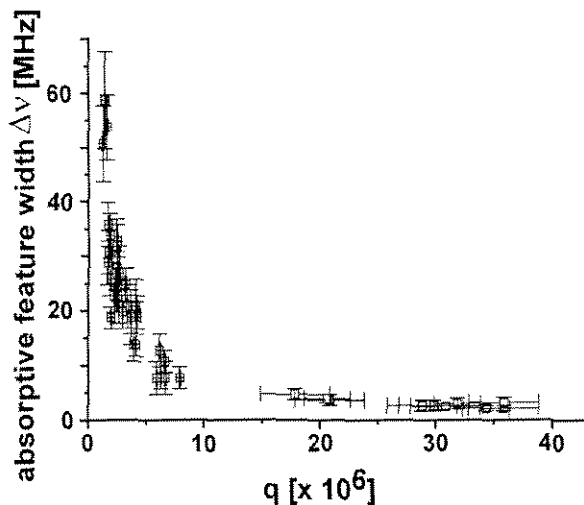
Figure 4.5: The width $\Delta\nu$ of the absorptive feature plotted against $q \equiv \omega_{\text{cavity}}/\Delta\Omega$ ($\Delta\nu, \Delta\Omega$ defined in Fig. 4.4), where the relationship of q to the actual mode Q is discussed in the text.

that $\kappa/\kappa_p(d_0) \sim 5$, the factor by which the intra-cavity photon number would be underestimated if based solely upon the power at the loss channel measured (i.e., via the prism at a mean separation $d_0 \sim 200$ nm). Another factor of two must be included to account for the use of the precessing modes and the two outcoupled beams in the prism.

Operationally, it is ensured that the data are acquired in a linear regime with measurements of the sort shown in Fig. 4.6(a). For a specific mode with $Q \sim 1.5 \times 10^6$, the depth of the absorptive feature on resonance as a function of the transmitted intensity on resonance is seen to exhibit a linear relation up until $m_0 \sim 10$ intracavity photons, beyond which it begins to saturate. More generally, using the procedure outlined above and a calibration of the power out of the transmitted port, the intracavity photon number is estimated m_0 to vary between $0.5 \leq m_0 \leq 30$ for our data, with saturation for $m_0 \gtrsim 10$.

4.3 Model for the Interaction

The starting point in an attempt to model these observations is the set of Heisenberg equations of motion for a collection of moving, two-level atoms (atomic lowering operators $\{\sigma_{j,-}\}$, velocities $\{\mathbf{v}_j\}$ and excited state linewidth $\gamma_\perp$) coupled strongly (dipole coupling strengths $\{g_j\}$) to a single WGM (wave vector $\mathbf{k}$, photon annihilation operator a). In the weak-field limit [9, 68], with $\langle a \rangle = \alpha$ and $\langle \sigma_{j-} \rangle = \beta_j$, these equations can be reduced to a coupled set of equations for the field and the atomic dipoles,

$$\dot{\alpha} + (\kappa - i\delta_{\text{cavity}})\,\alpha = \sum_j g_j \beta_j + \epsilon \qquad (4.1)$$

$$\dot{\beta}_j + (\gamma_\perp - i\,(\delta_{\text{atom}} + \mathbf{k}\cdot\mathbf{v}))\,\beta_j = -g_j\alpha\,.$$

Here, $\kappa = \omega_{\text{cavity}}/2Q$ is the cavity HWHM with no atoms, $\epsilon e^{-i\omega_L t}$ is the driving field and $\delta_{\text{cavity, atom}} = \omega_L - \omega_{\text{cavity, atom}}$ are the cavity and atomic detunings from the driving field at ω_L. The replacement $\sum_j \to \int d^3\mathbf{v}\,d^3\mathbf{r}_0\,p\,(\mathbf{v},\mathbf{r}_0)$ is made for $\bar{N}_T$ atoms all with the same velocity distribution $p\,(\mathbf{v}) = \int d^3\mathbf{r}_0\,p\,(\mathbf{v},\mathbf{r}_0)$ which is assumed to be Maxwell-Boltzmann, and a uniform position distribution $p\,(\mathbf{r}_0) = \int d^3\mathbf{v}\,p\,(\mathbf{v},\mathbf{r}_0) = \bar{N}_T/V_m \equiv \rho$, with ρ as the atomic density and V_m the mode volume. Furthermore, taking $g_j\,(t) = g_j\,(\mathbf{v}_j t + \mathbf{r}_0)$, this set of equations 4.1 can be reduced to the following single equation for the field,

$$
\begin{aligned}
\alpha\,(t) = \; & -\int_0^{t-t_0} dt_1\, e^{-(\kappa - i\delta_{\text{cavity}})t_1} \int d^3\mathbf{v}\,d^3\mathbf{r}_0\,\rho\,p\,(\mathbf{v})\,g\,((t - t_1)\,\mathbf{v} + \mathbf{r}_0) \qquad (4.2) \\
& \int_0^{t-t_0-t_1} dt_2\,\alpha\,(t - t_1 - t_2)\,g^*\,((t - t_1 - t_2)\,\mathbf{v} + \mathbf{r}_0)\,e^{-(\gamma_\perp - i(\delta_{\text{atom}} + \mathbf{k}\cdot\mathbf{v}))\tau} \\
& + \epsilon/\,(\kappa - i\delta_{\text{cavity}})\,.
\end{aligned}
$$

Assuming a time-independent steady-state for the intracavity field $\alpha\,(t) = \alpha_{\text{ss}}$ and classical atomic trajectories unaffected by the cavity field, the transmission function $t(\omega_L) = \kappa\alpha_{\text{ss}}/\epsilon$ for the ratio of transmitted to incident field amplitudes can be sim-

plified into the following form:

$$t\left(\omega_L\right) = \frac{\kappa}{\kappa - i\delta_{\text{cavity}} + g_0^2 \overline{N}_T \chi(\omega_L)} \ . \tag{4.3a}$$

Using the mode function $\psi\left(\mathbf{r}\right)$, the atomic dipole coupling rate (vacuum Rabi frequency) for a single atom is rewritten as $g\left(\mathbf{r}\right) = g_{\text{max}}\psi\left(\mathbf{r}\right)$ with $g_{\text{max}} = \sqrt{3c\lambda^2\gamma_\perp/4\pi V_m}$ so that $g_0 = g\left(a\right)$ is the value at the surface of the sphere (though the WGM field maximum is actually inside the sphere close to the surface as shown in Fig. 2.2, the maximum value accessible to the atomic vapor, $g_0/2\pi \sim 20$ MHz, is right at the surface). The quantity

$$\chi(\omega_L) \equiv \frac{1}{V_m} \int d^3\mathbf{v}\, p\left(\mathbf{v}\right) \int d^3\mathbf{k}\frac{\left|\phi\left(\mathbf{k}\right)\right|^2}{\gamma - i\left(\delta_{\text{atom}} + \mathbf{k}\cdot\mathbf{v}\right)}, \tag{4.4}$$

plays the role of an effective susceptibility for the atomic sample in its interaction with the WGM. The Fourier transform of the mode function,

$$\phi\left(\mathbf{k}\right) = (2\pi)^{-3/2} \int d^3\mathbf{r}\,\psi\left(\mathbf{r}\right)\exp\left(-i\mathbf{k}\cdot\mathbf{r}\right), \tag{4.5}$$

is normalized such that $V_m = \int d^3\mathbf{k}\left|\phi\left(\mathbf{k}\right)\right|^2 = \int d^3\mathbf{r}\left|\psi\left(\mathbf{r}\right)\right|^2$. Because it is extremely difficult to evaluate $\chi(\omega_L)$ exactly for the actual functions $\{\psi\left(\mathbf{r}\right), p\left(\mathbf{v}\right)\}$, calculations have been performed numerically for simplified approximations to $\psi\left(\mathbf{r}\right)$ external to the microsphere (e.g., $\psi\left(\mathbf{r}\right) \sim \exp\left(-2\pi\left(r-a\right)/\lambda\right)\exp\left(-\theta^2/\theta_0^2\right)\exp\left(im\phi\right)$ as an approximation to $\psi\left(\mathbf{r}\right) \sim h_l^{(1)}\left(kr\right)Y_{lm}\left(\theta,\phi\right)$). Via numerical integration, transmission functions $T(\omega_L) \equiv \left|t\left(\omega_L\right)\right|^2$ are found that are in quantitative accord with the measured spectra for low $Q \lesssim Q_0 = 5 \times 10^6$, but which deviate from the observations for $Q \gtrsim Q_0$ due to a near absence of *narrow features of width* $\sim \gamma$.

4.3.1 Ansatz for the Three Contributions to the Susceptibility

Nonetheless, these calculations motivate an *ansatz* which takes

$$\chi(\omega_L) \rightarrow \chi_A(\omega_L) \equiv \frac{1}{\bar{N}_T} \left(\bar{N}_d f_d \left(\delta_{\mathrm{atom}} \right) + \frac{\bar{N}_t}{\Delta\omega_t - i\delta_{\mathrm{atom}}} + \frac{\bar{N}_a}{\gamma - i\delta_{\mathrm{atom}}} \right), \qquad (4.6)$$

with $\bar{N}_d + \bar{N}_t + \bar{N}_a = \bar{N}_T$. The first component in Eq. (4.6) is physically motivated by noting that there must be a Doppler-broadened response

$$f_d \left(\delta_a \right) \sim (1/\Delta\omega_d) \exp \left(-\delta_{\mathrm{atom}}^2 / \Delta\omega_d^2 \right), \qquad (4.7)$$

due to velocity components tangential to the sphere in the direction of circulation of the mode. In addition, due to the geometry of the WGM, there is also significant transit broadening due to residence times of only $10^{-2}\tau$ for motion along the radial coordinate to $10^{-1}\tau$ along the $\hat{\mathbf{e}}_\theta$ direction (for which there is no Doppler broadening). Though any given atomic trajectory will yield a complicated function of both of these mechanisms (as in Eq. (4.4)), in Eq. (4.6), a transit broadened component of HWHM $\Delta\omega_t/2\pi \sim 25$ MHz is simply *added* on, corresponding to a linear trajectory of length $l_t \sim \sqrt{a\lambda/\pi}$ through the mode.

The solid lines through the data of Fig. 4.4 are based on Eq. (4.3a) with the *ansatz* of Eq. (4.6). For $Q \lesssim Q_0$, only the first two components with $\bar{N}_d = 0.75 \pm 0.05$ and $\bar{N}_t = 0.25 \pm 0.03$ are needed in order to explain *all traces*. From this, it is inferred that the Doppler-broadened set of atoms act only as a broad absorber (since $\Delta\omega_t < \kappa < \Delta\omega_d$) and that the absorptive dip at line center is accounted for by the width $\Delta\omega_t$, implying that cavity geometry is a dominant factor below Q_0. That is, the geometry of the cavity correctly accounts for the coexistence of both transit and Doppler broadening, where of course the simple sum of contributions suggested phenomenologically in Eq. (4.6) is more properly interpreted as an interplay of frequency scales as in Eq. (4.4).

By contrast, for $Q > Q_0$ it is essential to include a small component $\bar{N}_a \sim 0.015$ of

atoms which respond with their natural linewidth γ (the inclusion of which does not change the quality of the fits for $Q \lesssim Q_0$). In fact, this component now completely determines the properties of the narrow absorptive feature since $\kappa < (\Delta\omega_t, \Delta\omega_d)$. Although the need for this small subset of atoms moving slowly enough and in directions such that they are neither appreciably Doppler- nor transit-broadened is thus operationally motivated, their existence is also supported within the context of other measurements near dielectric surfaces, as, for example, in the work on Doppler-free evanescent-wave spectroscopy [69].

This simple model also allows the issue of the relationship of the quantity q of Fig. 4.5 to the actual empty cavity Q to be addressed. For $Q \lesssim Q_0$, the relationship $q \approx Q$ holds, with the inferred empty cavity transmission shown as the dashed trace in Fig. 4.4(a). However, for $Q > Q_0$, the two broadly absorbing components in $(\bar{N}_d, \bar{N}_t)$ (which account for most of the atoms) significantly alter the lineshape relative to that inferred for the empty cavity with $q \simeq Q/2.5$ for $Q = Q_2$ and the peak transmission of the cavity reduced by a factor ~ 4.5. In fact, within the context of the *ansatz* (Eq. (4.6)) for χ_A, the sub-natural widths in Fig. 4.5 are an artifact of how these different contributions (each of width $\geq \gamma$) combine to produce $T(\omega_L)$, as shown by the solid curve in Fig. 4.4(b).

Finally, the results of this phenomenological model are summarized in Fig. 4.6(b) where the inference of the effective atomic susceptibility χ_A in Eq. (4.6) is shown. The parameters $(\bar{N}_d, \bar{N}_t, \bar{N}_a) = (0.75, 0.25, 0.015)$ which best fit the data across the whole range in Q are used. Note that $\bar{N}_d + \bar{N}_t + \bar{N}_a \approx 1$, which agrees rather nicely with the previous estimate based upon V_m^e and ρ. Interestingly, the profile of Fig. 4.6(b) bears a striking resemblance to those seen in ultrahigh resolution transit broadening-limited molecular saturation spectroscopy [70].

4.3.2 What About the Extremely Narrow Features?

Because $\bar{N}_a/\bar{N}_T \sim 10^{-2}$, it is perhaps not surprising that attempts to simplify the full integral of Eq. (4.4) failed to provide an accurate accounting of the narrow component
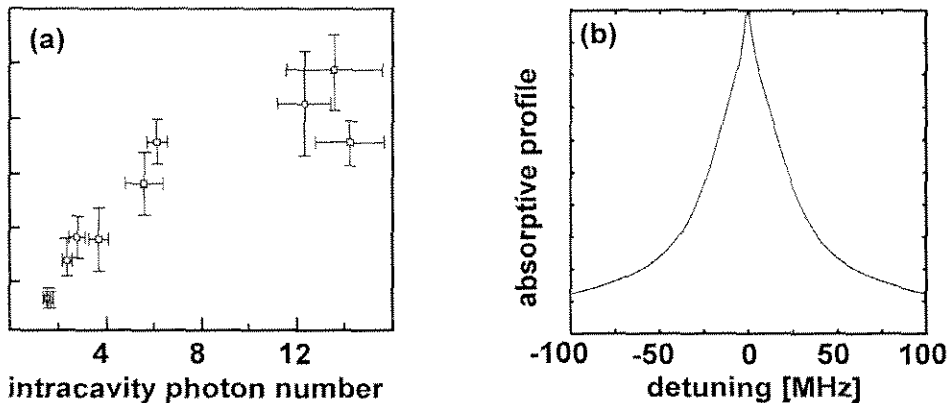
Figure 4.6: (a) Dependence of the size of the narrow absorption dip on intracavity photon number in the low Q regime of Fig. 4.4(a). (b) The atomic response $|\chi(\omega_L)|^2$ (normalized to unity) inferred from the phenomenological model discussed in the text [see Eq. (4.4)].

of $\chi(\omega_L)$. Nonetheless, even assuming an exact evaluation, there are several mechanisms which could produce narrow features and are not accounted for in Eq. (4.3a). First, as Q increases, a greater percentage of the counter-propagating $(q, l, -m)$ mode is excited, with a corresponding increase in the possibility for intracavity standing wave structure [71] along the direction of mode propagation. Such structure is capable of producing narrow features by isolating the slow atom components in a thermal gas. In addition, the $\exp\left(-\theta^2/\theta_0^2\right)$ dependence of the mode function in the transverse direction is strictly only valid for the $m = l$ mode with $\theta_0^2 \sim 2/l$, and, as one moves away from $m = l$, the WGM dependence on θ develops auxiliary maxima [72]. Second, $p(\mathbf{v})$ may depart from a Maxwell distribution, especially for those atoms with $v_r > 0$ which are leaving the surface. Obviously, a distribution which was peaked at lower velocities or which favored directions orthogonal to the direction of propagation of the mode would lead to narrow features. Finally, possible atomic level shifts [73] $(\delta_a \rightarrow \delta_a + \Delta)$ and modifications to the width $(\gamma \rightarrow \gamma')$ due to enhancement or inhibition [74, 75] of radiative decay in the vicinity of the sphere's dielectric boundary have not been taken into account. This would be extremely difficult to do correctly (e.g., one must consider both non-idealities such as asphericity which splits the de-

generacy in mode number m and Q's which are typically non-radiatively limited *and* the spatial dependence of γ' and Δ).

4.4   An Update

Since the completion of this work nearly two and a half years ago, there have been several interesting developments in this field which deserve mention. Recently, there have been first results at spectroscopy of a coupled WGM/quantum dot system [76] (with $Q's$ of 10^8 most recently measured *in situ*) representing a very exciting future direction for high finesse microcavity work. Much work has focused on coupling mechanisms into spheres for which the experimental coupling efficiency has been pushed as high as 80% [77] for the prism coupling technique used in the work here. New couplers, which are more compatible with "integrated optics" technologies, have also been developed based on fiber "half-block" couplers [78, 38], fiber tapers [79, 80, 81, 82, 83] and a hybrid technique [84]. A major focus of these efforts is to eliminate free-space beams with an eye towards possible applications in fiber-based communication systems. For such devices, Q will be sacrificed in favor of increased coupling efficiency. The possibility exists of using a sphere as a reference oscillator in an ultra-compact opto-electronic microwave oscillator [85]. Finally, very low threshold lasing has been seen in doped silica spheres [86].

From the perspective of our group, the long-term future of microspheres depends on the ability to maintain extremely high Q in very small spheres, where the ratio g/κ is expected to get very large. Work with small spheres also holds the promise of doing interesting non-linear optical work with very small thresholds, perhaps even at the single photon level. Joe Buck has continued this effort by trying to develop the group's expertise with smaller spheres.

Part II

CM QUANTIZATION IN CAVITY QED

Chapter 5   Well-Dressed States for Wavepacket Dynamics in Cavity QED

5.1   Introduction

This chapter is a theoretical investigation of the structure and dynamics for an atom strongly coupled to a quantized field in the presence of an external potential. Here, the dipole coupling energy $\hbar g$ is comparable to the atomic kinetic energy E_k [35]. With cold atoms, a fully quantized treatment of the atomic c.m. degrees of freedom is necessary in order to account for the wavepacket nature of the c.m. state. This situation has not been important for previous experimental work in cavity QED in which atoms from a thermal beam transit through a quantized cavity field with kinetic energy E_k large compared to the coupling energy $\hbar g$ [9] and for which the c.m. motion could be treated classically.

That the atom-field coupling for the internal degrees of freedom could have important consequences for the external c.m. motion was recognized in the seminal work of Refs. [87, 26, 88, 89], where scattering from the localized potential $\hbar g\left(\mathbf{r}\right)$ as well as trapping was first considered. Since then, a number of treatments of quantized motion in cavity QED have appeared related to diverse problems in optical physics, including cooling and trapping in a cavity with $n \sim 1$ quanta [26, 90, 91], atomic position measurements at the standard quantum limit [92, 93, 94], and quantum non-demolition detection of the intracavity photon number based upon atomic deflections [95, 96, 97, 41]. Also analyzed have been the role of atomic motion on the intracavity radiative process, as for example in Refs. [98], and other progeny in cavity QED, including most importantly the recent work on the micromaser with quantized c.m. motion [99].

Following this general theme, the current analysis explores the interplay of the

41

finite spatial extent of a c.m. wavepacket $\psi(\mathbf{r})$ with the quantum field mode structure $g(\mathbf{r})$, as is relevant to several important areas, including quantum logic with atoms in a cavity [100, 101] and quantum state synthesis in cavity QED [102, 105]. The material in this Part II will lay some of the groundwork for the next Part III, in which experimental investigations of some of these phenomena have been undertaken.

5.2   Field-Wavepacket Overlaps

A trapped atom which is cooled into a definite vibrational level of the trap will have a quantized c.m. wavefunction whose wavepacket extent is set by the trap parameters. I undertook some calculations [34] to see what these c.m. bound states would look like in the case of a novel trap configuration devised by Hideo and Jeff consisting of a red-detuned plus blue-detuned FORT (see Sec. 7.2.1 for a very detailed introduction to FORT traps) in a microsphere [40]. The interesting result is that these wavepackets can have spatial structure on the same scale as the light forming the trap. Hence, if an atom could be cooled in such a trap and then allowed to interact with a quantized field in the same spatial region, the finite spatial extent of the c.m. wavepacket could have a profound impact upon the usual atom-field coupling. An examination of results from such a calculation in Figs. 5.1(a),(b) shows that this is nothing like the "pinball" regime for the atomic motion which has been typically considered. This calculation (for a very specific external potential) led to much more general considerations of the impact of atomic c.m. quantization on the usual Jaynes-Cummings Hamiltonian, which is discussed in what follows.

5.3   The Well-Dressed States

The familiar dressed-states of the Jaynes-Cummings Hamiltonian are modified in Sec. 5.4 to include bound c.m. states that arise either because of the intrinsic spatial variation in the atom-field coupling $g(\mathbf{r})$ or because of an externally applied atomic potential $V_{\text{ext}}(\mathbf{r})$, e.g., as in an RF Paul trap [20]. Spatially localized eigenstates for

(a)   (b)
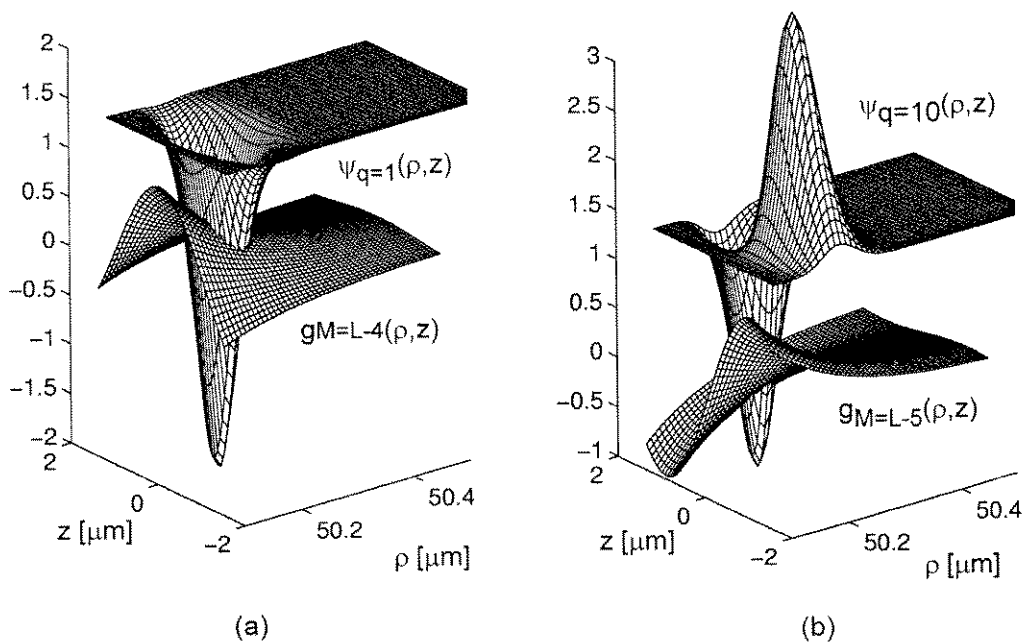
Figure 5.1: Comparison of the c.m. bound states $\psi_{q=10}(\mathbf{r})$ with the coupling coefficient $g(\mathbf{r})$ for the WGM of a microsphere of radius 50 μm and mode number (a) $(l = 521, m = 517)$ and (b)$(l = 521, m = 516)$. A dipole force trap of depth 2 μK provides V_{ext} (the atom gallery of [40]). Note that in (b) $g_{\text{eff}}^{(1)} = 0$ while $g_{\text{eff}}^{(1)} \neq 0$, with $g_{\text{eff}}^{(1)}$ defined in Eq. (5.7).

both the external motion in a potential well and for the internal atom-field interaction
are termed "well-dressed" states, with the eigenvalue spectra in three distinct regimes
illustrated in Fig. 5.2 and described in more detail shortly.
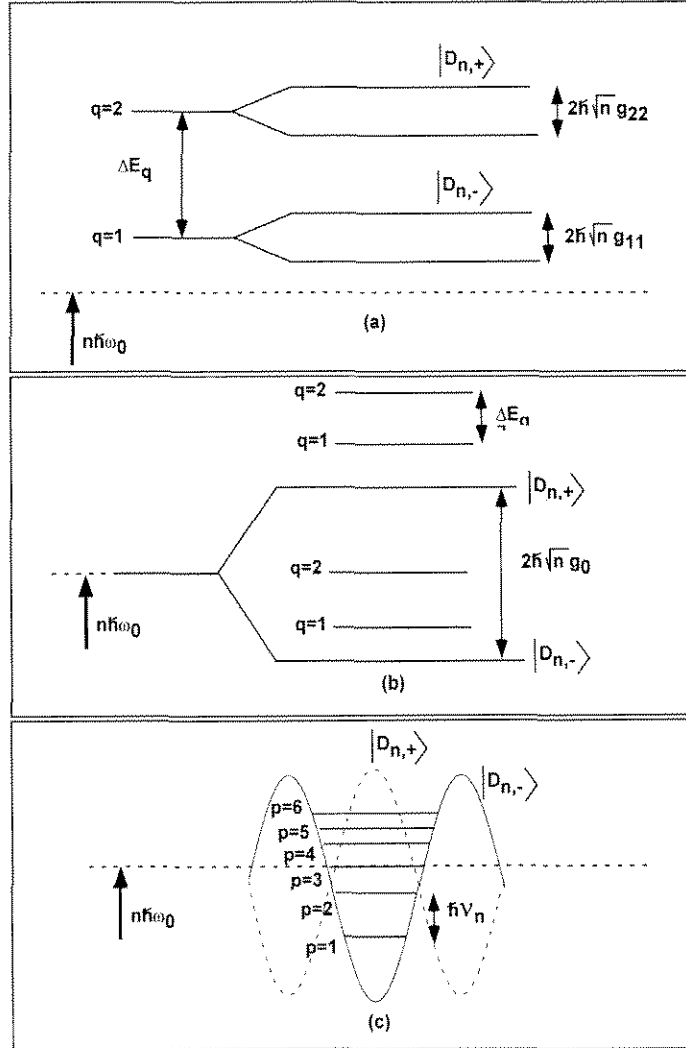
Figure 5.2: Eigenvalue spectra for the "well-dressed" states. Shown is the n-excitation
manifold for the three cases (a) $V_{\text{ext}} \gg \hbar g_m \sqrt{n}$, (b) $\hbar g_m \sqrt{n} \gg V_{\text{ext}}$, and (c) $V_{\text{ext}} = 0$,
where in (c), the curvature in $g(\mathbf{r})$ supports bound states. The quantities $\mathcal{V}_n$ and
$g_{qq} = \langle \psi_q \mid y(\mathbf{r}) \mid \psi_q \rangle$ are discussed in the text.

To illustrate the type of dynamical phenomena that can arise, Sec. 5.5 considers
an atom initially localized in the mode $g(\mathbf{r}) = g_0 U(\mathbf{r})$ with one photon which leads
to substantial modifications to the familiar Rabi nutation rate $2g(\mathbf{r})$. New coupling

strengths $g_{\text{eff}}^{(1,2)}$ characterize the initial evolution of the atomic dipole and inversion which are in general distinct quantities with a strong dependence on the atomic c.m. state, being given by overlap integrals of $g(\mathbf{r})$ and the c.m. wavefunctions $\psi(\mathbf{r})$. More generally, already implicit in Fig. 5.2 for the eigenvalues of the well-dressed states are new c.m. dependent spatial and temporal scales, τ_i, where for $g_0\tau_1 \gtrsim 1$, wavepacket delocalization can lead to a "collapse" of internal atom-field coherences while for $g_0\tau_2 \gg 1$ "revivals" of this coherence are possible.

An emphasis on localized bound states distinguishes this from most previous treatments of quantized motion in cavity QED, which have largely dealt with scattering of unbound momentum eigenstates. Perhaps the treatments with the greatest impact on the development here has been the work of Refs. [98, 99]. In Ref. [98], for example, a quantum mechanical treatment of an atom in a standing wave optical cavity is used to study the diffusion in momentum space of a c.m. momentum eigenstate and the modifications of the spontaneous decay rates due to c.m. quantization. Although the eigenstates of Fig. 5.2(c) here are for the case of a $1D$ standing wave introduced in Ref. [98], the formalism is applied there to delocalized momentum states which extend over many wavelengths (e.g., see Figs. 1 - 3 there). By contrast, the emphasis here is on the structure and dynamics of spatially localized bound states which are complex superpositions of the delocalized Bloch states and for which the dynamical processes have not been previously considered.

The bound state structure does play a critical role in the beautiful treatment in Ref. [99] of the "mazer," for which incident cold atoms are transmitted or reflected from the quantized field of a micromaser. The resonances in the scattering process are associated with bound states in the potential formed by quantized field. This treatment, however, tended not to emphasize the size scale of the initial c.m. wavepacket with respect to the typical wavelength of the quantum field. The analyses in [41, 106], though very interesting in their own right, also do not place the same emphasis on the c.m. wavepacket or its expansion in terms of the bound states of the optical potential as is done here.

Note that all this work builds to some extent on preceding work with *classical*

fields outside the realm of quantized optical fields in which both internal and external (c.m.) atomic degrees of freedom must be quantized in the presence of resonant or quasi-resonant excitation. Optical molasses [107, 108, 109, 110, 111], trapped ions [112, 113, 114], atom lasers [115, 116] and novel atomic cooling and trapping schemes [117, 118, 119] using classical light fields and their associated forces have all been treated in this way. Often, either the Raman-Nath approximation (for atoms) or the Lamb-Dicke limit (for ions) is invoked, which tends to de-emphasize either the extent of the atomic wavepacket with respect to the quantized field or the motion of the atom over its internal state lifetime. These are things that are incorporated here, contingent upon the relative magnitudes of the typical energies in the problem, as will be developed further in Sec. 5.4.

5.4 Structure

5.4.1 Hamiltonian

Turning to the details, the system Hamiltonian to be considered is expressed as

$$H = \frac{\mathbf{p}^2}{2m_a} + V_{\text{ext}}(\mathbf{r}) + \hbar g(\mathbf{r}) H_{IF}, \qquad (5.1)$$

where $H_{IF} = \left(\sigma_- a^\dagger + a\sigma_+\right)$ is the Jaynes-Cummings interaction written in a rotating frame *at resonance*, so that $\omega_{\text{atom}} = \omega_{\text{cavity}} \equiv \omega_0$. Here, $\mathbf{r}, \mathbf{p}$ are c.m. position and momentum operators for an atom of mass m_a, σ_+ is the internal atomic raising operator, and $a^\dagger$ is the creation operator for the cavity field mode. V_{ext} is assumed to have a bound-state structure $\left\{|\psi_q\rangle, E_q\right\}$ when $g(\mathbf{r}) = 0$, and similarly, the term in $g(\mathbf{r})$ can be interpreted as an internal state-dependent potential where, for $V_{\text{ext}} = 0$, we have eigenstates $\left\{|\phi_p\rangle, E_p\right\}$ of H. The well known dressed-states of H_{IF} are

$$|D_{n,\pm}\rangle = \frac{1}{\sqrt{2}}\left(|e, n-1\rangle \pm |g, n\rangle\right), \qquad (5.2)$$

with $E_{n,\pm} = \pm\sqrt{n}$ and with the convention that $g(\mathbf{r}) > 0$ $(g(\mathbf{r}) < 0)$ corresponds to a decrease (increase) in energy for $|D_{n,-}\rangle$ $(|D_{n,+}\rangle)$. For the time being, dissipation is neglected.

Rather than specify a particular form for $g(\mathbf{r})$, the generic behavior of $g(\mathbf{r})$ is studied around a field extremum z_0 (in one dimension for simplicity) where $g_m \equiv g(z_0)$ and ξ characterizes the magnitude of the curvature of $g(z_0)$, with η its sign. In a harmonic approximation, the bound states $\{|\phi_p\rangle\}$ associated with the dressed state $|D_{n,-}\rangle$ (in the case of a single field maximum with $\eta < 0$) have an energy spectrum $E_p = \left(p + \frac{1}{2}\right)\hbar\mathcal{V}_n$, $(p = 0, 1, 2, \ldots)$, where

$$\hbar\mathcal{V}_n = \sqrt{2\left(\hbar g_m\sqrt{n}\right)\left(\frac{\hbar^2}{2m_a\xi^2}\right)}. \tag{5.3}$$

It is worthwhile to note from this equation that both the potential well depth and the recoil energy set the energy scale for the vibrational spectrum. In general, the requirement for bound states is that $\sqrt{2R_n} < 1$, with

$$R_n \equiv \frac{\left(\frac{\hbar^2}{2m_a\xi^2}\right)}{\hbar g_m\sqrt{n}}. \tag{5.4}$$

Note that R_1 is analogous to the parameter R in [98].

As the intention here is to identify generic features brought by the c.m. state-dependence to the usual dressed state structure, the general solution of Eq. (5.1) with arbitrary functional forms for $g(\mathbf{r})$ and $V_{\text{ext}}(\mathbf{r})$ will not be considered. Instead, with the straightforward definitions and observations above, the bound-state structure of H in several limiting cases of experimental relevance can be understood. The three energy scales necessary for determining the appropriate c.m. eigenbasis are the coupling energy $\hbar g_m\sqrt{n}$, the energy splitting ΔE_q for the bound states $\{|\psi_q\rangle\}$ of V_{ext} and the energy splitting $\hbar\mathcal{V}_n$ associated with the bound states $\{|\phi_p\rangle\}$ of $\hbar g(\mathbf{r})$.

5.4.2   The Three Different Regimes

Perhaps the simplest case to consider first is that for which the external potential is dominant, namely $\Delta E_q \gg \hbar g_m \sqrt{n}$. In this regime, the well-dressed state structure is solved using $\left\{ \left| \psi_q \right\rangle \right\}$ as a fixed basis for the c.m. and $\hbar g(\mathbf{r}) H_{IF}$ is viewed as a perturbation. The eigensolutions of H are $\left\{ \left| \psi_q \right\rangle \otimes \left| D_{n,\pm} \right\rangle, E_q \pm \hbar \sqrt{n} g_{qq} \right\}$, where the matrix element g_{qq} is defined by

$$g_{qq} \equiv \left\langle \psi_q \mid g(\mathbf{r}) \mid \psi_q \right\rangle. \tag{5.5}$$

The finite size of the wavepacket inherent in g_{qq} distinguishes this case from much of the previous work in cavity QED. It can certainly be the case that $\left\langle g(\mathbf{r}) \right\rangle_q \neq g\left(\left\langle \mathbf{r} \right\rangle_q \right)$ for the bound states of V_{ext}, which was the intended "punch-line" of Figs. 5.1(a,b). One sees that this condition arises when the atomic c.m. wavefunction has spatial structure on a scale commensurate with that of the quantum field to which it is coupled. Variations in atomic wavepacket probability density strongly influence the coupled atom-field evolution.

More generally, the c.m. dependent Jaynes-Cummings ladder (i.e., the well-dressed states) for this regime is illustrated in Fig. 5.2(a). Note that "Rabi flopping" proceeds at the c.m. state dependent rate $2\sqrt{n} g_{qq}$, which can be completely suppressed ($g_{qq} \rightarrow 0$) due to the spatial structure of $g(\mathbf{r})$ with respect to $\psi_q(\mathbf{r})$. Spectroscopic investigation of the structure would, in general, involve c.m. state dependent transitions within each manifold.

A second regime interchanges the roles of $V_{\text{ext}}(\mathbf{r})$ and $\hbar g(\mathbf{r})$, such that $\hbar g_m \sqrt{n} \gg \Delta E_q \gg \hbar \mathcal{V}_n$. Here, ξ is assumed sufficiently large so that the coupling $g(\mathbf{r}) \sim g_0$ acts simply as a global shift to $\{E_q\}$. In this regime, the well-dressed states of H are $\left\{ \left(\left| \psi_q \right\rangle \otimes \left| D_{n,\pm} \right\rangle \right), \left(\pm \hbar \sqrt{n} g_0 + E_q \right) \right\}$ as illustrated in Fig. 5.2(b). The large curvature ξ in the cavity field allows the atomic c.m. to remain coupled predominantly to the bound states of $V_{\text{ext}}(\mathbf{r})$. The interaction energy associated with the internal degrees of freedom appear more or less as in the standard Jaynes-Cummings ladder, modified now by the fine structure associated with the atomic c.m. In fact there are

additionally *small* shifts g_{qq} of each eigenstate due to the spatial dependence of $g(\mathbf{r})$. These shifts are assumed to be of higher order and are not shown. Note that the separate limits of Figs. 5.2(a,b) begin to converge as the bound state spacings of $g(\mathbf{r})$ and $V_{\text{ext}}(\mathbf{r})$ approach one another, opening the way for more complicated structure (as for example with increasing n) and dynamics than will be discussed here.

Finally, a third regime takes $\hbar g_m \sqrt{n} \gg \hbar \mathcal{V}_n \gg \Delta E_q$. In fact, $V_{\text{ext}}(\mathbf{r})$ is considered only a means of providing a well-defined initial state for an atomic wavepacket, after which its effect is assumed negligible compared to the cavity field. For a given n-manifold, the Jaynes-Cummings ladder in the dressed-state picture is not split by $\pm \hbar g$. Instead, the well-dressed states $\{|\phi_p\rangle\}$ are associated with the minima of the respective potentials $V_{\pm}(\mathbf{r}) = \pm \hbar \sqrt{n} g(\mathbf{r})$ for $|D_{n,\pm}\rangle$ as in Fig. 5.2(c) for the bound states of V_{-}, with the repulsive barrier seen by $|D_{n,+}\rangle$ at that spatial location omitted. This is a consequence of the fact that the dressed state $|D_{n,-}\rangle$ is attracted towards the regions of negative curvature in $g(\mathbf{r})$ [$\eta < 0$] while $|D_{n,+}\rangle$ is repulsed, and conversely for $\eta > 0$. This structure is heavily dependent on well depth and changes with the manifold level n. Nevertheless, it must be emphasized that in the harmonic approximation (and indeed for more general potentials as well) the level spacing within a given n-manifold is given by $\hbar \mathcal{V}_n$ and scales as $(n)^{\frac{1}{4}}$. Note that this same factor $(n)^{\frac{1}{4}}$ plays a central role in the work of [99], for scattering of a cold wavepacket from a potential formed by the cavity field. In that case, ξ is set by the length L of the well and successive scattering resonances in the low energy limit for increasing $g_0 L$ are associated with increments of the round trip phase in units of 2π, which is precisely the condition for the addition of another bound state in the associated square well potential of depth g_0. Implicit in that analysis is the use of an external mechanism, such as the potential $V_{\text{ext}}(\mathbf{r})$, to produce the initially cold wavepacket.

In terms of a physical implementation, an example relevant to the two regimes of Fig. 5.2(a,b) is a trapped ion interacting with a cavity mode. In the microwave domain [103], typical cavities have $\frac{g_0}{2\pi} \sim 20$ kHz, while the vibrational frequencies for an RF Paul trap acting as $V_{\text{ext}}(\mathbf{r})$ are $\frac{\Delta E_q}{\hbar} \sim 1$ MHz and $\xi \ll \lambda_{\mu\text{-wave}}$, so that the conditions for Fig. 5.2(a) are satisfied. By contrast, in the optical domain [9, 64]

$\frac{g_0}{2\pi} \sim 10$ MHz , as is appropriate to Fig. 5.2(b), where for a heavy atom, $\frac{\nu_n}{2\pi} \sim 200$ kHz $\leq \frac{\Delta E_q}{h}$ in an optical standing wave.

For the regime of Fig. 5.2(c), one can consider a light atom such as He*, initially prepared in a c.m. eigenstate of $V_{ext}(\mathbf{r})$, which could be switched on in the form of a dipole-force trap as in Ref. [104] to provide this initial set of well-defined eigenstates with $g(\mathbf{r}) = 0$. The atom is then allowed to interact with a single mode of an optical cavity. This requires a transition to $V_{\text{ext}}(\mathbf{r}) = 0$ with $g(\mathbf{r}) \neq 0$ and could be accomplished for $V_{\text{ext}}(\mathbf{r})$ by simply gating the intensity of the dipole-force trap, while $g(\mathbf{r})$ could be controlled via the mechanism discussed in Refs. [102, 120]. Here, the effective coupling is given as a product of $g(\mathbf{r})$ and an external control field Ω, with the two-level atom being the ground states in a Λ configuration driven respectively by $g(\mathbf{r})$ and Ω.

5.5 Dynamics

Rather than focus on any one of the diverse applications of the eigenvalue structure of Fig. 5.2, dynamics are now discussed in an attempt to emphasize some of the generic features encountered for wavepackets in a quantized cavity field. Atomic spontaneous emission in the regime of Fig. 5.2(a) is first considered. The well-dressed states for an atom bound near the surface of a dielectric microsphere (as in Fig. 5.1) have been used to calculate modifications of radiative processes *including* the c.m. state and have found significant (100%) state-to-state variations in the spontaneous decay rates associated with the finite extent of $\psi_q(\mathbf{r})$ as compared to $g(\mathbf{r})$ via g_{qq}. As well, the dynamics accompanying heating of the atomic c.m. motion in the *atom gallery* [40] depend strongly on $\psi_q(\mathbf{r})$, with sharply decreasing rates of heating with increasing q, as discussed in detail in [34].

A simple example in the regime appropriate to Fig. 5.2(c) is now used to address more directly issues of wavepacket dynamics in cavity QED in a non-perturbative regime (i.e., coherent coupling $\gg$ cavity or atomic dissipative rates). For an initial c.m. wavepacket $|\Psi_{c.m.}(0)\rangle = \int d^3\mathbf{r}\, f_0(\mathbf{r})\,|\mathbf{r}\rangle$ and a coupled field and internal atomic

state $(c_+ |D_{n,+}\rangle + c_- |D_{n,-}\rangle)$, the full quantum state at any later time t is given by

$$|\Psi_{TOT}(t)\rangle = \sum_{\epsilon=\pm} \left(c_\epsilon e^{-\frac{i}{\hbar}H_\epsilon t} |D_{n,\epsilon}\rangle \right) |\Psi_{c.m.}(0)\rangle, \qquad (5.6)$$

with $H_\pm = \frac{\mathbf{p}^2}{2m_a} \pm \hbar\sqrt{n}g(\mathbf{r})$ and with dissipation neglected. The usual c.m. state $f_0(\mathbf{r}) = \delta^3(\mathbf{r} - \mathbf{r}_0)$ leads to Rabi oscillations with frequency $\Omega_n = 2\sqrt{n}g(\mathbf{r}_0)$. However, the wavepacket nature of the c.m. gives rise to new issues which are illustrated in the following $1D$ problem with the atom initially confined in some V_{ext} which is quickly switched off (so that $|\Psi_{c.m.}(0)\rangle$ cannot adiabatically follow the change). The atom is then coupled to a resonant cavity with mode function $g(z)$. As it is known that the pre-eminent requirement for possible experimental implementation of wavepacket dynamics in cavity QED is that $\hbar g \sim E_k$, here it is assumed that the bound state energies of V_{ext} are initially of the same order as $\hbar g_0$ so that an atom prepared in one of these states will remain localized when coupled to the cavity.

For $gt \ll 1$, it possible to find analytical expressions for the atomic dipole $\langle\sigma_-(t)\rangle$ and the excited state probability $P_e(t) = \langle\sigma_+(t)\sigma_-(t)\rangle$. For an atom initially in the ground state and $n+1$ quanta in the field, $|\Psi_{TOT}(t=0)\rangle = |g, n+1\rangle \otimes |\Psi_{c.m.}(0)\rangle$ (i.e., $c_\pm = \pm\frac{1}{\sqrt{2}}$), then $\langle\sigma_-(t)\rangle = -i\sqrt{n}g_{\text{eff}}^{(1)}t$, where

$$g_{\text{eff}}^{(1)} \equiv \int dz\, g(z)\, |f_0(z)|^2. \qquad (5.7)$$

This reproduces the usual expression $\langle\sigma_-(t)\rangle = -i\cos\left(\sqrt{n}gt\right)\sin\left(\sqrt{n}gt\right) \sim -i\sqrt{n}gt$ for small t if $g \rightarrow g_{\text{eff}}^{(1)}$. Furthermore, $P_e(t) = n\left(g_{\text{eff}}^{(2)}\right)^2 t^2$ with

$$g_{\text{eff}}^{(2)} \equiv \int dz\, |g(z)|^2\, |f_0(z)|^2, \qquad (5.8)$$

which is the small t equivalent of the Rabi probability $\sin^2\left(\sqrt{n}gt\right)$ with $g \rightarrow g_{\text{eff}}^{(2)}$. Note that the dependence of $\langle\sigma_-(t)\rangle$ and $P_e(t)$ on $f_0(z)$ can be profound and unlike anything that a "billiard ball" model for the atomic c.m. might predict. For example, for the particular atom gallery state shown in Fig. 5.1(b) interacting with the WGM

$g_{M=L-5}$, $g_{\text{eff}}^{(1)} = 0$ so that $\langle \sigma_- (t) \rangle = 0$, while $g_{\text{eff}}^{(2)} \neq 0$ such that $P_e (t) \neq 0$.

More generally, defining time-evolved dressed-state wavepackets,

$$f_\pm (z,t) = \langle z | \, e^{-\frac{i}{\hbar} H_\pm t} \int dz' \, f_0 (z') \, | z' \rangle , \qquad (5.9)$$

associated with $| \Psi_{TOT} (0) \rangle$ leads to the excited state probability for all times as

$$P_e (t) = \frac{1}{2} + c_+^* c_- \, \text{Re} \left(\int dz \, f_+^* (z,t) \, f_- (z,t) \right) . \qquad (5.10)$$

Here, $P_e (t)$ is given as an overlap (interference) of *amplitudes* for the dressed-state wavepackets associated with the two potentials $V_\pm \equiv \pm \hbar g (z)$. Significantly, coherent internal state dynamics are now linked self-consistently with the coherent evolution of the external c.m. state. A qualitatively similar linkage has been analyzed in the context of the micromaser operating with cold atoms [99].

The c.m. state dependency of these various expressions is made explicit by assuming a standing-wave cavity with $g (z) = g_0 \cos (kz)$ and an infinite square well for V_{ext},

$$V_{\text{ext}} = \begin{cases} \infty, & z < z_1, \, z > z_1 + a \\ 0, & z_1 < z < z_1 + a \end{cases} , \qquad (5.11)$$

with $a \sim \frac{\lambda_0}{2\pi} = \frac{1}{k}$, which has bound states

$$\{ \psi_q (z) \} = \left\{ \sqrt{\frac{2}{a}} \sin \left(\frac{q\pi}{a} (z - z_1) \right) \right\} , \qquad (5.12)$$

for $z_1 < z < z_1 + a$ and integers $q \geq 1$. The bound state energies are $\{ E_q \} = \left\{ \frac{\hbar^2 \pi^2 q^2}{2 m_a a^2} \right\}$. Fig. 5.3 illustrates the situation for the two bound states $q = 1, 2$.

The quadratic short time dependence of $P_e (t)$ with characteristic curvature given by the c.m. state dependent rate $g_{\text{eff}}^{(2)}$ of Eq. (5.8) for the initial c.m. states $q = 1, 2$ is shown in Fig. 5.4. The dependence on q of these curves can be understood from the difference in the overlap integrals of $\psi_q (z)$ with $| g (z) |^2$ as predicted by Eq. (5.8).

Turning now to dynamics on longer time scales, in Figs. (5.5, 5.7), we illustrate
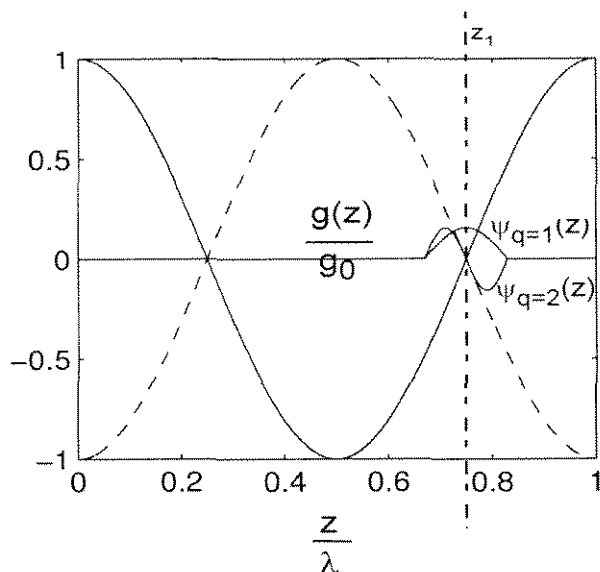
Figure 5.3: An illustration of the situation in which bound states $\psi_{q=1,2}$ [Eq. (5.12)] of $V_{\text{ext}}(z)$ [Eq. (5.11)] evolve dynamically when starting in the atomic ground state in the one-photon field of a cavity with mode function $g(z) = g_0 \sin(kz)$. The dressed states $|D_{1,\pm}\rangle$ will see the potentials labelled by V_+ (dashed) and V_- (solid), respectively.
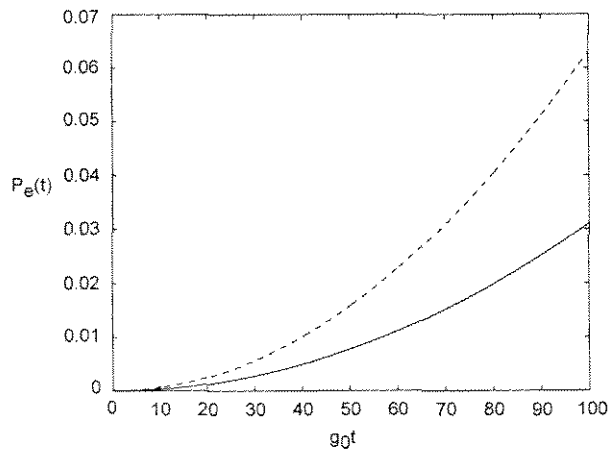
Figure 5.4: Quadratic short time evolution of $P_e(t)$ for the two states $q = 1$ (solid) and $q = 2$ (dashed) of Fig. 5.3. The different rates of growth here are due to the different overlap of these two wavefunctions with the quantum field profile $g(z)$ as quantified by $g_{\text{eff}}^{(2)}$ of Eq. 5.8.

various aspects of the interplay of the c.m. and internal dynamics for several choices of the parameters (m_a, g_0, R_1) and $f_0(z)$, where in all cases $c_\pm = \pm\frac{1}{\sqrt{2}}$. From the insets in Fig. 5.5, $f_0(z)$ is taken to be either the ground state ($\psi_1(z)$) or the first excited state ($\psi_2(z)$) of V_{ext}. It is clear that for the choices of z_1 shown, the wavepackets $f_\pm(z, t)$ will move into adjacent potential wells because the dressed states $|D_{1,\pm}\rangle$ see potentials $V_\pm \equiv \pm\hbar g_0 \cos(kz)$.

More quantitatively, $f_\pm(z, t)$ are computed by re-expressing $f_0(z)$ in terms of the well-dressed states $\left\{\phi_p(z), E_p = \hbar\omega_p\right\}$ as

$$f_\pm(z, t) = \sum_p c_p e^{-i\omega_p t} \phi_p(z).$$ (5.13)

As expected, the expansion coefficient is given by

$$c_p = \int dz' \, \phi_p^*(z') f_0(z').$$ (5.14)

It is worth re-iterating that in order to distinguish $f_\pm(z, t)$ in Eq.(5.13), the appropriate $\left\{\phi_p(z)\right\}$ to use is the set localized to the (spatially distinct) potential minima seen by $|D_{1,\pm}\rangle$. Taking $\frac{g_0}{2\pi} = 20$ MHz (as is relevant to Fig. 5.5(a)), for example, the potential $V_+ = \hbar g(z)$ for $n = 1$ is found numerically to have 177 bound states. For the initial states here with $a \ll \lambda_0$, the validity of evaluating the time evolution in terms of $\left\{\phi_p(z)\right\}$ only (i.e., neglecting the continuum) has been verified with independent calculations using the split operator method [121]. In Fig. 5.6, the decomposition of the initial states $q = 1, 2$ in terms of the set of 30 bound states of V_+ is shown for the parameters of Fig. 5.5(b,c). It is clear that this basis is completely adequate for these particular states, and that the use of a more general basis (such as the Bloch states) would only obscure the dynamics. Of course, as q increases, it would be important to extend the basis over multiple wavelengths to account for tunnelling of these higher energy states.

From Fig. 5.5(a), there is a time dependence for $P_e(t)$ reminiscent of the well-known "collapse" of Rabi oscillations caused by a spread in values $\Omega_n = 2g\sqrt{n}$ asso-

54
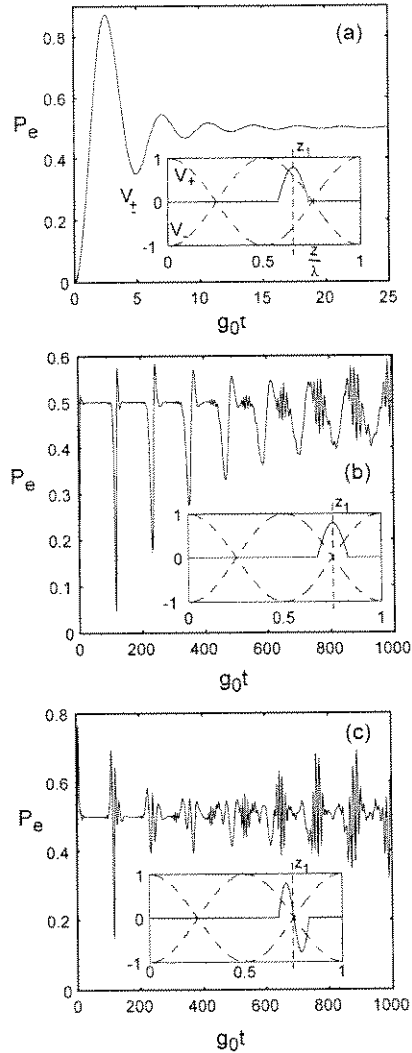
Figure 5.5: Evolution of $P_e(t)$ for three different initial c.m. wavepackets in the $n = 1$ manifold with $m_a = 133$ amu. In (a) $g_0/2\pi = 20$ MHz and $R_1 = 1 \times 10^{-4}$ while in (b) and (c) $g_0/2\pi = 1$ MHz so that $R_1 = 2 \times 10^{-3}$. Insets show $f_0(z)$ (solid line) centered at $z = z_1$ for the $q = 1$ state in (a), (b) and $q = 2$ in (c), and the (normalized) dressed-state potentials $V_\pm$ (dashed lines).
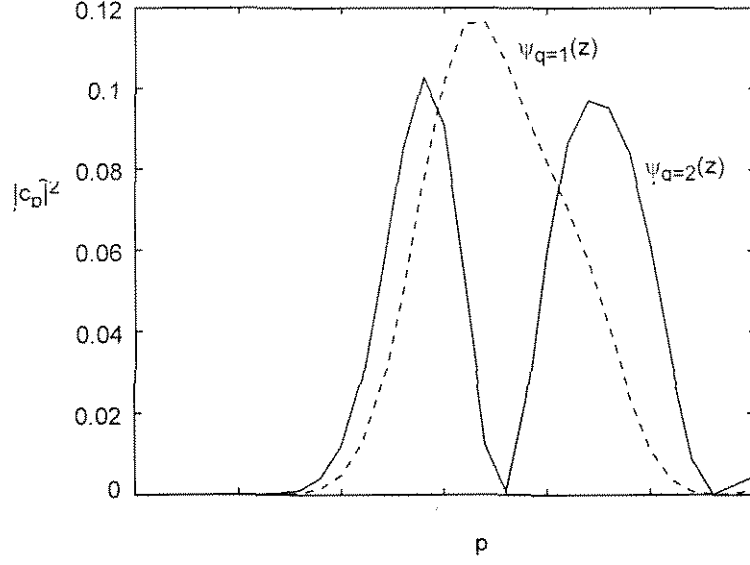
Figure 5.6: Decomposition of the states $q = 1$ (dashed) and $q = 2$ (solid) of Fig. 5.3 in terms of the 30 bound states of $\{\phi_p(z)\}$ of $V_\pm$ as is relevant to the parameters of Figs. 5.10 (b) and (c). We plot $|c_p(t)|^2$ from Eq. 5.14 as a function of bound state p. In both cases, $\sum_p |c_p|^2 > 98\%$.

ciated with a distribution in n [122]. Similarly, here the collapse is brought about in part by dispersion in Ω_1 (now for *fixed* $n = 1$) set by the structure of $f_0(z)$ relative to $g(z)$. In addition, on a time scale τ_1 given by

$$g_0 \tau_1 \sim \sqrt{\frac{ka}{2R_1}}, \qquad (5.15)$$

the wavepackets $f_\pm(z, t)$ separate due to their evolutions along $V_\pm$, driving the overlap of amplitudes in Eq. (5.10), and hence dynamical evolution of $P_e(t)$ to zero. A completely analogous evolution occurs for an initially excited atom with no photons in the cavity, which might be termed a "vacuum-Rabi" splitting [122] where now the atomic wavepacket is split by its own radiation reaction field.

The longer term evolution of $P_e(t)$ is illustrated in Figs. 5.5(b,c) for different choices of $f_0(z)$. Without delving into the details, it should be clear that there is a profound dependence of the dynamics on $f_0(z)$. For example, the initial rise of $P_e(t)$ for small t is given by $g_{\text{eff}}^{(2)}$ in each case, but with a ratio $g_{\text{eff}}^{(2)}[q = 1] / g_{\text{eff}}^{(2)}[q = 2] \simeq 1.4$.

Further note that $g_{\mathrm{eff}}^{(1)} [q = 1, 2] = 0$ in Fig. 5.5(b,c) while $g_{\mathrm{eff}}^{(1)} [q = 1] \neq 0$ in Fig. 5.5(a) as a consequence of the different initial c.m. states.

Beyond the initial "collapse" regime, $P_e (t)$ is quiescent with then a "revival" occurring near $g_0 \tau_2 = 110$ as in Figs. 5.5(b,c). From the previous discussion of Fig. 5.2(c), an estimate of the "oscillator" frequency for the c.m. is $\frac{\mathcal{V}_1}{g_0} \sim \sqrt{2R_1} \sim \frac{2\pi}{100}$. Clearly, the overlap integral between $f_\pm (z, t)$ in $P_e (t)$ in Eq.(5.10) has non-zero contributions at $z \sim z_1$ when the two dressed-state components of the wavepacket interfere, connecting the c.m. time scale $\frac{2\pi}{\mathcal{V}_1}$ to the long term dynamical evolution of $P_e (t)$ via τ_2. In fact, the resulting identification of τ_2 as

$$g_0 \tau_2 \sim \frac{2\pi}{\sqrt{2R_1}}, \tag{5.16}$$

produces reasonable agreement with τ_2 in Fig. 5.5(b,c).

The particular details of the fine structure of $P_e (t)$ at multiples of the initial revival time τ_2 (i.e., τ_2, $2\tau_2$, ...) depend upon the overlap of $f_0 (z)$ with $\{\phi_p (z)\}$. In qualitative terms, the oscillations for $q = 1$ have twice the frequency as for $q = 2$ since the probability density for $\psi_2 (z)$ has twice the number of maxima as $\psi_1 (z)$, illustrating the dependence of the dynamics on the initial c.m. state q. Beyond the first few revivals, the anharmonic character of $V_\pm$ enters to disperse the wavepacket.

To illustrate further the interplay of internal atom-cavity and external c.m. time scales, Fig. 5.7 presents two examples which emphasize the role of the parameter R_n. Since the characteristic frequency interval for the bound states of $g (z)$ given by $\frac{\mathcal{V}_n}{g_0 \sqrt{n}} \sim \sqrt{2R_n}$, R_n should set the separation of time scales between the internal and external state dynamics, as Fig. 5.7 indeed demonstrates. Displayed is the quantity $P_e (t)$ from Eq. (5.10) with $c_\pm = \pm \frac{1}{\sqrt{2}}$ and with $f_0 (z)$ as in Fig. 5.5(b). Fig. 5.7(a) is computed for $R_1 = 1 \times 10^{-4}$. Fig. 5.7(a) is representative of a rather large well depth ($\frac{g_0}{2\pi} = 20$ MHz) and small energy spacing of the eigenvalues $\{E_p\}$ as for an optical transition in a heavy atom like Cs, whose D2 transition wavelength $\lambda_0 = 852$ nm and mass $m_a = 133$ amu. On the other hand, Fig. 5.7(b) has $R_1 = 2 \times 10^{-2}$, corresponding to a shallow well ($\frac{g_0}{2\pi} = 2.5$ MHz) with a less pronounced separation of

time scales between internal and external state dynamics. In this case, the parameters for a light atom, such as the metastable transition at 1.08 μm in He* of mass $m_a = 4$ amu are appropriate.
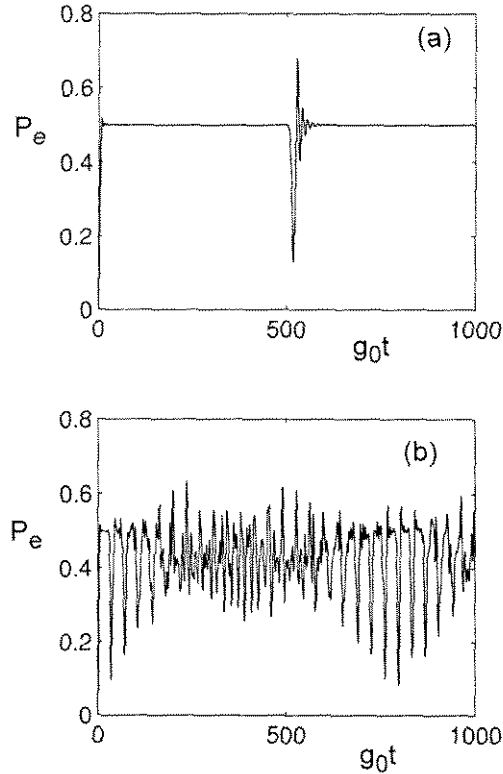
Figure 5.7: The dependence of $P_e(t)$ on the ratio R_n is illustrated. (a) Evolution of $P_e(t)$; here, $R_1 = 1 \times 10^{-4}$, with $m_a = 133$ amuand $g_0/2\pi = 20$ MHz as appropriate to the D2 line in Cs at 852 nm. In (b) $R_1 = 2 \times 10^{-2}$ with $g_0/2\pi = 2.5$ MHz and $m_a = 4$ amu for the transition at 1.083 μm in He*.

Note from Fig. 5.7(b) that in addition to the revivals themselves at τ_2 associated with the c.m. oscillations, there is yet a much larger time, τ_3, for the recurrence of the revivals around $g_0\tau_3 = 800$ that arise because of the small size of the basis set $\{|\phi_p\rangle\}$, which in Fig. 5.7(b) contains only the bound states necessary for an accurate decomposition of $f_0(z)$. In this case, the potential wells $V_\pm$ contain only 12 bound states and the decomposition of the initial state $f_0(z)$ uses only about 5 of these. If the potential well were harmonic with evenly spaced eigenstates, for example, the decomposition of the initial c.m. state into eigenstates of the well could

be considered like a Fourier series with only a finite number of components. In this case, the whole c.m. state time evolution is periodic at the highest eigenfrequency (Fourier component) in this c.m. state decomposition. This is the physical origin of the time scale τ_3. Note that although only the $n = 1$ manifold has been employed in Figs. (5.5, 5.7), even more complex dynamics would follow from superpositions of other n-manifolds. Beyond the context of this work, such behavior is familiar, for example, in the dynamics of wavepackets formed from sums of Rydberg states [123]. A distinguishing characteristic within the setting of cavity QED is the possibility for modifications of the external state potential via the internal state dynamics, and conversely. In fact, the inextricable interweaving of the atomic c.m. motion and the evolution of the cavity field via coupling to the atomic dipole leads to a host of exciting new phenomena at the frontier of quantum measurement [92].

5.5.1   Dissipation

A few qualitative comments about the role of decoherence due to atomic spontaneous emission at rate Γ and cavity decay at rate κ in this analysis are in order. As a realistic example of Fig. 5.2(c), consider the 2S $\rightarrow$ 2P transition at 1.083 μm in He* for which $\frac{\gamma_\perp}{2\pi} = \frac{\Gamma}{4\pi} \sim 800$ kHz. When coupled to a Fabry-Perot microcavity with $\frac{g_0}{2\pi} \sim 120$ MHz and $\frac{\kappa}{2\pi} \sim 2.9$ MHz (length $= 12$ μm, finesse $= 2 \times 10^6$ [54]), this gives $\frac{\nu_n}{2\pi} \sim 3.3$ MHz $> \frac{(\gamma_\perp,\kappa)}{2\pi}$ which opens up the possibility for experimental verification of modification to the Jaynes-Cummings manifold due to quantized c.m. even in the presence of dissipation. An optical microsphere of ~ 20 μm diameter has $\frac{g_0}{2\pi} \sim 125$ MHz and $\frac{\kappa}{2\pi} \sim 100$ kHz for a reasonable $Q \sim 10^9$, which would again allow resolution of the well-dressed state splitting. In fact, $g_0 \sim 10^4 \kappa$ seems feasible for microspheres [45, 32] as has been discussed experimentally in Part I. Generally in the optical domain, $\frac{g_0}{\Gamma} \le 10^2$, although the role of Γ can be greatly mitigated through the use of dark-state resonances [100]. By contrast, present technology in the microwave domain has already achieved $\frac{g_0}{\kappa,\Gamma} > 10^3 - 10^4$, albeit with $\left[\left(\frac{\hbar g_0}{k_B}\right) \sim 1 \ \mu\text{K}\right] \ll \frac{E_k}{k_B}$.

With regard to recoil kicks from atomic decay, note that significant heating of the

c.m. wavepacket requires a time $T_H \sim \left(\frac{\Delta E_q}{E_{\text{recoil}}} \right) \Gamma^{-1}$ [34] where ΔE_q is the level spacing of the relevant well-dressed states (Fig. 5.2) and $E_{\text{recoil}} = \frac{\hbar^2 k^2}{2m_a}$. As an example, for the case of Fig. 5.2(c), with $\xi \sim \frac{\lambda_0}{2\pi}$, shows that $g_0 T_H \sim \frac{g_0}{\Gamma} \frac{1}{\sqrt{R_n}} \gg \frac{g_0}{\Gamma}$ for R_n small as in Figs. (5.5, 5.7).

Part III

TRAPPED ATOMS IN CAVITY QED

Cavity quantum electrodynamics (QED) offers powerful possibilities for the deterministic control of atom-photon interactions quantum by quantum [124, 125]. Indeed, modern experiments in cavity QED have achieved the exceptional circumstance of strong coupling, for which single quanta can profoundly impact the dynamics of the atom-cavity system. Cavity QED has led to many new phenomena, including the realization of a quantum phase gate [24], the creation of Fock states of the radiation field [126, 16], and the demonstration of quantum nondemolition detection for single photons [17].

These and other diverse accomplishments set the stage for advances into even broader frontiers in quantum information science for which cavity QED offers unique advantages. For example, it should be possible to realize complex quantum circuits and quantum networks by way of multiple atom-cavity systems linked by optical interconnects [127, 128], as well as to pursue more general investigations of quantum dynamics for continuously observed open quantum systems [129]. The primary technical challenge on the road toward these scientific goals is the need to trap and localize atoms within a cavity in a setting suitable for strong coupling. Furthermore, all proposed schemes for quantum computation and communication via cavity QED rely implicitly on the development of techniques for atom confinement that do not interfere with cavity QED interactions.

Part III of this thesis now documents a major experimental effort to try to localize individual atoms inside of high finesse optical resonators for an appreciable amount of time (> few tens of milliseconds). The design of an experiment dedicated to this task must first identify the trapping mechanism to be used. For neutral atoms, possible candidates include magnetic trapping [130], far off-resonance dipole force traps (FORTs) [131] and optical lattices [132]. The approach taken here was initially to try a combination of the two optical traps (FORT + optical lattice) for two reasons. First, it appeared that both traps could be implemented with minimal perturbation to the somewhat inflexible super-cavity technology, and second, it appeared a combination of both of these traps would provide *both* the trapping *and* cooling required for long atom storage lifetimes.

As an aside, I will briefly mention another option, which is to move from neutral atoms to ions in an attempt to decouple the trapping forces (in an ion trap, an electrostatic pseudo-potential coupling to the ionic charge) from the atomic (or ionic) internal state. In fact, considerable time was invested in an attempt to further a collaboration which was started by Jeff and Quentin Turchette with Lute Maleki and Nan Yu from JPL's Time and Frequency Division. This experiment now has a "cavity-compatible" micro-ion trap for Yb^+ ions mounted on a stable 3-axis translator in UHV, but further progress has been difficult due to the fact that my effort has been devoted to the neutral atom work at Caltech to be discussed here. The ion trap work will not be discussed in this thesis, but remains an attractive option for the future and is being vigorously pursued elsewhere at the moment [133] for implementation as an "ion trap laser" [134].

Part III begins in Chap. 6 with a rather detailed discussion of the new experimental ground which has been broken, including detailed discussions of the preparation of the cold atom source and the means by which the atoms are detected. The experiment must necessarily integrate the techniques of laser cooling and trapping with those of cavity QED to deliver cold atoms (kinetic energy $E_k \simeq 30~\mu K$) into the mode of the high finesse optical cavity. In a domain of strong coupling, the trajectory of an individual atom within the cavity mode can be monitored in *real time* (so-called "atom transits") by a near resonant field with mean intracavity photon number $\bar{n} < 1$. Ever since the pioneering work of [64], this has become a very rich area and has been followed by a flood of experimental investigation [135, 136, 137, 138, 21, 22, 23].

The discussion in Chap. 7 then turns to the report of a significant milestone in this quest, namely the first trapping of a single atom in cavity QED. Here we exploit the real-time detection capability to trigger *on* an auxiliary field that functions as a FORT, providing a confining potential to trap the atom within the cavity mode. Likewise, when the FORT is turned *off* after a variable delay, strong coupling enables detection of the atom. Repetition of such measurements yield a trap lifetime $\tau = (28\pm6)$ms, which is currently limited by fluctuations in the intensity of the intracavity trapping field (FORT). Much attention has recently been devoted to understanding

the root cause of this limitation, and a comprehensive survey of the results of this investigation are included.

Chap. 8 concludes this thesis with some brief indications of the direction this experiment could eventually take. Included among the very real near-term possibilities is an extension of the trap lifetime upwards of 100 ms and even towards 1 s by eliminating the residual heating and then using a cooling mechanism inherent in the atom-field interaction Hamiltonian in the presence of the FORT. Finally, returning to a common theme throughout this thesis, the prospects for cooling a single atom near the motional ground state in order to resolve motional sidebands associated with the "well-dressed states" is discussed as a tantalizing possibility.

Chapter 6   Cold Atoms and High Finesse Microcavities - Experimental

6.1   Introduction

The drive to localize a single atom inside a high finesse optical resonator requires the integration of techniques at the experimental state-of-the-art on two different fronts. First, there is the issue of preparation of the atomic sample, which is discussed in Sec. 6.2. Even though the techniques of atomic cooling and trapping are becoming fairly routine, this part of the experiment remained a major challenge because the necessity of successfully loading the cold atoms into a 40 μm long cavity was the issue always at the fore of the design process.

The cold atoms work needed to be linked with the major contributions made by Christina, Theresa and Mike in cavity construction [65], and Quentin, Hideo and Jun in cavity stabilization [136]. It was very fortunate that the group has so much accumulated experience in both of these areas. Nevertheless, the construction and successful integration of all of this technology remained a second major challenge, and Secs. 6.3 and 6.4 are devoted to recording the experimental details.

6.2   Delivering Cold Atoms to the Cavity

6.2.1   Cesium Level Structure

Since it will be useful to refer periodically to the level structure of the atom, Cesium (Cs^{133}), that is used in the experiments, this is shown below in Fig. 6.1 along with the hyperfine level structure of the $6S_{1/2} \rightarrow 6P_{3/2}$ D2 transition in Table 6.1 and the transition amplitudes for an $F = 4 \rightarrow F' = 5$ transition in Table 6.2.
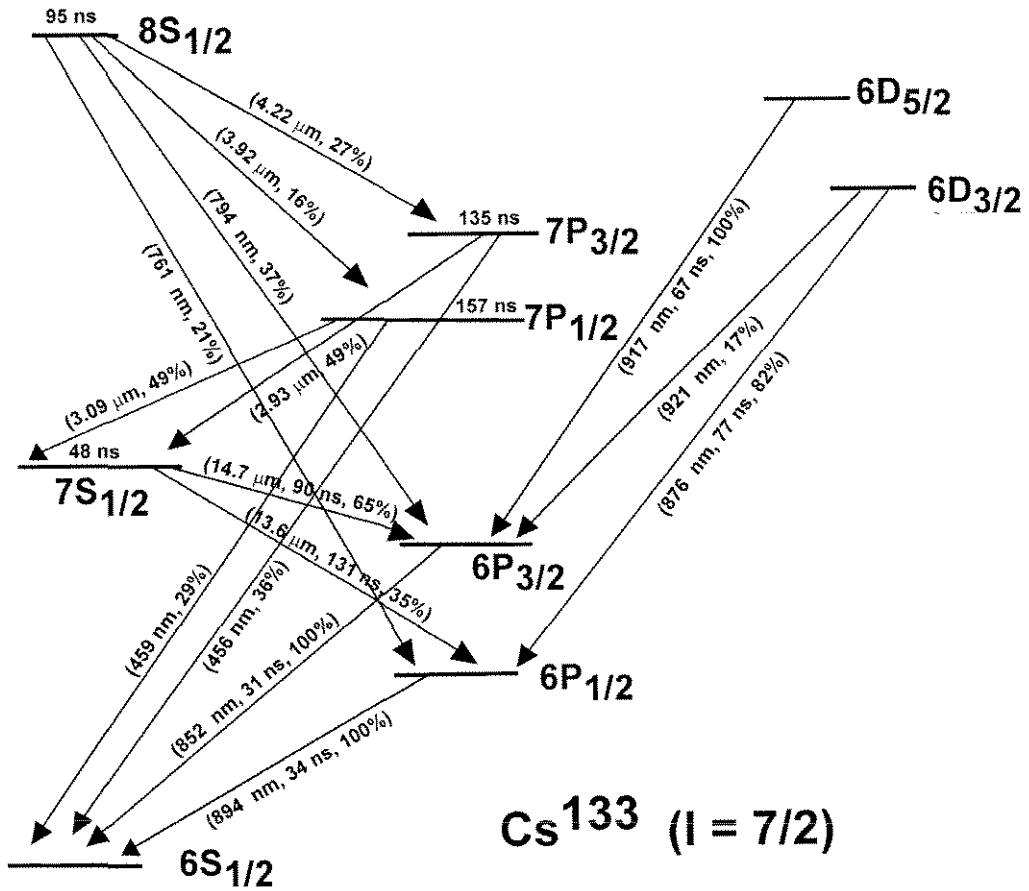
Figure 6.1: The level structure of Cs^{133} is shown in (a) and will be referred to throughout the text. The $6S_{1/2}$ $F = 4 \rightarrow 6P_{3/2}$ $F' = 5$ cycling transition near 852 nm is the one used for much of the work here. The information on the diagram in brackets is of the form (transition wavelength, lifetime, branching ratio).

Fine Structure	Hyperfine Level	Energy
$6S_{1/2}$	$F = 3$	-9.2 GHz
	$F = 4$	0 (reference) ·
$6P_{3/2}$	$F' = 2$	$f_0 - 607$ MHz
	$F' = 3$	$f_0 - 456$ MHz
	$F' = 4$	$f_0 - 253$ MHz
	$F' = 5$	f_0 ($= c/852.359$ nm)

Table 6.1: Hyperfine structure for the Cs $6S_{1/2} \rightarrow 6P_{3/2}$ D2 line at 852 nm.

		$m_{F'} = 0$	$m_{F'} = 1$	$F' = 5$ $m_{F'} = 2$	$m_{F'} = 3$	$m_{F'} = 4$	$m_{F'} = 5$
	$m_F = 0$	$\sqrt{5/9}$	$\sqrt{1/3}$				
	$m_F = 1$	$\sqrt{2/9}$	$\sqrt{8/15}$	$\sqrt{7/15}$			
$F = 4$	$m_F = 2$		$\sqrt{2/15}$	$\sqrt{7/15}$	$\sqrt{28/45}$		
	$m_F = 3$			$\sqrt{1/15}$	$\sqrt{16/45}$	$\sqrt{4/5}$	
	$m_F = 4$				$\sqrt{1/45}$	$\sqrt{1/5}$	1

Table 6.2: The coupling coefficients for an $F = 4 \rightarrow F' = 5$ transition.

6.2.2 System Overview and Introduction to the MOT

Our experimental apparatus consists of a high finesse cavity and two-stage magneto-optical traps (MOTs) as shown in Fig. 6.2. Roughly $N_{\text{MOT}_1} \sim 10^8$ Cs atoms are accumulated in an "upstairs" MOT_1, cooled with polarization gradients to 3 μK, and then transferred with 10% efficiency to a "downstairs" MOT_2, located in a UHV chamber with background pressure 10^{-10} Torr. The captured atoms are next cooled to 2 μK and dropped from a position 5 mm above a high finesse optical cavity. Some of these atoms finally fall between the cavity mirrors, and thence through the cavity mode itself.

A final stage in the protocol for delivering cold atoms into the mode volume is provided by a set of cooling beams located in the $x - y$ plane perpendicular to the cavity axis (see Fig. 6.15). These beams form two independent standing waves along the $\pm 45°$ directions in the $x - y$ plane, each with helical polarization, and are switched on for 1.5 ms to remove the residual fall velocity of atoms arriving at the cavity mode from MOT_2, leading to final velocities $v \sim 5$ cm/s for atoms in the immediate vicinity of the cavity mode.

The magneto-optical trap (MOT) [139] has become the workhorse technique for preparation of a cold atomic gas over the last 10 years and is vital to the success of the work to be described here. There are many excellent, detailed descriptions of the different MOT varieties [140], so only the rudimentary physical idea will be presented as an introduction. In the standard configuration, six counter-propagating laser beams are arranged along three mutually orthogonal directions. They are tuned
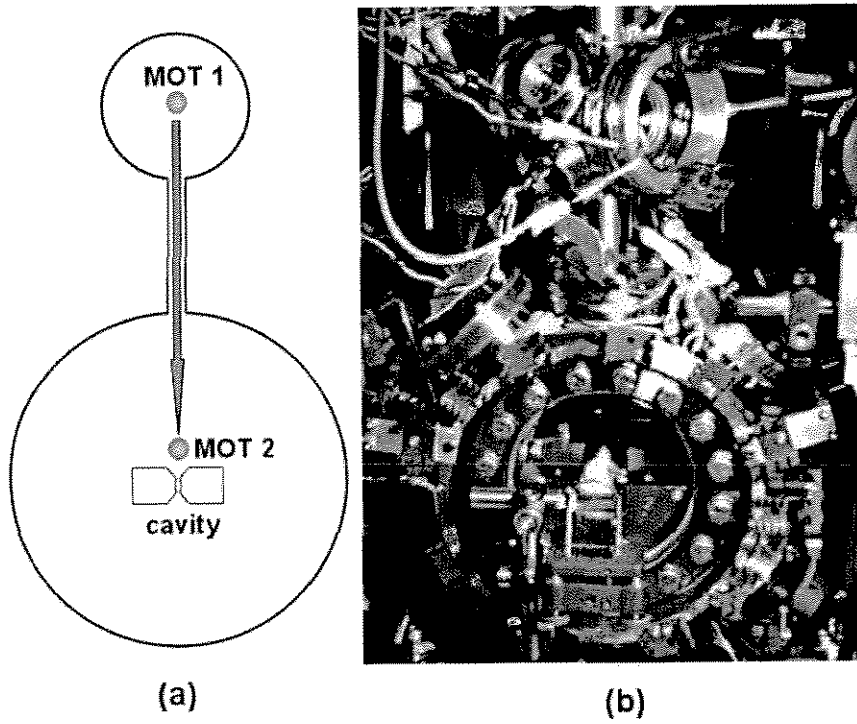
Figure 6.2: A schematic of the physical layout of the two-stage MOT setup in (a) is shown alongside a photograph of the actual system in (b).

approximately one linewidth below the atomic resonance to provide initial radiation pressure cooling to a room temperature atomic gas. A magnetic field gradient is used to create a spatially varying Zeeman shift, typically using coils in the anti-Helmholtz configuration to provide a quadrupole field with a zero at the common intersection of the laser beams. The beam polarizations are carefully chosen such that an atom tending to leave this intersection area in any direction will be shifted closer to (the now Zeeman-shifted) resonance for the beam travelling *opposite* to its motion (it is shifted further from resonance for the beam travelling parallel to it, and hence does not interact with this beam). This will cause it to scatter more light from the counter-propagating beam and cool, which returns it to the center of the trap. Using this configuration, atoms can be cooled to the so-called Doppler limit T_D, where $k_B T_\mathrm{D} = \hbar \gamma_\perp$ is limited by the heating rate associated with the unavoidable momentum diffusion due to photon scattering [141]. For Cs, the Doppler limit is approximately 120 μK. Fig. 6.3 shows the geometry relevant to MOT_1 and MOT_2 used in this experiment. After a quick digression to the vacuum system developed for this experiment, the discussion will build on this brief overview to illuminate many of the technical issues associated with the preparation of the cold atoms.

6.2.3 The Vacuum System

The design of the vacuum system was the overriding concern in this experiment because it was felt that the eventual limit to trap lifetime could be dominated by collisions with the background gas if the design wasn't done carefully. A quick estimate of the collisional time scale τ_{coll}, given the collision cross-section σ and mean velocity v is given by

$$\frac{1}{\tau_{coll}} = n\sigma v_\mathrm{th} = \frac{p}{k_B T}\sigma\sqrt{\frac{3k_B T}{2m}}, \tag{6.1}$$

with T the gas temperature and m the atomic mass. For our systems, with a thermal Cs ($m = 133$ amu) background vapor at 300 K and a collisional cross-section $\sigma \sim 1 \times 10^{-17}$ m^2 [142], the collisional lifetime is about 5 s at a pressure of 10^{-9} Torr. Hence, much effort was invested in improving upon the typical vacuum levels of 10^{-8}
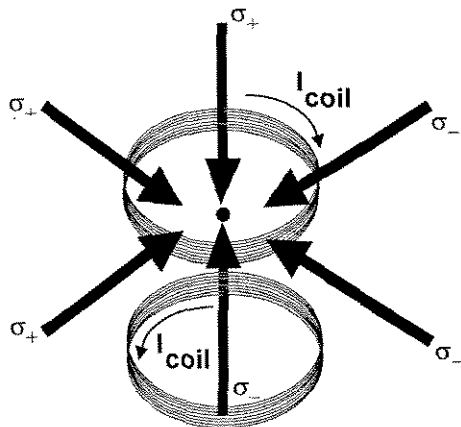
Figure 6.3: In this sketch of a typical MOT geometry, the arrows representing the direction of the laser beams are meant to be orthogonal to the faces of a cube. A set of anti-Helmholtz coils lies along one of the principal axes to provide a linear magnetic field gradient. Zeroing coils (not shown) lie along all threee axes to compensate for stray magnetic fields. This geometry is used for both MOT_1 and MOT_2.

Torr used to date in these experiments in our group.

In any design it is important to try to ensure the success of trapping one atom inside the mode volume on each experimental cycle. Due to geometric constraints, MOT_2 can be no closer than about 5 mm from the cavity mode volume, and the mode has a cross-section of about 40 μm $\times$ 20 μm. If the initial MOT_2 cross-sectional area is 1 mm^2, an atom has a probability of about 1×10^{-5} of hitting the cavity mode volume and being detected. If we assume $\sim 1\%$ of these are actually trapped, then it is necessary to collect about $N_{MOT_2} \sim 10^7$ atoms above the cavity mode volume. The steady state number of atoms in a MOT is given by [140, 143]

$$N_{ss} = \frac{3\sqrt{\pi}}{2} \left(\frac{p_{Cs}}{p_{Cs} + p_B} \right) \frac{v_{rec}^2 \Gamma_{scatt}^2}{\sigma v_{th}^3 v_{coll}} d^4 , \tag{6.2}$$

with the scattering rate Γ_{sc} written as

$$\Gamma_{scatt} = \gamma_\perp \frac{I/I_s}{1 + I/I_s + (\delta/\gamma_\perp)^2} . \tag{6.3}$$

Here $(v_{rec}, v_{th}, v_{coll})$ are the (recoil, thermal, trap collisional) velocities respectively,

I/I_s is the ratio of the light intensity to the saturation intensity, d is the beam diameter, $(p_{\text{Cs}}, p_{\text{B}})$ are the Cs and background vapor pressures and $(\delta, \gamma_\perp)$ are the detuning of the laser light from the atomic transition and the excited state half-linewidth respectively. Clearly, this expression is maximized if $p_{\text{Cs}} \gg p_{\text{B}}$. In the UHV environment surrounding the cavity, however, we require the total pressure $p = p_{\text{Cs}} + p_{\text{B}}$ to be dominated by p_{B} (i.e., $p_{\text{B}} \gg p_{\text{Cs}}$). This rules out the possibility of loading the trap from a background vapor in the vicinity of the cavity. An attractive option was to load MOT_2 from a cold atomic beam [144]. The LVIS technique [145], for example, was optimized for atomic flux, but was eventually deemed unnecessary because of the relative simplicity of the "double-MOT" technique.

Fig. 6.4 shows the overall layout and specific detail of the vacuum system that was finally built. A double-MOT was adopted because of the flexibility of this strategy and its capability of separating the cold atom "source" from the physics to be done with those cold atoms [146]. In this system, many atoms ($N_{\text{MOT}_1} \sim 5 \times 10^8$) are collected in an upper chamber from a dilute vapor such that $p_{\text{Cs}} \gg p_{\text{B}}$ in order to maximize N_{ss} as in Eq. (6.2). These atoms are transported (in our case, dropped) in the form of a cold atomic beam through a differential pumping hole to a UHV chamber below.

The differential pumping hole geometry of length $L = 2$ cm and diameter $D = 4$ mm was designed to support the pressure difference between the two chambers. Given a pumping speed $S \sim 20$ l/s and a conductance C for a cylindrical tube of

$$C = 12.1 \frac{D^3}{L + 1.33D} \text{ [l/s] if } D, L \text{ [cm]}, \tag{6.4}$$

the pressure difference ΔP is given by

$$\frac{\Delta P}{P} \sim \frac{P_{\text{upper}}}{P_{\text{lower}}} = \frac{S}{C}, \tag{6.5}$$

which indicates this geometry should easily allow 2 orders of magnitude in pressure between the upper and lower chambers. The hole size of 4 mm still allows many
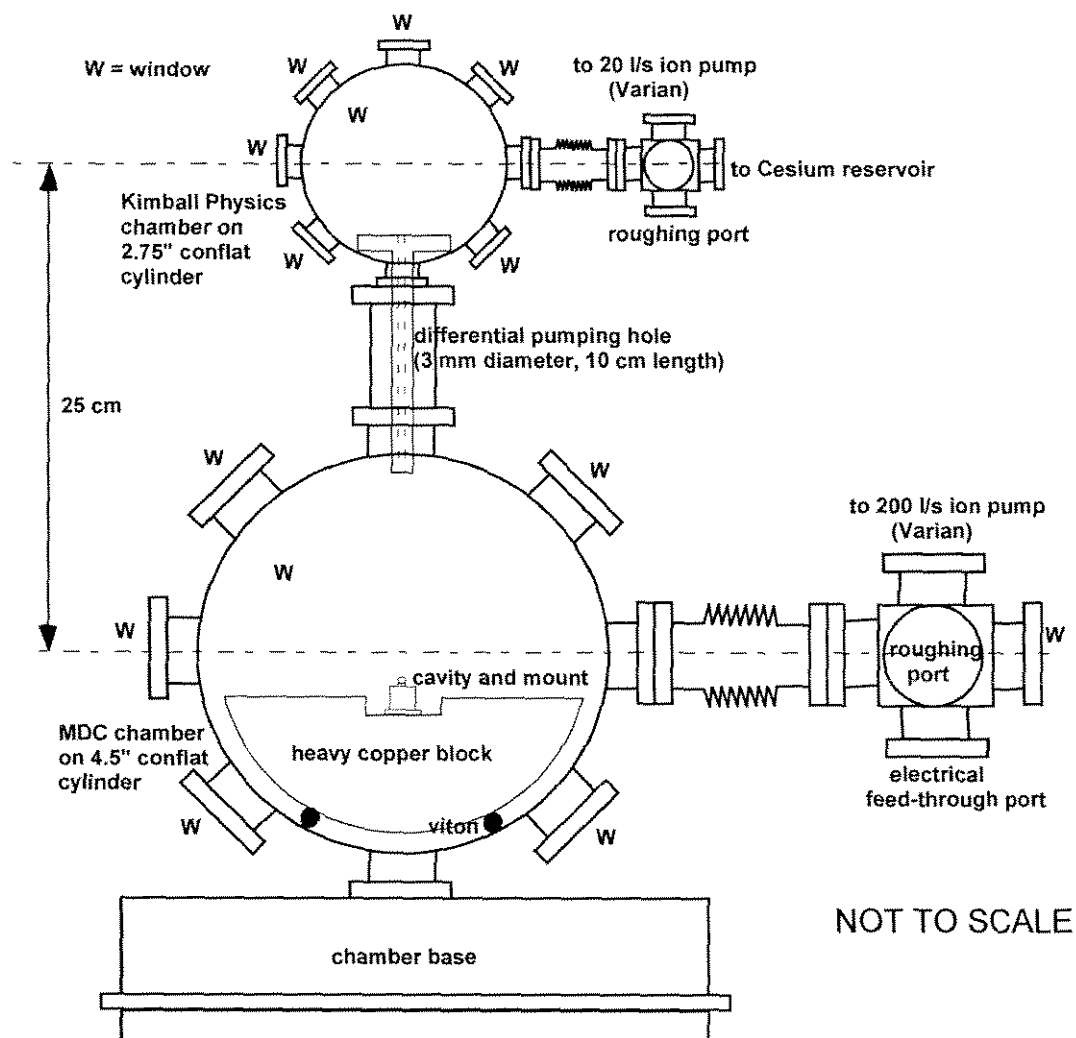
Figure 6.4: This sketch (not to scale) provides all information relevant to the layout of the vacuum system, including an identification of the major components used and an indication of the important distances. Note that the differential pumping hole was inserted manually into the assembled system.

atoms to pass from the upper chamber to the lower, given typical expansion rates (temperatures) and initial sizes for MOT_1.

The Cs reservoir was a very simple design consisting of a stainless steel cup surrounded by insulation and attached to several peltier heating elements to allow temperature control of the Cs vapor pressure in the upstairs chamber. The temperature was monitored by a thermistor and was typically held at 5 °C except for a couple of hours every morning when the temperature would be raised to 20 °C to allow more Cs to enter the upstairs chamber. A valve was included to isolate this reservoir during the bakeout period and in the event of any power outage.

Standard vacuum techniques were used to prepare and assemble all of the components, but there were several significant challenges worth mentioning. First, bakeout temperatures of the assembled system were ultimately limited to about 200 °C by the bakeability of the materials associated with the cavity. These included viton for vibration damping, epoxy to hold the assembled cavity structure, solder to make electrical connections, kapton wires and PZT materials for allowing cavity tuning. Significant surface areas of copper and aluminum were also necessary for the cavity mounting and support structure. For this reason, an aggressive cleaning protocol [147] consisting of ultrasonic cleaning, vapor degreasing, alcohol rinsing, acid etching (for the copper) and vacuum oven bakeout to 250 °C before assembly was used to help compensate. A further step of baking all the stainless steel components in air to 400 °C was not used but would probably give even better results. After assembling the chambers and all of the components, a comprehensive two-week bakeout procedure under vacuum at 200 °C was initiated. Each significant coupling point and window was covered by a band heater and temperature sensors (the ion pumps had their own separate elements) and the entire structure was covered by many layers of oil-free aluminum foil.

At the end of the bakeout period, the system was isolated from the turbo pumping system and the ion pumps were turned on. The steady state pressure after cool-down reached 2×10^{-9} Torr in the upstairs chamber as monitored by the ion pump current and 3×10^{-10} Torr downstairs as measured by a nude ion gauge. After almost two

years, the downstairs pressure has reached a minimum of 1.5×10^{-10} Torr, but this number fluctuates seasonally by up to 50% depending on the relative humidity in the lab. The upstairs pressure fluctuates depending on the Cs background vapor pressure, but typically sits at 1×10^{-8} torr, which verifies the differential pumping geometry design.

6.2.4 The Upstairs MOT$_1$

The role of the upstairs MOT$_1$ was to collect as many cold atoms as possible in order to maximize the transfer efficiency through the differential pumping hole to the downstairs MOT$_2$. A picture of MOT$_1$ is shown in Fig. 6.5, as seen looking down through the upper window of the upper chamber in Fig. 6.4. The dark hole in the picture is the differential pumping hole (a 3 mm diameter hole machined in an aluminum cylinder) through which the cold atoms will eventually fall into the lower chamber.
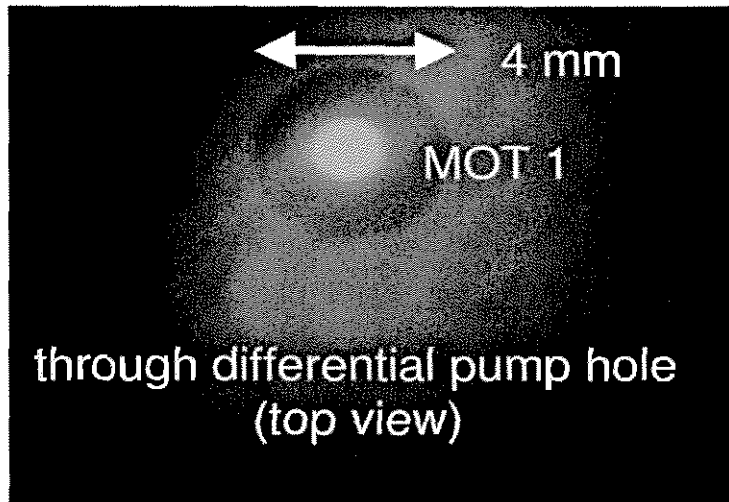
Figure 6.5: Fluorescence from the approximately 10^8 atoms in the upstairs MOT$_1$ can be seen looking down along the vertical axis through the top window in the upper chamber of Fig. 6.4. The 4 mm diamter differential pumping hole can be seen as the dark hole *below* the atom cloud, through which the atoms will fall.

Examination of the expression for N_{ss} in Eq. 6.2 shows that the easiest way to trap many atoms is to use large beam diameters d and maintain enough power in the beams such that they are well above the saturation intensity of $I_s \sim 3$ mW/cm^2 for the Cs D2 $6S_{1/2}, F = 4 \rightarrow 6P_{3/2}, F' = 5$ line at 852 nm. The window size for the upstairs chamber limited the beam size to 1.5 cm in diameter so that about 6 mW of power was necessary for each of the three (retroreflected beams) to saturate the transition. In addition, an optical fiber was used to eliminate the day-to-day hassle of having to realign the MOT beams. This is typically necessary due to the Littrow mounting of the gratings on our homemade external cavity diode lasers [42], which will cause the beam to move horizontally if the grating is adjusted for wavelength tuning. The drawback of the fiber is the typical 50% reduction in power due to coupling losses. Furthermore, there is often a need for great flexibility in frequency and intensity adjustment of the light in order to optimize the MOT temperatures, which implies that several acousto-optic modulators with finite (single pass $\sim$ 80%, double-pass $\sim$ 60%) efficiencies are necessary.

In the end, the decision was made to go to an injection-locking scheme [148] to eliminate some of these losses from the beam path. For example, very little power (approximately 10 μW or less) of master laser light is necessary to injection lock a slave laser, so that much of the frequency manipulation can be done to the master laser without compromising the ultimate output power of the slave. The assumption is that the injection lock is fast enough that the slave laser will follow the intentional frequency changes of the master. One further improvement to the set-up would be to remove the grating from the slave laser and injection-lock the free-running diode, because there is intrinsic competition between the injection-locking light and the feedback from the external grating. The grating was used initially only to provide a simple way to tune the slave laser wavelength close enough to the master such that the injection lock would "grab," while at the same time avoiding the need for temperature and current tuning of the diode wavelength.

The master laser was locked using a simple Pound-Drever-Hall rf saturated absorption locking technique [52], and a beat-note between the master and slave was
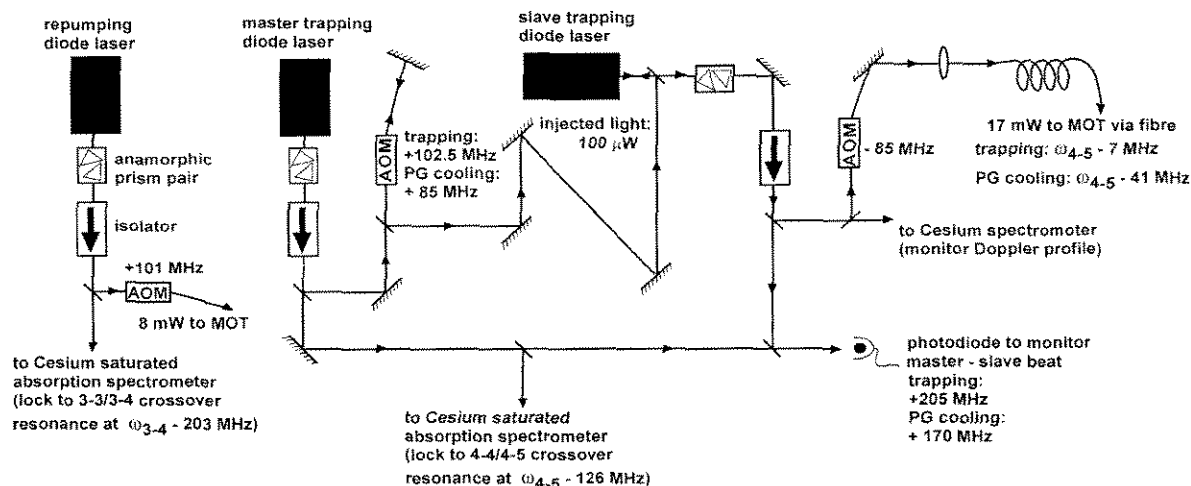
Figure 6.6: The basic layout for the three upstairs diode lasers are shown, along with the most relevant information about the laser frequencies. Note that, for simplicity, most routine beam shaping optics (such as lenses) and polarization determining optics (such as polarizers and waveplates) have been omitted to keep the overall layout as clear as possible.

monitored daily on a homemade fast photodiode. Another added bonus of using an injection-locked slave for trapping is that it does not carry any residual frequency sidebands from its locking technique which could tend to shift a portion of the light closer to resonance and cause heating of the atoms. In addition, a repumping laser locked to the $6S_{1/2}, F = 3 \rightarrow 6P_{3/2}, F' = 4$ line is necessary to repopulate those atoms that end up decaying to the $F = 3$ state due to off-resonant (unintentional) driving of the $6S_{1/2}, F = 4 \rightarrow 6P_{3/2}, F' = 4$ transition (see Table 6.1). Fig. 6.6 gives the optical table layout for the upstairs MOT laser scheme.

A few words are in order about the diode lasers used in the MOT work. They are all homemade of the external cavity grating-stabilized type [42], using Littrow configuration with weak feedback of about 13% from the grating (the diodes, SDL 5421-G1 200 mW single-mode, are not AR coated). The grating stabilized linewidth is about 200 kHz. The low noise temperature and current controllers are ever-evolving, but all generations can be traced back readily to the original Libbrecht-Hall work [149]. The lasers, which are locked electronically to a Cs line, employ rf modulation for

the Pound-Drever-Hall technique on their injection current and a dual-stage feedback loop to both the current and temperature controllers. As both the spectroscopy technique for the generation of the error signal and the design of the PI servo loop itself have been discussed extensively, only a few details will be mentioned here. An excellent discussion can be found in [150] for diode laser work. In practice, it was found that the best lock was obtained with a bandwidth of about 10 Hz to the grating and 200 kHz to the laser injection current, and that feedback down to DC to the laser current helped the long-term stability. Finally, actual integration was found to be much preferred to low-pass filtering. Note that the details of the saturated absorption spectroscopy and electronic feedback loops are omitted from the figures (such as Fig. 6.6) which attempt to give overviews of the optical table. These locks were critical because much of the data involved averaging and counting sessions which could last up to 1/2 hour long. Furthermore, the end of the lab with the diode lasers tended to have major temperature fluctuations until the door at that end of the lab was permanently closed.

Table 6.3 shows all of the relevant physical parameters for both of the MOTs. The upstairs MOT_1 routinely collected about 2×10^8 atoms as estimated by the cloud volume of about 1.5 mm^3 and the atomic density $\rho_{MOT_1} \sim 1 \times 10^{11}$ atoms/cm^3 inferred from the intensity of scattered light (fluorescence) from the atom cloud. Note that this number is consistent with Eq. 6.2 above and the data in Table 6.3 for MOT_1. With this success in hand, the next task was to achieve as cold a temperature as possible to maximize the transfer efficiency to the lower MOT_2.

The Doppler limit in a MOT is due to the near-resonant ($\delta \sim -\Gamma$) frequency of the beams necessary for efficient capture of the atoms. That is, Doppler cooling relies upon efficient scattering of light by the atoms, and they scatter most efficiently when that light is close to resonance. This limit is roughly $k_B T_D \sim \hbar\Gamma/2$, which for Cesium corresponds to cooling from room temperature to about 120 μK. However, with such a cold sample *already prepared*, it is possible to cool below this limit as will be explained below. Even though advanced atomic cooling techniques were very well known [151] by this point in the atomic physics community, no serious effort at

	MOT$_1$ (upstairs)	MOT$_2$ (downstairs)
Coil radius	4 cm	8.5 cm
Number of turns	50 (AWG 20 wire)	142 (AWG 20 wire)
Coil separation	8 cm	14 cm
Coil current	3 A	10 A
Coil turn-off time	100 μs	200 μs
Magnetic field gradient	15 Gauss/cm	8 Gauss/cm
Trapping beam diameter	1 cm	5 mm
Trapping beam power	6 mW/beam	4 mW/beam
Trapping beam detuning	- 7 MHz	- 8 MHz
Repumping power	10 mW	7 mW
MOT size	1.5 mm diameter	750 μm diameter

Table 6.3: Comparison of the parameters for the upstairs and downstairs MOTs.

achieving sub-Doppler temperatures had ever been necessary in our labs.

6.2.5 Polarization Gradient Cooling (PGC)

The basic idea behind one popular sub-Doppler cooling technique, known as polarization gradient cooling (PGC) can be explained by the following simple $1D$ example [151]. Suppose two counter-propagating laser beams with orthogonal linear polarizations and a fixed relative time phase (the so-called "lin⊥lin" configuration) are detuned by δ below the atomic resonance of linewidth $\Gamma = 2\gamma_\perp$ (FWHM) for a $J = 1/2 \to J' = 3/2$ transition. The appropriate Clebsch-Gordan coefficients for such a transition are shown in Fig. 6.7(a), and the field can be written as

$$\psi = \mathbf{x}e^{ikz} + \mathbf{y}e^{-ikz} = \mathbf{x} + \mathbf{y}e^{-i2\pi(2z/\lambda)}, \qquad (6.6)$$

whose polarization will change from linear to circular in a spatial distance of $z = \lambda/8$. Referring to Fig. 6.7(b), an atom at any point in space in the $m_J = -1/2$ ($m_J = 1/2$) state will see a potential given by the solid (dashed) curve, where the magnetic sublevel dependence is due to the polarization gradient as shown in the diagram. Hence, an atom in the state $m_J = 1/2$ (pumped here due to the σ_+ polarization) moving to the right at point A will climb the potential well associated with the dashed curve. However, by the time it reaches point B, the polarization has changed to σ_- and

the atom has the highest probability of being optically pumped into the $m_J = -1/2$ state and gets transferred through the excited state to point C. It again climbs the same potential well, but this time on the solid curve as appropriate to its change of internal state. As it approaches point D, it is most likely to get pumped by the σ_+ light back into $m_J = 1/2$, and the process repeats itself.
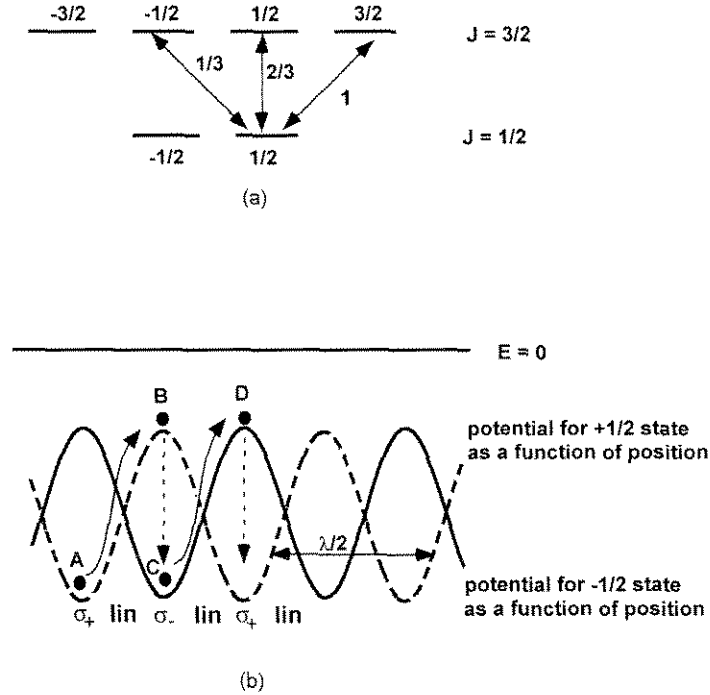
Figure 6.7: The mechanism for lin$\perp$lin polarization gradient cooling (PGC) can be explained as a Sisyphus effect for a $J = 1/2 \rightarrow J' = 3/2$ transition (a), in which the atom is forced to primarily "climb" potential wells. This is due to the spatial asymmetry in the scattering (optical pumping) rate caused by the polarization gradient (b).

In order to get some indication of the ultimate temperature limit T_{PGC} to this technique, we must first examine the expression for the potential U' (level shift of the ground state) seen by an atom in a low intensity ($I/I_{\mathrm{sat}} \ll 1$), far detuned optical field ($\delta/\Gamma \gg 1, \Gamma/2 = \gamma_\perp$),

$$U' = \frac{\hbar\delta}{2} \log\left(1 + \frac{I/I_{\mathrm{sat}}}{1 + (2\delta/\Gamma)^2}\right) \sim \frac{\hbar\Gamma^2 I/I_{\mathrm{sat}}}{8\delta}. \tag{6.7}$$

For typical parameters $(I/I_{\text{sat}} \sim 1/2, \delta/\Gamma \sim -6)$, it is clear that $T_{PGC} \sim T_D/100$ is possible as the atom is confined to the well depth U'. Another way to see this is to realize that the "Sisyphus" mechanism fails when the atom does not move the distance of about a half-wavelength in an optical pumping time (equal to the inverse scattering rate $1/\Gamma'$). The expression for the scattering rate is given by Eq. 7.16, which, in the large δ limit, reduces to

$$\Gamma' = \Gamma/2 \frac{I/I_{\text{sat}}}{1 + I/I_{\text{sat}} + (2\delta/\Gamma)^2} \sim \Gamma \frac{\Gamma^2 I/I_{\text{sat}}}{8\delta^2}, \tag{6.8}$$

so that this condition can be written $v > \Gamma'\lambda/2$, which gives $T_{PGC} \sim T_D/100$ as before.

The two expressions 6.7 and 6.8 also show that U' falls off much more slowly (as $1/\delta$) with δ than does Γ' $\left(\text{as } 1/\delta^2\right)$. In the limit of very large δ, the potential is completely conservative because no cooling occurs with the scattering rate vanishing as $1/\delta^2$. This is the far off-resonant trap (FORT) situation to be discussed in Sec. 7.2.1. However, if δ is too small, the situation reverts to the Doppler cooling picture which is limited by a saturation of the scattering rate. Hence, the typical parameters mentioned above are a compromise between these two limits.

It should also be noted that there exists a second configuration, the so-called σ_+/σ_- configuration, which also provides sub-Doppler cooling and will work for a $J = 0 \rightarrow J' = 1$ transition. Here, two opposing circularly polarized fields form a rotating linear polarization via

$$\psi = \sigma_+ e^{ikz} + \sigma_- e^{-ikz} = \mathbf{x} \cos(kz) + \mathbf{y} \sin(kz). \tag{6.9}$$

The atomic polarization for a moving atom cannot follow this change, and hence it lags behind the local field polarization. The result is a population imbalance in the $m_{J'} = \pm 1$ sublevels of the excited state, depending on which direction the atom moves, which will force it to scatter more from the σ_- (σ_+) (due to excess population in the $m_{J'} = -1$ ($m_{J'} = +1$) state) if it is moving to the right (left) for the field of Eq. (6.9).

Again, this technique can reach sub-Doppler temperatures because the mechanism will fail if the atom begins to adiabatically follow the field polarization. Since it takes scattering through the excited state for the atom to "know" its polarization, the same condition of $v > \Gamma'\lambda/2$ holds as before. This scheme has the practical advantage that the σ_+/σ_- configuration is identical to what is found in a MOT, so the conversion from MOT beams to σ_+/σ_- PGC requires no polarization change, but simply intensity and detuning changes for the MOT beams. The frequency switching was accomplished with an AOM on the master trapping laser for the upstairs MOT_1, and an auxiliary AOM in the slave trapping laser beam path did the intensity switching. For the downstairs MOT_2, both functions were accomplished with the same double-passed AOM in the trapping laser beam path.

Before assessing the practical performance of the sub-Doppler PGC technique in our experiment, it is necessary to digress and comment upon the implementation of the magnetic fields. The anti-Helmholtz magnetic fields are turned off during PGC, with the assumption that the cloud remains at a zero of the magnetic field such that there is no splitting in the magnetic hyperfine sublevels m_F. In practice, this has several very important implications. For example, it is necessary to compensate for stray magnetic fields by placing a set of shimming coils along each of the co-ordinate axes. These are easily implemented by using a Helmholtz coil configuration and making sure to get the settings roughly correct with a Gaussmeter while the vacuum chamber is open.

Once these are used to cancel stray fields at the position of the beam intersection (the intended trap center), then it is necessary to move the anti-Helmholtz coils so that their field zero is at this same position, allowing for optimum loading from the MOT into PGC. Hence, it is advantageous to put the trapping coils on a moving stage to allow this process to be finely tuned through several iterations. Finally, it is important to have a method to turn the trapping magnetic field quickly and precisely in order not to apply transient forces to the cloud. For the 3 A current required by the coil geometry of our MOT_1 (for relevant parameters, see Fig. 6.3) we were able to find an integrated circuit (LMD18400) which could do this in less than 100 μs.

The next technical challenge was the implementation of the imaging system necessary for characterizing the performance of the PGC. At the time the experiment was designed, there was no really good, inexpensive and easy-to-use combination of hardware and software which would allow gated camera triggering and frame grabbing. Furthermore, the CCD cameras that we used (SONY XC-75) preferred to "free-run" and did not lend themselves easily to adaptation as slaves to external timing. Therefore, the vertical drive (VD) and horizontal drive (HD) pulses of one of the cameras were used to slave each of the other imaging cameras in the lab. The composite video signal for each of the cameras has this timing information imbedded in it, which was stripped off and used by the frame grabber hardware (Data Translation DT3152). As a result, the VD signal (at approximately 57 Hz) was used as the master experimental time-base for the *entire* experiment, so that the experimental duty cycle is a multiple of the VD period. This would allow any subsequent timing pattern generated to be stable with respect to the camera and therefore allow pictures to be taken at precise moments. Unfortunately, the CCD camera would still integrate for an entire video cycle of 17.5 ms, so it was necessary to use short pulses of laser light and eliminate stray light to avoid saturation of the video signal before readout of the CCD array. Once this (albeit awkward) protocol was ironed out, the system has worked very nicely for the two years thereafter.

The main point here is that two single most important ingredients necessary to the optimization of the PGC parameters are precise control over the compensating (zeroing) magnetic fields and a good, real-time imaging system. With these in place, it was very easy to quickly optimize the PGC parameters. By illuminating the atom cloud with resonant light a fixed time after the PGC period has ended, the expansion rate of the cloud (and hence, the temperature) can be directly measured. The relevant polarization gradient cooling information for both MOTs is summarized in Table 6.4. Fig. 6.8 shows cross-sections through two images of the MOT$_1$ cloud taken using the above imaging system 24 ms and 36 ms respectively after the PGC cycle was finished. The difference in spatial widths (0.02 cm) of the cloud over this time gives a spreading velocity for the cloud of approximately 1.8 cm/s, corresponding to a final

temperature of 3 μK after the PGC protocol. This was more than adequate to allow the atoms to fall the 25 cm distance through the differential pumping hole to the position where they would be captured in the lower MOT_2.

	MOT_1 (upstairs)	MOT_2 (downstairs)
PGC detuning	- 41 MHz	- 36 MHz
PGC intensity	2 mW/beam	1.5 mW/beam
PGC duration	6 ms	12 ms
Final temperature	3 μK	1 μK

Table 6.4: Comparison of the polarization gradient cooling (PGC) parameters used for the two MOTs.

Once this labor-intensive protocol had been followed once, a short-cut was found which allowed the PGC to be tweaked easily every day. At the very end of the PGC, instead of dropping the atom cloud, it was exposed to a burst of resonant light. The cloud would get "blown away" because of the resonant nature of the light, and the exact way it would expand as seen on a video monitor could be correlated with its temperature. A signature of good PGC was a very slow "puffing" of the cloud even under intense, resonant excitation.

6.2.6 The Downstairs MOT_2

After falling for 250 ms, the cold atom cloud arrives at a position of about 5 mm above the cavity in the UHV portion of the vacuum system. In place here is a second completely independent MOT_2 setup for catching these atoms and re-cooling and trapping them before allowing them to fall the final distance into the cavity. The placement of the cavity with respect to the expected position of the falling atoms was an important design consideration, because there was expected to be very limited tunability (± 1 cm in all directions) of the overall position of the lower MOT_2 once everything was aligned. To overcome this problem, a very crude but effective solution turned out to be the use of a 40 cm long "plumb bob" hanging the vertical length of the vacuum chamber. A point on this axis was made to pass through the expected position of the upstairs MOT_1 and also through the geometric center of the
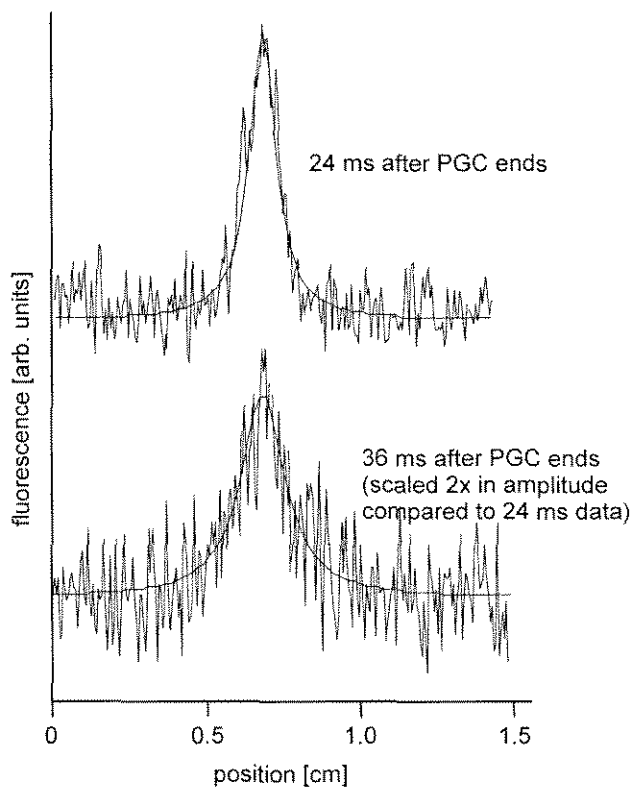
Figure 6.8: The temperature of the atom cloud is measured by determining its expansion rate. The change in the width of the cloud's fluorescence image from (a) at 24 ms after the end of the PGC cooling cycle to (b) at 36 ms after PGC gives an upstairs MOT_1 temperature of approximately 3 μK, allowing the cold ball to pass easily through the differential pumping hole into the lower chamber.

lower vacuum chamber. A point 1 cm below the end of the bob then defined the correct position of the cavity, assuming the atoms fell straight down only under the influence of gravity from the PG cooled cloud of MOT_1. Great care was taken to avoid introducing contaminants onto the cleaned vacuum parts and the assembled cavity throughout this procedure.

Fig. 6.9 shows the table layout for the locking, frequency, and intensity control of the downstairs MOT_2 beams. The downstairs lasers use a somewhat different locking technique implementation to avoid putting frequency sidebands on the trapping laser. Here, the re-pumping laser is locked with an FM Pound-Drever-Hall [52] pump-probe scheme as usual, but now it is also used as the weak probe in a second saturated absorption scheme involving the trapping laser as the strong pump. In this case, the modulation of the re-pumper is transferred *through the excited state* and can be used to derive an error signal for the trapping laser. This is known as a modulation-transfer type spectroscopy [152]. The trapping light is then double-passed through another AOM for frequency and intensity control, as mentioned above, before being coupled into a fiber. The fiber again serves to both improve its spatial mode structure (so that roughly 11 mW of trapping light is available) and to aid in minimizing MOT_2 misalignment.

The actual alignment of the beams is much trickier in this case. First, the 852 nm light cannot be seen by the naked eye. In addition, there is very little inside the vacuum chamber which clips the beams to allow them to scatter and be seen by an infrared viewer. Finally, there is no background atomic vapor around as in MOT_1, whose fluorescence can be used to align each set of beams to the other. In the end, the easiest thing to do is use the geometry of the vacuum chamber itself and align the beams to be geometrically centered on the cylindrical chamber structure. This procedure tended to work well as quantified by the roughly 10% transfer efficiency of atoms from the upstairs MOT_1 to the downstairs MOT_2, which is consistent with other numbers reported for this type of double-MOT loading unaided by any magnetic guiding. This number was found to be most sensitive to the parameters of the *upstairs* MOT_1, whereas up to 30% variations in MOT_2 parameters (such as beam
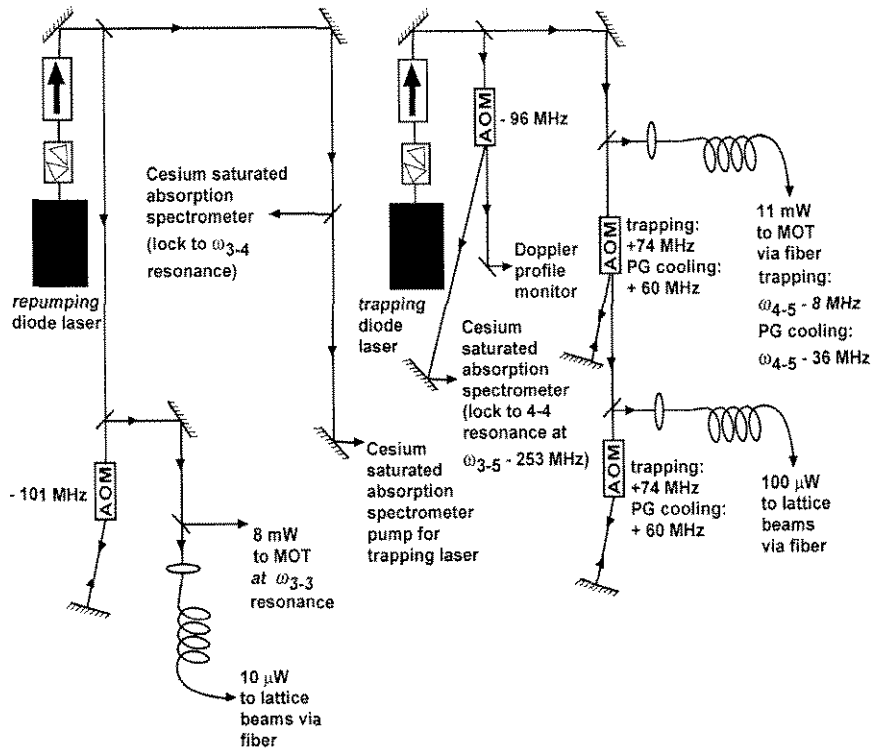
Figure 6.9: A schematic similar to Fig. 6.6 is shown now for the downstairs trapping laser set-up. In this case, an injection locking scheme was not used, but extra complication for these lasers arises from the fact that they are also used to derive the "lattice" or "cooling" beams which are discussed in Section 6.2.7.

intensity, detuning and coil current) typically did not significantly effect the capturing capabilities.
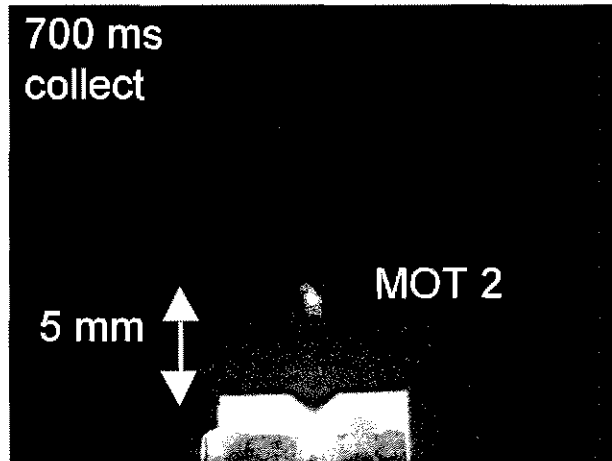
Figure 6.10: An image of the downstairs MOT_2 resting approximately 5 mm above the cavity (glowing from scattered light) shows the approximately 10% transfer efficiency of the 10^8 atoms from the upstairs MOT_1.

The magnetic field coils were again placed on a three-axis translator for this part of the experiment. Independent of the previous discussion about correct placement of the field zero crossing, there is another reason for not attaching the coils rigidly to the chamber. The downstairs coils are geometrically constrained to be farther away from the MOT center, which means more current (approximately 11 A) was necessary to achieve the required trapping field gradient. This current also needs to be turned off quickly, tending to cause some mechanical motion of the coils. The motion is enough to drive vibrations of the type 304 stainless steel (and hence, somewhat magnetic) chamber, which in turn can couple in to cause vibrations of the cavity mount. Physically decoupling the coils from the chamber as we did here definitely mitigates this problem, but still there is a residual signature of this turn-off transient on every single laser lock on the table due to mechanical coupling through the optical table itself. One very interesting side note here is that the correct compensation coil setting changed quite dramatically when the Ti:Sapphire pump laser was switched from a 20 W Ar^+ laser (Coherent Innova 100, 20W) to a 5W diode pumped solid

state laser (Coherent Verdi) after about 1 year. This was due to the large magnetic field generated by the confining magnet around the plasma tube of the ion laser which does not exist in the solid state pump laser.

PGC was implemented and optimized in much the same way as described for the upstairs MOT_1, and Table 6.4 summarizes the final parameters. Verification that the atoms were indeed falling vertically towards the cavity gap was accomplished by fluorescence imaging the falling cloud. The sequence of pictures in Fig. 6.11 depicts the falling of the atom cloud towards the cavity as a function time after the 12 ms PGC cooling cycle has ended. Note that the end of the downstairs PGC cycle, denoted as $t = 0$ for Fig. 6.11, is assumed to be $t = 0$ for all future discussion of atom transits unless otherwise noted.

6.2.7 Lattice/Cooling Beams I

A simple estimate shows that a single atom falling from 5 mm above the cavity will acquire a velocity of 31 cm/s, which corresponds to a temperature of about 7 times the Doppler limit of 120 μK (or a Doppler velocity of 12 cm/s). It was necessary to devise a way to dissipate some of this energy before loading the atom into the intracavity trap. Looking further ahead, the anisotropic intracavity trapping mechanism will have approximately 30 times greater confinement along the cavity axis compared to the transverse dimensions (basically the ratio of the waist w_0 to λ for the intracavity field) and one might expect that cooling of these radial dimensions once a single atom is trapped will become a very serious issue.

The solution first implemented was based upon a $2D$ analogue of the $1D$ PGC model introduced in Sec. 6.2.5. In $2D$, two retro-reflected beams which have orthogonal linear polarizations whose time phases are locked 90° out of phase with respect to one another can form a structure known as an *optical lattice* [132] as shown in Fig. 6.12. In the plane of the beams, the circular polarization components are unbalanced almost everywhere. In fact, there are sites of pure circular polarization (denoted by ↻ and ↺ in Fig. 6.12) where the atoms are optically pumped to their maximal m_F val-
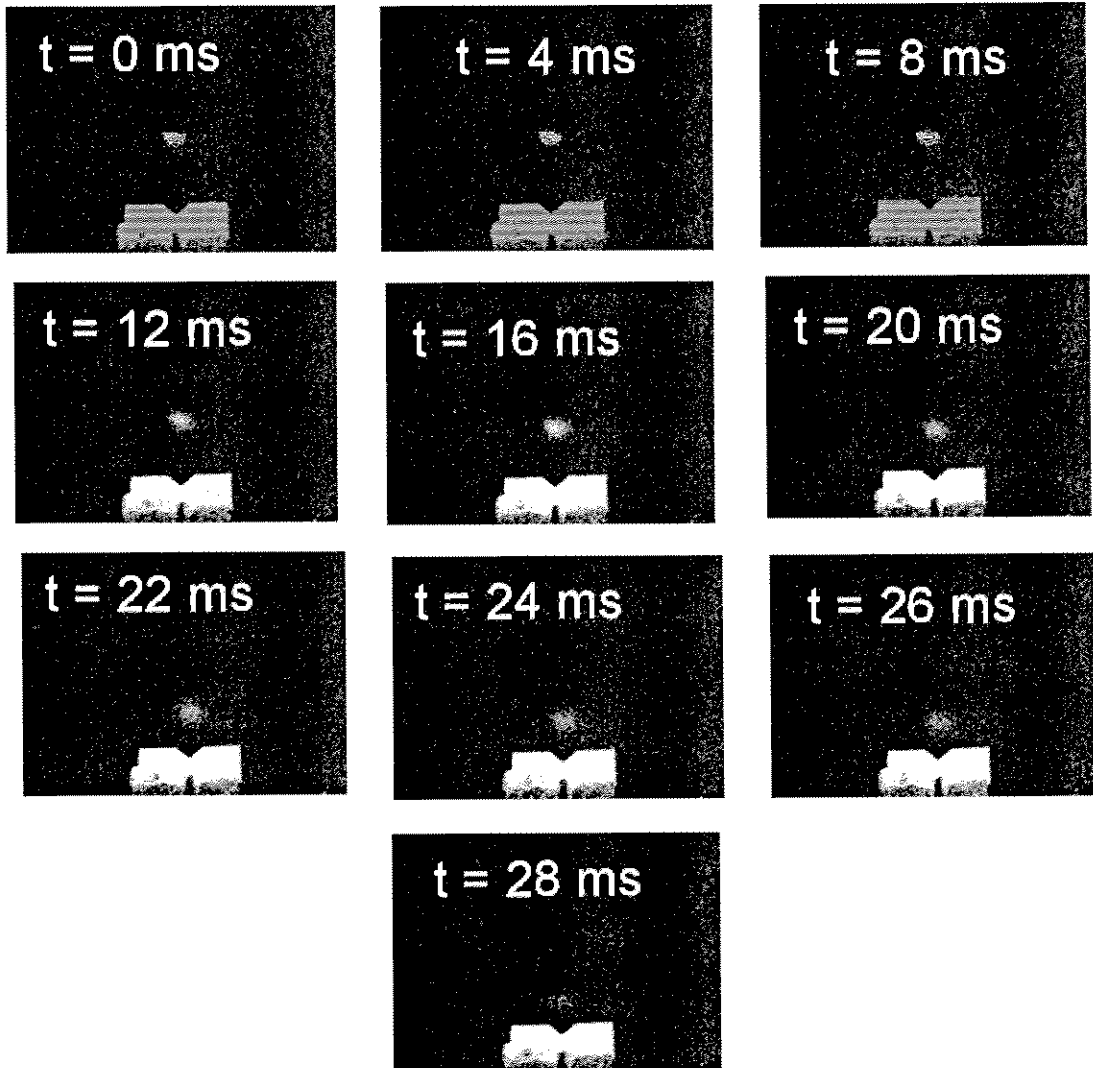
Figure 6.11: At sequential delay times after the end of the downstairs PGC cooling cycle, the atom cloud was (destructively) imaged to ensure it was falling vertically towards the gap in the cavity mirrors. Note that the fluorescence gets weaker at longer times not only because of the dilution of the atomic density due to expansion, but also because it begins to fall out of the cross-section of the MOT_2 beams which were also used for the imaging with a 2 ms resonant pulse at the indicated delay time.

ues. At these locations, the atom can be trapped in $2D$ with a potential depth given by Eq. 6.7 with the spatial dependence in I/I_{sat} of $(\cos kx + \cos ky)^2$. Furthermore, an atom which heats up and escapes the trap will encounter severe polarization gradients and will cool according to the previously discussed Sisyphus mechanism, as long as the lattice is not detuned too far from resonance. For *both* cooling and trapping, typical parameters are $(I/I_{sat} \sim 1, \delta/\Gamma \sim -7)$ as for PGC above.
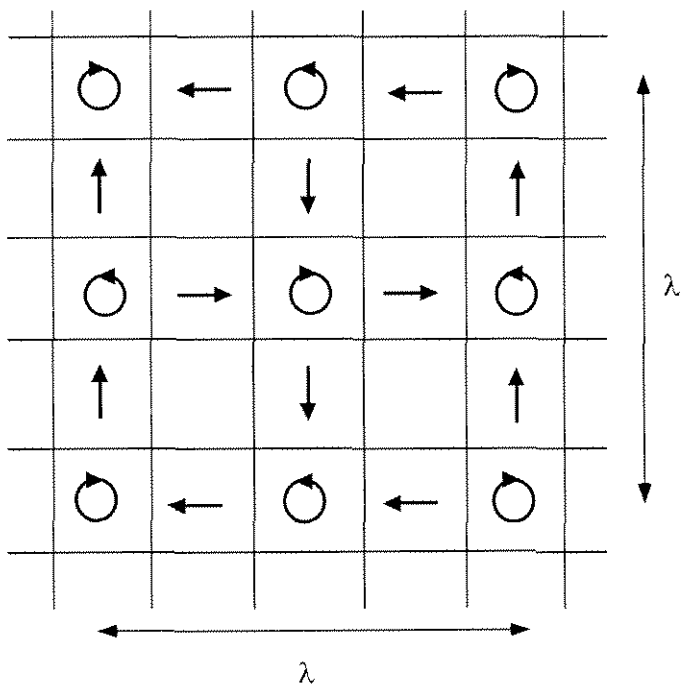
Figure 6.12: The spatial polarization structure of the optical lattice in the plane of intersection of the **k** vectors of the beams whose time phases are locked by 90° with respect to one another. ($\circlearrowleft, \circlearrowright$ and $\rightarrow, \leftarrow, \uparrow, \downarrow$) represent "pockets" of pure (circular and linear) polarizations. Atoms will be trapped at places of pure circular polarization. Note the spatial scale with respect to the wavelength λ indicated in the diagram.

With these parameters in hand, we can estimate the cooling rate for an atom arriving at the lattice with a speed of $v_0 = 31$ cm/s, as expected for atoms falling from MOT$_2$. Rewriting Eqs. 6.7 and 6.8 as

$$U' \sim \frac{\hbar\delta}{2}s \qquad (6.10)$$

$$\Gamma' \sim \frac{s\Gamma}{2(1+s)},$$

for small s, where the saturation parameter s is given by

$$s = \frac{I/I_{\text{sat}}}{1 + (2\delta/\Gamma)^2}, \tag{6.11}$$

then the parameters $(I/I_{\text{sat}} \sim 1, \delta/\Gamma \sim -7)$ give a well depth of $U' \sim \hbar\Gamma/60$ for $s \sim 5 \times 10^{-3}$. Assuming that an energy of approximately U' is lost per scattering event, it will take approximately $(1/2mv_0^2)/U' \sim 200$ scattering (optical pumping) cycles. With an optical pumping time of $1/\Gamma' = 400/\Gamma = 13$ μs, this will take approximately 2.5 ms, in which time the atom will have moved approximately 0.8 mm, or approximately all the way through the cavity. The solution to this perhaps unacceptable situation is to do the slowing in two stages. In the first, we detune much closer to resonance $(I/I_{\text{sat}} \sim 3, \delta/\Gamma \sim -1/2)$ for a short period of time (2 ms) to do most of the slowing and then go farther off resonance $(I/I_{\text{sat}} \sim 1, \delta/\Gamma \sim -7)$ to use the lattice in much more of a trapping role. Note that closer to resonance, the cooling effect is primarily Doppler cooling, where each scattering event tends to cool by the atomic recoil of $T_R = 100$ nK, meaning that $(1/2mv_0^2)/k_BT_R \sim 8000$ scattering events are needed. With $s = 3$, this would take approximately 500 μs. Timing diagrams will be shown soon in Sec. 6.2.8 to clarify this protocol, and the experimental results will be discussed in depth in Sec. 7.1.2. Note that this protocol has a hidden catch in that it actually heats the atoms up along the axis orthogonal to the lattice plane (i.e., the cavity axis) because it relies on spontaneous emission for its cooling effects. This causes momentum diffusion due to the random nature of the recoil kicks. So far, no mention has been made of any cooling protocol along this axis, and Section 8.3 will include a very brief discussion of recent theoretical work in this area.

The experimental implementation of this lattice proved to be extremely challenging. Light for these beams was taken from the unused zeroth order light of the downstairs trapping laser's frequency and intensity control AOM. This was passed through another AOM for further frequency control, and then combined with a small

amount of re-pumping light into an optical fiber. The lattice light needed to be focused down *from the side* through the 40 μm gap of the physics cavity (inside the vacuum chamber). This was accomplished by using a set of 15 cm focal length cylindrical lenses mounted outside the chamber to make "light sheets" which would pass cleanly through the gap. It was necessary to get a little bit creative to allow independent steering control of these beams independent of the MOT$_2$ light, even though both sets of beams are spatially very close to one another. In fact, both sets of beams shared the same retro-reflecting optic. In the end, the mounting of the lenses on a three-axis translation stage proved critical for independent alignment of the lattice beams. Once they were aligned and retro-reflected along the two nominally orthogonal axes, in a plane itself orthogonal to the cavity axis (see Fig. 6.15 for a clarification of everything that is going on around the cavity), it was time to satisfy the 90° phase lock requirement. For this, the retro-reflection from the two arms was re-combined on a photodiode, and then spatially overlapped to complete a Michelson interferometer. The photodiode output was used as the input to a servo whose goal was to fix the relative phase of the two beams, with one of the retroreflecting mirrors piezo-mounted to act as an actuator. This servo bandwidth of about 100 Hz was found to be adequate, though care had to be taken to turn off the integrating stage when no light fell on the photodiode (the lattice beams were not on 100% of the time). It must be noted that the the direct use of the error signal derived from this interferometer does not guarantee a 90° phase lock at the position of the beam overlap inside the cavity (where it matters!) and an adjustable phase offset knob was incorporated in practice.

As will be discussed shortly in Section 7.1.2, there was never any clear evidence that the special lattice arrangement was worth the extra hassle involved with keeping the time phase locked. Furthermore, it was very easy to rearrange the optics to change the input polarization scheme for the "lattice beams" from the lin$\perp$lin arrangement to a σ_+/σ_- arrangement. The σ_+/σ_- arrangement has the experimental convenience that these beams can now share all of the same polarization optics as the MOT$_2$ beams. The physical drawback is that there is no longer any trapping mechanism in this scheme, only cooling. In fact, there is no longer a lattice at all, but two

independent $1D$ "optical molasses" beams [153]. Nevertheless, these beams should still provide the cooling that is needed in the plane transverse to the cavity axis. For the rest of this thesis, the special intra-cavity cooling beams discussed in this section are referred to interchangeably as the "lattice beams" or the "cooling beams."

6.2.8 Timing Diagram

At the beginning of the experimental construction, the timing was all performed in hardware with a (ghastly) combination of slaved timing generators (Stanford DG535) and a submultiple of the camera VD frequency used as the master trigger as mentioned previously. As the experiment grew more complex and more of the timing became established (after significant trial and error), it was decided to use a software-programmable timing generator to hardwire much of the timing and free up some of the equipment for other tasks. The board eventually chosen (Gage Scientific Instruments T30) has 32 output lines, each of which is independently programmable to approximately 3400 bits. The meaning of a "bit" in time (board resolution) is determined by an external input, which in our case was set to 0.5 ms so that the total duty cycle of the experiment was roughly 1.7 s (3400 bits × 0.5 ms/bit). Finally, the board was triggered by the same submultiple of the camera VD pulse as before to preserve the capability of doing imaging with the camera. The board had the advantage of having its own stand-alone processor and memory, needing only power from the host PC, but there were also several drawbacks. First, programs had to be written in C to allow simple, user-friendly changes to the timing patterns. This has been corrected in newer versions which are now fully Labview compatible and programmable. Second, because the board was originally intended by the manufacturer to be used as a test-vector generator for debugging digital circuits, the outputs are not capable of driving multiple loads and need to be independently buffered (and inverted, if necessary). Otherwise, it has performed quite well and has certainly simplified the timing generation process for further additions to the experiment.

In order to summarize this section, the timing diagram of Fig. 6.13 below gives

a comprehensive review of all of the experimental timing relevant to the delivery of cold atoms to the cavity. This timing diagram will be used as a reference point in all subsequent discussion of experimental timing, and note, once again, the designation of $t = 0$ as the end of the downstairs PGC cycle.

6.3 The High Finesse Cavity

In the following section, the properties of the high finesse Fabry-Perot cavity used in the experiment will be discussed. In order to avoid significant overlap with the thesis of Christina Hood, who has devoted much effort to improving the group's knowledge and state-of-the-art in this area, I will keep the discussion brief and focus mainly on those areas unique to our experiment.

6.3.1 Construction

The cavity is formed by two nominally identical super-polished mirrors based on 1 cm long, 3 mm thick cylindrical fused silica substrates. One face of the substrate is flat and anti-reflection coated, while the other face has been superpolished to an $R_c = 20$ cm radius of curvature and interference-coated to have a nominal total (combined transmissive T, absorptive A and scattering S) loss of $L = T + A + S = 7$ ppm at 852 nm. The manufacturer (Research Electro-Optics) has specified the scattering plus absorptive contribution to be $A + S \sim 2$ ppm. If the scattering losses of the assembled cavity structure are assumed negligible, a symmetric cavity will thus have total losses $2L = 2(T + A)$. The highly reflective surface on each mirror has been mechanically turned down to a diameter of 1 mm which facilitates optical access to the center of the cavity by allowing for a wider field of view as seen from the cavity side. Great care is taken to ensure the cleanliness of the highly reflecting surface and each mirror is manually "swiped" clean as often as it takes to produce a surface free of particles under high (100 X) optical magnification.

Cavity construction proceeds by way of a "jig" developed by Christina and Mike Chapman for a previous generation of cavities. Each mirror is first glued into an
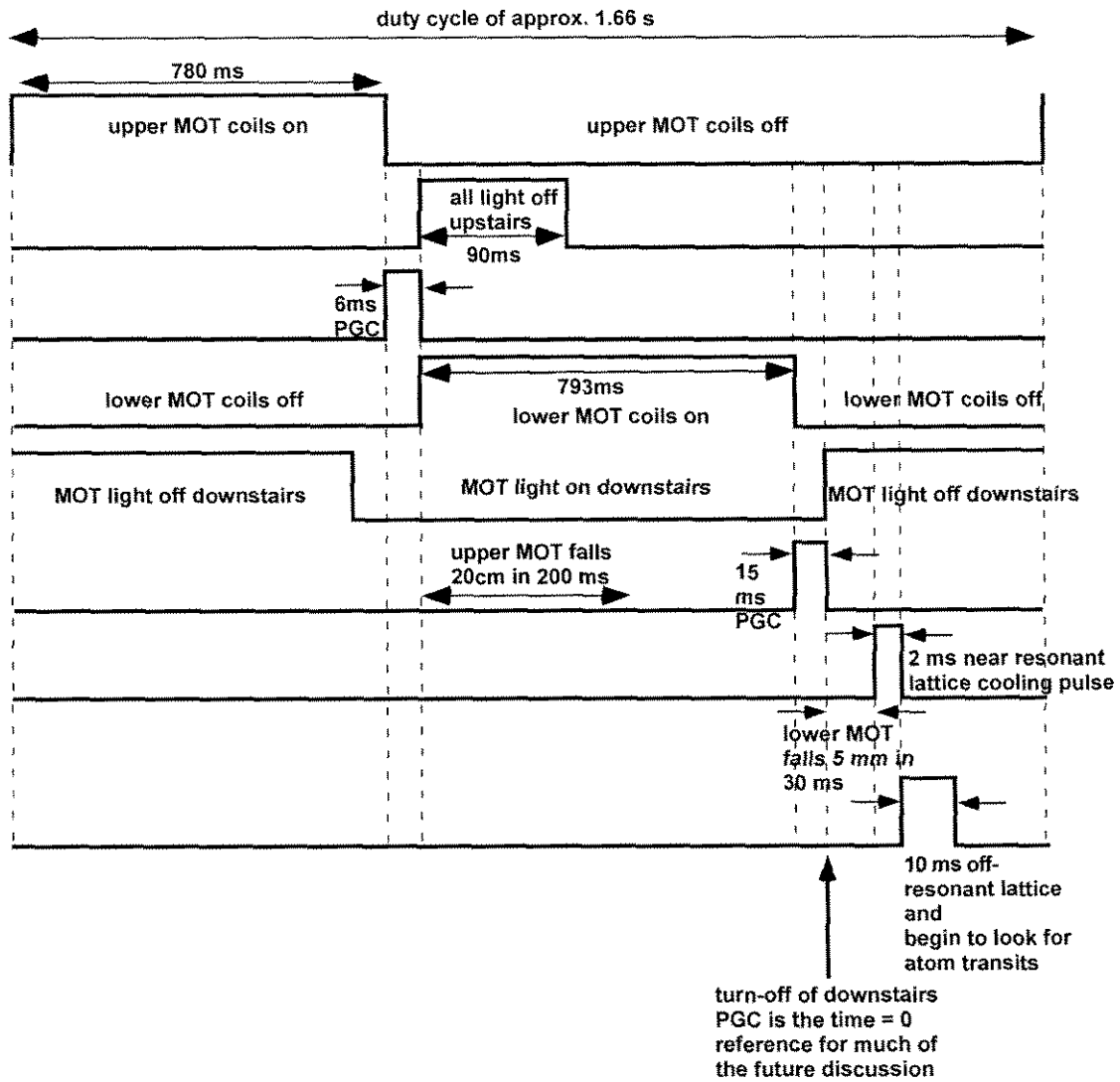
Figure 6.13: The timing diagram above attempts to clarify the pulse sequence for the preparation of cold atoms over the ~ 1.7 s experimental duty cycle. The time which will be nominally denoted $t = 0$ for much of the future discussions at the end of the downstairs PGC is indicated on the diagram.

aluminum V-block so that the mirror position can be manipulated with ease, while reducing the possibility of contamination of the (already cleaned) highly reflecting surface. One of the mirrors is rigidly attached via its V-block to the cavity support structure while the other mirror's position, and hence the cavity length, is adjusted using a micrometer and a high resolution (10 μm at a few cm working distance) optical microscope. A fringe of very low finesse is then made using a HeNe laser (at 633 nm) to get the cavity roughly aligned, and the adjustable mirror epoxied in place. The fringe is monitored and the cavity position adjusted accordingly to compensate for any residual motion as the epoxy sets. With this technique, it is possible to hit a desired cavity length l within about 5% for a given cavity construction.

6.3.2 Determination of Cavity Parameters

The cavity length can be specified most precisely with a measurement of its free-spectral range, given by $\nu_{\text{FSR}} = c/2l$. This can be done by holding the cavity length fixed and measuring as many different resonant wavelengths as possible. For example, with the cavity length held fixed such that it was (arbitrarily) resonant at 848.303 nm, other cavity resonances were measured by tuning the Ti:Sapph laser as shown in Table 6.5.

mode order	wavelength [nm]	frequency [THz]
$n + 4$	817.222	367.097
$n + 3$	824.772	363.740
$n + 2$	832.468	360.374
$n + 1$	840.309	357.012
n	848.303	353.647
$n - 1$	856.449	350.284
$n - 2$	864.747	346.922
$n - 3$	873.209	343.560
$n - 4$	881.832	340.201
$n - 5$	890.619	336.844

Table 6.5: The measured wavelengths used in a determination of the cavity free spectral range.

The story is complicated by the fact that the highly reflective coatings are dis-

persive, which means that they have a frequency-dependent phase shift $\phi(\nu)$. The relationship for mode order n to frequency $\nu(n)$ is given by [154]

$$\nu(n) = \frac{c}{2l}\left(n - \frac{\phi(\nu)}{\pi} - \frac{\phi_D}{\pi}\right),\tag{6.12}$$

where ϕ_D is the diffractive phase shift which is calculated to be a small correction for the Gaussian mode supported here by the cavity. It is necessary, however, to have information about $\phi(\nu)$ to extract l and the mode order n. Expanding $\phi(\nu) \sim \phi(\nu_c) + (v - \nu_c)\,d\phi/dv$ about the coating center wavelength v_c to get

$$\nu(n) = \left(\frac{c}{2l + \frac{c}{\pi}\frac{d\phi}{dv}}\right)\left(n - \frac{\phi_0(\nu)}{\pi}\right),\tag{6.13}$$

with $\phi_0(\nu) \sim \phi(\nu_c) - \nu_c d\phi/dv$, the frequency dependent resonance spacing (free spectral range) $\sigma(\nu)$ is identified as

$$\sigma(\nu) = \frac{c}{2l + \frac{c}{\pi}\frac{d\phi}{dv}}.\tag{6.14}$$

A plot of $\sigma(\nu)$ using the data of Table 6.5 is shown for our cavity in Fig. 6.14.

Fitting this data to

$$\sigma(\nu) = \sigma_0 - k(\nu - \nu_c)^2,\tag{6.15}$$

gives a max spacing $\sigma_0 = 3.3631$ THz at $\nu_c = 354.2$ THz, or $\lambda_c = 847.3$ nm, with $k = 21.5$ MHz/THz^2. Using the Kramers-Kronig relations, $\phi(\nu)$ can be found in the general case from the frequency dependence of the reflectivity of the mirror coatings [155]. Here the high reflectivity comes from a multilayer dielectric coating of Ta_2O_5/SiO_2 with index contrast $n_H : n_L = 2.09 : 1.46$. For such a coating at $\nu = \nu_c$, the phase shift and its derivative are given analytically by [156]

$$\begin{aligned}\phi_0(\nu_c) &= \pi\left(1 - \frac{1}{n_H - n_L}\right)\\[2mm]\frac{d\phi}{dv} &= \frac{\pi}{\nu_c(n_H - n_L)},\end{aligned}\tag{6.16}$$
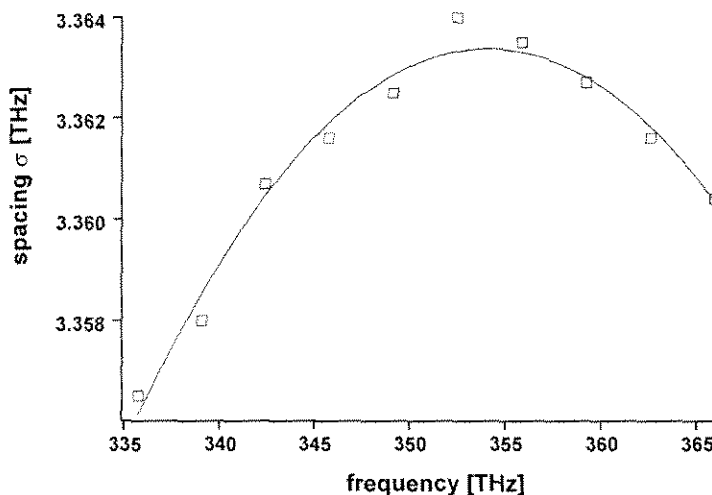
Figure 6.14: The frequency dependent mode spacing $\sigma(\nu)$ is plotted for the physics cavity in order to determine some of the cavity parameters. The solid line is a fit discussed in the text.

allowing the cavity length to be determined at ν_c as $l_c = 44.0$ μm with a mode number $n_c = 104.6$. The fact that n_c turns out not to be an integer here is due to both the fact that ϕ_D was neglected and that l is really a somewhat arbitrary definition for the cavity length via Eq. (6.12) and does not account for the fact that there is a significant evanescent field penetration into the 10 μm thick mirror substrates. Defining l_{eff} using Eq. (6.14),

$$\frac{c}{2l_c + \frac{c}{\pi}\frac{d\phi}{d\nu}} = \frac{c}{2l_{\text{eff}}} \tag{6.17}$$

gives an effective length of $l_{\text{eff}} = 44.6$ μm using $d\phi/d\nu$ from Eq. (6.16). Assuming the "extra" length $l_{\text{eff}} - l_c = 0.6$ μm resides in the substrates (300 nm in each), the effective round trip phase shift is $\phi_{\text{eff}} = k_c l_c + k_{\text{eff}}(l_{\text{eff}} - l_c)$ where $k_c = 2\pi/\lambda_c$, $k_{\text{eff}} = n_{\text{eff}} k_c$ and the effective substrated index of refraction is given by $n_{\text{eff}} = (n_H + n_L)/2$. Using this, $\phi_{\text{eff}}/\pi = 106.1$, which is as close to an integer as can be expected for the approximations made in this analysis. Christina has spent much time interacting with the mirror manufacturer and has used the transfer matrix method to model the field in the mirror substrates. She will have much more to say about the physical origin of $l_{\text{eff}} - l_0$ in her thesis.

Finally, the cavity length l as defined in Eq. (6.12) at $\nu_{\text{atom}} = 852.359$ nm (where the physics is done) is given by $l = l_c + n_c \left(\lambda_{\text{atom}} - \lambda_c\right) = 44.6$ μm. The obvious sources of error in this measurement are (primarily thermal) drift of the cavity length during the course of the measurements and the accuracy of the Burleigh wavemeter which was used for the measurements of the resonant wavelengths.

All of this discussion applies to the fundamental TEM_{00} mode. With the origin at the center of one of the mirrors (referring to Fig. 6.16), it can be described by the function

$$\psi_{\text{TEM}_{00}}\left(\mathbf{r}\right) = \psi_0 e^{-\left(x^2 + y^2\right)/w_0^2} \sin\left(2\pi z/\lambda_{\text{cavity}}\right), \tag{6.18}$$

and is the one most easily mode-matched by a Gaussian profile input laser beam. This fundamental mode tends to have the highest finesse of all the transverse modes because it minimizes diffractive losses by minimizing the mode spot profile at the mirror surfaces.

The second important measurement is the cavity linewidth $\Delta\nu = 2\kappa/2\pi$, which determines the photon storage lifetime. For this cavity, it is not necessary to go to the sophistication of a ringdown measurement (Sec. 3.1.2), since the use of simple phase modulation sidebands as frequency markers is sufficient to determine $\Delta\nu = 8$ MHz for the mode of interest. This gives a cavity finesse of $\mathcal{F} = \nu_{\text{FSR}}/\Delta\nu = 4.5 \times 10^5$, which represents approximately the number of bounces light will make between the two mirrors before it leaks out of the cavity. The finesse is determined only by the mirror losses via $\mathcal{F} = 2\pi/\sum \left(\text{losses}\right)$, suggesting that each mirror has a total measured loss of $L = 7.2$ ppm, which agrees fairly well with the manufacturer's number of 7 ppm quoted above.

It is clear from the above discussion that the photon storage lifetime can be made longer (and the cavity linewidth narrower) simply by extending the length of the cavity. However, this would be counterproductive with respect to the final important

parameter characterizing our cavity, its mode volume V_{m} given by

$$V_{\mathrm{m}} = \pi w_0^2 l / 4. \tag{6.19}$$

The cavity waist w_0 is calculated (see [157], for example) using

$$w_0 = \sqrt{\frac{l\lambda}{2\pi}\sqrt{\frac{R_{\mathrm{c}}}{l}}\left(2 - l/R_{\mathrm{c}}\right)}, \tag{6.20}$$

which gives a waist of $w_0 = 20.1$ μm and a mode volume for the TEM$_{00}$ mode of $V_{\mathrm{m}} \sim 14,000$ μm^3. This can be used to determine the coupling rate g_0 with

$$g_0 = \sqrt{\frac{3c\lambda^2\gamma_{\parallel}}{8\pi V_{\mathrm{m}}}}, \tag{6.21}$$

resulting in $g_0/2\pi = 32$ MHz.

To summarize, the final parameters for the cavity used in all the following work are length $l = 44.6$ μm, waist $w_0 = 20$ μm, and finesse $\mathcal{F} = 4.2 \times 10^5$, and hence a cavity field decay rate $\kappa/2\pi = 4$ MHz. The atomic transition employed for cavity QED is the ($g \equiv 6S_{1/2}, F = 4, m_F = 4 \rightarrow e \equiv 6P_{3/2}, F = 5, m_F = 5$) component of the D_2 line of atomic Cs at $\lambda_{\mathrm{atom}} \equiv c/\nu_{\mathrm{atom}} = 852.4$ nm. For our cavity geometry and from the atomic transition properties, we have $(g_0, \gamma_{\perp})/2\pi = (32, 2.6)$ MHz, with g_0 as the peak atom-field coupling coefficient and $\gamma_{\perp}$ as the dipole decay rate for the $e \rightarrow g$ transition. These rates lead to critical photon and atom numbers $(m_0 \equiv \gamma_{\perp}^2/2g_0^2, N_0 \equiv 2\kappa\gamma_{\perp}/g_0^2) = (0.003, 0.02)$. The cavity free spectral range is determined to be $\nu_{\mathrm{FSR}} = 3.363$ THz corresponding to a mode spacing of about $\Delta\lambda \sim 8$ nm. Therefore, a cavity tuned to resonance at $\lambda_{\mathrm{atom}} = 852.36$ nm will also be resonant (to explicitly identify a few other modes) at about 828.61 nm, 836.38 nm (used for locking), 844.29 nm, 860.58 nm, 868.96 nm (used for the FORT), and 877.51 nm. Fig. 6.15 shows all of the fields which are finally coupled into the cavity and the geometry for the definition of the mode function $\psi_{\mathrm{TEM}_{00}}(\mathbf{r})$ in Eq. 6.18.
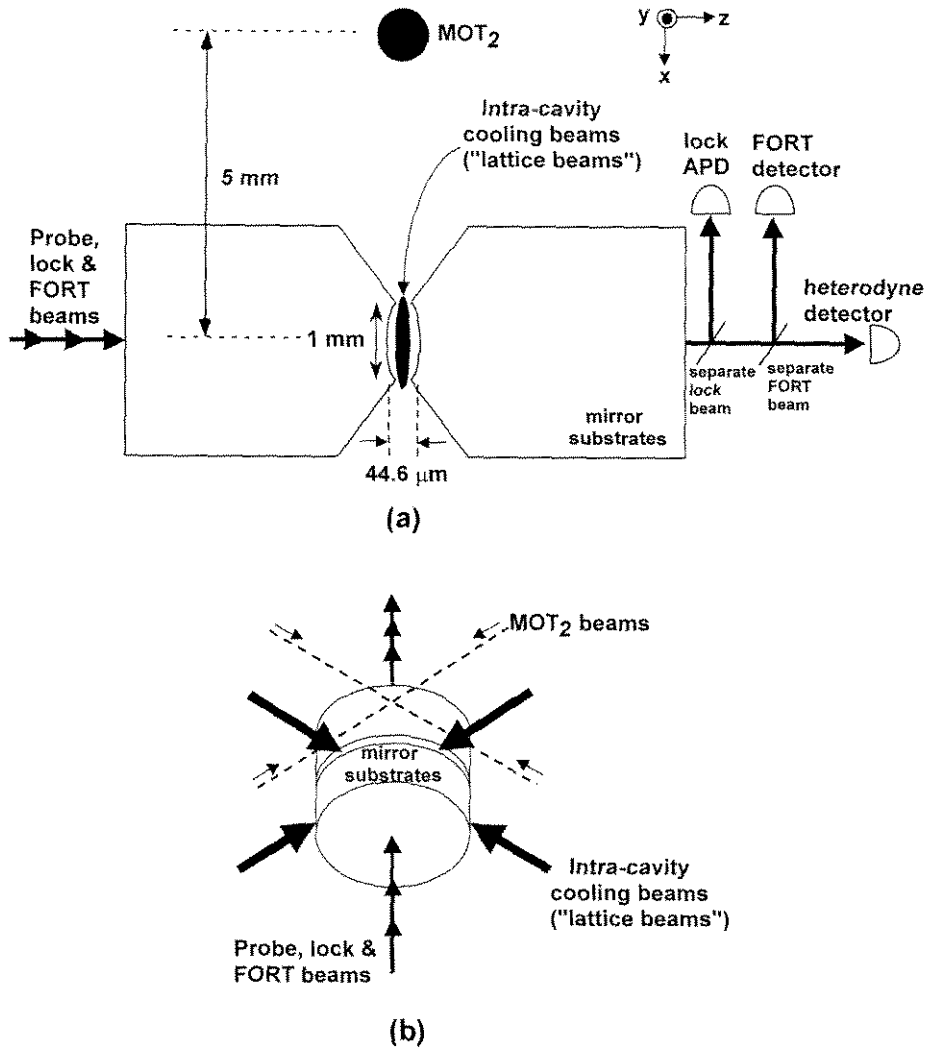
Figure 6.15: For reference, (a) shows the geometry of the cavity and indicates that three different laser frequencies (probe at 852 nm, lock at 836 nm and FORT trap at 869 nm) are all coupled into the cavity and separated with dichroic optics at the output. In (b), the MOT_2 and cooling beam geometries with respect to the cavity are indicated.

6.3.3   Passive Vibration Isolation and the Cavity Support Structure

One of the major concerns with this microcavity structure was mechanical stability and passive vibration isolation. The first layer of isolation is provided by floating the optical table, which eliminates frequency components below about 1 Hz or so. The main chamber housing the cavity and support structure was connected to the rest of the vacuum system only by way of flexible bellows, and we bolted this chamber directly to an extremely heavy piece of stainless steel. This steel piece then sits on three alternate layers of vibration damping material and a thick piece of copper with none of this structure rigidly attached to the table (though there are restraints in place to restrict any possible movement). Once inside the vacuum chamber, there is a heavy bed of copper that is mechanically isolated from the chamber interior by means of viton strips. Finally, the cavity support itself sits on a heavy block of copper which rests on more viton strips sitting on the copper bed.

The cavity support structure is shown in Fig. 6.16. There is a 1/2 inch tube PZT (Channel Industries, Santa Barbara) which separates the two pieces of the aluminum structure, half of which is rigidly attached to the copper block, and the other half of which is free to move. A bolt runs the length of the mount, which is held in place by nuts and a split-spring washer which is pre-tensioned to mechanically bias the structure. High voltage applied to the tube PZT will allow the cavity length to be scanned, with one FSR (about 1 μm) corresponding to approximately 300 V. The drawback of the tube PZT is that it has low frequency resonances in the range of a few kHz and therefore cannot be driven at frequencies much above 100 Hz. This makes it unsuitable as an actuator for suppressing acoustic cavity instability in the range of 10 Hz to 10 kHz.

For this reason, a second PZT was added to the cavity structure to allow for a much wider bandwidth in the frequency response. This PZT was a thin, rectangular "shear mode" PZT (EDO, Salt Lake City) which tended to perform a factor of 5 better than the specified electrostrictive constant of 1 pm/mV (perhaps due to pre-stressing).

NOT TO SCALE
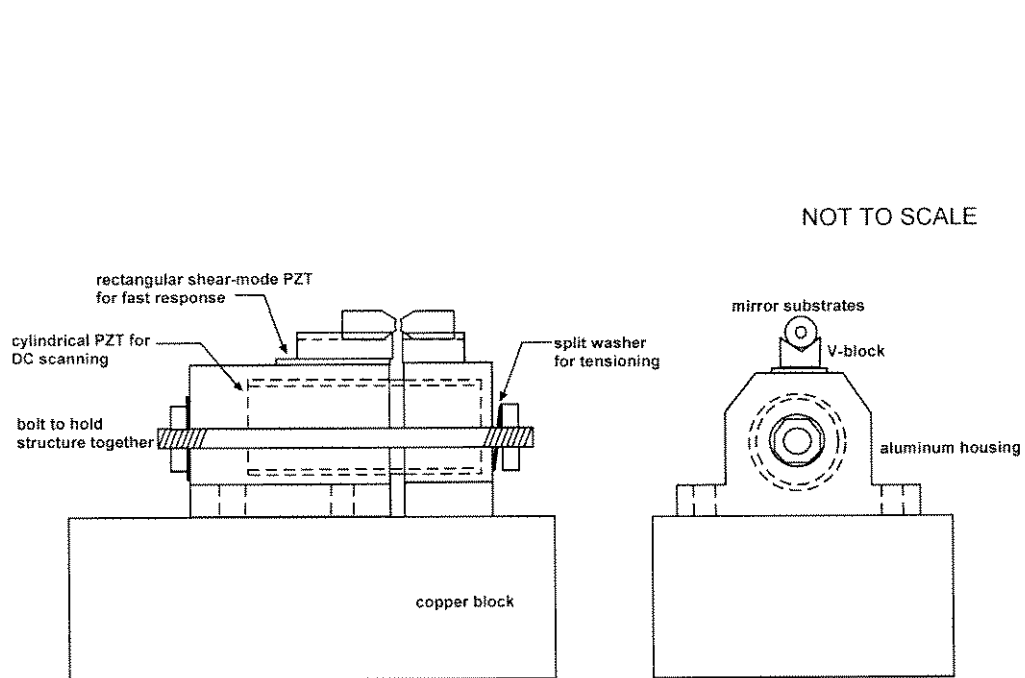
(a)
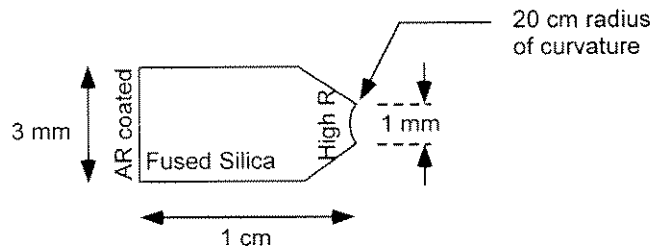
(b)

Figure 6.16: The cavity support structure in (a) was constructed around a 1/2-inch PZT cylinder to allow for coarse scanning and biasing of the resonator length, with a thin rectangular PZT for faster "tweeter" action. In (b), the mirror geometry is shown.

Furthermore, its frequency response in Fig. 6.17 showed resonances starting at about 11 kHz allowing an order of magnitude increase in the servo bandwidth. The PZT was glued with conductive epoxy to the top of the cavity support structure, and one of the mirror V-grooves was epoxied to the top.

Care was taken to install the cavity mount inside the vacuum chamber such that the gap between the mirrors remained vertical in order to allow cold atoms to be able to fall into the mode volume. This was done by aligning the cavity axis such that back-reflected light remained parallel to the table surface, which itself was checked with a bubble level. Furthermore, extra care had to be taken to ensure that the side "lattice beams" could also access the cavity gap. The plumb bob technique mentioned above was used to ensure that the gap was within ±1 mm of the center-line of the chamber.

All elements of the cavity mount were baked in a vacuum oven at 10^{-2} Torr to 250 °C before the cavity was assembled. Once placed into the chamber, a HeNe laser was reflected off of the cavity and a fringe formed between the front face of the first substrate and the highly reflecting surface of the second substrate. While the entire chamber was baked to about 250 °C, this interference was monitored and found to move 12 fringes (or about 8 μm) which was considered not to be a big problem due to the 40 μm gap. On cool-down, the cavity returned to its original length to within less than 1% as measured by ν_{FSR}.

6.3.4 Mode-Matching and Cavity Birefringence

In order to eliminate as much resonant scattered light from the cavity substrates as possible, and thereby prevent heating of the atoms due to the random spatial direction of the recoil kick, care was taken to try to maximize the mode-matching of the light into the cavity. A further benefit of efficient mode matching is that less light is scattered randomly into the heterodyne detection set-up (Sec. 6.4.3), though one of the major virtues of heterodyne detection is that it is supposed to discriminate against scattered light which is not both spatially mode-matched to the LO beam

and at the correct frequency. With the Ti:Sapph probe beam, approximately 40% mode-matching was attained, but a spatial filter was necessary to achieve even 20% mode-matching with the much worse spatial profile of the locking diode laser. A 15 cm lens was typically used to focus into the cavity from outside of the vacuum chamber. Such a long working distance is sufficient because propagation of the gaussian beam parameters of the mode show that the spot size at the mirror surface is not much greater than the mode waist.

Due to the way the cavity is constructed, the mounting of the mirrors into the V-groove structures can introduce stress-induced birefringence to the mirror coatings. Christina will discuss in her thesis the efforts made during her cavity construction experiences to minimize this birefringence. However, it should be noted here that the resultant differential phase shift between the linear eigenpolarizations of the physics cavity was measured to be $\Delta\beta = 2$ μrad/bounce. Note that this is an experimentally determined "average" phase shift for the cavity as a whole, and does not necessarily imply either that the phase shift is identical for each mirror or that the polarization eigenaxes are the same for each of the mirrors.

This is a problem for the σ_+ polarized light used to drive the cycling atomic transition $6S_{1/2}, F = 4, m_F = 4 \rightarrow 6P_{3/2}, F' = 5, m_{F'} = 5$, because incident circularly polarized light will not remain circularly polarized in the cavity. In practice, measurements of the polarization state of the transmitted light for our cavity show that nominally σ_+ light will be "σ_- contaminated" by about 7% in power, which is about 25% contamination of the field. Such a measurement can be made by inserting a $\lambda/4$ plate in front of the cavity to provide a circularly polarized input, and then use a rotatable polarizer (e.g., $\lambda/2$ plate plus fixed polarizer) at the output. In this way, it is possible to see the decomposition of the incident superposition of linear polarizations performed by the cavity in frequency space as the cavity is scanned.

Fortuitously, however, the σ_- Clebsch-Gordan coupling for $6S_{1/2}, F = 4, m_F = 4 \rightarrow 6P_{3/2}, F' = 5, m_{F'} = 3$ is down by a factor of $1/\sqrt{45}$ from the $6S_{1/2}, F = 4, m_F = 4 \rightarrow 6P_{3/2}, F' = 5, m_{F'} = 5$ amplitude as shown in Table 6.2. Furthermore, the frequency splitting associated with this phase shift $\Delta\beta$ is given by $\Delta f = \nu_{FSR}\Delta\beta/\pi =$

2 MHz, which is well below the cavity full width of $2\kappa/2\pi = 8$ MHz meaning that the birefringent splitting is largely unresolved in the first place.

6.3.5 The Cavity Servo

Although the details of the optical system used to derive the error signal for use in the cavity locking will be described fully in Sec. 6.4, some background information about the cavity servo serves as a useful introduction. The choice between the thin rectangular PZT and thick cylindrical PZT (see Fig. 6.16) to act as the principal actuator in the cavity servo was determined by their resonance structures. Extensive experience with the cylindrical PZTs had shown that at most a 100 Hz bandwidth servo could be used with them to avoid driving their intrinsic 1.5 kHz resonance. The native noise spectra of thin rectangular PZT on the physics cavity is shown in Fig. 6.17, which was measured using a 100 kHz bandwidth dynamic signal analyzer (HP3562A DSA). A fringe was made using the HeNe between the front (AR coated at 850 nm) face of the first mirror and the high reflector face of the second cavity mirror, detected by a photodiode, conditioned and sent to the input of the DSA. A battery generated bias voltage placed on the tube PZT and the output of the DSA was ac-coupled to the thin PZT. The first clear resonance occurs at 11 kHz, which means that a 1- 2 kHz bandwidth "aggressive" PI-based cavity servo is possible.

Although the measurements are not shown here, characterization of the mechanical stability of the cavity structure was tested using a similar method with a set of speakers at acoustic frequencies. This revealed structural resonances near 4 kHz, 19 kHz and 30 kHz despite the extensive passive vibration isolation precautions taken. It was not possible to isolate the direct cause of these resonances, although the 30 kHz frequency corresponding to a sound wavelength in a metal of about 21 cm is suggestive of twice the length of main copper cavity support structure. Floating the optical table does nothing to attenuate acoustic coupling at these frequencies. Furthermore, the limited servo bandwidth could not significantly affect any of these resonances, and oscillations of the servo invariably contained primarily a 4 kHz component. The
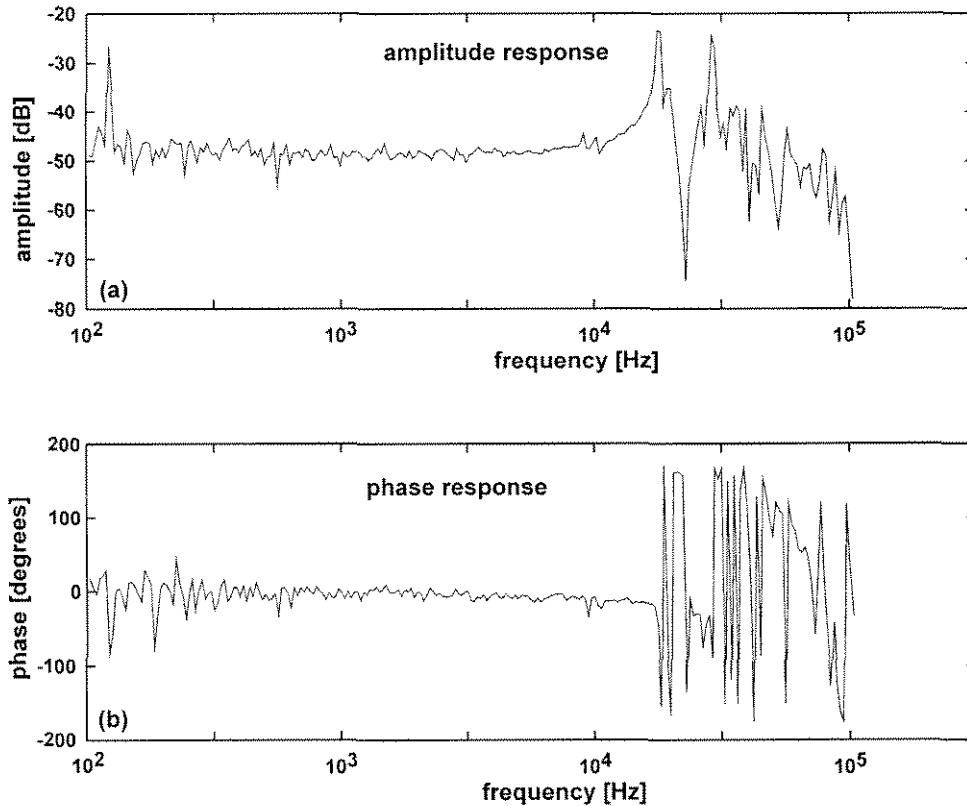
Figure 6.17: The amplitude (a) and phase (b) response of the thin PZT as it was incorporated into the cavity strucuture of Fig. 6.16 is shown. The first resonance near 11 kHz is the major limit to the bandwidth of the servo. The excess "DC noise" in both amplitude and phase below 200 Hz is an artifact of the *white noise* mode of the HP8562A Dynamic Signal Analyzer used for this work. This mode was found preferable to a *swept-sine plus auto-integrate* mode in order to get a quick, rough, wide-bandwidth idea of the frequency domain response.

group's experience with these cavity structures continues to evolve; for example, the most recent generation of Christina and Theresa has eliminated the use of the tube PZT in favor of two rectangular PZTs. This is a major step forward because it allows a more mechanically rigid mount and has pushed the PZT oscillations up more towards 30 kHz. One final note is that the mechanical response of the vacuum chamber to the switching of the magnetic field coils could be seen on the error signal of *every* servo on the optical table. For this reason, a significant margin of error in time (few ms) was budgeted to allow the servos to recover from this mechanical impulse.

6.4 The Laser System, Cavity Locking and Heterodyne Detection of the Intracavity Field

Aside from the laser system used for our far off-resonance intracavity trap (FORT), the other piece of technical infrastructure necessary for success in this experiment is the system of lasers which stabilize the physics cavity, drive the atom-cavity system and are integral to ultra-sensitive shot-noise limited heterodyne detection. The present experimental setup builds to a certain extent upon work done by Hideo Mabuchi and Quentin Turchette, and later work done by Jun and Hideo. Hideo has recorded his efforts in his thesis [159], and an attempt will be made here not to overlap too significantly with this work, but rather to document important changes and additions that have been necessary. A basic overview of the table emphasizing the lasers involved in physics cavity probing and locking is shown in Fig. 6.18.

6.4.1 Ti:Sapphire Laser

Our optical table is almost literally divided in half, with all of the cooling and trapping work done on one side, and the majority of optics needed to produce and detect the single-photon intracavity field occupying the other. At the heart of the experiment is a Coherent 899 ring Ti:Sapphire laser which is pumped by a Coherent Verdi single frequency diode pumped solid state laser at 532 nm (intracavity doubled Nd:YAG).

New Focus 6200 locking diode laser (836 nm)

9 mW

transfer cavity

TWM #2
150 MHz (nom.)

EOM

APD to lock
physics cavity
to locking
diode laser

physics cavity

probe for Cs
spectrometer

- 80 MHz

AOM

AOM

+ 200 MHz

EOM

TWM #1
240 MHz (nom.)

pump for Cs
spectrometer
locked on $\omega_{4\text{-}5}$
resonance

1 mW

detect the
FORT laser
through the
cavity

Coherent Verdi
diode-pumed
solid state
pump laser

4 W

local oscillator cleaning cavity

5 mW of LO power

balanced
heterodyne
detection @
+ 40 MHz (nominal)

200 mW

- 40 MHz
(arbitrary)

Coherent 899 Ti:Sapphire
Laser (852 nm)

TUI Optics FORT diode
laser (869 nm)

AOM

+100 MHz
(arbitrary)

Figure 6.18: The complementary side of the table to the trapping lasers is shown here, including the Ti:Sapph, locking diode and trapping diode lasers. This figure should be used in conjunction with Fig. 6.20, which explains the table layout in frequency space. The optical table (8 feet × 16 feet) is now getting so dense with optics that two 8 foot × 2 foot breadboards and numerous platforms are mounted in a "second layer" around the table.

The history of our 899 Ti:Sapphire laser has been well-documented [158, 68, 159]. The Verdi replaced a Coherent Innova-100 20W Ar$^+$ ion laser about 1 year ago, and has been an excellent replacement as a pump laser for several reasons. The following chart compares and contrasts the two lasers as pump sources for a Coherent 899 Ti:Sapph based on roughly one year of experience with the Verdi. Though most of

	Coherent Verdi	Coherent Innova-100 Ar$^+$
issue		
daily set-up	1 hr. (beam pointing)	5 hrs. to stabilize power, pointing and mode
daily follow up	never need to touch	tweak once every 2 hrs. after warm up
electrical power	120 V/10 A	480V, 20 A three phase, special wiring
cooling	Neslab chiller	Caltech chilled water, significant plumbing
maintenance	new diodes in 4 yrs.	new tube every 1.5 yrs., clean every 3 mons.
power needed	4 W @ 532 nm	8 W typical @ 514 nm (all lines)
other	no stray fields	stray magnetic fields (plasma confining)
	compact, sits on table	large frame/power supply, sits under table
	quiet in operation	noisy power supply

Table 6.6: A comparison of the Coherent Innova-100 Ar ion laser and Coherent Verdi as pump sources for a Coherent 899 Ti :Sapphire laser.

the comments here are qualitative, this chart gives an idea of some of the practical advantages of the solid state pump over the gas laser. In addition, some quantitative measurements were made of the intensity noise of the Ti:Sapph laser output under different pump conditions, which are presented in below in Fig. 6.6. It is clear that the ion laser pumped Ti:Sapph has about 30 dB more noise out to about 600 kHz compared to a Ti:Sapph pumped by a Verdi. Furthermore, the peaks at 100, 200 and 300 kHz in the latter case also appear on the intensity spectrum of the Verdi on its own. Both pump lasers have the same effect on the Ti:Sapph out beyond about 3 or 4 MHz. It is important to understand that this intensity noise directly written onto the Ti:Sapphire light will eventually contaminate the purity of the Ti:Sapph-derived LO for the balanced heterodyne detection set-up, and it is clearly preferable to be pumping with the Verdi for this reason.

Having already completed a discussion of the diode laser systems for the MOTs, I will now proceed with a brief overview of the "second half" of the optical table. The 120 mW Ti:Sapph output is first double-passed through an external acousto-
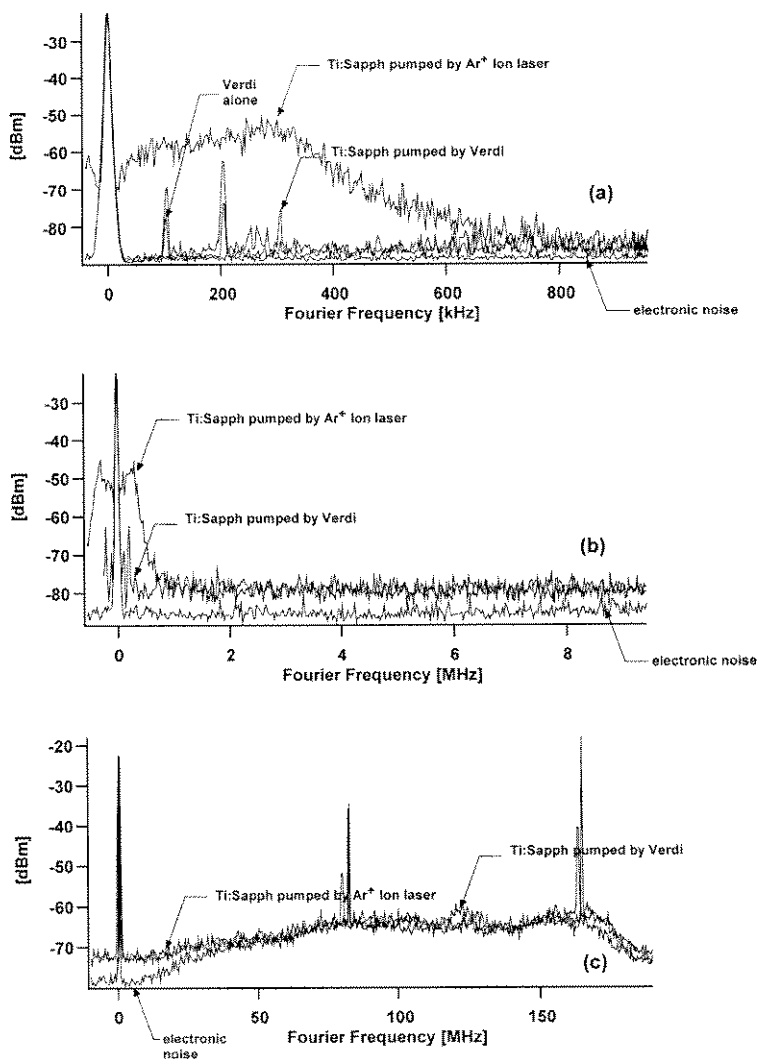
Figure 6.19: An interesting series of measurements discussed in the text show that the exchange of the Innova-100 Ar$^+$ ion for a Verdi solid state pump laser had a major impact on the intensity noise spectrum of the Ti:Sapphire. Clearly, the best improvement occurred in a bandwidth up to about 1 MHz as in (a), while the improvements are less dramatic beyond this frequency in (b) and (c).

optical modulator (AOM) for a large bandwidth (1-100 kHz) loop to its frequency servo, and then split into four different paths. The first path is sent to a 100 kHz wide spatial-mode-cleaning cavity and produces the approximately 4 mW local of oscillator beam necessary for the balanced heterodyne detection setup. This light is at a frequency of 40 MHz above the Cs D2 $\left(6S_{1/2}, F = 4 \rightarrow 6P_{3/2}, F = 5\right)$ resonant frequency at $\lambda_{4\rightarrow5} \equiv \lambda_{\mathrm{atom}} = 852.359$ nm.

The second path is the locking path for the Ti:Sapphire, which gets coupled into the 20 kHz wide "transfer cavity." An error signal for the Pound-Drever-Hall [52] type lock is derived using the reflected light from the cavity and is fed back to the external AOM, the tweeter mirror, the etalons and the Brewster plate galvo inside the laser cavity. The purpose of the transfer cavity will be explained more fully in Sec. 6.4.2.

The third path goes to a Cs spectrometer which uses a modulation transfer saturated absorption spectroscopy [152] technique plus an intra-spectrometer AOM at -80 MHz to offset-lock the "transfer cavity." Incidentally, this -80 MHz AOM is the source of the $+40$ MHz offset of the Ti:Sapphire from the Cs resonance.

The final path is the light that eventually gets coupled into the physics cavity. It first gets upshifted by $+200$ MHz with the first order beam from an AOM to produce a carrier frequency of $\omega_{4\rightarrow5} + 240 = \omega_{\mathrm{atom}} + 240$ MHz. It is then sent through a homemade broadband travelling wave electro-optic modulator (TWM), driven at 240 MHz and denoted for our purposes here as TWM$^{\#}1$. The lower sideband of TWM$^{\#}1$, which is denoted as the "probe light" at a frequency ν_{probe}, is now nominally on resonance with the Cs D2 line and can be exactly tuned simply by changing the rf frequency of the synthesizer (HP 8656B) which drives the modulator. Furthermore, the intensity of this light can be easily controlled by changing the modulation index via the amplitude of the same synthesizer. The details of the coupling of the light into the cavity have been explained in Sec. 6.3.4 and the detection techniques will be discussed shortly in Sec. 6.4.3.

There have been several ongoing issues with the Ti:Sapphire laser which should be mentioned. To begin with, the crystal itself is not in the greatest condition, and a

replacement is expected to result in an immediate 50% improvement in output power [160]. One problem was that the cooling water for the crystal had been far too cold in the past, allowing moisture from the air in the lab to condense on the crystal and leave dirty deposits upon evaporation. The cooling line is presently plumbed into the same Neslab chiller used to cool the baseplate for the Verdi laser, and is kept at a constant temperature of 18 °C (above the lab temperature of 16 °C). It is also the case that the Ti:Sapphire needs to be cleaned approximately once every two weeks under continuous use. The alcohols (acetone, methanol) and abrasive cleaning motions tend to take their toll on the lifetime of the optics, and plans are under way to put the whole laser in a box under slightly positive pressure of dry air to keep the dust and moisture out. This has been shown in other labs to reduce the required cleaning to as little as once every 3 or 4 months. The laser itself is in excellent shape, however, as was proven by a Coherent service technician [160] who was able to get the laser to scan the specified 25 GHz by setting all of the feedforward gains correctly. This is something that needs to be done every time the laser is cleaned.

6.4.2   The Transfer Cavity and Locking Diode Laser

The major problem facing the experiment is the issue of how to maintain the cavity length fixed at the correct position. For example, a one-photon field inside the cavity has a transmitted power of about 6 pW which is not enough power from which to derive an error signal indicating the position of the cavity. The way this was overcome in the past was to chop the input power to the cavity between 6 pW and 10 μW respectively, with a duty cycle and frequency that would allow sufficient bandwidth for the servo to lock the cavity. This approach will not be acceptable for an experiment whose goal it is to trap an atom for upwards of 100 ms, primarily because 10 μW of transmitted power would mean a buildup of 1.5 W inside the cavity.

The solution at the moment is to use another laser (New Focus 6200) tuned 2 longitudinal modes *above* the cavity QED mode at $\nu_{\text{cavity}} \approx \nu_{\text{atom}}$ to lock the physics cavity. In this case, the wavelength of the locking laser is $\lambda_{\text{lock}} \equiv c/\nu_{\text{lock}} \approx 836$

nm as shown in Table 6.5. This laser is stabilized relative to ν_{atom} by way of a technique using the auxiliary "transfer cavity" mentioned above [161]. This is done by separating the 9 mW diode laser output into two separate paths. In the first path, the diode laser carrier is locked in reflection using a Pound-Drever-Hall technique to another longitudinal mode of the transfer cavity by injecting the light from the opposite end of the cavity to the Ti:Sapph input port. The second path is sent through a second TWM (referred to here as TWM$^{\#}$2), whose purpose is to "bridge" the residual frequency gap of typically 150 MHz between the physics cavity resonance at 836.43 nm and the transfer cavity resonance closest to this wavelength. This light is mode-matched into the physics cavity and detected in transmission using an APD/transimpedance amplifier module (EG&G C30998).

The physics cavity error signal is derived once again using the Pound-Drever-Hall technique, where the locking sidebands are superimposed as an FM signal on top of the rf driving signal sent to the diode laser TWM$^{\#}$2. FM spectroscopy of the physics cavity will yield two error signals out-of-phase with one another, corresponding to each of the TWM$^{\#}$2 sidebands. The carrier produces no error signal. Furthermore, the use of a TWM$^{\#}$2 sideband for locking the physics cavity has the advantage of permitting easy frequency and amplitude tunability by way of an rf synthesizer (HP ESG 4000A). The use of approximately 10 nW for locking creates a small AC Stark shift of 50 kHz in ν_{atom}, and the non-intrusive nature of this lock is further verified by the absence of a noticeable effect of the atoms on the cavity locking error signal (see Sec. 7.2.8). The performance of this lock has been discussed above in Sec. 6.3.5.

Fig. 6.20 presented below gives a pictoral representation of where all of the laser frequencies reside with respect to one another. The middle "physics cavity line" in the diagram contains the physics cavity longitudinal mode structure, where the probe, lock and FORT lasers reside at modes $n + 2$ (836 nm) and $n - 2$ (869 nm) respectively, centered about mode n at the nominal probe wavelength of 852 nm. The FORT laser, which will be discussed extensively in Sec. 7.2.3, is shown here and in Fig. 6.18 for reference. The optical carriers of the probe and locking beams are tied together in frequency space by the mode structure of the transfer cavity to which each

is independently locked. This structure is shown schematically on the top "reference cavity line" and reinforces the first key point of this laser stabilization method that the distance in frequency space between these two carriers is *always fixed*, connected by the transfer cavity longitudinal mode structure. The bottom "atom line" shows the fixed (by nature!) atomic resonance frequency, and the frequency of the LO beam, which also never changes from $\nu_{\rm LO} = \nu_{\rm atom} + 40$ MHz in our set-up.

The second point about Fig. 6.20 is to emphasize its role in helping to understand the tunability of the system through the use of TWM$^{\#}$1 and TWM$^{\#}$2 to control the three frequencies ($\nu_{\rm probe}, \nu_{\rm atom}, \nu_{\rm cavity}$). It is clear from the expanded view of the dashed area that TWM$^{\#}$1 can be used to control the detuning $\delta_{\rm pa} = \nu_{\rm probe} - \nu_{\rm atom}$ of the probe light from the atomic frequency. The intensity and detuning of this pW-level field are set by rf synthesizer control of TWM$^{\#}$1, because the probe field is the lower sideband (LSB$^{\#}$1 in Fig. 6.20) of Ti:Sapph carrier after this modulator.

It is perhaps a bit more subtle to see how TWM$^{\#}$2 is used to control the detuning $\delta_{\rm ca} = \nu_{\rm cavity} - \nu_{\rm atom}$ of the cavity with respect to the atomic frequency. The LSB$^{\#}$2 of the locking diode laser carrier, whose frequency is determined by TWM$^{\#}$2, is locked to the longitudinal mode $n + 2$ of the physics cavity. At the present, neither of the upper sidebands (USB$^{\#}$1 and USB$^{\#}$2) of these modulators are used. When TWM$^{\#}$2 is tuned (e.g., increased), the modes $\{ \ldots n-2, n-1, n, n+1, n+2 \ldots \}$ of the middle "physics cavity line" slide to the left with respect to the bottom "atom line." Note that the FORT diode laser carrier also "slides" to the left with respect to the fixed atomic frequency by virtue of the fact that it is locked to the physics cavity (see Sec. 7.2.3). The locking diode laser carrier, Ti:Sapph carrier and its LSB$^{\#}$1/USB$^{\#}$1 do not move with respect to the atom line because of their fixed relationship to the upper "reference cavity line," while the USB$^{\#}$2 of the locking diode laser moves to the left as TWM$^{\#}$2 is increased (for example) here. Hence, mode n, having a fixed relationship to mode $n + 2$ by virtue of the fact that they are both modes of the same "physics" cavity, is tuned with respect to the atomic frequency. Using a combination of these two controls, any arbitrary $\delta_{\rm ca}$ can be accessed, and, for fixed $\delta_{\rm ca}$, any line profile (see, e.g. Eqs. (7.7) and (7.27)) scanned using $\delta_{\rm pa}$.
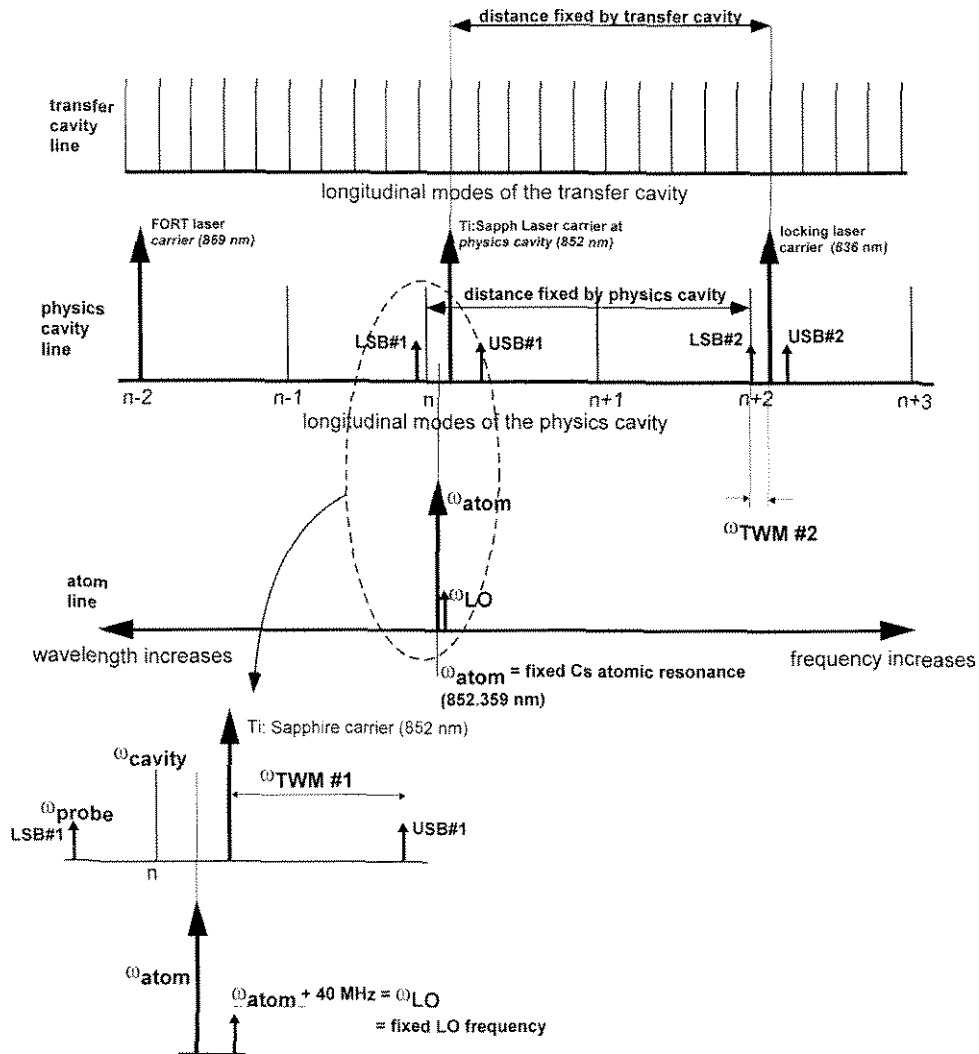
Figure 6.20: This figure should be considered one of the most useful in this thesis, because it demonstrates exactly how all of the frequencies used in the experiment are generated, made tunable, and, most importantly, referenced to one another. The text goes through it in detail, and Fig. 6.18 is a complementary diagram which shows the physical layout of all of the lasers on the optical table.

Downstream from the cavity, dichroic beamsplitters are used to separate the beams and send them to their respective detectors. First, the 836 nm light is separated and sent to the APD detector with an optic which is approximately $(85, 15)\%$ transmission/reflection at 836 nm and better than 99% reflection at 852 and 869 nm. The 869 nm light is then separated by a second optic which is approximately $(10, 90)\%$ transmission/reflection at 869 nm and $(85, 15)\%$ transmission/reflection at 852 nm. The remaining 852 nm light is sent to the heterodyne detection set-up.

6.4.3 Heterodyne Detection

This section deals with a few comments about the heterodyne detection scheme for the low (pW-level) intra-cavity light fields shown in Fig. 6.18. The reader is referred to some of the historical work of our group, which has used this powerful technique extensively, for excellent discussions [158, 68, 159]. One of the most forgiving aspects of this type of detection compared to a direct detection method such as photon counting is its insensitivity to stray light which does not have exactly the correct frequency and spatial structure. We rely on these properties because there are so many optical beams (probe, lock, FORT) coming through the cavity of fairly closely matched colors that it would be impossible to completely separate one from the others. For example, even the 3% of contamination of the 10 nW level locking light which is not completely separated by the first dichroic mirror would swamp the probe signal if the detection scheme were not frequency selective. Heterodyne detection's other major advantage is its potential sensitivity to the intracavity *field*, so that phase information is also available in the photocurrent. This important feature was not used, however, for any of the work to be presented here [36].

Two main issues are to ensure both that the heterodyne efficiency has been made as large as possible and that an accurate calibration of the intracavity photon number $\bar{n}$ is maintained from day to day. The former can be arranged by minimizing the losses (from reflection, absorption, etc.) of the probe light from the cavity output to the detector area, by maximizing the spatial and polarization overlap of the LO

beam with the signal probe field and by maximizing the intrinsic detector quantum efficiency (QE). The heterodyne efficiency η_{het} for this experiment was verified in two ways. In the first, a $V = 88\%$ visibility homodyne fringe between the LO and signal beams was made for identical powers in each beam. This number is squared and multiplied by both the detector QE of 70% and the $T = 70\%$ transmission factor from the cavity to the detector to give $\eta_{\text{het}} = (\text{QE})TV^2 = 47\%$. A second method is to take a known amount of output power from the cavity and calibrate this against *the signal-to-noise ratio recorded via the beatnote size on a calibrated rf spectrum* analyzer. The details were worked out by Rob Thompson [158] and implemented by Quentin [68] in his beat.mcd Mathcad program for the HP70000 spectrum analyzer used here. With 20.3 nW of optical power, 30 kHz rf bandwidth, 3.5 mW of LO power and the measured (beatnote size, shot noise level and electronic noise levels) of (-18.9 dBm, -80.5 dBm and -85.5 dBm) respectively, this program calculates $\eta_{\text{het}} = 47\%$ for remarkable agreement with the measurement based on the homodyne fringe visibility. Note that this LO level makes the measurement shot-noise limited by about 5 dB.

In the data to follow, one typically quotes the average intracavity photon number $\bar{n}$ at which the data was acquired. This number needs to be compared to the saturation photon number, $n_0 = 4\gamma_\perp^2/3g_0^2$ ($= 10^{-2}$ for an optimally coupled atom in the work here), to decide how "hard" the atom was driven. The condition $\bar{n} \ll n_0$ means the system is operating in a linear regime. The meaning of an intracavity photon number $\ll 1$ can be deduced from the definition of $\bar{n} = \langle \hat{a}^\dagger \hat{a} \rangle$, so that $\bar{n} \ll 1$ means that *on average* the intracavity field is primarily in the state $|0\rangle$. Note that throughout the rest of the work here, $\bar{n}$ specifies the mean intracavity photon number for the empty cavity (i.e., no atoms) *at the actual detuning* δ_{pa}.

The relationship of the actual transmitted power to the intracavity photon number requires a slight digression. Assuming two identical mirrors of transmission T and absorptive losses A such that the total cavity losses are $2(T + A)$, then a fraction $2A$ of the circulating intracavity power is absorbed, while a fraction T is transmitted out of each mirror. Since κ is a *field* decay rate, $1/2\kappa$ is the energy storage time, so that

the total intracavity power is $\bar{n}\hbar\omega_{\text{cavity}}(2\kappa)$ and the transmitted power is

$$P_{\text{trans}} = \frac{T}{2T + 2A} 2\kappa\bar{n}\hbar\omega_{\text{cavity}} = \bar{n}T\nu_{\text{FSR}}. \qquad (6.22)$$

It is possible to use this equation to calibrate the intracavity photon number with the size of the electronic beatnote by using the known values of T and ν_{FSR}, and measuring P_{trans} with a calibrated photodetector. Once this number was calibrated to a specific rf power level on the synthesizer creating the probe sideband on TWM$^{\#}1$, periodic checks over an eight month period showed that it remained valid if the alignment of the detection apparatus was continually tweaked.

The theoretical 3 dB improvement in SNR of a balanced heterodyne receiver containing two matched detectors is achieved only by careful subtraction of the photocurrents from each of the detectors. This was accomplished by adjusting the amplitude and phase of the photocurrent from each detector using rf attenuators and variable cable lengths before the rf 180° splitter. When adjusted correctly, residual amplitude modulation on the LO measured in the difference photocurrent at the beat (detection) frequency is minimized.

6.4.4 Data Acquisition

This chapter concludes with a few brief words about the experimental data acquisition system used. The primary method of analyzing the balanced heterodyne photocurrent was to use a spectrum analyzer (HP 70000 SA) set to the (nominal) +40 MHz offset between signal and LO in the balanced heterodyne set-up. The exact frequency of the SA was tuned manually by optimizing the rf level in zero span on the SA's visual display, with about a 20 kHz offset typically necessary. Even with its internal oscillator slaved to the master probe frequency synthesizer's oscillator, this manual tuning was necessary. The HP 70000 can be externally triggered and has a "video out" signal which was sent to a digitizing oscilloscope (Lecroy 9400) so that both real-time monitoring and averaging of the photocurrent could be accomplished. A GPIB interface between the oscilloscope and the computer allowed simple transfer

of the data via a LABVIEW interface and routine analysis was performed with either MATLAB or IGOR. Most of the data was filtered in hardware at rather low rf bandwidths of about 3 kHz to maximize the signal-to-noise ratio as seen on the oscilloscope because much of the optimization of different experimental parameters was performed by visual inspection of this signal. It is expected that future experiments looking to monitor more carefully atomic motion while the atoms are trapped will require much greater bandwidths approaching 1 MHz (see Sec. 8.2). The capabilities to do this are already in place in the form of either a 100 MSamples/s 12 bit ADC board (Gage Compuscope 8012/A) or a 1 MSample/s 16 bit ADC board (National Instruments AT-MIO-16E-1).

Chapter 7 Trapping a Single Atom Inside a High Finesse Cavity

This chapter will present the experimental results, roughly in chronological order, leading up to the trapping of atoms inside the cavity. The discussion will build extensively on the jargon and technical details introduced in the previous chapter and will refer to the relevant sections there where necessary.

7.1 Atom Transits and Trapping with a Single Photon

The "trajectory" of an individual atom is monitored in real time as it enters and moves within the cavity mode by recording modifications of the (pW-scale) cavity transmission for a circularly polarized probe field $\mathcal{E}_{\text{probe}}$ of frequency $\nu_{\text{probe}} = \nu_{\text{atom}} + \delta_{\text{pa}}$. For our Fabry-Perot cavity, the spatially dependent coupling coefficient is given by

$$
\begin{aligned}
g(\mathbf{r}) &= g_0 \sin(2\pi z/\lambda_{\text{cavity}}) \exp(-(x^2 + y^2)/w_0^2) \\
&\equiv g_0 \psi(\mathbf{r}, \lambda_{\text{cavity}}),
\end{aligned}
\tag{7.1}
$$

with the mirrors located at $z = (0, l)$. Heterodyne detection of the transmitted probe (with overall efficiency 47%) allows inference of the atomic position in a fashion that can be close to the standard quantum limit [91].

7.1.1 Eigenvalue Spectra and Downgoing Atom Transits

"Atom transits" arise from the modification of the intracavity field a due to the presence of a two-level atom $(|e\rangle, |g\rangle)$ at position $\mathbf{r}$ (and dipole coupling $g(\mathbf{r})$). The Hamiltonian governing this interaction is written as

$$H = H_{\text{atom}} + H_{\text{field}} + H_{\text{int}} = \hbar\omega_{\text{atom}}|e\rangle\langle e| + \hbar\omega_{\text{cavity}}a^\dagger a + \hbar g(\mathbf{r})\left(a^\dagger|g\rangle\langle e| + a|e\rangle\langle g|\right).$$
(7.2)

Even though this is essentially the same as Eq. (5.1), it has been rewritten here to de-emphasize the c.m. effects and also to include a finite atom-cavity detuning (i.e., $\omega_{\text{atom}} \neq \omega_{\text{cavity}}$ in general). It is instructive to look at the spatial dependence of the eigenvalues in the presence of a closed system of $(|e\rangle, |g\rangle$ for the atomic internal state) $\otimes$ $(|0\rangle, |1\rangle$ for the photon number in the cavity). In the basis $(|g, 0\rangle, |g, 1\rangle, |e, 0\rangle)$, the eigenvalues of the matrix

$$\frac{H}{\hbar} = \begin{pmatrix} -\omega_{\text{atom}} & 0 & 0 \\ 0 & \Delta_{\text{ca}} & g(\mathbf{r}) \\ 0 & g(\mathbf{r}) & 0 \end{pmatrix}$$
(7.3)

are

$$\lambda_0 = -\omega_{\text{atom}}$$
(7.4)

for the ground state $|g, 0\rangle$,

$$\lambda_\pm = \frac{\Delta_{\text{ca}}}{2} \pm \sqrt{\frac{\Delta_{\text{ca}}^2}{4} + g^2(\mathbf{r})}$$

for the first two excited states $\frac{1}{\sqrt{2}}(|g, 1\rangle \pm |e, 0\rangle)$.

These are just the dressed states $|D_{0,\pm}\rangle$ of Eq. (5.2). Fig. 7.1 (a),(b) shows the spatial dependence of these eigenvalues for $g(\mathbf{r})/2\pi = 32\sin(2\pi z/\lambda_{\text{cavity}})$ [MHz] and $\Delta_{\text{ca}}/2\pi = 0, 10$ [MHz] respectively. Clearly, with $\Delta_{\text{ca}}/2\pi = 0$, the two eigenvalues are degenerate at spatial positions where $g(z) = 0$ and have a maximum splitting of $2g_{\text{max}}$, which is the single photon Rabi frequency. It is also worth pointing out

that the global ground state (which, of course is lower in energy than the two excited states shown here by one quanta of excitation, or $\hbar\omega_{\text{atom}}$) is flat as a function of position. This situation will change when the FORT potential is introduced into the Hamiltonian.

In order to take into account both cavity and atomic decay $(\kappa, \gamma_\perp)$, a set of Heisenberg equations with $g(\mathbf{r}) = g_0$ can be written for the driven system as

$$
\begin{aligned}
\dot{a} &= -(\kappa + i\Delta_{\text{ca}})\,a + g_0\sigma_- + \epsilon e^{-i\Delta_{\text{pa}}t} \\
\dot{\sigma}_- &= -\gamma_\perp\sigma_- + g_0 a\sigma_z \\
\dot{\sigma}_z &= -2\gamma_\perp(\sigma_z + 1) - 2g_0\left(a^\dagger\sigma_- + a\sigma_+\right),
\end{aligned}
\tag{7.5}
$$

in a frame rotating at the atomic frequency $\omega_{\text{atom}} = 2\pi\nu_{\text{atom}}$, with $\sigma_- = |g\rangle\langle e|$ and $\sigma_z = |e\rangle\langle e| - |g\rangle\langle g|$. In the *weak-field limit* of small excited state population ($\langle a\sigma_z\rangle = -\langle a\rangle = -\alpha, \langle \sigma_z\rangle = -1, \langle\sigma_-\rangle = \beta$), the equations for the expected operator values α and β take a form very similar to those for the many atom case of Eq. (4.1)

$$
\begin{aligned}
\dot{\alpha} + (\kappa + i\Delta_{\text{ca}})\alpha - g_0\beta &= \epsilon e^{-i\Delta_{\text{pa}}t} \\
\dot{\beta}_j + \gamma_\perp\beta_j + g_0\alpha &= 0.
\end{aligned}
\tag{7.6}
$$

The weak field limit essentially means the following discussion is limited to one excitation in the system, so that an exploration of anything but the first excited states of the Jaynes-Cummings Hamiltonian (7.2) is not possible. The steady state complex cavity transmission function analogous to (4.3a) discussed in the microsphere work of Sec. 4.3 is

$$
t(\Delta_{\text{pa}}) = \frac{\kappa\alpha_{ss}}{\epsilon} = \frac{\kappa(\gamma_\perp - i\Delta_{\text{pa}})}{(\lambda_+ + i\Delta_{\text{pa}})(\lambda_- + i\Delta_{\text{pa}})},
\tag{7.7}
$$

and contains all of the information about amplitude and phase modifications to the system driving (probe) field $\epsilon e^{-i\omega_{\text{probe}}t}$. Here $\lambda_\pm$ are the roots of the characteristic equation

$$
(\lambda + \kappa + i\Delta_{\text{ca}})(\lambda + \gamma_\perp) + g_0^2 = 0.
\tag{7.8}
$$
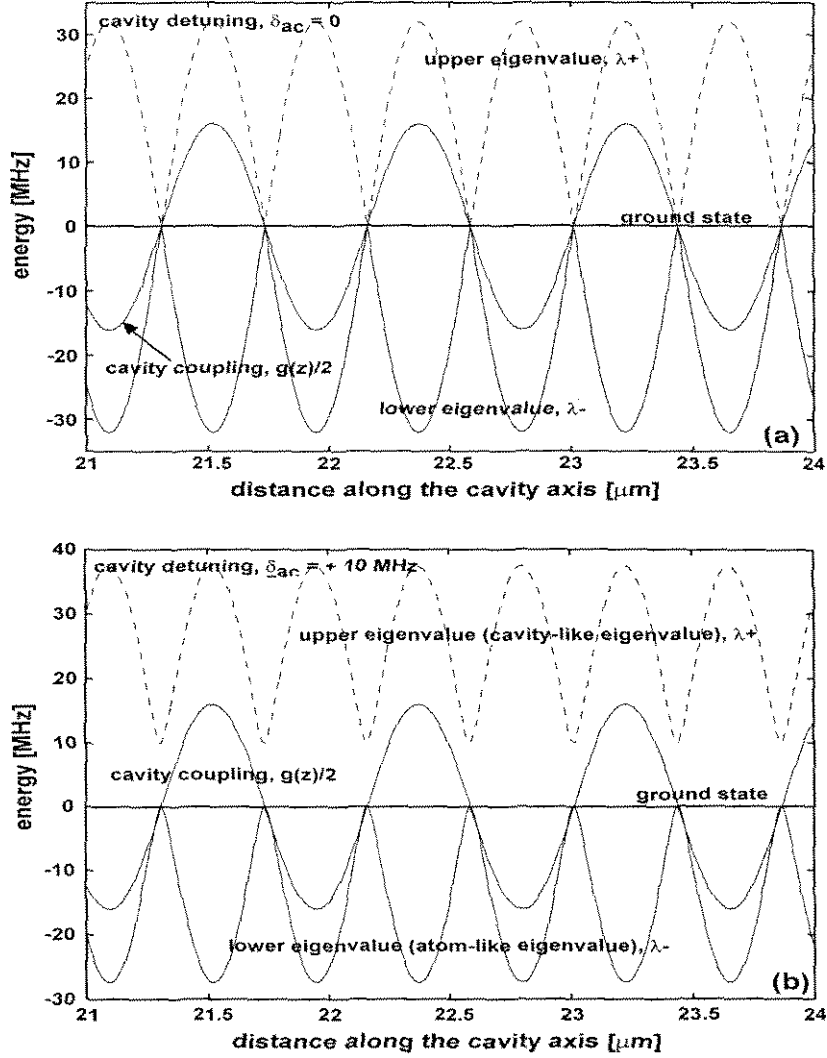
Figure 7.1: The spatial dependence of the eigenvalues (the upper is dashed, and the lower, solid) of Eq. 7.2 is shown in (a) for $\Delta_{ca}/2\pi = 0$ and in (b) for $\Delta_{ca}/2\pi = 10$ MHz, with $g\left(\mathbf{r}\right)/2\pi = 32\sin\left(2\pi z/\lambda_{\text{cavity}}\right)$ as in the experiment shown also a solid line ($\div 2$ for convenience). This diagram should be compared to the series of later diagrams (Figs. 7.18, 7.19 and 7.20) which show the impact of the FORT trap on this Hamiltonian. The flat ground state is actually one quanta ($= \hbar\omega_{\text{atom}}$) lower in excitation than either of the excited states.

Fig. 7.2 shows the cavity transmission $T\left(\Delta_{\mathrm{pa}}\right) = \left|t\left(\Delta_{\mathrm{pa}}\right)\right|^2$ for the case of $\delta_{\mathrm{ca}} = \Delta_{\mathrm{ca}}/2\pi = 0$ and parameters $\left(g_0, \kappa, \gamma_\perp\right)/2\pi = (32, 4, 2.6)$ MHz relevant to the experiments here. The two excited eigenstates labelled "single atom, optimally coupled" are split by an amount $2g_0/2\pi = 64$ MHz, and each has a half-width $\left(\kappa/2 + \gamma_\perp/2\right)/2\pi \sim$ 3.3 MHz because these states are an equal admixture of cavity excitation and atomic excitation: $\left|\psi_\pm\right\rangle = \frac{1}{\sqrt{2}}\left(\left|g,1\right\rangle \pm \left|e,0\right\rangle\right)$ (with $\left(\left|e\right\rangle, \left|g\right\rangle\right)$ and $\left(\left|0\right\rangle, \left|1\right\rangle\right)$ the weak-field-allowed cavity and atom Hilbert spaces respectively). The global ground state is, of course, $\left|g,0\right\rangle$ in which no excitation exists in the system. For reference, the cavity transmission spectra with no atom is shown as a dashed line.

This simple picture can now be used to explain "downgoing" atom transits. If the cavity resonance coincides with the atomic resonance ($\delta_{\mathrm{ca}} = 0$), and if the probe is also placed on resonance at a detuning $\delta_{\mathrm{pa}} = 0$, then the cavity transmission will have a value of "1" if no atom is present (dashed curve), but a single atom optimally coupled at $g(z) = g_0 = g_{\max}$ will pull the transmission at $\delta_{\mathrm{pa}} = 0$ down essentially to "0," as shown in Fig. 7.2 by the solid curve in the center of the figure. The one caveat is that not every atom will be optimally coupled at $g_0 = g_{\max}$. For example, the curve labelled "single atom, not optimally coupled," has $g(z) \sim g_{\max}/6$ and it is clear that the transmission at $\delta_{\mathrm{ca}} = 0$ is not pulled down as far, so that the contrast between "atom present" and "no atom present" will be worse in this case. Of course, virtually any value of $g(z)$ is accessible within the intracavity standing wave geometry.

The inclusion of finite atom-cavity detunings $\delta_{\mathrm{ca}} = +10$ MHz and $\delta_{\mathrm{ca}} = +60$ MHz is shown in Fig. 7.3, where it is clear that the effect of the detuning is to imbalance the transmission of the two eigenstates of the system as seen through the cavity. In this case, the coefficients (c_1, c_2) of the eigenstate expansion $\left|\psi_\pm\right\rangle = c_1\left|g,1\right\rangle \pm c_2\left|e,0\right\rangle$ reflect this change, where for $c_1 \gg c_2$ ($c_1 \ll c_2$) one speaks of the "cavity-like" ("atom-like") eigenstate. The fact that the cavity-like resonance is biggest is because the cavity transmission is the quantity plotted in the figure (and detected in our experiments). If one was to look at the atomic fluorescence out the side of the cavity, which is the complementary loss port for this system, the appearance of the eigenstates in the measured spectrum would be reversed because this would
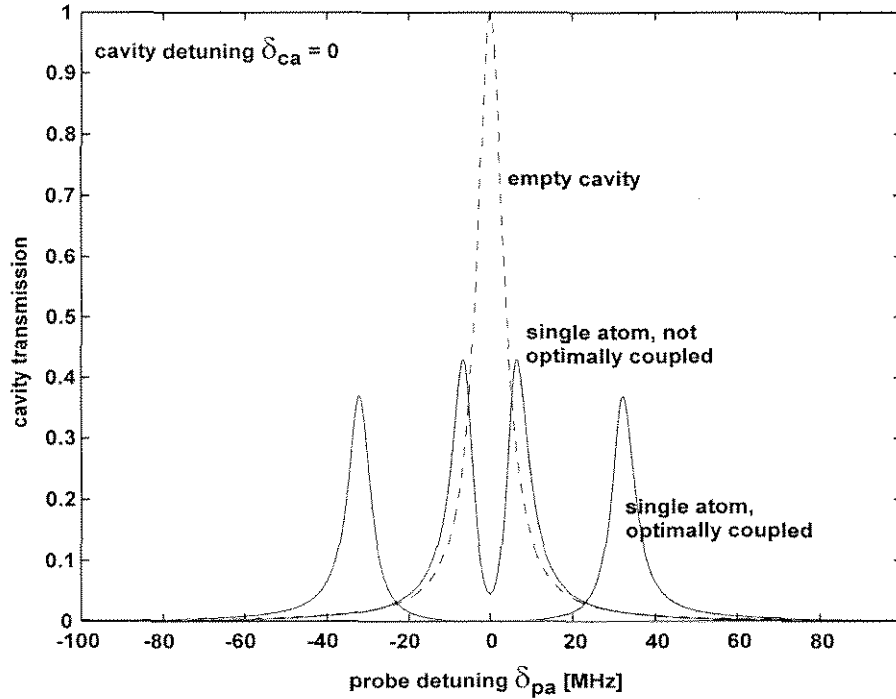
Figure 7.2: The cavity transmission $|t\left(\Delta_{\mathrm{pa}}\right)|^{2}$ is shown for an empty cavity (dashed) and a single atom with coupling $g_{0} = g_{\max}, g_{\max}/6$ (two solid curves) with a detuning $\delta_{\mathrm{ca}} = 0$. The position $\delta_{\mathrm{pa}} = 0$ has a huge contrast between the empty cavity case (transmission approaches unity) and the single atom case (transmission is pulled down close to zero). The ability to achieve this contrast for a single atom is already a statement that the system is in the "strong-coupling" regime, and single atom detection via "downgoing atom transits" use this effect to detect single atoms. Note that "upgoing transits" are the ability to detect atoms with $\delta_{\mathrm{pa}} = g_{\max}$ (32 MHz in our experiment). Here the empty cavity transmission is low, but a single atom will pull the cavity transmission significantly higher so that now an increase in cavity transmission corresponds to single atom detection.

now be a measurement of atomic excitation [162]. The cavity loss port is chosen here experimentally because of the high detection efficiency it affords compared to the rather low efficiency of detection for atomic fluorescence into (approximately) 4π solid angle.
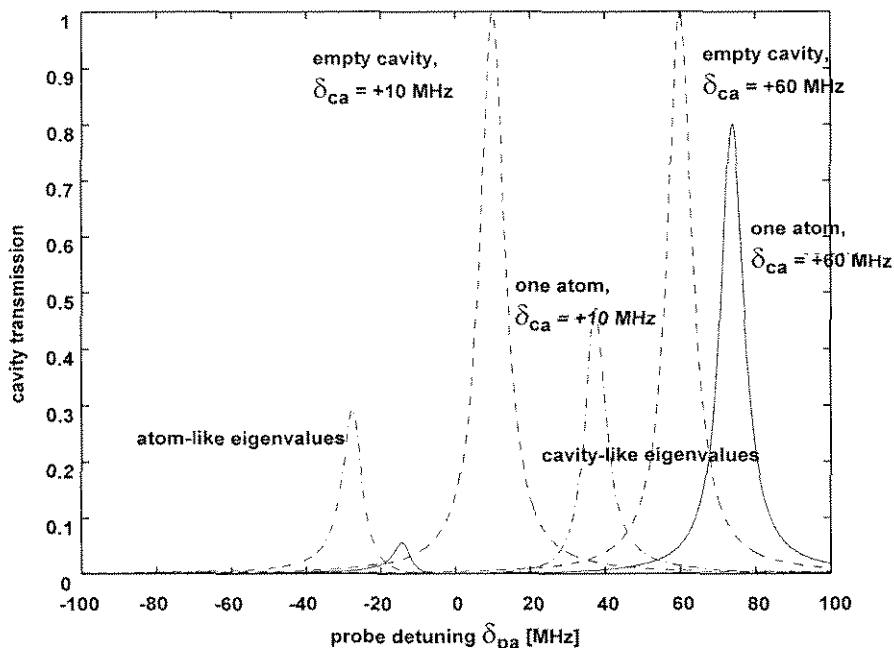
Figure 7.3: The role of $\delta_{ca} \neq 0$ on the cavity transmission is emphasized here. Two cases $\delta_{ca} = +10, +60$ MHz for a single atom (both with coupling $g_0 = g_{max}$) are shown, along with their respective associated "empty-cavity" traces. As the detuning increases, the disparity in heights between these eigenvalues increases, and one becomes more similar to the "empty-cavity" trace than the other. This is the "cavity-like" eigenvalue whose decay path is primarily in the forwared direction along the cavity axis (which is detected here). The other "atom-like" decays primarily out of the side of the cavity, and hence its contribution to cavity transmission is diminished.

The first atom transit data of the experimental set-up described here are presented in Fig. 7.4. For reference, Fig. 7.4(a) shows the photocurrent trace as a function of time with alternately the atom source blocked (by blocking the upstairs trapping beams) and the cavity output blocked. The former indicates the detectability of a field of approximately $\bar{n} = 0.05$ photons with respect to the latter trace of the shot-noise level for the heterodyne detection system due to the intense LO beam. Both

traces taken together demonstrate nicely the signal-to-noise ratio here for detecting single atoms.

Fig. 7.4(b) shows the cavity transmission with the atom source unblocked, which allowed us to see transits *directly* from the upstairs MOT_1 without the need for a downstairs MOT_2. For us, this was absolutely amazing because it meant that some small fraction of the 1 mm^3 atom source had to be hitting the 40 μm mirror gap (not to mention the 22 μm mode waist within) from $\Delta z = 25$ cm away. This finding helped to verify both our alignment procedure and the effectiveness of the cooling of our atom source. Note that the time delay from the shutoff of the PGC from the upstairs MOT_1 is roughly 220 ms, consistent with a fall time $\Delta t = \sqrt{2\Delta z/g} = 223$ ms under gravity $g = 10$ cm/s^2. Fig. 7.4(c) exhibits the influence of the downstairs MOT_2 used as an intermediary collection tool for the falling atoms. Clearly, many more atoms arrive at the cavity with delay time from the end of MOT_2 PGC of $\Delta t = 37$ ms consistent with a drop from $\Delta z = 7$ mm.

The difference between these two situations becomes more evident when individual transit events are considered, as shown in Figs. 7.5 and 7.6 for the upper and lower MOTs respectively. Falling from the upper MOT_1, the atoms acquire an estimated velocity of 2.2 m/s, meaning that they would transit the $2w_0 = 44$ μm mode waist in about 18 μs. This is indeed what is observed in Fig. 7.5. To make the same measurement for transits from the downstairs MOT_2, it was necessary to reduce the atom number relative to the data of the lower graph of Fig. 7.4(c) to ensure that only a single atom trace was analyzed. Fig. 7.6 shows a transit time of approximately 120 μs, which is close to the expected 110 μs for atoms acquiring a velocity of 37 cm/s from 7 mm above the cavity. These transits can be seen for the range of intracavity photon numbers $0.1 \lesssim \bar{n} \lesssim 10$ where the lower range is limited by the signal to noise ratio for transit detectability and the upper by a combination of saturation of the atomic response and adverse mechanical effects due to the large scattering rate.

The above discussion has been left intentionally qualitative because the purpose of this chapter is to develop enough of an understanding to be able to follow the discussion leading up to intracavity atom trapping. Excellent discussions about signal-
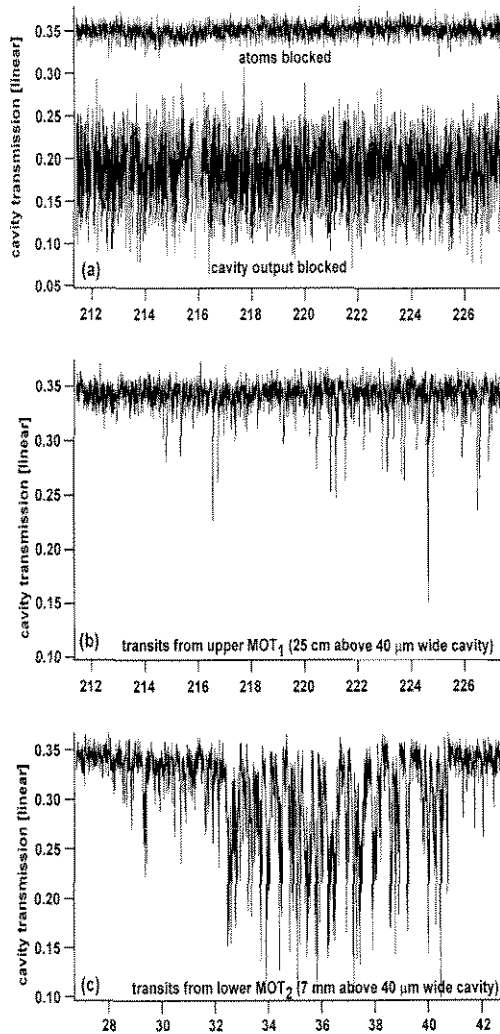
Figure 7.4: The very first set of downgoing atom transits data was finally seen after approximately 1 year of building the apparatus. These traces show the detected heterodyne photocurrent as a function of time referenced to the origin $t = 0$ at the end of the downstairs PGC cycle. In (a), the upper trace shows the atom source "blocked" (i.e., no trap was made) and the lower trace shows the probe beam blocked, giving the native "shot-noise" floor. The electronic noise floor (not shown) is approximately 10 dB further down. In (b), each "spike" is associated with a single atom transitting the cavity directly from the upstairs MOT_1, with no lower MOT_2 formed. In (c), the atoms were re-collected and cooled in MOT_2 and then dropped through the cavity. For the large atom numbers of this particular trace, it cannot be guaranteed that there is just a single atom in the cavity mode volume at any given time. The atom source can simply be reduced (by, e.g., trapping less atoms initially) for "single atom" work.
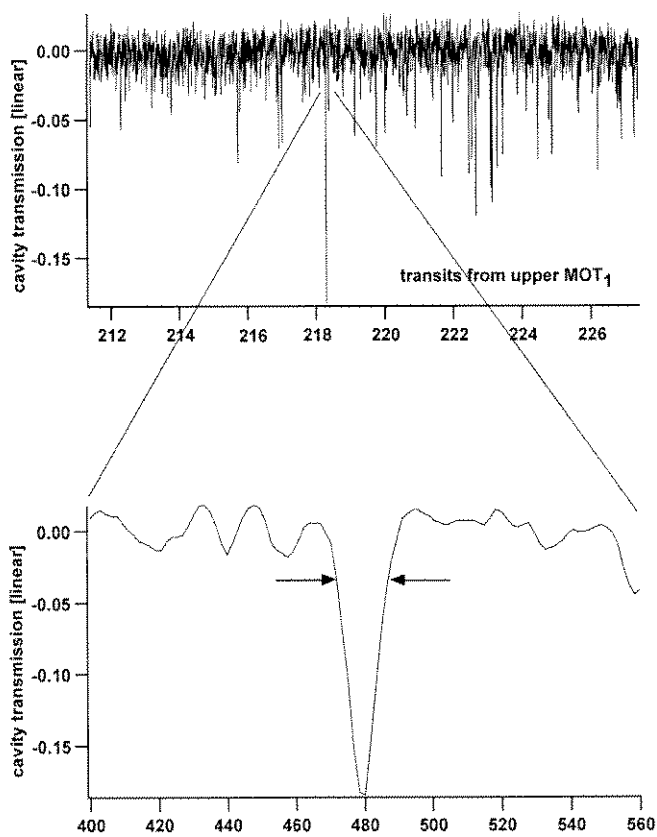
Figure 7.5: The width of a single atom transit event from the upstairs MOT associated with Fig. 7.4(b) is completely consistent with vertical free-fall from rest over 25 cm.
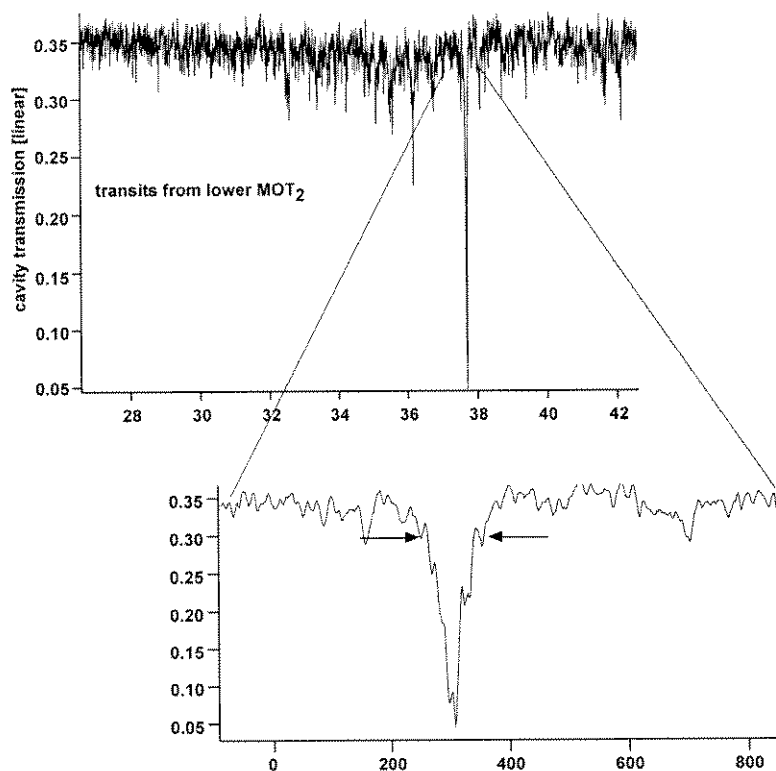
Figure 7.6: The transit widths for data similar to Fig. 7.4(c), but now in a highly-probably single-atom limit, show transit times closer to 110 μs, consistent with a 5 mm freefall under gravity.

to-noise ratio issues (e.g., using the phase quadrature of the *complex* function $t\left(\Delta_{\mathrm{pa}}\right)$ at large detunings δ_{ca} to maximize the SNR) and optimal detection strategies can be found elsewhere [36]. The task of cooling the atomic motion (extending the information of Sec. 6.2.7) in preparation for trapping is discussed next.

7.1.2 Lattice (Cooling) Beams II

Even the 37 cm/s atomic arrival velocity achieved in the previous section is already three times above the Doppler velocity of 12 cm/s, meaning that the atomic energy of 1 mK is already about ten times above the Doppler limit of $T_D = 120\ \mu$K. In order to load the intracavity trap, considerable attention was paid to reducing this number as much as possible. The first avenue by which this was done was simply to lower the position of the MOT with respect to the cavity. By walking all of the trapping beams, moving the magnetic field coils and then re-optimizing the PGC by adjusting the zeroing coils, the MOT could be moved to 5 mm (to 3 mm in later work) above the cavity, and seemed to be limited due to scattering of the trapping beams on the cavity substrate. This reduced the arrival velocity to about 31 cm/s (24 cm/s) and the energy to 800 μK (500 μK), with an arrival time of 32 ms (24 ms) after downstairs PGC ends.

The lattice beams (or cooling beams) were focused down to a 40 μm $\times$ 1.5 mm elliptical spot size by a cylindrical lens, so that the saturation intensity $I_{\mathrm{sat}} \sim 3$ mW/cm^2 could be reached with as little as 1 μW in these beams. In practice, the effect of the beams on the atomic cloud was studied by pulsing them on to cool the atoms just before their arrival time at the cavity mode volume ($t \sim 30$ ms). A sequence of these measurements is presented in Fig. 7.7 (a)-(d). This work turned away, for the moment, from measurement of individual atom transit events and concentrated on an averaging technique to look for overall trends. The traces labelled "no cooling beams" had the cooling beams blocked while averaging about 100 drop traces of the sort shown in Fig. 7.4(c) and it is clear that the typical arrival time at the cavity under free-fall is approximately $t = 32 - 34$ ms. The traces labelled "cooling beams

on" had them pulsed from $t_1 = 10$ ms to $t_2 = 27 - 30$ ms (a typical pulse is shown above Fig. 7.7(a)) so that the whole atom cloud would see their influence. The final "best" result, obtained when all of four of the parameters (zeroing magnetic fields, cooling beam intensity, cooling beam detuning and pulse length) had been optimized, is shown in Fig. 7.7(c). It is clear from this figure that the beams are capable of moving $25 - 30\%$ of the atoms over in time by an astounding 10 ms from the "no cooling beam" case, and roughly 12 ms from the final edge of the cooling pulse. The details of the different parameters used for the other traces are shown in the caption, but the basic summary is that (a) has the zeroing coils far from optimal, in (b) the cooling pulse is too weak and in (d), too intense. The results were relatively insensitive to the detuning δ_{cool}, as long as $3\Gamma \lesssim \delta_{\text{cool}} \lesssim \Gamma$, leading to the understanding that what is happening here is simply Doppler cooling. It should also be noted that no attention was paid in this work to having these beams operated as a "lattice" by locking the time phase, simply because the Doppler cooling mechanism studied at the moment does not require this.

A very simple picture was developed which seems to explain what is observed. Because of the way the lattice beams are focused through the cavity with a cylindrical lens, the unfocused axis in fact protrudes roughly 250 - 350 μm above (and below) the mirror substrate, which has been turned down to 1 mm diameter at the high reflector surface. Hence, the lattice beam size is about 1.5 mm in the long dimension. Now, using the part of the discussion below Eq. 6.11 related to Doppler cooling, with a scattering rate of approximately $\Gamma/2$, it will take about 500 μs for the atoms to lose the 800 μK worth of energy ($v_0 = 31$ cm/s), and they will move about 150 μm in this time. Referring to Fig. 7.8, the explanation is that the atoms are basically "stopped" in this very short time by the portion of the lattice beams protruding above the mirror substrates. Therefore, when the cooling pulse ends, the atoms fall roughly 700 - 800 μm to the center of the cavity (where the mode diameter is only $2w_0 = 44$ μm) and are detected. This fall, from rest to an acquired velocity of 13 cm/s at the cavity, takes approximately 12 - 13 ms and tends to explain the "moving over" time of the cloud from the end of the cooling pulse in Fig. 7.7. Note that this model also
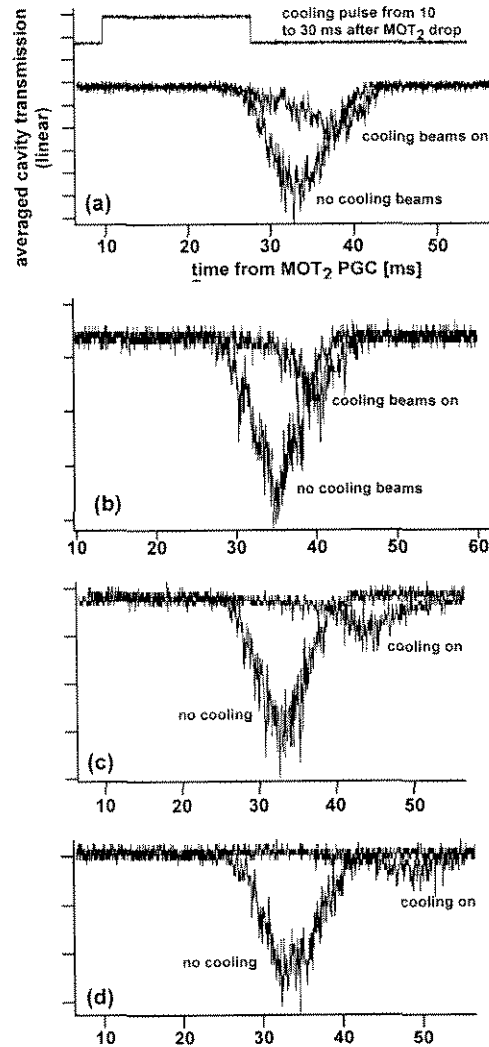
Figure 7.7: In each diagram, approximately 100 transit records of the sort in Fig. 7.4(c) were averaged both with the cooling beams off (the larger signal in all traces), and then on (the weaker signal due to about 10% cooling efficiency in the best cases). The timing of the cooling pulse is shown above (a). The differences between (a)-(d) are discussed in the text, but generally traces close to (c) were interpreted to be "good" cooling, and this scenario was most sensitive to stray magnetic fields and cooling beam intensities.
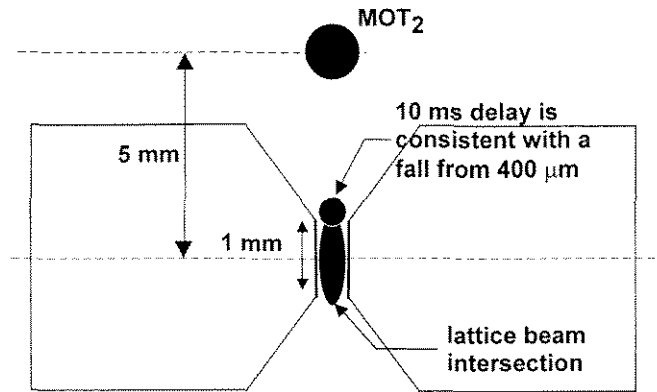
Figure 7.8: This diagram is an attempt to explain the behavior of the cooling beams. The idea is that a fraction $\sim 20\%$ of the atoms get cooled and then "stuck" in the intersection of the cooling beams just above the cavity gap. The atoms then fall approximately 800 μm to the center of the cavity, where they are detected. This fall time accounts for the delay between the "no cooling" and "cooling on" traces in Fig. 7.7.

helps explain the further delay of the cloud going from Fig. 7.7(c) to Fig. 7.7(d): as the intensity of the cooling beams is turned up, the scattering rate increases and the atoms are stopped more quickly, and as a result take longer to drop from this further distance above the cavity.

With this model in hand, an attempt was made to try to "catch" the atoms *not* 800 μm above the cavity as in Fig. 7.8, but *inside* the cavity mode volume itself where they could be directly loaded into the FORT. A sensible way to do this was to use the timing of the cooling pulse, as shown in Fig. 7.9(a). It was known from the "no cooling pulse" traces that most of the atoms arrive inside the mode at $t \sim 30-32$ ms. If the lattice beams were pulsed on for this 2 ms stretch, then any atoms about 100 μm above the mode should drift into the mode volume as they are Doppler cooled. Atoms already through the cavity would be missed by the pulse, and those above the cavity should behave as in Fig. 7.7. The result of this pulse is shown in the upper traces of Figs. 7.9(a)-(c), where the cooling parameters used were those found to be optimal for the work of Fig. 7.7 (and repeated in the lower traces of Fig. 7.9(a)). Though an exact interpretation of these results is somewhat difficult, the long "tail"

exhibited in each was considered to be the sign that the atoms cooled by the pulse were then falling slowly through the mode.

There were two very curious features in these traces, which were extremely reproducible. The first, shown by the downwards pointing arrow in Figs. 7.9(b),(c) was a small gap at the exact moment when the cooling pulse turned on and is possibly explained by a turn-on transient. The second feature, identified by the upwards arrows in these figures, is the presence of two (very repeatable, see Fig. 7.9 (a)-(c)) bumps at the beginning of the long decay tail, indicating a marked increase in atoms transiting the cavity at these times. No convincing explanation of these bumps has been found, and time was not spent on any further investigation.
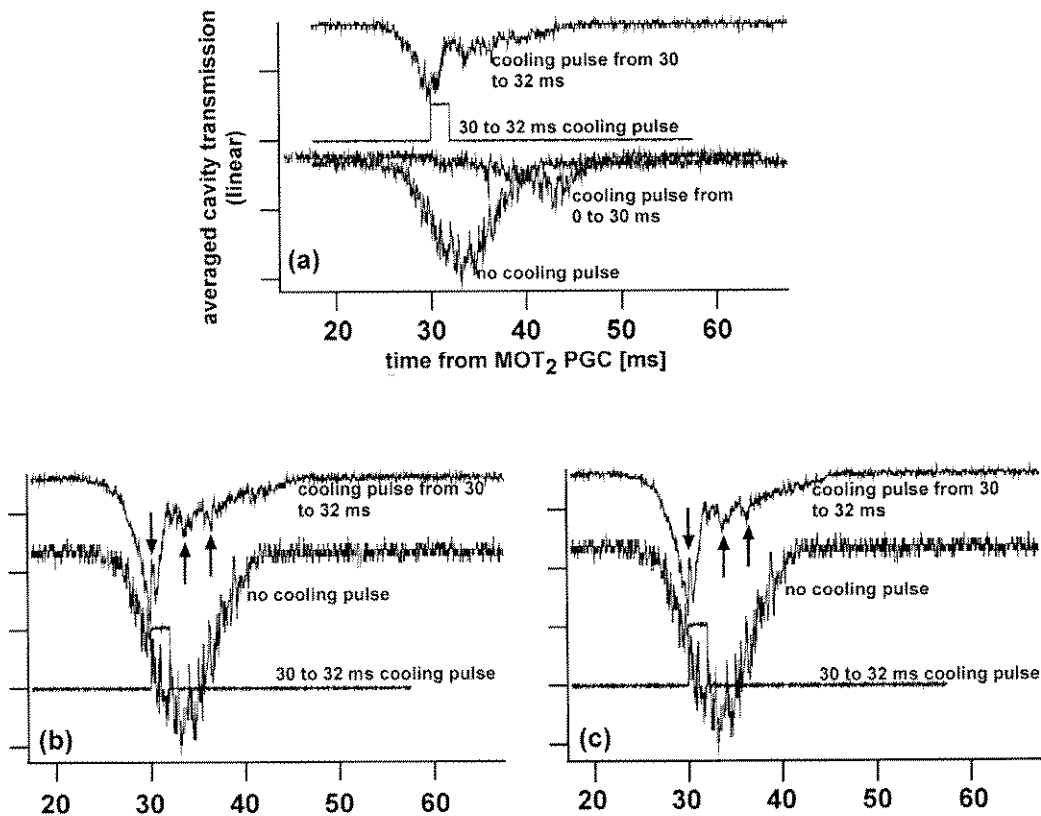
Figure 7.9: The long cooling pulse of Fig. 7.7 was substituted for the short cooling pulse shown in (a) - (c) here. The idea was now to try to catch the atoms *inside* the mode volume, rather than have them get stuck just above the substrate as in Fig. 7.8. Two curious features (which are still unexplained) are mentioned in the text.

At this point, our efforts were directed towards an implementation of the second "lattice" cooling stage, whereby these quasi-resonant cooling beams would be detuned much further in the spirit of the shift from Doppler to PG cooling in a MOT. The lattice phase lock was also implemented in the hopes of providing some trapping in two dimensions. The above work (Figs. 7.7 and 7.9) was compelling enough evidence that the near-resonant cooling beams were functioning as intended. At this point, it was time to abandon the averaging work, and return to an examination of individual atom transits as shown by 13 individual events in Fig. 7.10 taken with $0.1 \lesssim \bar{n} \lesssim 1$ to keep the scattering rate to a minimum for this resonant detection scheme. With transit times now ranging from 350 μs to upwards of 900 μs, it was clear that compared to the work of Fig. 7.4(c) without cooling where the free-fall transit time was closer to 120 μs, the cooling beams were having a serious impact.

In fact, further dissection of this data in Table 7.1 reveals that the data can be sub-grouped into three sections (it should be noted that these transits were recorded as the "best events" for the cooling parameter settings shown, and that the column labelled "delay" is again the delay of the transit from the end of the downstairs PGC pulse). The first two transits (a),(b) had only the near-resonant cooling pulse and have a typical transit time of about 350 μs, corresponding to a velocity of 11.5 cm/s, which is very close to the Doppler velocity of 12 cm/s as expected for the near-resonant Doppler cooling explained above. These transits were seen within 1 - 3 ms of the turn-on of the cooling pulse, consistent with the 500 μs estimate above needed for Doppler cooling with these parameters. The next three transits, (c)-(e), abandoned the near-resonant pulse and moved farther off-resonance for a longer period of time. With a typical transit time closer to 500 μs, they suggest a terminal velocity of closer to 8 cm/s and are seen significantly longer (6 ms) after the cooling pulse begins, suggestive of sub-Doppler cooling in far off resonance laser fields. It is not too surprising that this far off resonant molasses is capable of capturing the atoms moving at 31 cm/s even without the near-resonant pulse, as the simple estimate below Eq. 6.11 suggests a cooling time of close to 3 ms for far off-resonant beams as opposed to the 500 μs for resonant beams suggested above. Finally, a combination of the

two cooling strategies implemented in (f)-(m) shows an average transit time of 730 μs and a terminal velocity of 5.5 cm/s, which allows the definitive identification of sub-Doppler cooling at work here.
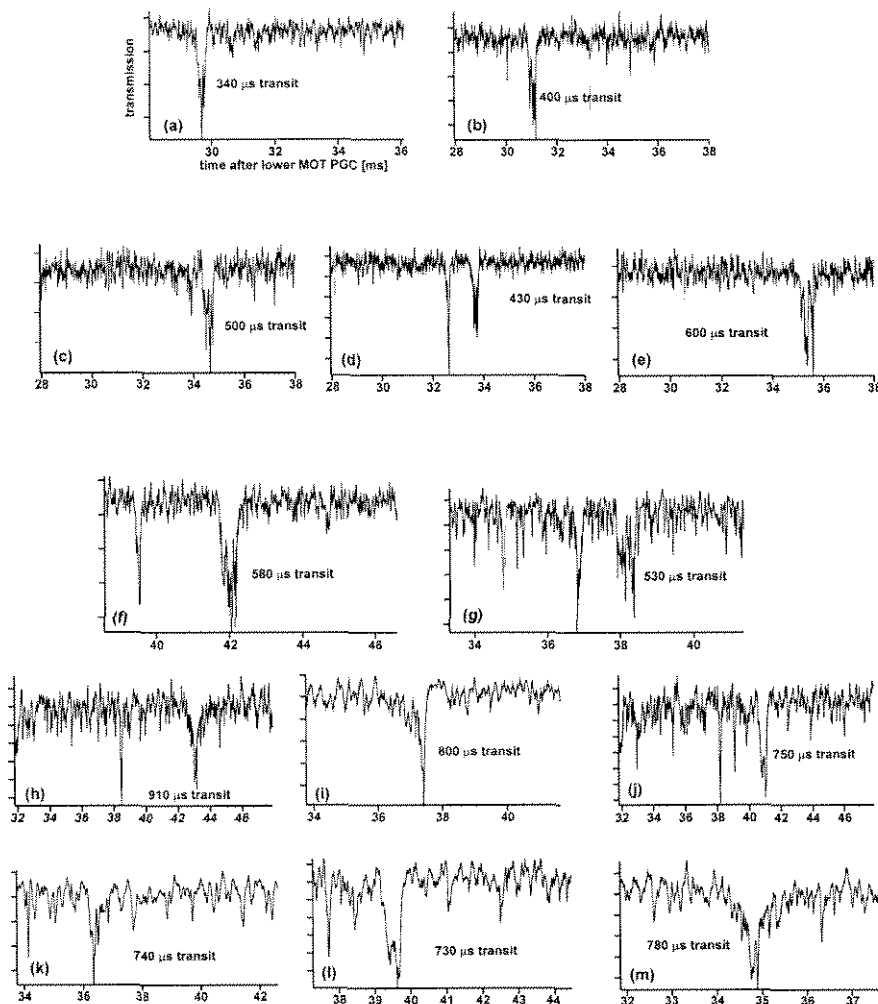
Figure 7.10: Thirteen individual transit events are grouped in three different bunches ((a)-(b), (c)-(e),(f)-(m)) to emphasize the effects of different cooling parameters of the lattice beams on downgoing atom transits. The data is summarized in Table 7.1, and trends are noted in the text.

At this point, these very encouraging initial results meant that success could tentatively be declared for the "cold atomic preparation" stage of the experiment. The atoms are now prepared *inside the cavity* with a temperature of 24 μK (15 μK in the best cases) in the vertical direction. However, a few general comments are in

138

Fig. 7.10	near resonant pulse	off-resonant pulse	transit time	delay
(a)	28 - 32 ms, -1 MHz	none	340 μs	29 ms
(b)	28 - 32 ms, -3 MHz	none	400 μs	31 ms
(c)	none	28 - 40 ms, -40 MHz	500 μs	34.5 ms
(d)	none	28 - 40 ms, -60 MHz	430 μs	33.5 ms
(e)	none	28 - 40 ms, -60 MHz	600 μs	35.5 ms
(f)	30 - 32 ms, -3 MHz	32 - 45 ms, -40 MHz	580 μs	42 ms
(g)	30 - 32 ms, -3 MHz	32 - 45 ms, -40 MHz	530 μs	38 ms
(h)	30 - 32 ms, -3 MHz	32 - 45 ms, -40 MHz	940 μs	43 ms
(i)	30 - 32 ms, -1 MHz	32 - 40 ms, -36 MHz	800 μs	37.5 ms
(j)	30 - 32 ms, -1 MHz	32 - 40 ms, -36 MHz	750 μs	35 ms
(k)	30 - 32 ms, -1 MHz	32 - 40 ms, -36 MHz	740 μs	36.5 ms
(l)	30 - 32 ms, -1 MHz	32 - 40 ms, -36 MHz	730 μs	39.5 ms
(m)	30 - 32 ms, -1 MHz	32 - 40 ms, -36 MHz	780 μs	35 ms

Table 7.1: A comparison of the cooling parameters for the long downgoing transits.

order. First, there is no indication from these measurements of the atomic energy *along the cavity axis*, and surely the randomness of the recoil kicks converts some fraction of the cooled vertical velocity into extra velocity in the orthogonal direction. Ideas about cooling along this axis will be mentioned in Sec. 8.3. Second, this effect might be offset by the fact that *all* of the atomic detection in Fig. 7.10 was done with a cavity QED probe beam on-resonance, with the implication that the act of watching the atom in this way could be heating it. Experimental investigation of a different probing technique to possibly provide cooling will be presented next in Sec. 7.1.3. Finally, it should be noted that in-depth studies of effects such as the width of the delayed cloud in Fig. 7.7 were not undertaken once the protocol of a near-resonant pulse from 30 - 32 ms and off-resonant pulse from 32 - 40 ms proved to be successful. In the last several months, however, it has become clear that lowering the initial temperature is extremely desirable for efficient FORT loading, and it is quite probable that more systematic work on the initial atomic preparation will be required.

7.1.3 Upgoing Transits and Trapping with 1 Photon

One of the primary implications of Sec. II of this thesis is that the one-photon cavity QED field can have a profound influence on the c.m. motion of an atom, because its spatial dependence along the cavity axis $g(\mathbf{r}) = g_0 \sin(kz)$ can act as a potential well. To maximize this effect, one should therefore try to maximize the value of $\hbar g(\mathbf{r})$ by, for example, minimizing the cavity mode volume. Christina and Theresa have taken this approach by making cavities whose lengths are approaching $l \sim 7~\mu$m giving values of $g_0/2\pi \sim 120$ MHz for astounding well depths close to 6 mK. Even the modest $g_0/2\pi \sim 32$ MHz in the experiments here provides a 1.5 mK depth, and it should be the case that our 24 μK cold atoms (with $v \sim 5$ cm/s) become trapped. Christina will cover this approach extensively in her thesis, including some beautiful recent results [22]. Furthermore, there are some excellent theoretical discussions available concerning cooling and trapping with a single-photon field [167, 168].

Nevertheless, a brief discussion of work done here with smaller g_{max} is worthwhile. According to the previous discussions, the act of probing the atoms "on resonance" provides excellent contrast for detection in the form of downgoing transits, but forces the atom to scatter at or near its saturated scattering rate. A quick return to Fig. 7.2 shows that if the intracavity system is probed off resonance (say, $\delta_{pa} = g_0 = 32$ MHz), then with no intracavity atom, the (dashed) intracavity transmission is down from its maximum by the Lorentzian factor $1 + (g_0/\kappa)^2 \sim 60$. However, the presence of an optimally coupled atom will pull the transmission up to the level of the solid curve, indicating that one would see an "upgoing" transit. A reduced contrast in detection is traded off for reduced heating of the atom.

There is a second important effect which is now illustrated in Fig. 7.11 by considering once again the spatially dependent eigenvalue structure of the two eigenstates. When the system loses one quanta of excitation due either to cavity or atomic decay (at similar rates, in our experiment), the system can be repopulated from the global ground state. There are two different strategies for maintaining the atom in a "trapped" eigenstate, depending on the choice of atom-cavity detuning. For $\delta_{ca} > 0$

as in Fig. 7.11(a), driving the system with $\delta_{\text{pa}} = \delta_{\text{ca}}$ would preferentially keep the atom populated ("trapped") at the bottom of the upper potential well. This *blue detuned* situation tends to localize the atoms at field nodes of $g(z)$, but is problematic because of the probability $\sim \gamma^2/\Delta_{\text{ca}}^2$ to mistakenly populate the lower atom-like eigenstate at this same position. This would put the atom at the top of the potential well for that eigenstate.

However, for $\delta_{\text{ca}} < 0$ as in Fig. 7.11(b), the lower eigenstate is now the cavity-like eigenstate, and the obvious strategy here is to drive the system at the bottom of the lower potential well. In this *red detuned* situation, atoms are localized at the antinodes of $g(z)$. For a given cavity detuning δ_{ca}, the correct probe detuning is $\delta_{\text{pa}} = \delta_{\text{ca}}/2 - \sqrt{(\delta_{\text{ca}}/2)^2 + g_0^2}$ (where $\delta_{\text{ca}} = -|\delta_{\text{ca}}|$ in Fig. 7.11(b), for example). In addition, the probability of off-resonantly exciting the atom-like eigenstate at these positions is reduced to $\sim \gamma_\perp^2 / (\Delta_{\text{ca}}^2 + 4g_0^2)$, which is small due to the strong coupling condition. Note that in the case of Fig. 7.11(b), driving mistakenly with $\delta_{\text{pa}} = \delta_{\text{ca}}$ would, in fact, repopulate from the ground state to the *top* of the potential well of the lower Rabi sideband and cause significant heating.

Finally, the situation of $\delta_{\text{ca}} = 0$ in Fig. 7.11(c) means that driving on resonance $(\delta_{\text{pa}} = 0)$ tends to distribute the atom evenly between upper and lower sidebands which, in one case, is the bottom of the potential well and, in the other, is the top. A much better strategy is to detune to $\delta_{\text{ca}} = -g_0$ which is the bottom of the well for the lower sideband.

These arguments are suggestive of an inherent one-photon trapping mechanism, and the ideas can be put on more firm theoretical ground by calculating the spatial dependence of the force (to first order) from the Hamiltonian of Eq. (7.2),

$$f = -\hbar \nabla g(\mathbf{r}) \left\langle a^\dagger |g\rangle\langle e| + a|e\rangle\langle g| \right\rangle . \tag{7.9}$$

For the general situation of Fig. 7.11(b), with a driving field ϵ at Δ_{pa} (see the
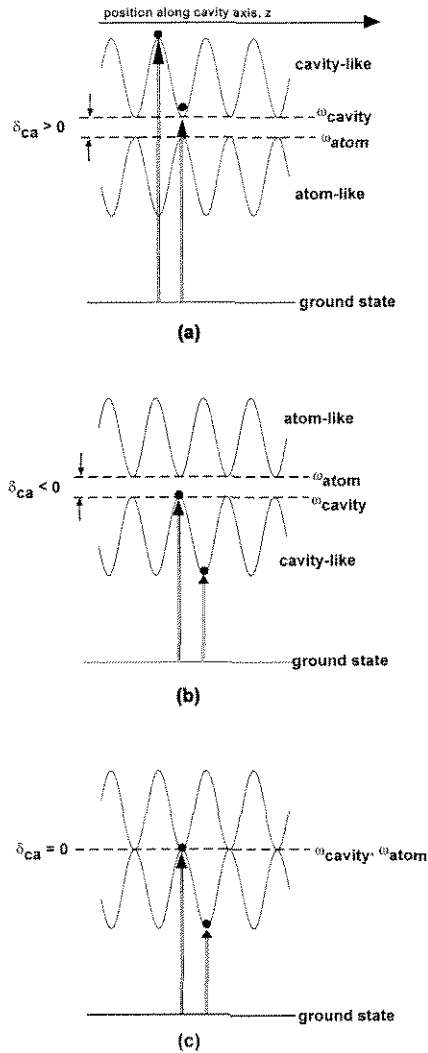
Figure 7.11: Detuning the probe beam to detect upgoing atom transits can have a simultaneous mechanical trapping effect on the atomic motion. As shown in (a) - (c), and discussed in the text, different values of the cavity detuning δ_{ca} require different probe detunings δ_{pa} to capitalize on the inherent one-photon potential well. The data of Fig. 7.13 were taken in a scheme similar to (c), with $\delta_{pa} \sim -g_0$ to populate the bottom of the potential well formed by the spatial dependence of $g(\mathbf{r})$.

Heisenberg equations (7.5)), this is evaluated as

$$f_z = -\hbar\epsilon^2 \frac{\Delta_{\mathrm{pa}}\nabla g^2(z)}{\left[\gamma_\perp\kappa + g^2(z) - \Delta_{\mathrm{pa}}(\Delta_{\mathrm{pa}} - \Delta_{\mathrm{ca}})\right]^2 + \left[\Delta_{\mathrm{pa}}\kappa + (\Delta_{\mathrm{pa}} - \Delta_{\mathrm{ca}})\gamma_\perp\right]^2}. \qquad (7.10)$$

As an example, consider the simple picture of Fig. 7.11(c) with $\Delta_{\mathrm{ca}} = 0$. As discussed above, this scenario intuitively suggested a trapping mechanism for $\Delta_{\mathrm{pa}} = -g_0$, and the spring constant K can be calculated by

$$K \sim \frac{2\hbar k^2 \epsilon^2 g_0}{(\kappa + \gamma_\perp)^2}. \qquad (7.11)$$

Noting that the driving field ϵ is related to the intracavity photon number $\bar{n}$ for the empty cavity at a detuning $\Delta_{\mathrm{pa}} = \Delta_{\mathrm{pc}} = -g_0$ by $\epsilon^2 = \bar{n}(\kappa^2 + g_0^2)$, the trap frequency should be given by

$$\omega_{\text{1-photon}} \sim 2g_0\sqrt{\bar{n}}\sqrt{\frac{\omega_{\mathrm{rec}}g_0}{(\kappa + \gamma_\perp)^2}}. \qquad (7.12)$$

Using a recoil frequency $\omega_{\mathrm{rec}}/2\pi = hk^2/4\pi m = 2$ kHz, this predicts an oscillation frequency of $\nu_{\text{1-photon}} \sim 2\sqrt{\bar{n}}$ [MHz] for motion along the cavity axis. The approximations involved in this estimate assume $\bar{n} < (\kappa + \gamma_\perp)^2/g^2 \sim 0.05$ (because the Hilbert state space has been truncated to include only the lowest 3 eigenstates) indicating axial oscillation frequencies up to $\nu_{\text{1-photon}} \sim 500$ kHz are expected for trapped atoms in the low photon number limit.

This type of analysis has been extended to higher order to include the calculation of friction and diffusion coefficients [168], and a velocity dependent component the force has been identified. This is very exciting because it implies one photon is capable of both trapping and cooling the atomic motion and a rather simple picture has eventually emerged.

Referring to Fig. 7.12 drawn for the case of Fig. 7.11(b), an atom at A *moving up* the potential formed by the cavity-like eigenvalue encounters a driving field ε equivalent to the buildup the field would have had at position B. The reason for this delay is due to the fact that this eigenstate is continually decaying to the ground state and then being repopulated at a rate $\sim \kappa$. Hence, the intracavity field does not

adiabatically follow the atomic position and is dependent on its velocity. To see that the force on the atom depends explicitly on the actual intracavity photon number (which will be called $\langle a^\dagger a \rangle$ and is a variable quantity as a function of positon to distinguish it from the fixed empty cavity intracavity photon number $\bar{n}$), the force of Eq. (7.10) may be rewritten

$$f_z = -\hbar \left(\frac{\Delta_{\mathrm{pa}}}{\Delta_{\mathrm{pa}}^2 + \gamma_\perp^2} \right) \nabla g^2 (z) \langle a^\dagger a \rangle = \frac{dp_z}{dt}. \qquad (7.13)$$

Because the driving field is on resonance with this eigenstate at B, the field has a maximal value and the atom feels a larger force when climbing the potential than it would if the intracavity field was the same for an atom at rest at that same position. The opposite occurs for an atom *moving down* the potential at C. Here, the intracavity field is equivalent to what it would have been for position D, where the driving field ϵ is maximally detuned leading to a minimal intracavity field $\langle a^\dagger a \rangle$. The atom therefore feels a smaller force when descending compared to an atom at rest at the same position, and the reduction in this force is again dependent on its velocity due to the non-adiabatic following of the intracavity field with respect to the atomic position. Similar to the PGC explanation of Sec. 6.2.5, this is also reminiscent of a Sisyphus-type effect.

Unfortunately, neither of the (extremely unwieldy) explicit expressions for the friction or diffusion coefficients that come from this analysis yield significant further insights. However, it is clear that the above mechanism will begin to fail when the atomic velocity is cooled to the point where it does not move "very far" in an eigenstate decay/re-excitation cycle. In general, this cycle time is determined by the linewidth of the particular eigenstate, namely of order $(\gamma_\perp/2 + \kappa/2)^{-1}$. For the particular scenario depicted in Fig. 7.12, if the detuning δ_{ca} is large enough to make the lower eigenstate primarily "cavity-like," then the excitation time $\sim 1/\kappa$. The cooling limit in this case, $v_{\mathrm{min}} \sim \lambda \kappa / 2\pi$, is similar to the well-known Doppler-cooling limit with the atomic linewidth $\gamma_\perp$ replaced by the cavity width κ, prompting the identification of "cavity-assisted" cooling.
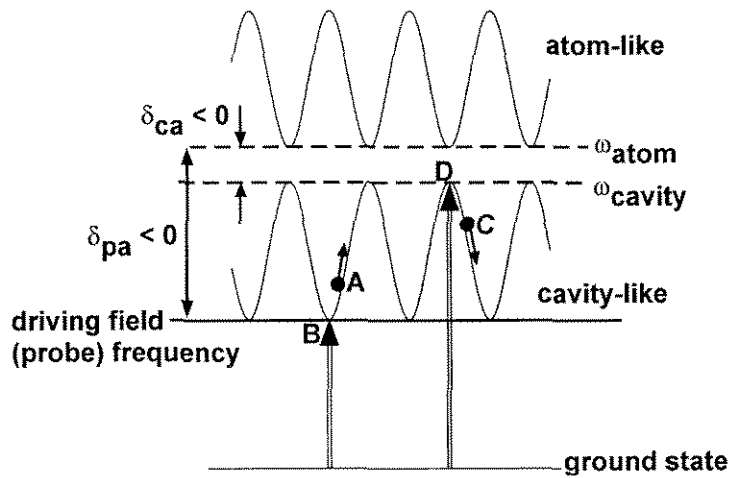
Figure 7.12: An atom at B moving up the potential formed by the cavity-like eigenvalue encounters a driving field equivalent to the buildup the field would have at A. Because the driving field is on resonance with this eigenstate at A, the field has a maximal value and the atom sees a larger force according to Eq. 7.13. The opposite occurs for an atom moving down the potential at C. Here, the intra-cavity field buildup is equivalent to what it would have been for position D, where the driving field is maximally detuned from the lower eigenstate and the buildup is a minimum. As explained in the text, this leads to a Sisyphus-type cooling effect.

Fig. 7.13(a)-(i) now presents the best experimentally observed results for long up-going transits over two evenings of data-taking, with Table 7.2 summarizing the results. The cooling protocol was the same as was used for transits (i) - (m) of Table 7.1, and intracavity photon numbers $\bar{n} \gtrsim 0.05$ were necessary to get reasonable detection contrast for these atoms. This work was done with $\delta_{ca} = 0$, implying that, according to the simple discussion about Fig. 7.11, the probe detunings should be $\delta_{pa} \sim -g_0 = -32$ MHz. In practice, it was found that a detuning closer to $\delta_{pa} = -25$ MHz produced the longest transits, approaching $T = 1.5$ ms in the very best cases. This is a factor of two improvement upon the best case downgoing transits and is good evidence for a combination of both reducing heating associated with resonance probing and trapping when detuned closer to the lower Rabi sideband.

Expected trap lifetimes $\tau_{1\text{-photon}} \sim 2mU_z/D$ for the best case transit events can be estimated from the diffusion coefficient D, the atomic mass m and the height U_z of the "effective potential" calculated by integrating the force f_z of Eq. (7.10). Though the calculation of U_z can be done analytically for $g(z) = g_0 \cos(kz)$ and results in

$$U_z = \frac{\hbar \epsilon^2 \Delta_{pa}}{\Delta_{pa}\kappa + (\Delta_{pa} - \Delta_{ca})\gamma_\perp} \tan^{-1} \left[\frac{g_0^2 \cos^2(kz) + \gamma_\perp \kappa - \Delta_{pa}(\Delta_{pa} - \Delta_{ca})}{\Delta_{pa}\kappa + (\Delta_{pa} - \Delta_{ca})\gamma_\perp} \right], \quad (7.14)$$

D requires numerical solutions and reasonable assumptions put an upper limit on the lifetime at $\tau_{1\text{-photon}} \sim 2 - 3$ ms [169]. Hence, it is very tempting to associate the transit widths T here with a trap lifetime $\tau_{1\text{-photon}}$ and indeed these transit times T are very similar to the widths of data presented in Refs. [22, 23] for which claims of truly "trapped" atoms have been made. It is most desirable to acquire clear evidence of oscillations at the axial frequency $\nu_{1\text{-photon}}$ and achieving the required signal to noise ratio at this bandwidth would be the major challenge if the experiment was to follow this route.

With the over-riding objective of our work to move on to trapping in an intracavity FORT, time was not spent on a systematic study of single-photon trapping times as a function of $(\delta_{pa}, \delta_{ca})$. This is probably an area worth a second look at some point, especially considering the nice theoretical work that has been done on this problem.

For example, Ref. [167] has pointed out that it may not necessarily be the best strategy to detune directly to the Rabi sideband, which can be understood from the fact that in the strong coupling limit the minimum of the effective potential U_z does not occur (for $\Delta_{ca} = 0$) at $\Delta_{pa} = -g_0$, but rather at $\Delta_{pa} = -g_0/\sqrt{3}$ (though note that this choice does not maximize the spring constant K). Our first results also show experimentally that the longest transits at $\delta_{pa} = -30$ MHz were about 50% shorter than seen at $\delta_{pa} = -25$ MHz, albeit without an overwhelming amount of data.

Fig. 7.13	transit duration	δ_{pa}
(a)	960 μs	-30 MHz
(b)	880 μs	-30 MHz
(c)	1.5 ms	-25 MHz
(d)	1.2 ms	-25 MHz
(e)	1 ms	-20 MHz
(f)	1.4 ms	-20 MHz
(g)	1.1 ms	-20 MHz
(h)	860 μs	-20 MHz
(i)	1.3 ms	-20 MHz

Table 7.2: A comparison of the cooling parameters for the long upgoing transits.

Finally, it is worth noting that the traces in Fig. 7.13(a),(b) show the cooling pulse sequence below the data, and these data sets are one example of an evening where the (quite painful) step of locking the lattice phase was taken. After trying many different "lock points" on the Michelson fringe, and also most permutations involving locking or unlocking this phase, it was quite inconclusive whether the act of locking the phases of the cooling beams to make a lattice was ever helpful. Again, a more systematic study is desirable, but with the added complexity of the FORT laser soon to be involved, the already complex experiment benefitted greatly by abandoning the lin⊥lin scheme and reverting to the experimentally simpler σ_+/σ_- configuration for the cooling beams. Data very similar to Fig. 7.7 were recovered in this new configuration and confirmed that the atomic preparation was similar to before and that the initial atomic temperatures were not compromised.
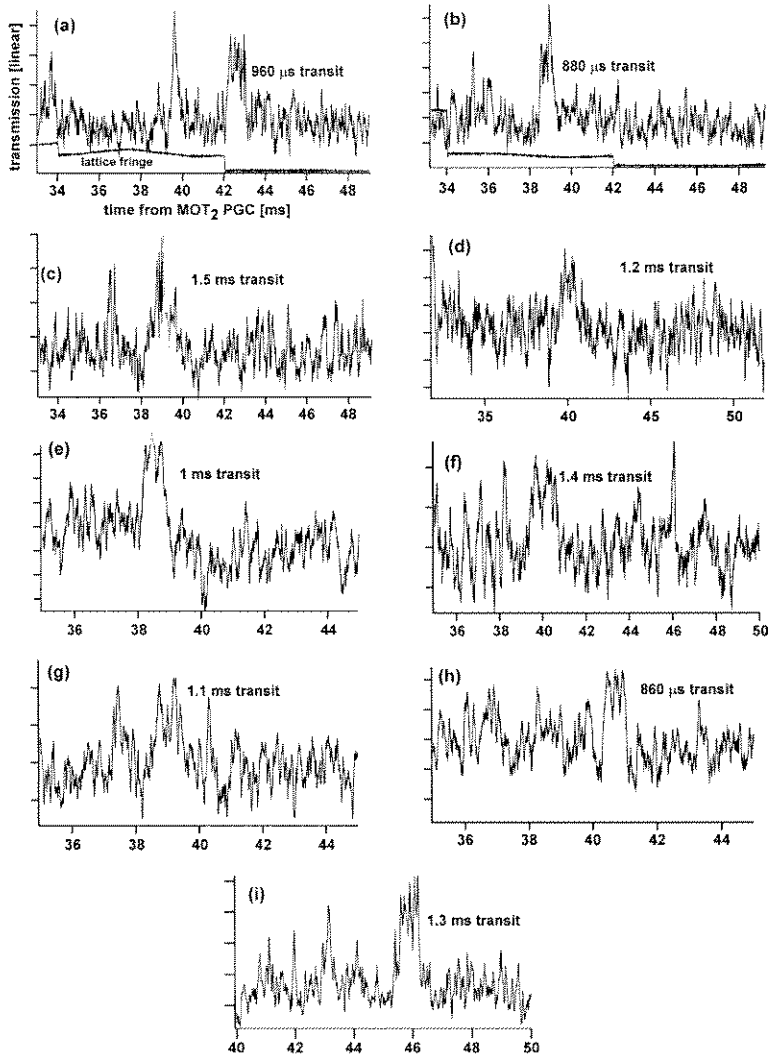
Figure 7.13: Nine different single-atom upgoing transits are shown to emphasize the confining capabilities of the one-photon potential well. The relevant parameters are noted in Table 7.2 for each event.

7.2 IntraCavity FORT

Having decided to use an all-optical approach for the implementation of the intra-cavity trap, three prime considerations were to achieve large potential well depths, to localize the atoms to a fraction of the optical wavelength, and to register this localization precisely with the cavity QED probe field. All of these conditions are satisfied by choosing the FORT wavelength as another longitudinal mode of the physics cavity.

7.2.1 Far Off-Resonance Traps (FORTs)

A FORT is based on the idea that an atomic dipole (which has been polarized by a near-resonant laser field) will be attracted to (repelled from) intensity maxima of this field if the field frequency is red (blue) detuned from the atomic resonance frequency [131]. For any given atomic level, the energy shift associated with this interaction can be calculated from perturbation theory using

$$\Delta E_i = \sum_{j \neq i} \frac{\left| \left\langle j \left| e\widehat{\mathbf{r}} \cdot \widehat{\mathbf{E}} \right| i \right\rangle \right|^2}{E_i - E_j}. \tag{7.15}$$

For an $S \rightarrow P$ transition, in the limit that the detuning of the field is much greater than the hyperfine structure, but comparable to the fine structure splitting, the expressions for the dipole potential (ground state shift) and scattering rate are given by

$$U_{\text{dip}}(\mathbf{r}) = \frac{\pi c^2 \Gamma}{2\omega_0^3} \left(\frac{2 + P g_F m_F}{\Delta_{2,F}} + \frac{1 - P g_F m_F}{\Delta_{1,F}} \right) I(\mathbf{r}) \tag{7.16}$$

$$\Gamma_{\text{scatt}}(\mathbf{r}) = \frac{\pi c^2 \Gamma^2}{2\hbar\omega_0^3} \left(\frac{2}{\Delta_{2,F}^2} + \frac{1}{\Delta_{1,F}^2} \right) I(\mathbf{r}).$$

Here $P = (1, 0, -1)$ for $(\sigma_+, \pi, \sigma_-)$ transitions, $\Delta_{1,F}$ $(\Delta_{2,F})$ is the detuning of the FORT field (of intensity profile $I(\mathbf{r})$ and frequency ω_0) from the $P_{1/2}$ $(P_{3/2})$ state, (F, m_F) are the hyperfine and magnetic sublevels and g_F is the Lande factor. For the case of the Cs $6S_{1/2}$ $F = 3$ and $F = 4$ ground states (which are connected most

strongly to the $6P_{1/2}$ and $6P_{3/2}$ states via the $D1$ and $D2$ lines respectively), the shifts as a function of magnetic sublevel m_F for an 868 nm FORT are shown in Fig. 7.14. It is interesting that in the case of a linear FORT, all sublevels are trapped in both cases. However, because the cavity QED field drives the $(F, m_F) = (4, 4) \rightarrow (F', m_{F'}) = (5, 5)$ cycling transition using σ_+ light, a σ_+ FORT was the one implemented in the lab due to experimental constraints (the FORT used the same polarizing optics as the cavity QED probe field). For this polarization, the $F = 4$, $m_F = -3, -4$ and $F = 3$, $m_F = 3$ states are not trapped. The latter has serious consequences for those atoms in our $F = 4$ implementation which are off-resonantly scattered from $F = 4$ (through $F' = 4$) into the $F = 3$ state and makes repumping of the atomic population out of this state critical on time scales comparable to the inverse scattering rate.
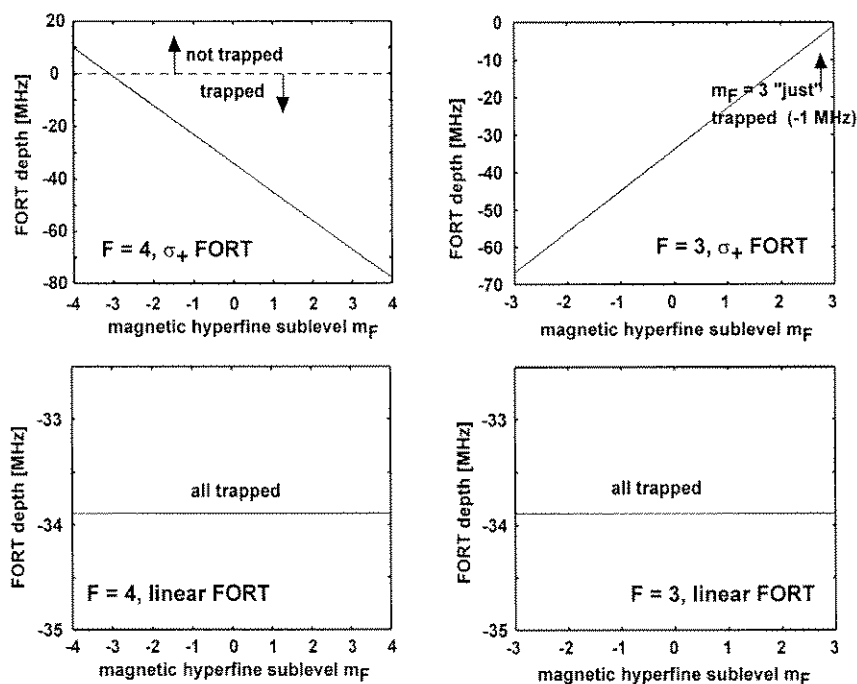
Figure 7.14: The AC Stark shift of the ground state due to the FORT trapping laser is shown as a function of hyperfine magnetic sublevel for both linear and circularly polarized FORT fields in both the $F = 4$ and $F = 3$ ground state manifolds. It is interesting to note that all states are trapped for linear FORTs, but not for circular. The numbers used in the calculation are typical of those for our experiment.

The wavelength dependence of the FORT potential is shown in Fig. 7.15 for the

relevant $6S_{1/2}$ $F = 4, m_F = 4$ state for both circular (a) and linear (b) polarizations. In the circular case, this state cannot be connected to the $6P_{1/2}$ state (D1 transition at 894 nm, see Fig. 6.1) due to selection rules and hence in (a), only the D2 line at 852 nm, with an $F = 5, m_F = 5$ state enters into the calculation. Finally, Fig. 7.16 shows the wavelength dependence of the scattering rate Γ_{scatt}. All three of these calculations (Figs. 7.14, 7.15 and 7.16) use parameters for $I\left(\mathbf{r}\right)$ which are very close to the experimentally implemented values. For a *standing wave* of power P,

$$I = \frac{2P}{\pi w_0^2}, \tag{7.17}$$

where in our case, the intracavity power at the eventual FORT wavelength was approximately 150,000 times the measured output power due to the high finesse cavity buildup. Hence, for a typical measured output power of about 8 μW at 868 nm, the experimentally implemented FORT depth and scattering rate are

$$U_{\text{dip}}\left(z\right) / \left(2\pi\hbar\right) \quad \sim \quad 75 \ \sin^2\left(2\pi z/\lambda_{\text{FORT}}\right) \ [\text{MHz}] \equiv \Delta_{\text{FORT}}\left(z\right)/2\pi \tag{7.18}$$

$$\Gamma_{\text{scatt}}\left(z\right) \quad \sim \quad 250 \ \sin^2\left(2\pi z/\lambda_{\text{FORT}}\right) \ [1/\text{s}].$$

The shift of the $6P_{3/2}$ excited state due to FORT excitation at 860 and 868 nm is the opposite of the ground state shift ($\Delta_{\text{FORT}}^e = -\Delta_{\text{FORT}}^g$) in the circularly polarized case (see Fig. 8.3), indicating that the excited state is not trapped. In fact, the finite scattering rate into this state is a major cause of heating in the FORT, because the dipole force seen by the atom as a whole tends to fluctuate. A possible strategy to overcome this limitation of the FORT will be discussed in Sec. 8.4.

The choice of FORT wavelengths was dictated, of course, by the available longitudinal modes of the physics cavity. According to Fig. 6.20, modes $n - 1$ and $n - 2$ at approximately 860 and 868 nm seemed like good candidates. There were various trade-offs between them, including the FORT depth and scattering rates which, according to Eqs. 7.16 (n.b., with detuning $\Delta = \omega_{\text{FORT}} - \omega_{\text{atom}}$ a *different* "Δ" from the well depth Δ_{FORT}) scale with detuning as $1/\Delta$ and $1/\Delta^2$ respectively. Hence,
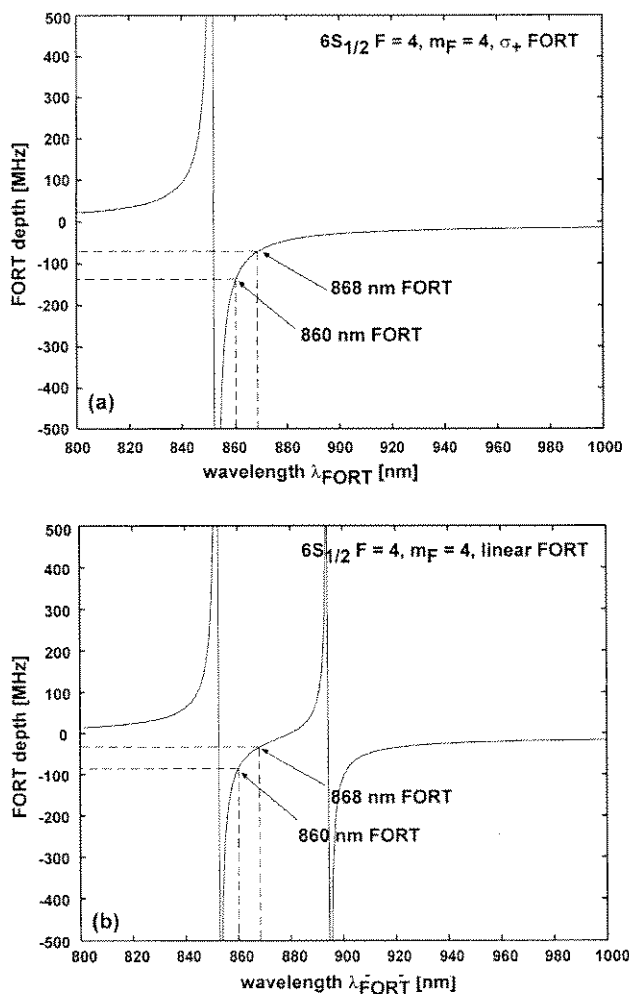
Figure 7.15: For realistic experimental parameters, the FORT potential depth $\Delta_{\mathrm{FORT}}(z_{\mathrm{max}})/(2\pi\hbar)$ of Eq. (7.18) for the $6S_{1/2}$ $F = 4, m_F = 4$ ground state as a function of wavelength is shown for both circularly (a) and linearly (b) polarized FORTs, with the two wavelenghts relevant to the experiments here shown explicitly. In the circular case of (a), the ground state only couples to the $D2$ line at 852 nm, whereas the effects of the $D1$ line at 894 nm must also be included in the linear case.
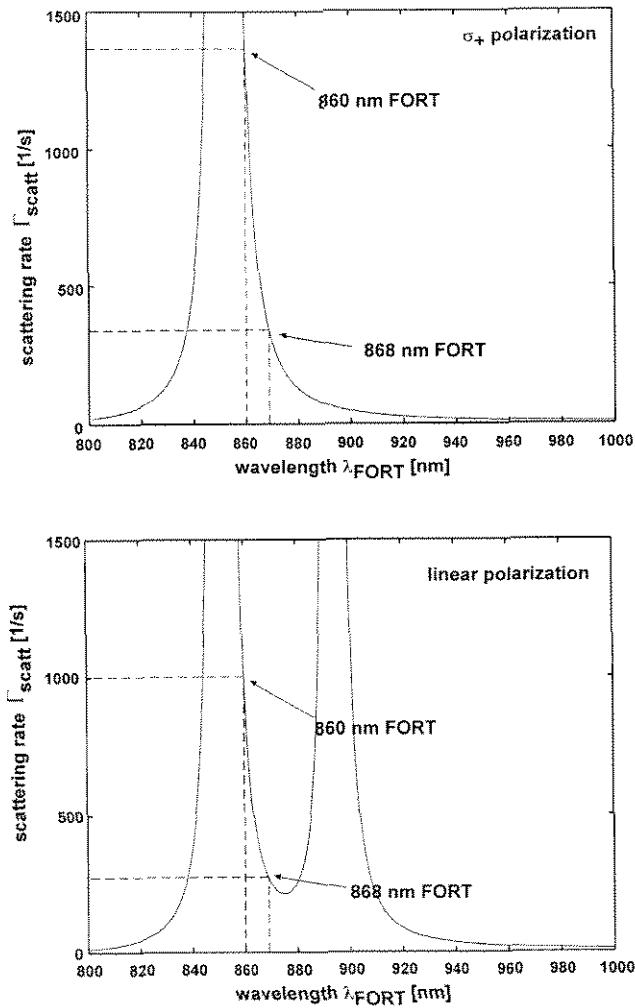
Figure 7.16: The scattering rates Γ_{scatt} at the position z_{max} associated with the FORT depths of Fig. 7.15 are shown for linear and circularly polarized FORTs. This scattering causes heating of the atom in the FORT as explained in Section 7.2.7.

going from 860 nm to 868 nm would only decrease the FORT depth by a factor of 2 (for the same intracavity power) but would reduce the scattering rate four-fold. Figs. 7.15 and 7.16 have these two wavelengths highlighted on them for convenience.

Fig. 7.17 investigates the registration of the FORT potential $U_0 \sin^2 (2\pi z/\lambda_{\mathrm{FORT}})$ [Eq. (7.18)] and the cavity QED field $\sim g_0 \sin (2\pi z/\lambda_{\mathrm{cavity}})$, with $\lambda_{\mathrm{cavity}} = 852$ nm. When the FORT is chosen to be only one mode order below the atomic line, at 860 nm, the FORT potential minima and cavity QED maxima coincide exactly only at the two mirror surfaces, and the FORT minima coincide with nodes of the cavity QED field at the cavity center, as shown in Fig. 7.17(a). This situation seems not to maximize the probability of "seeing" an atom using the cavity QED coupling (as in Sec. 7.1.1) once it is loaded into the FORT. On the other hand, moving one mode order further along to 868 nm, the standing-wave patterns of the two modes at $(\nu_{\mathrm{FORT}}, \nu_{\mathrm{cavity}})$ are such that there are approximately coincident antinodes near the center and ends of the cavity. Hence, the trapping potential of the FORT has maximum depths at the positions of maxima (g_0) for cavity QED coupling in these regions. Experimentally, work first started at 860 nm, but moved quickly to 868 nm in the hopes of taking advantage of this fortuitous overlap of fields at the center of the cavity.

This section concludes with a very quick estimate of the trap vibrational frequencies. The spatial dependence of the intensity takes the form

$$I(\mathbf{r}) = \frac{2P}{\pi w_0^2} \sin^2 (k_{\mathrm{FORT}} z) \, e^{-\frac{2\left(x^2+y^2\right)}{w_0^2}}, \tag{7.19}$$

so that

$$U_{\mathrm{dip}}(\mathbf{r}) = U_{\mathrm{FORT}}(\mathbf{r}) = \hbar \Delta_{\mathrm{FORT}} \sin^2 (k_{\mathrm{FORT}} z) \, e^{-\frac{2\left(x^2+y^2\right)}{w_0^2}}. \tag{7.20}$$

For the typical sized FORT of $\Delta_{\mathrm{FORT}}/2\pi = \delta_{\mathrm{FORT}} \sim 75$ MHz, we can use either Eq. (5.3) or a simple expansion of (7.20) to evaluate the radial (x, y) and axial (z)
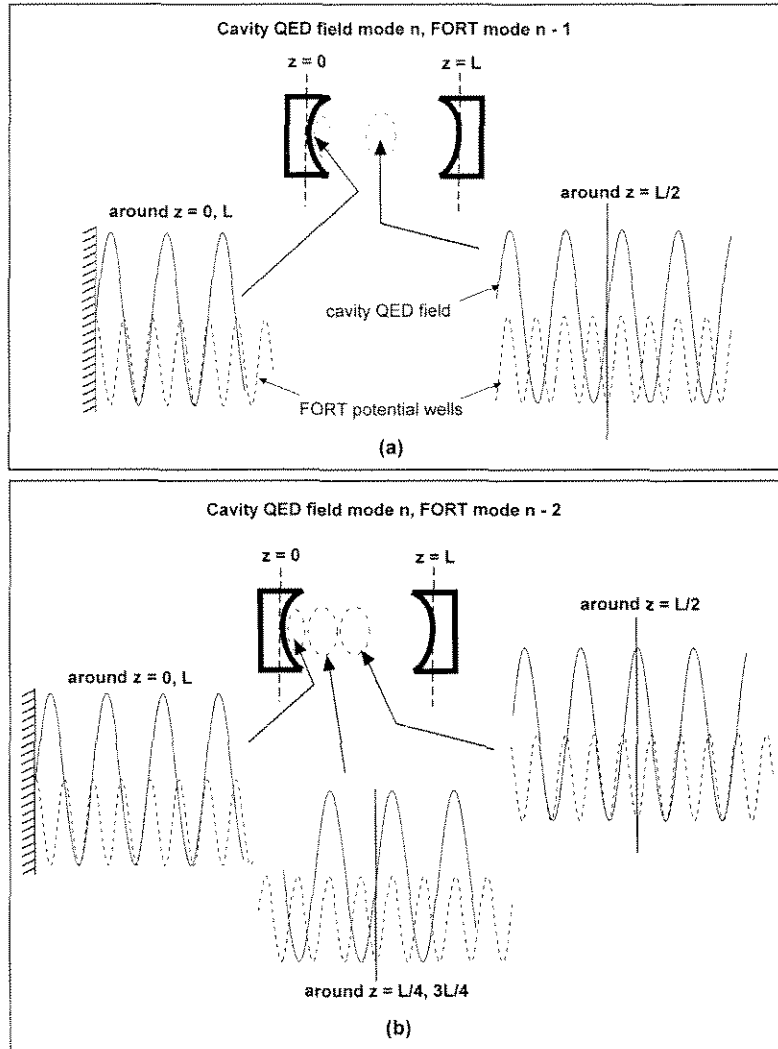
Figure 7.17: The alignment or registration of the (dashed) FORT potential *proportional to the square of the FORT field* with respect to the cavity QED coupling probe field is shown for two cases. In (a), they are offset by only 1 longitudinal mode of the cavity, so that an atom trapped in a FORT potential well at the center of the cavity will see a null of the cavity QED field. In (b), the perfect registration of maximum of the FORT with maximum of the probe field now occurs at the cavity center for a two longitudinal mode difference between the wavelengths.

trapping frequencies,

$$\left(\nu_{tr}^{\mathrm{axial}}, \nu_{tr}^{\mathrm{radial}}\right) = \frac{1}{2\pi\hbar}\left(\sqrt{2\hbar\Delta_{\mathrm{FORT}}\frac{\hbar^2 k_{\mathrm{FORT}}^2}{m}}, \sqrt{2\hbar\Delta_{\mathrm{FORT}}\frac{\hbar^2}{m\left(w_0/\sqrt{2}\right)^2}}\right) \sim (7, 770) \text{ kHz}.$$

(7.21)

7.2.2 The Hamiltonian and Eigenvalue Spectrum

It is very instructive to now complicate the Hamiltonian of Eq. (7.2) (i.e., both its spatially dependent eigenvalue structure of Fig. 7.11 and frequency dependent eigenvalue structure as depicted in Fig. 7.2) by including the presence of the FORT. The result of the previous section indicates that the FORT can be understood as a negative shift $\Delta_{\mathrm{FORT}}^g(\mathbf{r})$ to the ground state energy, and a corresponding positive shift $\Delta_{\mathrm{FORT}}^e(\mathbf{r})$ for the excited state. The FORT effectively provides a spatially dependent detuning that shifts the cavity QED interactions out of resonance, with the substitution

$$\begin{aligned}\Delta_{\mathrm{ca}} &\rightarrow \Delta_{\mathrm{ca}} + \Delta_{\mathrm{FORT}}^g(\mathbf{r}) - \Delta_{\mathrm{FORT}}^e(\mathbf{r}) \\ &= \Delta_{\mathrm{ca}} - 2\Delta_{\mathrm{FORT}}(\mathbf{r}),\end{aligned}$$

(7.22)

where here $\Delta_{\mathrm{FORT}}(\mathbf{r}) = |\Delta_{\mathrm{FORT}}^g(\mathbf{r})| = |\Delta_{\mathrm{FORT}}^e(\mathbf{r})|$. To calculate the probe transmission in this case requires an analysis of the eigenvalue structure incorporating both the coupling $g_0(\mathbf{r})$ as well as $\Delta_{\mathrm{FORT}}(\mathbf{r})$ [163].

Any complications arising from the effects of the FORT on the atomic c.m. motion will be ignored by assuming the atomic motion is trapped classically in a particular FORT potential well (according to the above discussion, the atom must spend most of its time in its internal ground state for this to be true). The modified Jaynes-Cummings Hamiltonian can be written

$$\frac{H}{\hbar} = \omega_a|e\rangle\langle e| + \omega_c a^\dagger a + \Delta_{\mathrm{FORT}}(\mathbf{r})\left(|e\rangle\langle e| - |g\rangle\langle g|\right) + g(\mathbf{r})\left(|g\rangle\langle e|a^\dagger + a|e\rangle\langle g|\right).$$ (7.23)

The term $\Delta_{\mathrm{FORT}}(\mathbf{r})\left(|e\rangle\langle e| - |g\rangle\langle g|\right) = \Delta_{\mathrm{FORT}}(\mathbf{r})\sigma_z$ shows explicitly the effect of the

FORT as a positive AC Stark shift $\Delta_{\mathrm{FORT}}(\mathbf{r}) = 2\pi\delta_{\mathrm{FORT}}(\mathbf{r})$ on the excited state $|e\rangle$ and a negative AC Stark shift $-\Delta_{\mathrm{FORT}}(\mathbf{r})$ on the ground state $|g\rangle$. Again, similar to Eq. (7.3), the eigenvalues of the matrix

$$\frac{H}{\hbar} = \begin{pmatrix} -\omega_{\mathrm{atom}} - \Delta_{\mathrm{FORT}}(\mathbf{r}) & 0 & 0 \\ 0 & \Delta_{\mathrm{ca}} - \Delta_{\mathrm{FORT}}(\mathbf{r}) & g(\mathbf{r}) \\ 0 & g(\mathbf{r}) & \Delta_{\mathrm{FORT}}(\mathbf{r}) \end{pmatrix} \tag{7.24}$$

are

$$\lambda_0 = -\omega_{\mathrm{atom}} - \Delta_{\mathrm{FORT}}(\mathbf{r}) \tag{7.25}$$

for the ground state $|g, 0\rangle$,

$$\lambda_\pm = \frac{\Delta_{\mathrm{ca}}}{2} \pm \sqrt{\frac{\Delta_{\mathrm{ca}}^2}{4} + g^2(\mathbf{r}) + \Delta_{\mathrm{FORT}}(\mathbf{r})(\Delta_{\mathrm{FORT}}(\mathbf{r}) - \Delta_{\mathrm{ca}})}$$

for the first two excited states $\frac{1}{\sqrt{2}}(|g, 1\rangle \pm |e, 0\rangle)$.

These eigenstates are very similar to well-dressed eigenstates of Eq. (5.1), with the subtle difference that $V_{\mathrm{ext}}(\mathbf{r})$ there does not have an internal state dependence. In Eq. (7.23), $\Delta_{\mathrm{FORT}}(\mathbf{r})$ does not have any bound eigenstates in the excited state. An experimental situation much closer to that envisioned in Part II of this thesis will be discussed shortly in Sec. 8.4.

The ground state shift $-\Delta_{\mathrm{FORT}}(\mathbf{r})$ must be taken into account when considering the shift of the resonance frequencies $\delta\omega_\pm$. The probe laser, at a detuning Δ_{pa} from the bare atomic resonance, will now see an "extra" shift due to the FORT of

$$\delta\omega_\pm = (\lambda_\pm - \lambda_0) - \omega_{\mathrm{atom}} = \lambda_\pm + \Delta_{\mathrm{FORT}}. \tag{7.26}$$

To complete the story, the analogous cavity transmission spectra to Eq. (7.7) can be written

$$t(\Delta_{\mathrm{pa}}) = \frac{\kappa(\gamma_\perp + i(2\Delta_{\mathrm{FORT}} - \Delta_{\mathrm{pa}}))}{(\lambda_+ + i\Delta_{\mathrm{pa}})(\lambda_- + i\Delta_{\mathrm{pa}})}, \tag{7.27}$$

with

$$\left(\lambda + \kappa + i\Delta_{\mathrm{ca}}\right)\left(\lambda + \gamma_\perp + 2\Delta_{\mathrm{FORT}}\right) + g_0^2 = 0. \tag{7.28}$$

These equations are derived from Eq. 7.7, by noting that the bare atomic resonance frequency (which was chosen as the "reference frequency" in Eq. (7.7)) is now modified by $\omega_{\mathrm{atom}} \rightarrow \omega_{\mathrm{atom}} + 2\Delta_{\mathrm{FORT}}\left(\mathbf{r}\right)$.

To make all of this very concrete, below in Figs. 7.18, 7.19, 7.20 and 7.21 are presented three specific examples using the actual experimental situation of an $l = 44$ μm long cavity and 868 nm FORT as in Fig. 7.17(b). In Fig. 7.18(a), the registration of $g(z)$ with a 20 MHz deep FORT $\Delta_{\mathrm{FORT}}\left(z\right)$ is shown for reference near the center of the cavity. In 7.18(b), the eigenvalue structure $\delta\omega_\pm$ is shown, along with $\Delta_{\mathrm{FORT}}\left(z\right)$, which represents the shift of the ground state. Note that $\Delta_{\mathrm{ca}} = 0$ for this example. Concentrating on the line AA', along which $g = g_{\mathrm{max}} = 32$ MHz and $\Delta_{\mathrm{FORT}} = 20$ MHz (perfect registration at the center of the cavity), Fig. 7.18(b) is the evaluation of Eq. (7.27) for the cavity transmission for an atom located at this position. If the probe was chosen to be on resonance $\Delta_{\mathrm{pa}} = 0$, then an atom which entered this particular potential well would be seen as a down-going transit. The effect of the FORT in this case is to reduce the splitting of the cavity-like eigenvalue from $g_{\mathrm{max}} = 32$ MHz in the "no-FORT" case to approximately 18 MHz here.

In Fig. 7.19, the eigenvalue spectra near the point $z = l/4$ is shown for the same parameters as in Fig. 7.18. Along the line AA' is the point where maximal cavity QED coupling coincides with a zero of the FORT, giving rise to the symmetric spectrum in (c), which has been seen before in Fig. 7.2. A shift to the left a fraction of a wavelength to the line BB' changes this situation drastically, as is shown in (d), where there is a clear identification of the cavity-like eigenvalue similar to Fig. 7.18, because the atom has moved away from the FORT node.

The third Fig. 7.20 illustrates the situation of a rather deep FORT of $\Delta_{\mathrm{FORT}} = 80$ MHz. In this case, all four quantities $(g(z), \Delta_{\mathrm{FORT}}(z)$ and $\delta\omega_\pm(z))$ are shown on the same graph so that (a) shows the situation around $z = l/2$ at the center of the cavity and (b) at $z = l/4$. There is very little relative effect along the line AA' at the cavity
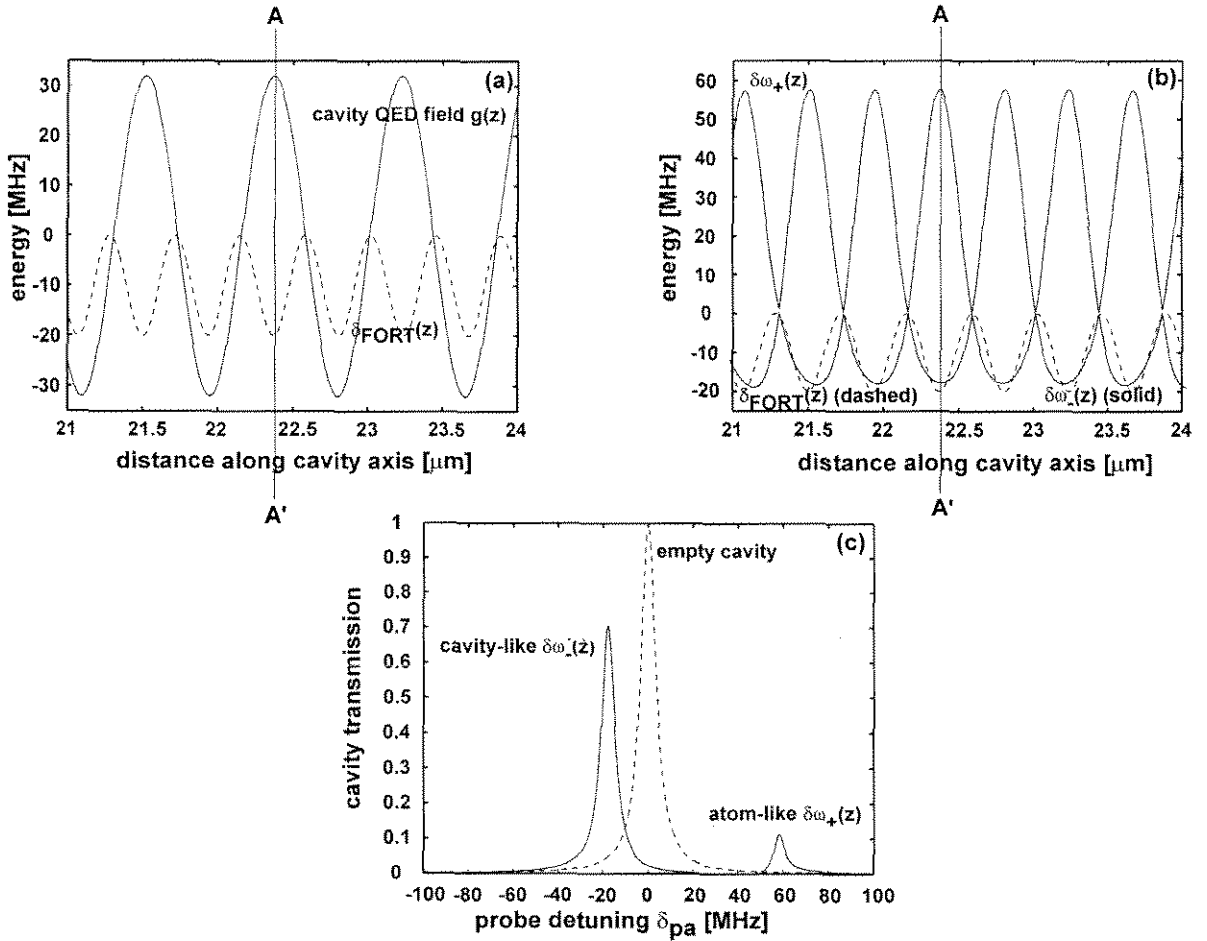
Figure 7.18: The situation for an atom trapped in a FORT potential well near the center of the cavity is depicted here. In (a), the FORT/cavity QED field registration is summarized again. Fig. (b) gives the spatial dependence of the upper and lower eigenvalues (both solid) along with the FORT potential (dashed). Finally for an atom trapped in the potential well along the line AA', the cavity transmission $|t\left(\Delta_{\mathrm{pa}}\right)|^2$ of Eq. 7.27 shows the lower eigenvalue as "cavity-like" and the upper as "atom-like." The empty cavity transmission is shown as a dashed line here.
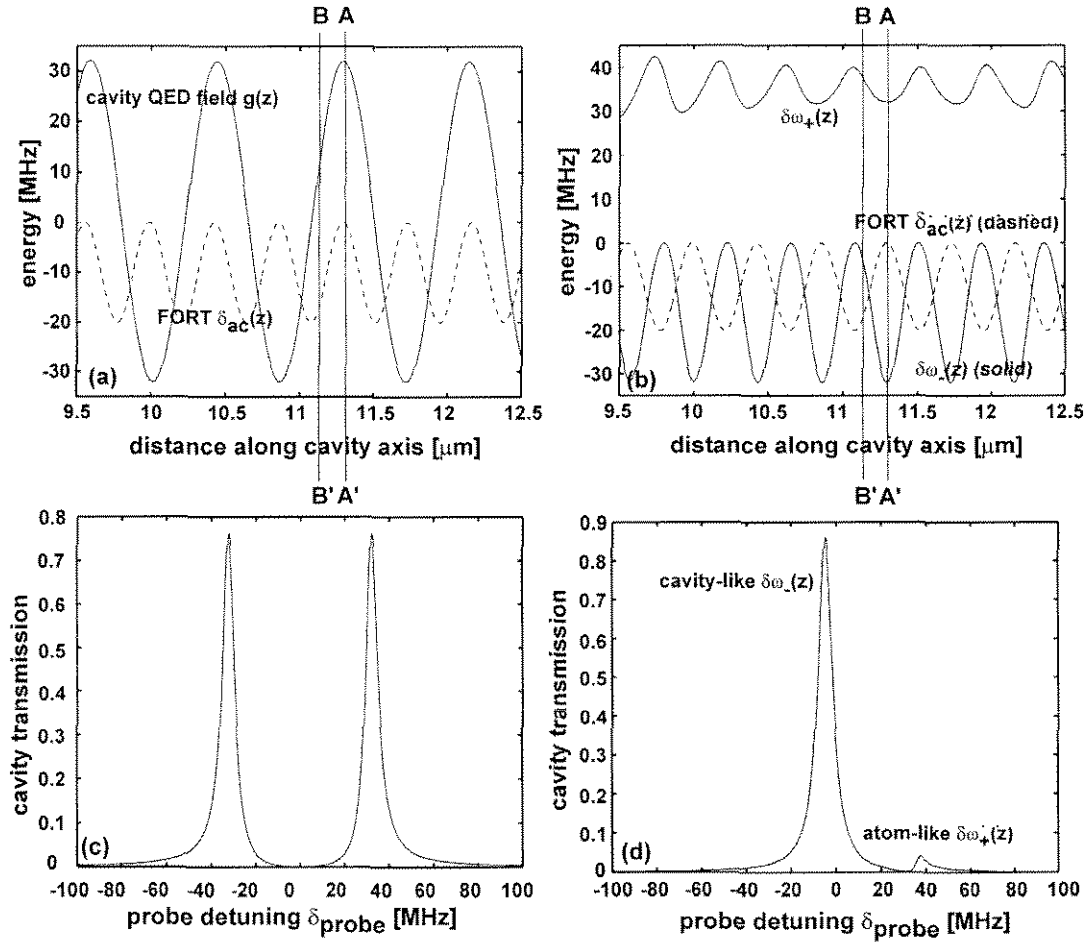
Figure 7.19: Moving to the situation close to 1/4 of the way along the cavity axis, there is now perfect anti-registration of FORT (dashed in (a)) and cavity QED field (solid in (a)). The spatial eigenvalues are shown in (b) as solid lines for the upper atom-like $\delta\omega_+(z)$ and lower cavity-like $\delta\omega_-(z)$ eigenvalues. An atom situated at the position AA' will see no FORT potential, so its cavity transmission in (c) is the same as in Fig. 7.2 with $g = g_{max} = 32$ MHz. There is no atom/cavity-like distinction here. Along the line BB', however, the situation changes drastically such that the FORT depth is approximately 16 MHz and the cavity QED coupling is $g = 13$ MHz to give the transmission spectra in (c).

center due to an atom trapped there, as the large FORT depth overwhelms the cavity coupling g and therefore the ability to see the atom when $\Delta_{ca} = 0$. Using Eq. 7.27, the fractional change in the intensity of the cavity transmission when probing on resonance ($\Delta_{pa} = 0$) is

$$1 - |t_{1\text{-}atom}|^2 \sim \left(g^2\left(z\right)/2\kappa\Delta_{\text{FORT}}(z)\right)^2, \tag{7.29}$$

which is just detectable only for the very best atoms with $g(z) \sim g_0$, assuming $\Delta_{\text{FORT}}(z) \sim \Delta_{\text{FORT}}(\text{max})$ for trapped atoms. This example illustrates that it is probably more worthwhile to turn *off* large FORTs (Sec. 7.2.5) or use $\Delta_{ca} \neq 0$ (Sec. 7.2.4) in order to see atoms trapped in them.

In the final Fig. 7.21, a neat proposal highlights the role of Δ_{ca}, which has been absent until now. Examining Eq. (7.25) shows that making $\Delta_{ca} = 2\max\left(\Delta_{\text{FORT}}\left(z\right)\right)$ should "remove" the presence of the FORT from the eigenvalue spectrum such that at positions where $\Delta_{\text{FORT}}\left(z\right)$ is a maximum, $\delta\omega_\pm = \Delta_{ca} \pm g\left(z\right)$. Furthermore, if $g(z)$ happens to be a maximum at this same point, as along the line AA' in Fig. 7.21, then detuning the probe to $\delta_{pa} = \delta_{ca}$ will allow one to "see" the atom as if the FORT were not there at all (i.e., without sacrificing any contrast in g). Unfortunately, for reasonably sized FORTs with $\Delta_{\text{FORT}} \geq 20 - 30$ MHz, the required δ_{ca} to implement *this scheme quickly moves out of the experimentally accessible dynamic range in* frequencies due to limitations on modulator and detector bandwidths. Furthermore, one must always keep in mind that any population in the atomic excited state will tend to cause heating, as shown by the "anti-registration" of the spatial dependence of the upper and lower eigenvalues (solid) with respect to the FORT (dashed) in Fig. 7.21. Here, these eigenvalues are once again equal combinations of atom and cavity (with the "atom-like" and "cavity-like" distinctions cleverly removed) so that any population in either of these states *at positions of a trapped atom* (FORT minimum) will tend to cause some heating.
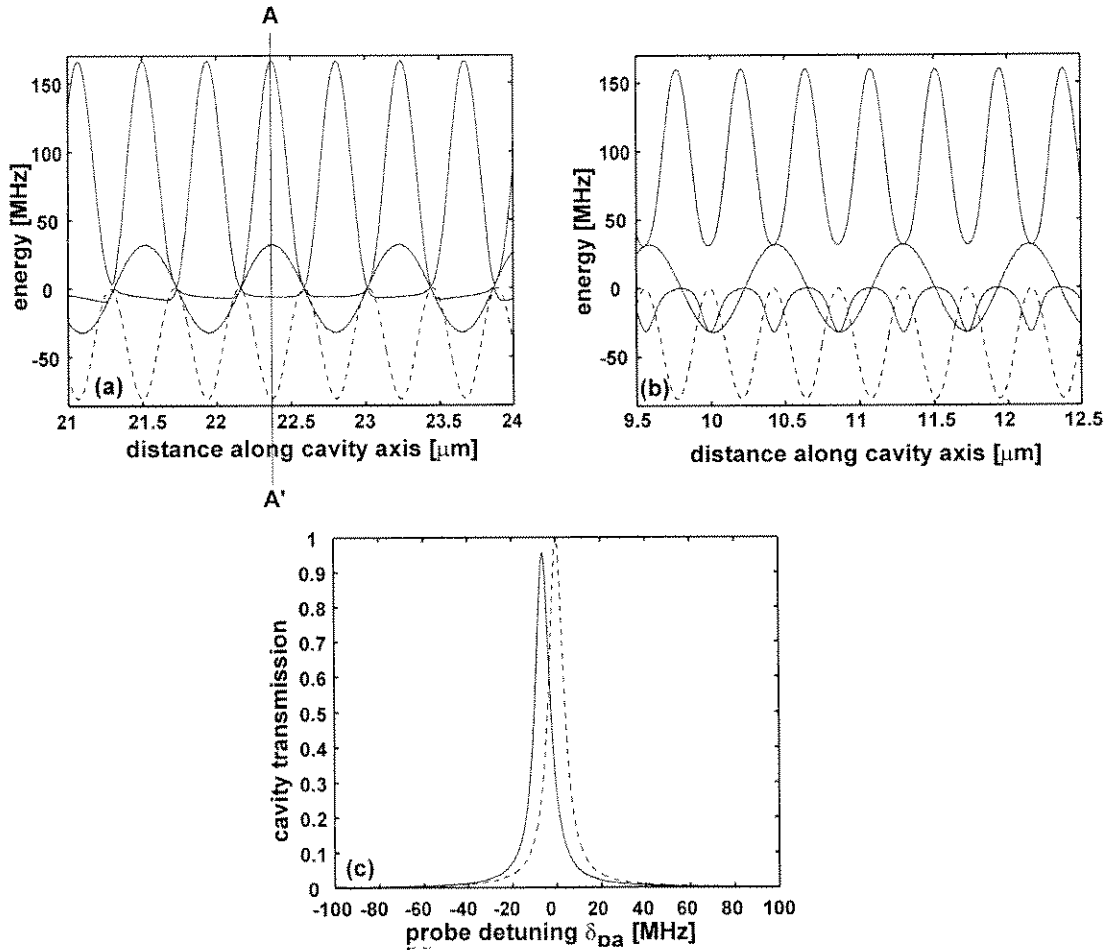
Figure 7.20: The limit of a very big FORT with $\Delta_{\text{FORT}} = 80$ MHz is shown near the center of the cavity (a) and $1/4$ of the way along the cavity axis in (b). The cavity QED field and upper and lower eigenvalues are shown as solid lines, and the FORT potential is dashed. Note that the eigenstates "meet" in (a) at positions where $g(\mathbf{r}) = \Delta_{\text{FORT}}(\mathbf{r}) = 0$. The problem of detecting an atom trapped in the well along the line AA' is emphasized in the spectrum of (c), where the cavity-like eigenvalue is only shifted by $\delta_{\text{pa}} \sim -g^2/2\Delta_{\text{FORT}}$ from the empty cavity case, versus the $\delta_{\text{pa}} \sim -g$ shift one would get in the case of no FORT field. As a result, the contrast for detecting single atoms on resonance (with $\Delta_{\text{ca}} = 0$) is poor for big FORTs.
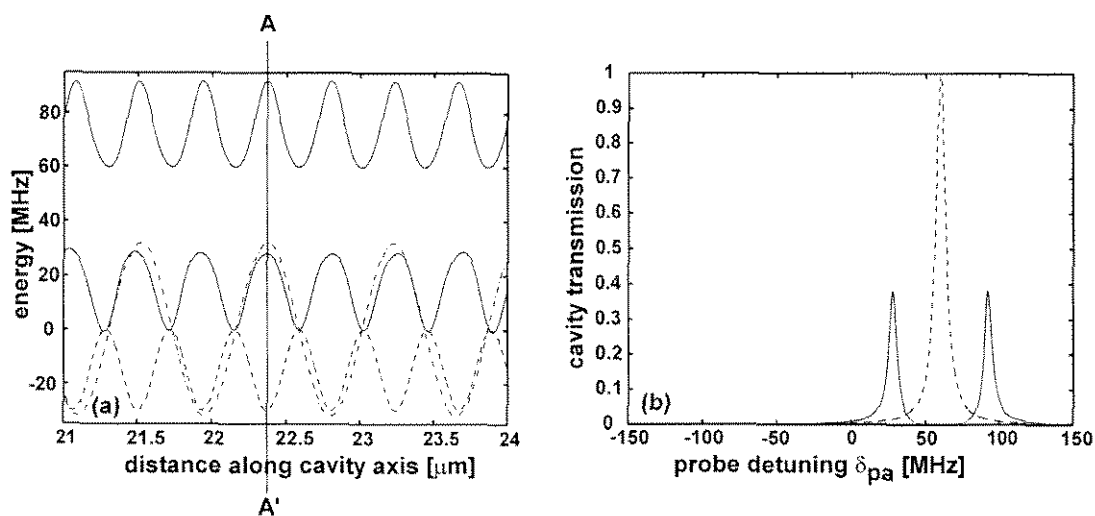
Figure 7.21: In an interesting proposal, an attempt is made to use the atom-cavity detuning Δ_{ca} to eliminate the effects of the FORT potential on the cavity transmission spectra. In (a), upper and lower eigenvalues (solid), cavity QED coupling (dot-dashed) and FORT potential (dashed) are all shown. The transmission spectra in (b) for the atom trapped at the position corresponding to the line AA' is once again the symmetric eigenvalue structure. Furthermore, the eigenvalue splitting is the maximal value of $2g$, allowing for maximum "visibility" of a trapped atom in the cavity transmission.

7.2.3 FORT Laser Implementation

To complement this review of the FORT physics, a few words about the experimental implementation are in order. An external cavity diode laser (TUI Optics LD100) with a tunable range from 860 nm to 870 nm was employed to make the light for the FORT. The performance of this laser turned out to be very poor. For example, the current controller had approximately 20 dB more noise in a 100 kHz bandwidth than the typical low-noise design in our labs [149]. Furthermore, an improper choice of grating was made by the supplier such that the amount of light fed back from the external cavity was insufficient to properly stabilize the laser diode. In the end (see Sec. 8.1), only the diode itself remained after it was removed from the commercial mount and installed into a home-made structure. The entire FORT laser setup was installed initially on a breadboard in the corner of the lab because there was not much room left on the main table at this point.

The trapping light was split into two paths, with the first coupled into an external 15 cm long, finesse $\mathcal{F} = 2000$ Fabry-Perot cavity to monitor the day-to-day behavior of the laser diode. The second path went through a single pass AOM for intensity control of the light (fine frequency control was accomplished by moving the grating on the laser cavity) and was then coupled into an optical fiber. One drawback of the fiber was that it did not maintain polarization, so waveplates were installed and adjusted every day to keep the power constant. On the other hand, the fiber did an excellent job of cleaning the spatial mode of the laser diode to allow as high as 30% mode-matching of this light into the physics cavity.

The mirror transmission at 868 nm was roughly $T = 6.3$ ppm, which combined with the $A = 2.3$ ppm absorption loss per mirror to give a finesse $\mathcal{F} = 350,000$ at 868 nm. For example, with approximately 30% mode-matching, 30 μW incident on the cavity builds up to approximately 0.8 W of circulating intracavity power (for a FORT depth of $\Delta_{\mathrm{FORT}} = 45$ MHz). Of the 9 μW of mode-matched incident power, 5 μW is detected in transmission and 3.5 μW is absorbed in the substrates. This absorption can be a major problem for cavity locking due to thermal bistability (the tendency

of the power buildup to cause a frequency shift due to the temperature-dependent length change) of the cavity. The initial locking strategy was to use yet another Pound-Drever-Hall style lock in transmission through the physics cavity. Once the physics cavity was locked to the locking diode laser, the error signal for this lock was integrated once again and fed back to the thick PZT on the cavity in the hopes of providing even more DC gain to compensate for possible thermal effects due to the absorption of the FORT light. This strategy turned out to work quite well, as long as the cavity servo gain was kept as high as possible. This physical effect of substrate heating tended to limit the maximum FORT depth to about 150 MHz in practice, though technical improvements might well make 1 GHz potentials realistic. As a 150 MHz well depth already corresponds to a temperature of 7 mK, this was considered to be completely adequate for our initial work. The last several months (winter, spring 1999/2000) have been devoted to improvements over this initial implementation of the FORT system, and the reasons for this will be explained in Sec. 8.1.

7.2.4 Atom Transits in the Presence of the FORT

As a step toward *in situ* monitoring of an atom within the FORT, Fig. 7.22 presents observations of the transmission of a cavity QED probe field in the presence of the FORT trapping potential for single atom transits. The transit time for these events ranges from $T = 1.3$ ms (close to the longest upgoing transit ever recorded without the FORT) to $T = 11.2$ ms for the remarkable 'transit' in Fig. 7.22(g) observed in real time. The latter event corresponds to a transit velocity $\bar{v} \equiv 2w_0/T \approx 4$ mm/s and associated kinetic energy $\frac{1}{2}m\bar{v}^2 \sim h\nu_{tr}^{\mathrm{radial}} \ll h\nu_{tr}^{\mathrm{axial}}$. A summary of the different FORT, probe and cavity parameters used for these transits is summarized in Table 7.3.

The experimental procedure here was to apply the usual cooling protocol outlined above. Under the assumption that the cooling occurs outside the mode volume, the FORT was left on all the time. This also facilitated the cavity locking protocol, which was still being worked out at the time due to the thermal problems mentioned
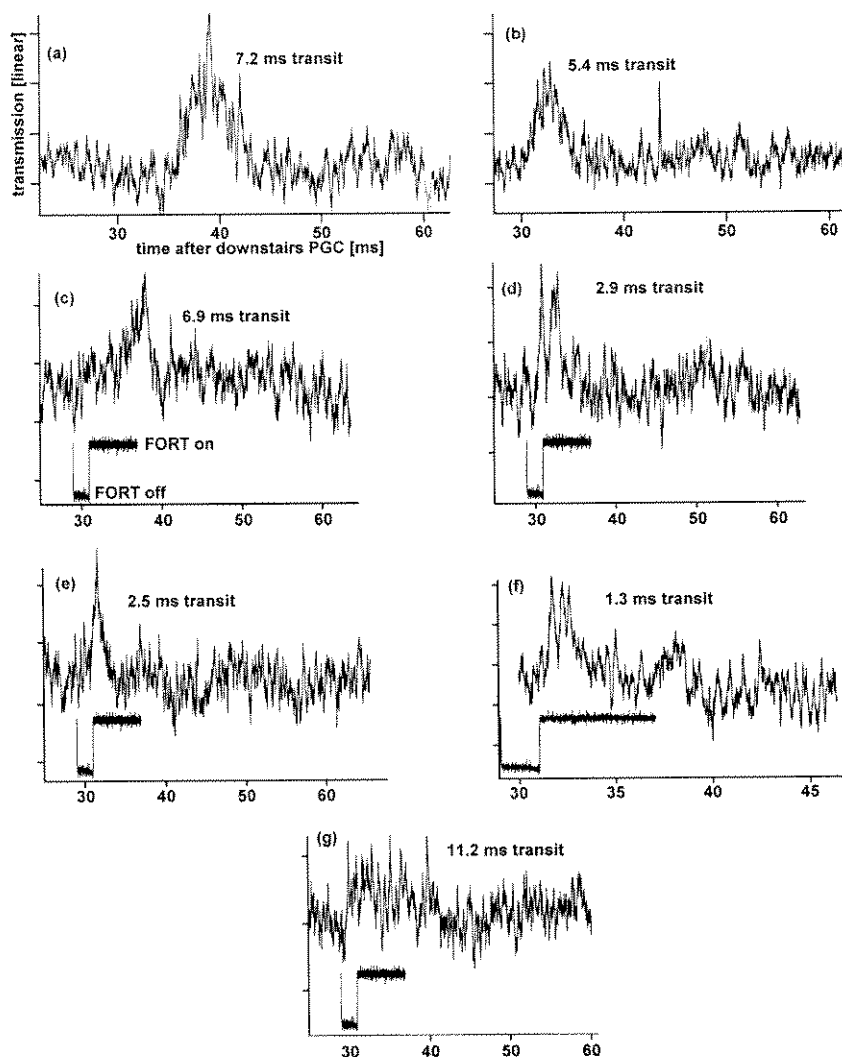
Figure 7.22: Seven transit events recorded with the FORT potential on are shown, and the parameters for these trapped atoms are shown in Table 7.3.

Fig. 7.22	transit time	δ_{ca}	δ_{pa}	FORT depth
(a)	7.2 ms	15 MHz	-10 MHz	30 MHz
(b)	5.4 ms	15 MHz	-10 MHz	30 MHz
(c)	6.9 ms	10 MHz	-10 MHz	45 MHz
(d)	2.9 ms	10 MHz	-10 MHz	45 MHz
(e)	2.5 ms	10 MHz	-10 MHz	50 MHz
(f)	1.3 ms	10 MHz	-10 MHz	30 MHz
(g)	11.2 ms	10 MHz	-10 MHz	40 MHz

Table 7.3: A comparison of the cooling parameters for the upgoing transits in the presence of the FORT.

above. The detunings $\delta_{\text{pa}} \sim -10$ MHz and $\delta_{\text{ca}} \sim +10$ MHz were chosen to enhance observation of a trapped atom via the composite eigenvalue structure associated with $g(\mathbf{r})$ and $\Delta_{\text{FORT}}(\mathbf{r})$, and typical intracavity photon numbers for these data were $\bar{n} \sim 0.5$. It is also expected that cavity-assisted Sisyphus cooling [168] should be effective in this setting. One can see from the eigenvalue spectra of Fig. 7.23, which has been calculated for $\delta_{\text{ca}} = +10$ MHz in presence of $\Delta_{\text{FORT}} = 30$ MHz, that it should be possible to see upgoing transits with reasonable contrast when red detuned from the bare atomic resonance by approximately $\delta_{\text{pa}} = -10$ MHz. The strategy with $\delta_{\text{ca}} \neq 0$ was chosen here (c.f., Fig. 7.20 with $\delta_{\text{ca}} = 0$) to try also to maximize the contrast for upgoing transits.
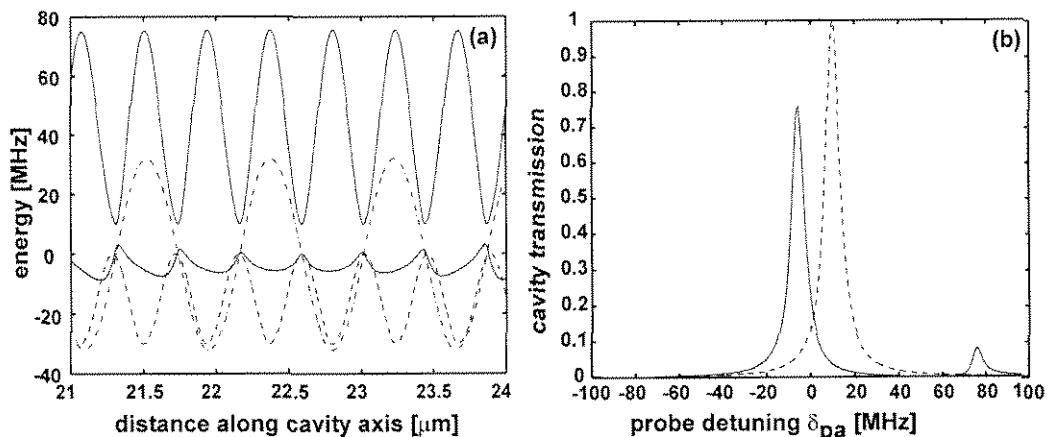
Figure 7.23: The eigenvalue spectra and cavity transmission show that the use of δ_{ca} $= +10$ MHz in the presence of $\Delta_{\text{FORT}} = 30$ MHz can be used to improve the contrast between the "empty cavity" and "atom-present" cases. In (a), the eigenvalues are solid, $g(\mathbf{r})$ is dot-dashed and $\Delta_{\text{FORT}}(\mathbf{r})$ is dashed. Note that the empty cavity sits 10 MHz blue of $\delta_{\text{pa}} = 0$ in (c) (which is the definition of $\delta_{\text{ca}} = +10$ MHz). This technique was used for the data of Fig. 7.22 where the probing was done with $\delta_{\text{pa}} \sim -10$ MHz to see upgoing transits.

Stated in units of the coupling parameter g_0 (where $2g_0$ is the single-photon Rabi frequency), a 10 ms long transit now achieves $g_0 T \simeq 10^6 \pi$, whereas prior experiments with cold atoms have attained $g_0 T \simeq 10^4 \pi$ [64, 135, 36, 136, 138] and experiments with conventional atomic beams have $g_0 T \simeq \pi$ [124, 125, 24, 126, 17], with T as the atomic transit time through the cavity mode. The above work is presented as

evidence that the FORT was working, and the next order of business was to try to get an indication of the FORT lifetime.

7.2.5 FORT Triggering with Single Atoms: Trapped Atoms

In order to maximize the probability that an atom is loaded into the trap, significant emphasis was placed upon using atom transits to trigger the FORT on and off. The fact that an atom transit is detected with good contrast in the absence of a FORT implies it is already in the mode volume, which increases its chances of being captured by the turn-on of the FORT. Furthermore, such a protocol would help rule out the possibility of loading multiple atoms.

An updated timing diagram for the switching of the various fields is given in Fig. 7.24. The basic idea is that the FORT was left on as long as possible, and only turned off when it was necessary to detect atoms inside the cavity mode volume for capturing or for verification that they remained trapped. The reason is because the FORT lock to the physics cavity uses the FORT transmission through the cavity. If there is no error signal provided to the servo for too long (in practice, about 5 ms), then the FORT will come unlocked, which most likely will cause the cavity itself to come unlocked and necessitate re-locking the whole experiment.

To solve this problem, a "window" or "gating period" was defined within which the atom needed to be detected in order to trigger the FORT on; otherwise, the FORT would turn back on of its own accord after a few ms of "dead-time." It was also possible to set the trigger threshold to discriminate against atoms detected at a place where the cavity QED coupling $g(z)$ was weak. It was felt that even though these may very easily get trapped in a large FORT (mechanical forces due to $\Delta_{FORT}(z)$ overwhelm anything due to $g(z)$), it would be hard to re-detect their presence when the FORT was turned off. Hence, an ideal event would be one with large $g(z)$ (so that the atom can be seen) sitting near a minima of $\Delta_{FORT}(z)$ (so that it is trapped). To reiterate, this most likely occurs at the geometric center of the cavity.

Once a "good" atom was detected, a trigger pulse ramped up the intensity in ~ 200

μs on the FORT laser AOM. The waveform of this turn-on edge was programmable (with an analog function generator, Stanford DS345) and was a compromise between turning the light on too quickly and kicking the atom out of the trap versus having the atom drift out of the mode volume during a slow turn-on period. Furthermore, the servo response was intimately coupled to how this waveform behaved, and too "hard" a turn on would often cause significant ringing.
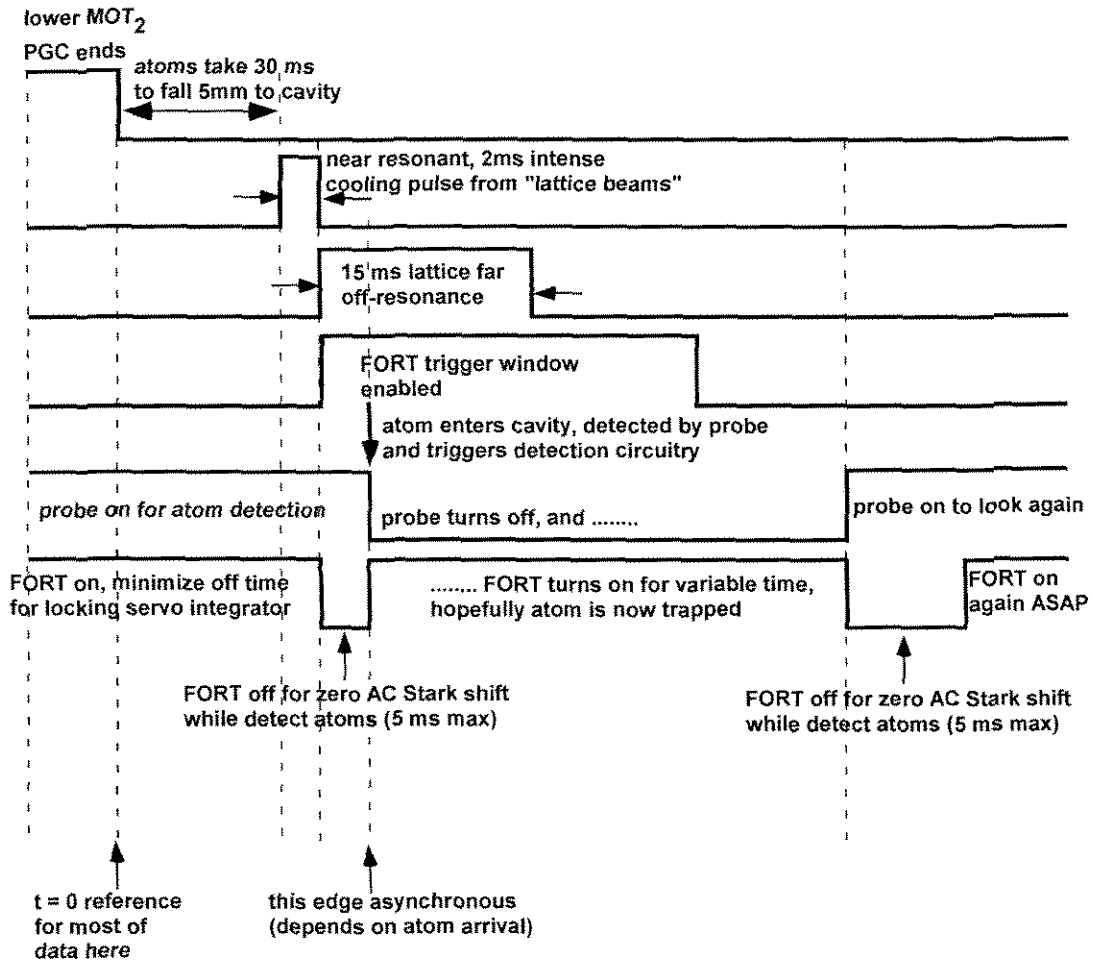

Figure 7.24: The timing diagram of Fig. 6.13 is updated here to include the edges needed to trigger the FORT light and the probe due to the presence of a single atom inside the cavity.

An example of FORT triggering by a single atom and subsequent trapping of that atom is shown in Fig. 7.26. The arrival of an atom is sensed by a reduction

in transmission for the probe beam (of photon number $\bar{n} \approx 0.1$). The falling edge of the probe transmission triggers *on* the FORT field, which then remains *on* until being switched *off* after a fixed interval. The presence of the atom at this second *off* time is likewise detected by modification of the probe transmission, demonstrating a trapping time of 29 ms for the particular event shown in the figure. Note that because the probabilities for atom trapping given a trigger $p_{tp|tg}$ and for detection given a trapped atom $p_{d|tp}$ are rather small ($p_{tp|tg}p_{d|tp} \sim 0.03$), we operate at rather high densities of cold atoms, such that the average atom number present in the cavity mode at the time of the trigger is $\bar{N}_{\text{atom}} \sim 0.5$ (but which then falls off rapidly with time). A series of "snapshots" of atom transit signatures around the time of trigger are shown in Fig. 7.25 to aid in determining $\bar{N}_{\text{atom}}$.

As a consequence, the atom that causes the trigger is not always the atom that is actually trapped when the FORT is gated *on*, with such 'phantom' events estimated to occur in roughly 1 of 4 cases. To aid in reducing this number, the cooling pulse (timing shown as an inset to the figure) is delayed to the far edge of the "transit envelope" compared to the work of Fig. 7.9. The near-resonant cooling had a 1.5 ms duration from $t = 33$ ms to $t = 34.5$ ms and the far off-resonant sub-Doppler pulse went another 1.5 ms from $t = 34.5$ to $t = 36$ ms, at which point the trigger window was enabled.

Two more examples of FORT triggering and trapping of single atoms are shown in Figs. 7.27(a),(b). In (a), the atoms are again detected as downgoing transits with a resonant probe. Note that although the probe field is left on for all times in Fig. 7.27(a), there is no apparent change in cavity transmission during the interval in which an atom is purportedly trapped within the cavity mode. The absence of atomic signatures during the trapping time, but not before or after, is due to AC-Stark shifts associated with the FORT and/or the mismatched antinodes between $(\nu_{\text{FORT}}, \nu_{\text{cavity}})$. In (b), an off-resonant probe is used to detect upgoing transits in the hopes of imparting less heating to the atoms during the detection period and thus maximizing the chances of the atoms actually being captured by the FORT. Furthermore, the probe here is once again triggered *off* for a significant fraction of
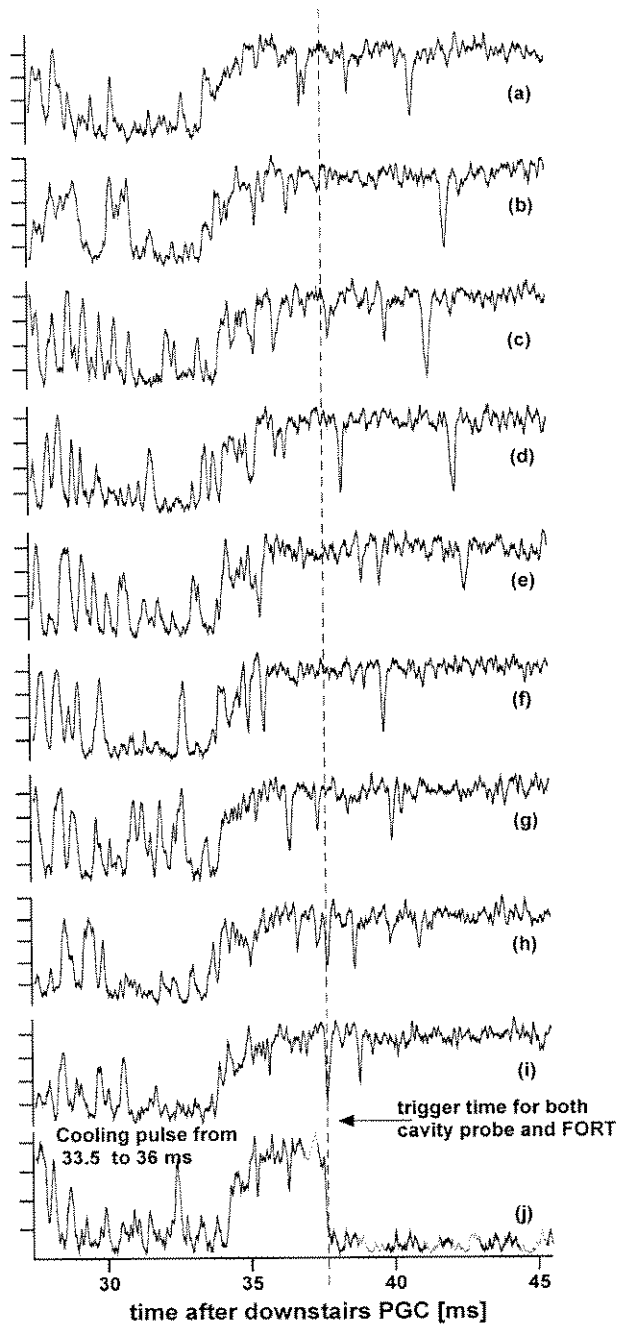
Figure 7.25: In order to determine the probability that an atom inside the cavity will be trapped by the FORT on any given drop cycle of the MOT, this data was used to determine the average atom number $\bar{N}_{\text{atom}} \sim 0.5$ in the cavity mode at the time the trigger was enabled. The dashed line indicates the beginning of the "FORT trigger enable" window of Fig. 7.24.
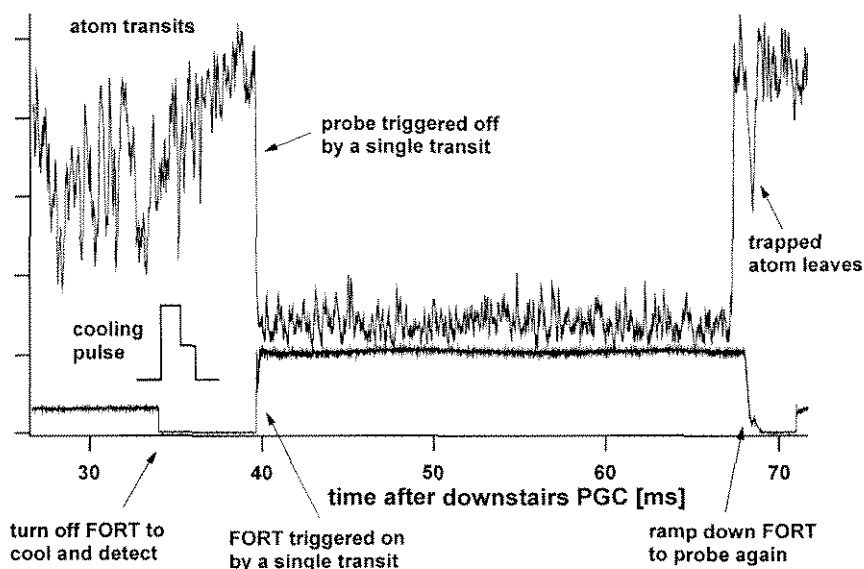
Figure 7.26: Single atom transits were used to simultaneously trigger *on* the FORT and trigger *off* the probe beam, in order that the atom not be accidentally heated by the probe while it is trapped. This atom was trapped for 29 ms.

the FORT *on* time, but typically neither of these changes (off-resonant detection, probe switched *off*) seem to make much of a difference.

7.2.6   FORT Lifetime Measurement

To avoid questions related to the complexity of the eigenvalue structure of Figs. 7.18 - 7.21 as well as to possible heating or cooling by the probe field, we returned to the situation of Fig. 7.26 to synchronously gate *off* the probe field $\mathcal{E}_{\mathrm{probe}}$ for measurements of trap lifetime, with the result displayed in Fig. 7.28. These data were acquired for repeated trials as in Fig. 7.26 (namely, with the presence of an atom used to trigger *on* the FORT now of depth $\Delta_{\mathrm{FORT}} = -50$ MHz and *off* the probe field). At the end of the trapping interval, $\mathcal{E}_{\mathrm{probe}}$ was gated back *on* and the success (or failure) of atomic detection was both recorded by an electronic counter and verified manually due to the long experimental duty cycle (2 s) and low trapping probability ($< 1\%$). The lifetime for single atoms trapped within the FORT using this triggering mechanism was thereby determined to be $\tau_{\mathrm{FORT}} = (28\pm6)$ ms, using a fit to the decay of recorded
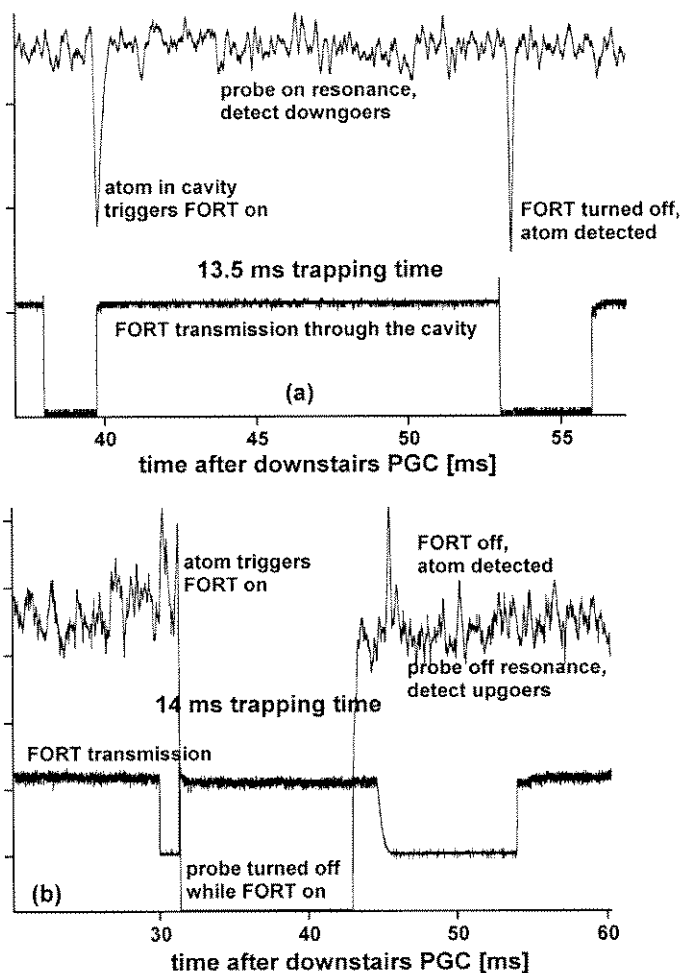
Figure 7.27: In (a), a technique similar to Fig. 7.26 was used to detect and trap a single atom, but the probe beam was not switched off during the FORT detection period. In the limit of a large FORT, there should be minimal heating from this. In (b), upgoing atom transits were used to trigger the FORT on and off, in the hopes that the upgoing atoms might be a little colder before being loaded into the trap. In both cases here, the atom was trapped for about 14 ms.

events.
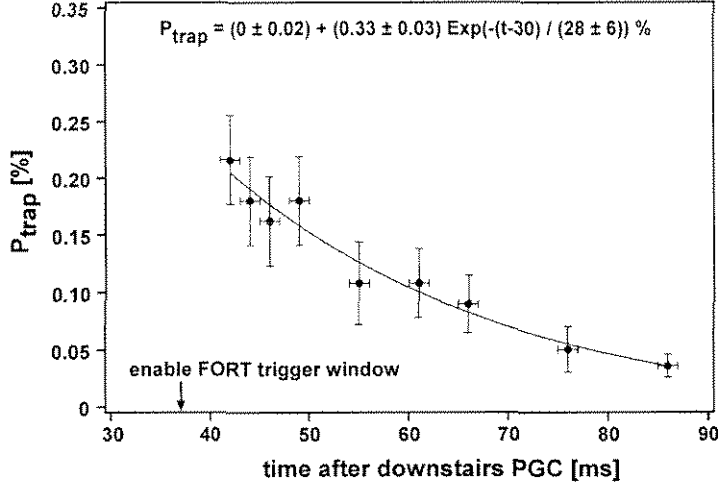
Figure 7.28: The probability that an atom remained trapped in the FORT as a function of time after the end of the downstairs PGC cycle. The beginning of the "FORT trigger enable" pulse of Fig. 7.24 is shown for reference. For this data, the FORT was triggered *on* by the presence of a single atom, and the probe field triggered *off*. This allows the determination of a trap lifetime close to 28 ms. Background counts have been subtracted from this data as will be explained in Fig. 7.29.

Note that at each of the time delays in Fig. 7.28, a subtraction of "background" events (atomic transits delayed by the intracavity cooling beams) has been made from the set of total detected events, with a record of these background events shown in Fig. 7.29. This background was determined by way of measurements following the same protocol as in Fig. 7.26, but without the FORT beam. For times $t < 49$ ms, the background dominates the signal by roughly 50 fold, precluding an accurate measurement of trapped events. However, because it has a rapid decay time ~ 3 ms, for times greater than about 52 ms it makes a negligible contribution.

This trap lifetime was confirmed in an independent experiment where the FORT is turned on and off at predetermined times without transit-triggering or probe triggering, yielding $\tau'_{\text{FORT}} = (27 \pm 6)$ ms as shown in Fig. 7.30. As mentioned in the discussion of Fig. 7.26, our ability to load the trap with reasonable efficiency via asynchronous turn-on is due to operation with large $\bar{N}_{\text{atom}}$. It is interesting to note one big difference between the data of Figs. 7.29 and 7.30, namely that the background
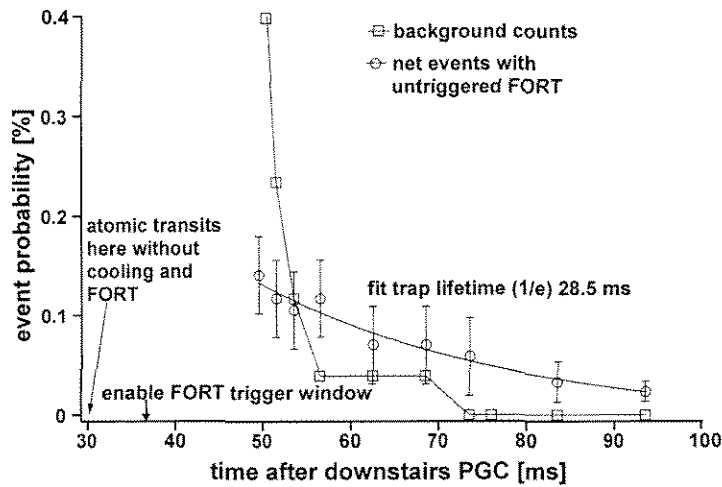
Figure 7.29: At times $t < 49$ ms for the data of Fig. 7.28, there are far too many residual atoms falling through the mode left over from the original MOT drop, which does not allow an accurate determination of the FORT lifetime at short times. However, this background falls extremely rapidly to very close to zero counts by 70 ms. Subtracting these background counts for times greater than about $t = 49$ ms allows a determination of the FORT time constant.

counts showed a very similar fast decay, but with the decay occurring at different points in time offset $\Delta t \sim 3$ ms along the time axis. In the case where the probe was not triggered off (Fig. 7.30), the background atoms decayed earlier (at ~ 49 ms). This was presumably due to the fact that the atoms interacted with the resonant probe (left on in the absence of a FORT) and its concomitant mechanical potential of Fig.7.11 (c), with the result that they left the mode volume more quickly. Note that the probe field was not triggered during the background measurement of Fig. 7.30 so that this background was determined in a consistent fashion to the way the trapped atoms were measured with the FORT on.

Using the data of Fig. 7.30, an indication of how the background behaved for much earlier times is presented in Fig. 7.31 to substantiate the claim made above that the background was too overwhelming to make reasonable measurements of the trapping probability at earlier times. The extremely large number of background events at these times are presumably due to residual atoms from the dropped MOT "envelope" of atoms (see the time history of atom transits for a single drop of the downstairs
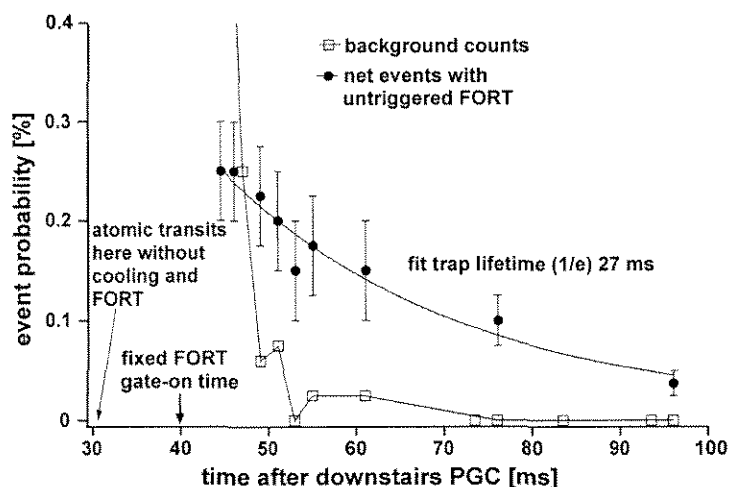
Figure 7.30: The FORT lifetime of Fig. 7.28 was independently verified in a separate experiment in which the FORT was not triggered by the presence of a single atom, but was gated on at the fixed time indicated. The resonant probe beam was also left on for this experiment. Here, a fit reveals a lifetime of about 27 ms. The background counts associated with this measurement are also shown.

MOT, albeit with an extremely large atom number, in Fig. 7.4(c)). Finally, care was taken to check the number of events seen when the atom source was blocked to rule out any other spurious signal source. This measurement always produced zero counts independent of time.

7.2.7   Limits to Trap Lifetime

An examination of possible limitations to the trap lifetime of 28 ms shows there are several candidates. As was estimated earlier [Eq. (6.1)], the trap lifetime set by background gas collisions at a pressure of 10^{-10} Torr is estimated to be ~ 100 s, which is certainly much longer than that actually observed.

The calculation of Fig. 7.16 shows that for a 75 MHz deep FORT, the spontaneous photon scattering rate is $\Gamma_{\text{scatt}} \sim 300$ s^{-1} which means it will be ~ 200 s^{-1} for the 50 MHz deep FORTs used here. This effective scattering rate can cause heating of the atomic motion in two ways. First, there is momentum diffusion due to the random direction of the spontaneously emitted photons (and hence randomly-directed recoil
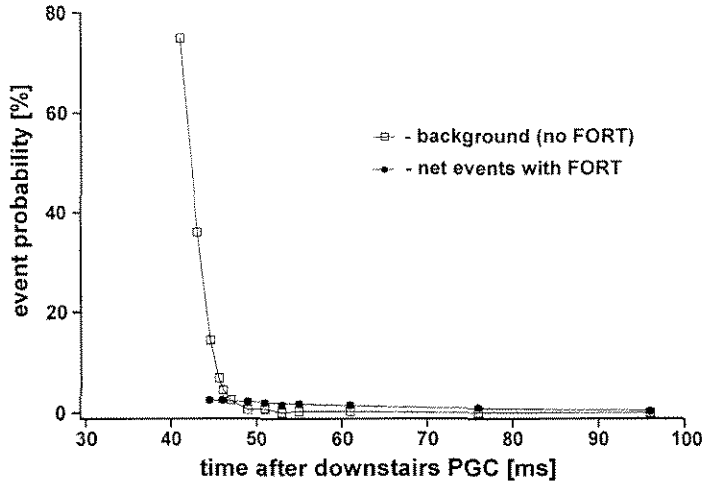
Figure 7.31: To complete the discussion of the FORT lifetime measurement, the sharp increase of the background counts for very short times associated with residual atoms from the falling MOT is shown for the measurement of Fig. 7.30.

kick) during the scattering cycle. The second component is due to fluctuations in the dipole force, which can be understood from the fact that for a two-level atom in a red-detuned FORT, the excited state sees a repulsive force. Repeated scattering cycles through the excited state tend to heat the atom due to the fact that the net force it feels fluctuates on this scattering time-scale between attractive and repulsive. As indicated in Eq. (7.16), both of these forces are spatially dependent because $\Gamma_{\text{scatt}}(\mathbf{r}) \propto I(\mathbf{r})$, with the spontaneous heating maximal at FORT field antinodes (where the light is maximal), and the dipole force fluctuations maximal at FORT field nodes. Cohen-Tannoudji has shown [164] that the *sum* of these two heating rates is actually spatially *independent* in a standing-wave FORT, and that the *maximum* value is the same for each of these contributions.

The combined effect of these heating rates on the atomic energy can be quickly estimated as follows. Each scattering process will heat the atom by approximately $2T_R = 200$ nK (remember, $k_B T_R = \hbar^2 k^2/2m$), so that the rate of change of atomic energy should obey

$$\dot{E} = 2k_B T_R \Gamma_{\text{scatt}}. \tag{7.30}$$

The atom will leave the trap when $E \sim \hbar\Delta_{\mathrm{FORT}}$ in time

$$\tau_{\mathrm{heat}} \sim \frac{\hbar\Delta_{\mathrm{FORT}}}{2k_B T_R \Gamma_{\mathrm{scatt}}} \sim \frac{\hbar\Delta}{2k_B T_R \Gamma}, \tag{7.31}$$

where the last equivalency comes from the general relation $\Gamma_{\mathrm{scatt}} \sim \Delta_{\mathrm{FORT}}\,(\Gamma/\Delta)$ for a detuning Δ of the FORT field from the excited state of width Γ, and shows the heating time is generally independent of FORT depth. The linear heating rate only works in the limit of $\hbar\Delta_{\mathrm{FORT}} \gg k_B T$, which is satisfied for the 2.5 mK deep FORT versus the initial atomic temperature of about 30 μK. In the case of our 868 nm FORT, the result is $\tau_{\mathrm{heat}} \sim 50$ s, which is ~ 200 times the observed τ_{FORT} and cannot explain the observations.

There is yet another heating mechanism which arises from fluctuations in the FORT potential. Two possible causes are variations in the spatial position of the potential well or time-dependent fluctuations in the depth of the potential. Even though the cavity length is servoed, there is no mechanism to determine (and stabilize) the overall position of the cavity with respect to a fixed point in space. However, the frequency content of this motion is expected to be mid- to sub-acoustic due to passive vibration isolation, so the former possible root cause of heating is all but ruled out. However, according to Eq. (7.16), $\Delta_{\mathrm{FORT}} \propto I(\mathbf{r})$ so that laser intensity noise can drive mean-square force fluctuations because the atom will see a time-dependent potential. In a harmonic trap, this mean square force is proportional to the energy, which means the heating rate will be proportional to the energy. Furthermore, x^2 perturbations will drive transitions between vibrational levels $|n\rangle$ and $|n \pm 2\rangle$, which makes the spectral density of fluctuations at twice the trap vibrational frequency $2\nu_{tr}$ the important quantity. These ideas are discussed in Ref. [165] and can be summarized by the following two equations for the heating rate $\dot{E}$ and time constant τ_e respectively,

$$\dot{E} = E/\tau_e \tag{7.32}$$
$$\tau_e^{-1} = \pi^2 \nu_{tr}^2 S_e(2\nu_{tr}).$$

Here ν_{tr} is the trap oscillation frequency (in Hz) and $S_e(2\nu_{tr}^{\text{axial}})$ is one sided power spectral density (PSD) of *fractional* intensity noise evaluated at frequency $2\nu_{tr}$ (in units of 1/Hz).

It should be noted that Eqs. (7.32) do not necessarily faithfully describe the details of the heating process [166]. The fluctuations of an initial distribution of trap levels $\{|n\rangle\}$ can grow very rapidly due to the $|n\rangle \rightarrow |n \pm 2\rangle$ heating process, such that the upper part of the distribution (and not the mean) is responsible for heating out of the trap. Nevertheless, τ_e gives a reasonable estimate for the timescale of this process.

For example, using Eq. 7.21, a modest FORT well depth of 1 mK ($\delta_{\text{FORT}} = 25$ MHz) will correspond to trap frequencies $\left(\nu_{tr}^{\text{axial}}, \nu_{tr}^{\text{radial}}\right) \sim (5, 450)$ kHz. This makes it clear that intensity noise on the intracavity light out at 900 kHz and beyond can have a devastating effect on the FORT. Direct measurements of the spectral density of photocurrent fluctuations for the FORT beam emerging from the cavity (calibrated by coherent AM at the requisite frequency $2\nu_{tr}^{\text{axial}} = 900$ kHz) lead to $\left(S_e(2\nu_{tr}^{\text{radial}}), S_e(2\nu_{tr}^{\text{axial}})\right) \approx (5 \times 10^{-9}, 2.3 \times 10^{-11})/\text{Hz}$, so that $\left(\tau_e^{\text{radial}}, \tau_e^{\text{axial}}\right) \approx (830, 23)$ ms. An example of such a measurement at 600 kHz (for a FORT depth of $\delta_{\text{FORT}} = 20$ MHz) is shown in Fig. 7.32. Fig. 7.32(a) shows transmission of resonant FORT light through the cavity, with $\sigma_{\text{AM,rms}} = 1.9$ % coherent AM purposely put on the TUI diode laser using an AOM at 600 kHz to calibrate the noise power spectrum. In (b), it is clear this peak shows up far above the light noise floor by a factor $G = 45$ dB in a $B = 300$ Hz rf bandwidth, with the electronic noise floor visible to prove that the measurement was light-noise limited. Using this, the PSD at $2\nu_{tr}^{\text{axial}}$ can be calculated as

$$S_e(2\nu_{tr}^{\text{axial}}) = \frac{\sigma_{\text{AM,rms}}^2}{B \times 10^{G/10}} = 3.8 \times 10^{-11}/\text{Hz}, \qquad (7.33)$$

which results in $\tau_e^{\text{axial}} = 24$ ms for this measurement. This number might be expected to be somewhat independent of frequency if a presumed single-time-constant 20 dB/decade roll-off in $S_e(2\nu_{tr})$ cancels the ν_{tr}^2 dependence in (7.32).

The heating rate for $1/\tau_e^{\text{axial}}$ in both of these measurements is in reasonable agree-

ment with the observed $(1/e)$ trap decay rate $1/\tau_{\mathrm{FORT}} \simeq 1/28$ ms, leading to the conclusion that fluctuations in intracavity intensity drive heating along the cavity axis and are the limiting factor in this work. Such fluctuations are exacerbated by the conversion of FM to AM noise of the FORT laser due to the high cavity finesse at the wavelength of the FORT (here, $\mathcal{F}_{\mathrm{FORT}} = 3.5 \times 10^5$). This conversion process, along with recent attempts to eliminate it, are the subject of current intensive work and will be covered in Sec. 8.1.
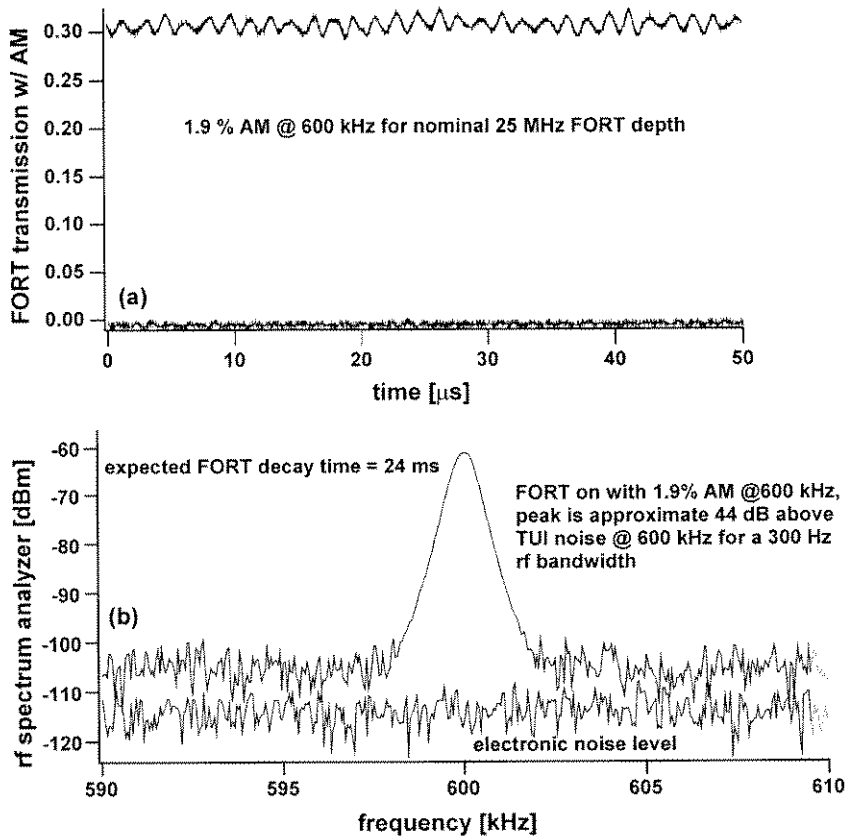

Figure 7.32: The power spectral density (PSD) of fractional intensity fluctuations $S_e(2\nu_{tr}^{\mathrm{axial}})$ was measured by correlating the time domain output (a) of the cavity with its frequency spectrum (b) after ensuring the measurement was limited by light noise. The 1.9% coherent amplitude modulation was used to calibrate the noise level.

7.2.8 Blue FORT attempt

One final thing worth mentioning is an attempt that was made to put a blue-detuned FORT inside the cavity. The fact that the locking diode laser sits two mode orders *above* the atomic resonance makes it a candidate, but in this case the blue detuning will repel atoms from the areas of maximal intensity. The zeros of this field at $z = L/4$ and $z = 3L/4$ coincide with the maximum of the probe cavity QED field, and these are the locations at which we might expect to "see" trapped atoms. Unfortunately, there is no mechanism for confinement in the transverse direction and the implementation of this FORT did not lead anywhere, even though "wall" depths of ~ 50 MHz were easy to make. However, this does bring up the related question of the possible harmful effects of the locking field itself. In order to answer this question, a quick estimate of the AC Stark shift (FORT shift) can be based on Fig. 7.15. This shows that the blue AC Stark shift for 10 μW of circularly polarized light (transmitted through the cavity) at 835 nm is approximately 40 MHz, so that the ~ 5 nW used for locking should produce a (presumably negligible) 20 kHz shift. To verify this experimentally, the locking error signal was monitored for evidence of an effect due to atom transits. In Fig. 7.33, 250 trap drops were averaged along with the locking error signal, and no noticeable effect due to the atomic transits can be seen on this signal.
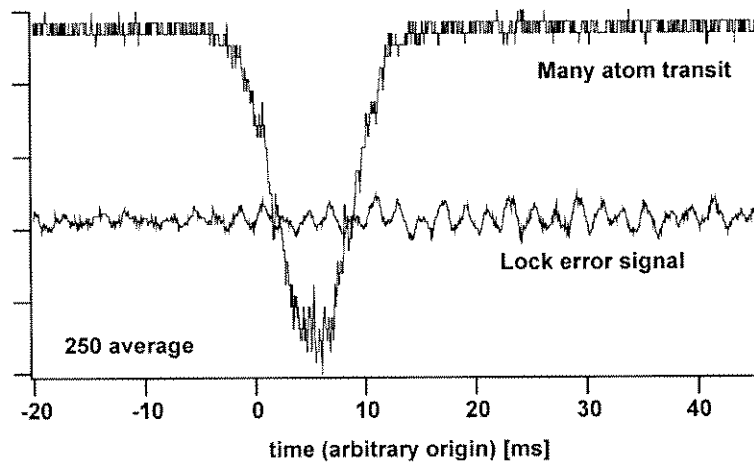
Figure 7.33: The error signal of the cavity lock is averaged along with about 100 atom transit drop records to verify that the intracavity locking beam has no noticeable mechanical effect on the atoms. The 500 Hz oscillation in the error signal here can presumably be blamed upon too much gain in the cavity locking servo.

Chapter 8 Next Steps

At the outset of Part III, it was mentioned that the localization of single atoms inside a high finesse resonator is expected to become an *initial condition* for a set of future experiments. One primary scientific goal here is to achieve atomic confinement in the Lamb-Dicke regime, meaning that the cold atomic wavepacket is localized to much less than an optical wavelength (i.e., $\eta_x \equiv 2\pi\Delta x/\lambda \ll 1$), or equivalently, that the energy associated with a recoil kick is much less than the trap vibrational spacing ($\omega_{\mathrm{rec}}/2\pi \ll \nu_{tr}^{\mathrm{axial}}$). Furthermore, it is desirable to achieve this in a setting for which the trapping potential for the atomic center-of-mass motion is independent of internal atomic state (see Sec. 8.4), as has been so powerfully exploited with trapped ions [176]. Once the heating problem (Sec. 8.1) is completely understood, this looks like a very promising future avenue as it would provide a nice experimental confirmation of the well-dressed state structure of Part II.

To further drive home the point about the "enabling" aspect of trapped atoms in high finesse cavities, I would like present in this final chapter a sampling of ongoing experimental work and possible future directions for the experiment. It is indeed very exciting to have been a part of this effort because I think the "era" covered in this thesis (along with the parallel work of Christina and Theresa and the Garching group of Gerhard Rempe) represents a whole new shift in paradigm for optical cavity QED work where the atomic motion and c.m. degrees of freedom begin to take center-stage.

8.1 Elimination of the Diode Laser Noise

With the identification of intensity noise on the intracavity trapping light as the major limitation to the FORT lifetime, a program was undertaken to identify and eliminate the source of this noise. Contrary to original hopes that the solution to this problem would be a minor footnote to this thesis, this learning process has occupied the better

part of 7 months and has led to some rather surprising results, which will be briefly outlined below. With the experiment itself beginning to get rather unwieldy, there has been a major division of labor to try to solve this problem. The experimental results of this section are mainly due to the work of Christoph Nagerl and myself, while Jeff has made tremendous theoretical contributions to build on some earlier theoretical and experimental work he had done on this problem [170].

Measurements of the sort presented in Fig. 7.32 suggest that the noise spectral density at $2\nu_{tr}^{\text{axial}}$ needs to come down by about 2 orders of magnitude to about 3.8×10^{-13} /Hz in order to achieve the ~ 1 s trap lifetimes envisioned at the outset of this effort 2 years ago. In order to examine whether this is even possible *in principle,* among the first measurements made were those of the intensity noise of the grating stabilized, free-running laser. As is well known, a free running diode is quiet in its amplitude quadrature [171], which was borne out in experiment showing $S_e(2\nu_{tr}^{\text{axial}}) \sim 5 \times 10^{-14}$ /Hz to 1×10^{-13} /Hz as measured at the output of the locking diode laser. This level was pretty much independent of whether the laser was locked to the transfer cavity. There is no way that this fractional intensity noise can be directly increased by the linear transfer function of the physics cavity, so alternative amplitude noise sources were investigated. Candidates included the optical fiber which brought the trapping light over to the optical table from the breadboard on which the FORT laser was originally mounted and the rf oscillators driving the AOM used to control the intensity. However, both were ruled out on the basis of the high frequencies (well above acoustic) and huge increases (3 orders of magnitude!) of the PSD involved here, and measurements indicated neither was the culprit.

The Lorentzian profile of the cavity resonance can also act as a discriminator for the conversion of frequency noise to intensity noise and diode laser phase noise was considered as the next possibility. A significant effort was placed on the improvement of the cavity-locking servo to reduce any offsets which might be causing the laser to be locked off of line center, but this did not have a huge impact due to the rather large 10 MHz width of the physics cavity. A really big breakthrough came when a calculation showed that the conversion process of FM to AM can be quite different depending

on whether one thinks in terms of coherent or incoherent modulation. For example, the Pound-Drever-Hall locking mechanism is an example of the case where coherent phase modulation at a frequency ν will produce no amplitude modulation on line center at the frequency ν, but tends to produce modulation at twice this frequency, 2ν. This leads to the notion that the only conversion process at $2\nu_{tr}^{\text{axial}} \sim 900$ kHz could be due to $\nu_{tr}^{\text{axial}} \sim 450$ kHz noise. Naively, one would guess that the noise in a small bandwidth around 450 kHz is not enough to explain the huge noise increase.

However, considering instead the impact of broadband incoherent frequency fluctuations with a PSD $\psi(\nu)$, the PSD of fluctuations in the detected photocurrent $\Phi(\nu)$ can be calculated. This is directly related to the PSD $S_e(\nu)$ because the light intensity is directly converted into a photocurrent with, of course, some finite efficiency. When locked to the side of the cavity at $\nu_{\text{lock}} - \nu_{\text{cavity}} = \kappa/2\pi$, then

$$\Phi(\nu) \sim \psi(\nu), \tag{8.1}$$

which is simply the FM to AM conversion discriminator action of the cavity slope. However, on the line center of the cavity resonance ($\nu_{\text{lock}} = \nu_{\text{cavity}}$),

$$\Phi(\nu) \sim \int d\nu' \psi(\nu - \nu') \psi(\nu'), \tag{8.2}$$

which predicts that $S_e(\nu)$ is proportional to the *convolution* of $\psi(\nu)$. This illustrates that it is not just the noise component at ν_{tr}^{axial} which affects the noise at $2\nu_{tr}^{\text{axial}}$ on line center (as the simple coherent modulation model suggested), but roughly *all* frequency components which sum to $2\nu_{tr}^{\text{axial}}$ within the 4 MHz cavity bandwidth must be included.

However, this immediately suggests a solution: If the original PSD of frequency fluctuations can be significantly narrowed, then the fractional intensity noise should be reduced. A test set-up by Christoph Nagerl in one of the other labs showed conclusively that initial filtering of the frequency noise spectrum by using the light transmitted through a narrow (~ 20 kHz wide) filter cavity did tend to reduce the

fractional intensity noise at the output of a wider cavity which followed. In fact, the typical suppression level was close to two orders of magnitude at 900 kHz.

This technique was recently implemented into the FORT diode laser path, as shown in Fig. 8.1. The optical fibre was also eliminated by moving the whole set-up to a breadboard above the main table, and major improvements were made to the grating-stabilized FORT laser mount (the commercial TUI housing was completely discarded and now only the original 860 nm diode chip remains of that investment). With the filtering cavity in place, very recent measurements have shown the intensity noise transmitted through the physics cavity has improved from $S_e\left(2\nu_{tr}^{\mathrm{axial}}\right) = 2.3 \times 10^{-11}/\mathrm{Hz}$ to $S_e\left(2\nu_{tr}^{\mathrm{axial}}\right) = 4 \times 10^{-12}/\mathrm{Hz}$. In fact, trap lifetimes on the order of $\tau_e^{\mathrm{axial}} = 150$ ms should now be possible, with further improvements at the cost of more work on the cavity locking servos.

It should be noted that this method could *also* be used for the locking diode laser because the present set-up uses light to lock the physics cavity which has been split off *before* the transfer cavity. The benefit of continuing to use the locking laser to lock the cavity, as opposed to the alternative of using the FORT laser to both trap atoms and lock the cavity, is that it allows the flexibility to trigger the FORT light on and off and can also be used as an independent montor of the cavity frequency. The above work suggests the transmitted light of the locking laser through the transfer cavity could result in a much quieter lock of the physics cavity. However, "much quieter" may mean a somewhat complicated redistribution of the noise in frequency space, possibly leading to even more noise at the frequencies of interest. The re-arrangement of the locking diode laser beam path to accomplish this is somewhat less trivial, and another strategy has been successfully pursued very recently. An external frequency stabilization loop using a double passed AOM in the FORT laser path has been included to add bandwidth to the frequency stabilization servo. This has been tested using the Ti:Sapph laser whose residual amplitude fluctuations at $2\nu_{tr}^{\mathrm{axial}}$ have been characterized to be roughly equivalent to those of the free-running diode (albeit with frequency noise assumed to be much less). The measurement of $S_e\left(2\nu_{tr}^{\mathrm{axial}}\right) = 1 \times 10^{-12}/\mathrm{Hz}$ gives great hope that a similar procedure applied

to the FORT diode laser will eliminate the problem once and for all, without the need for major surgery of the locking diode laser servo. This technique basically forces the FORT laser to follow the cavity frequency on all time scales, such that the intracavity intensity remains constant. Fluctuations in frequency of the FORT laser, which is already far off-resonance from the atomic frequency by definition, are of little consequence.
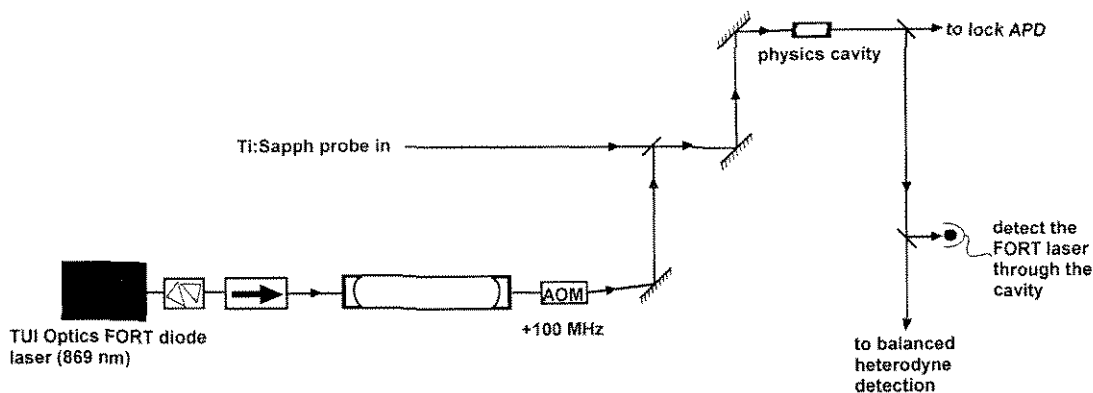
Figure 8.1: A very simple sketch of the new FORT laser set-up shows the addition of a "filter cavity" to cut down on the native frequency noise spectrum of the diode laser. As discussed in the text, this helped to eliminate some of the fractional intensity noise *of the intra-cavity light (and hence, the FORT potential) at twice the trap oscillation* frequency. Ultimately, the heating rate of the atoms due to this time-dependent potential should be reduced.

8.2 Resolved Sidebands

Given that the initial atomic c.m. temperature is expected to be $\sim 50~\mu$K, the c.m. level occupation will be thermally distributed via

$$\langle n_{\text{axial}} \rangle = \frac{1}{e^{\left(\hbar \omega_{tr}^{\text{axial}} / k_B T \right)} - 1} \tag{8.3}$$

with $\langle n_{\text{axial}} \rangle \lesssim 5$ for a 20 MHz deep FORT with an axial vibrational spacing of $\nu_{tr}^{\text{axial}} \sim$ 300 kHz = 14 μK. It therefore seems possible that evidence of these oscillations in the FORT potential well should be written onto the cavity transmission, as has been

seen in spectacular fashion recently for radial oscillations in the 1− photon potential work of Christina and Theresa [22].

Assuming that an atom undergoes oscillations about $z = z_0$ at a frequency ν (i.e., $z = z_0 \cos 2\pi\nu t$) with $g(z_0) = g_{max} = g_0$ then Eq. (7.7) predicts that with $\Delta_{pa} = -g_0$, the ratio R of the cavity transmission with an atom compared to that without (i.e., upgoing transits) will have the form

$$R = R_0 \left(1 - \frac{1}{2}k^2 z^2\right),$$ (8.4)

so that the oscillations will show up on the cavity transmission at a frequency 2ν. Because of Nyquist sampling limitations, a primary constraint is that the bandwidth of the detection system must be at least 4ν to see these oscillations, and typically much higher than this. For this reason, an attempt was made with rather shallow FORTs (about 15 MHz, with $\nu_{tr}^{axial} \sim 350$ kHz) to try to detect this peak in the Fourier spectrum of the transmitted cavity intensity.

For this work, a return to single atom triggering with upgoing transits was made, as shown by the remarkable (presumed) 17 ms single atom transit event in Fig. 8.2 in the presence of a 15 MHz FORT. An attempt was made here to "tune" Δ_{FORT}^{e} together with Δ_{ca} to produce regions within the cavity mode for which the spatially dependent level shift of a composite dressed state in the first excited manifold matched $\Delta_{FORT}^{g}(\mathbf{r})$ for the (trapping) ground state [174]. The cavity transmission as represented in the photocurrent was then digitized at a 5 MHz bandwidth and then Fourier analyzed, but no characteristic peak could be detected even after averaging the spectra of ~ 10 similarly long transits recorded with comparable FORT depths.

One possible reason for this could be insufficient initial cooling of the atomic motion, which again emphasizes the need to find and implement new cooling strategies. Another possible culprit is masking of the expected oscillation signal by the FORT laser intensity noise, whose PSD has been determined above already to be an order of magnitude higher than it need be (i.e., the filtering cavity has reduced $S_e(2\nu)$ by an order of magnitude) at frequencies comparable to those expected for the oscillation
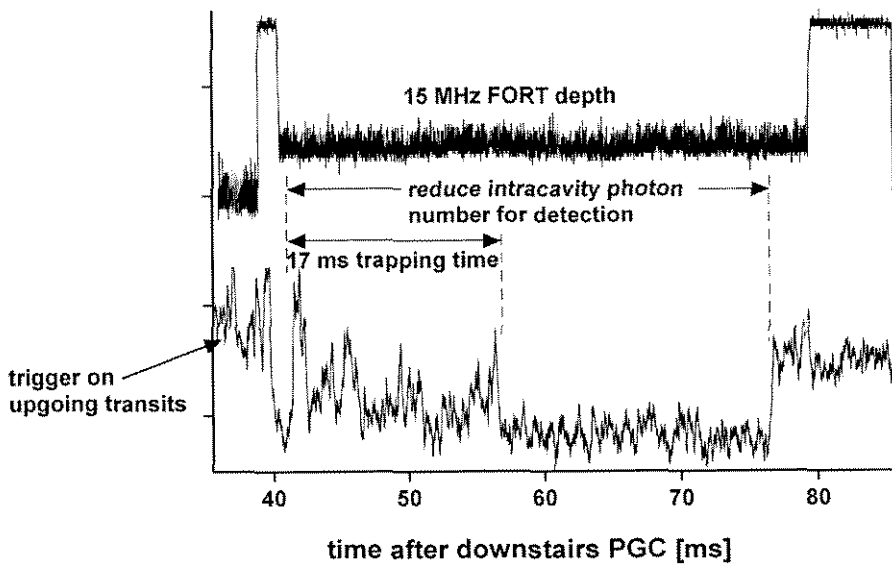
Figure 8.2: An extraordinarily long transit of 17 ms in the presence of the FORT was recorded at very high bandwidth > 1 MHz (a filtered version is shown here) in the hopes that a Fourier transform of this time-domain record might reveal information about c.m. atomic oscillations in the FORT potential well. Such oscillations have not been conclusively seen, and this is probably due to inadequate atomic cooling so that the ground state energy of the FORT has not yet been approached.

189

frequency. In fact, it is these *very* fluctuations at these *very* frequencies which we believe are driving the heating of the atoms in the FORT to begin with. A return to this measurement with the improved setup should be a priority.

8.3   Intracavity Cooling with a FORT

An absolutely critical next step is to try to figure out a way to implement cooling in the FORT-based trapped atom system to push the initial spread of vibrational states $\{|n\rangle\}$ towards $|n = 0\rangle$. In fact, a very simple simulation using a (rather aggressive) cooling rate of $1/\tau_{\mathrm{cool}} \sim 500$ Hz to counteract the $1/\tau_e^{\mathrm{axial}} \sim 50$ Hz heating rate was able to force a distribution of width $\sigma_n \sim 10$ centered at $n = 40$ towards $n = 0$ on millisecond timescales [166]. It seems logical that a cooling mechanism of the sort discussed in Sec. 7.1.3 is also present for the more complicated eigenvalue structure of the combination FORT/cavity QED field. Indeed, the registration of $\Delta_{\mathrm{FORT}}(\mathbf{r})$ with $g(\mathbf{r})$, the driving field strength ϵ and its detuning δ_{pa} and the actual magnitude of $\Delta_{\mathrm{FORT}}(\mathbf{r})$ with respect to $g(\mathbf{r})$ are all thought to play very important roles in determining the forces on the atom.

Steven van Enk has spent an appreciable amount of time tackling calculations of both friction/diffusion coefficients and verifications via simulations of individual atomic trajectories for such a system. In the low photon number limit $(\bar{n} \lesssim 0.05)$, he has found evidence for an extremely efficient axial cooling mechanism (i.e., along the cavity axis). The cooling seems to work best at positions along the cavity axis where there is some mixing between the atomic ground and excited states in the well-dressed eigenstates (i.e., $g \neq 0$), indicating some atomic excitation is necessary. Furthermore, it also seems necessary to drive the system red-detuned from any eigenstate which needs to be cooled. Both of these characteristics are typical of Doppler cooling, and one can infer that the final temperature after cooling will be limited by the eigenstate linewidth $\sim (\gamma_\perp, \kappa)$ for the states here. It will be a priority to attempt to see evidence for this cooling in the lab in the near future.

However, these calculations also suggest that the majority of heating could be

occurring in a plane transverse to the cavity axis, and that a different mechanism will need to be used to combat the radial diffusion of the atoms. The obvious solution is to try to incorporate the cooling beams which are already being used to slow the atoms from the downstairs MOT_2, but the excitation requirement of the Doppler cooling mechanism there competes with the desire of the atom to remain in the trapped ground state versus the anti-trapped excited state. Alternatives are to chop the FORT and provide cooling to the atom while the trap is off [131], to use a Raman cooling technique [172] or perhaps to search for some as-yet untested mechansim [173].

8.4   940 nm FORT

An outstanding problem with the dipole-force trap implemented here is that the excited state experiences a positive AC Stark shift ($\Delta^e_{FORT}(\mathbf{r}) = |\Delta_{FORT}(\mathbf{r})|$), leading to an excited state atom *in free space* being *repelled* from the trap. Note, however, that this work attempts to make an effective two-level atom out of the lowest two eigenstates (ground state, and the lower of the excited dressed states) of the well-dressed Hamiltonian (see Eq. (7.23) and, for example, Fig. 7.20), *both of which are trapped.* Nevertheless, it is not possible to appreciably drive atomic ground-excited *state transitions using the quantized atom-field dipole coupling $g(\mathbf{r})$ in this configu-*ration because the upper excited dressed state is not trapped due to the appreciable contribution of the atomic excited state to this dressed state. This will greatly diminish the trap's effectiveness for possible future experiments in which it will be necessary to put appreciable population in the excited state, and perhaps even invert the atom.

As well, the effective detuning from Eq. (7.22) $\Delta_{ca}(\mathbf{r}) \equiv \Delta_{ca} - 2\Delta_{FORT}(\mathbf{r})$ is a strong function of the atom's position within the trap. Fortunately, it turns out that a judicious choice of λ_{FORT} can eliminate both of these problems by making $\Delta^e_{FORT}(\mathbf{r}) = \Delta^g_{FORT}(\mathbf{r}) < 0$, so that $\Delta_{ca}(\mathbf{r}) = 0$ [175], which is something that Christina will discuss in her thesis. The basic idea is to find an appropriate FORT wavelength to possibly offset the positive shift of the $6S_{3/2}$ $F = 5$ state due to $6S_{1/2}$ $F = 4$ with an overcompensating negative shift from (see Fig. 6.1) the $6D_{5/2}$ $F = 6$

state at 917 nm (when using σ_+ polarized light, the $6D_{3/2}$ state at 917 nm does not enter the discussion). A wavelength longer than 917 nm is necessary to keep the ground state simultaneously trapped. Fig. 8.3 shows the results of a calculation demonstrating that the excited state (dashed) is trapped for wavelengths above about 920 nm. Furthermore, the excited ($\Delta_{\mathrm{FORT}}^e(\mathbf{r})$)and ground state ($\Delta_{\mathrm{FORT}}^g(\mathbf{r})$) FORT depths (solid) are in fact equal at 942 nm, which means that at this wavelength, the spatially dependent shifts of the atomic transition frequency due to the FORT *would completely disappear.*

This greatly simplifies the eigenvalue structure, because the Hamiltonian (7.23) becomes

$$
\begin{aligned}
\frac{H}{\hbar} &= \omega_a|e\rangle\langle e| + \omega_c a^\dagger a + \Delta_{\mathrm{FORT}}(\mathbf{r})\left(|e\rangle\langle e| + |g\rangle\langle g|\right) + g(\mathbf{r})\left(|g\rangle\langle e|a^\dagger + a|e\rangle\langle g|\right) \\
&= \Delta_{\mathrm{FORT}}(\mathbf{r})\,\widehat{1} + \omega_a|e\rangle\langle e| + \omega_c a^\dagger a + g(\mathbf{r})\left(|g\rangle\langle e|a^\dagger + a|e\rangle\langle g|\right) \quad (8.5)
\end{aligned}
$$

which is precisely of the form (5.1) considered for the "well-dressed" state work with $V_{\mathrm{ext}}(\mathbf{r}) = \hbar\Delta_{\mathrm{FORT}}(\mathbf{r})$, except now the possibility of atom-cavity detuning has been included. Furthermore, this Hamiltonian seems to be capable of studying *all* regimes for the well-dressed state structure of Fig. 5.2 because the external potential depth $\Delta_{\mathrm{FORT}}(\mathbf{r})$ is completely tunable with respect to $g(\mathbf{r})$ simply by varying the intensity of the FORT laser. The fact that $\Delta_{\mathrm{FORT}}(\mathbf{r})$ is capable of confinement to length scales $\ll \lambda$ is yet another reason that this approach merits a serious, sustained effort in the near future.

Certainly new experimental problems arise associated with this approach. The calculation of Fig. 8.3 assumes an intracavity intensity of 1 W. However, with the cavity finesse expected to drop to $\mathcal{F} \sim 2000$ at 940 nm, the mode-matched input power would need to be approximately 2 mW, which is turning out to be somewhat challenging at 940 nm without the use of a high-powered solid state (e.g. Ti:Sapphire) laser. It is possible that this amount of power injected through the substrates (with increased total absorption in the SiO_2 substrates due to the increased input power) will have a deleterious effect on the ability to lock the cavity, though the intracavity
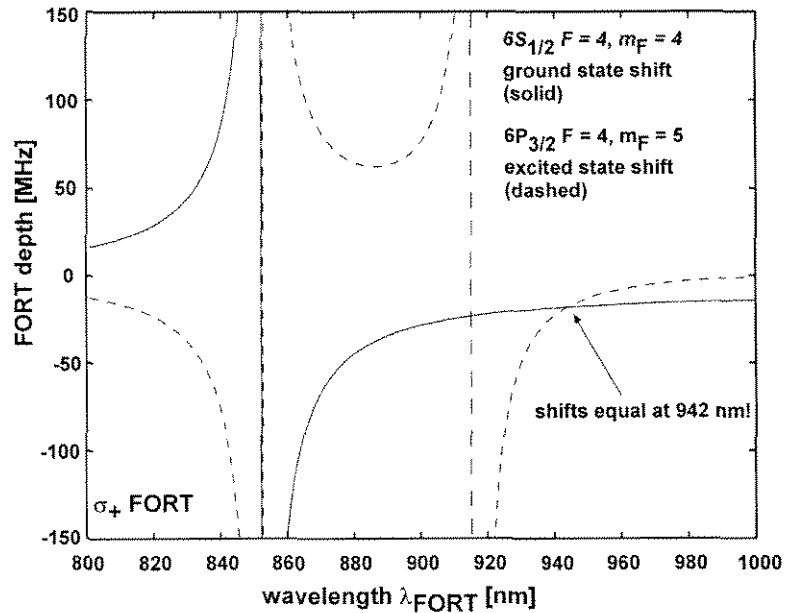

Figure 8.3: The AC Stark shifts of the ground (solid) $6S_{1/2}$ $F = 4$ and excited (dashed) states $6S_{3/2}$ $F = 5$ are shown. It is an exciting prospect for the future to note that the excited state is, in fact, trapped for FORT wavelengths longer than about 920 nm (as opposed to the anti-trapping now at 868 nm), and that the ground and excited state shifts equal one another close to 940 nm. Hence, a 940 nm FORT would trap both states, but have absolutely no effect on the atomic transition frequency, allowing cavity QED experiments to be performed without worrying about the spatial variation of these shifts or their effects on the eigenvalue structure. Of course, the spatial registration of the FORT field with respect to the cavity QED field needs to be taken into account.

circulating power ends up the same due to the reduced build-up. A series of systematic measurements of the cavity properties at 940 nm needs to be made.

8.5 Long-Lived Two-Level Atoms

An alternative to the above scheme (which attempts to eliminate heating problems in the excited state by causing it, too, to be trapped) is to eliminate the excited state from the story altogether. This would also eliminate the typically unobserved system decay channel via the excited state lifetime $\gamma_\perp$. Such a feat might be accomplished by creating an "artificial" two level atom between the hyperfine ground states $6S_{1/2}$ $F = 3$ and $6S_{1/2}$ $F = 4$ (split by 9.2 GHz as in Table 6.1), using Raman transitions off-resonance of the excited $6P_{1/2}$ or $6P_{3/2}$ states [102]. A configuration to implement this might arrange the cavity QED coupling on one arm of a "lambda" scheme, necessitating that it be phase-locked to a second laser 9.2 GHz away that would drive the other half of the lambda transition as a classical field. Since the atom never actually populates the excited state, any motional effects associated with recoil heating due to spontaneous emission could be eliminated.

8.6 Fluorescent Imaging of a Single Atom

A final thing that should be briefly mentioned is that very high quality lenses were purchased which are compatible with the lab stereomicroscopes (Zeiss Stemi SV11) and which should be able to image a 5 μm spot with a working distance of 12 cm, constrained by the vacuum chamber. In combination with these optics, the fast (20 ns) gating feature of the intensified CCD camera (Xybion) may be used to image the fluorescence of a trapped atom out the side of the cavity, even with the limited solid angle of the lens. One idea was to chop the trap on and off with a 1% duty cycle such that a resonant probe beam would briefly saturate the atom while the trap was off. The scattered light out the side of the cavity would be integrated by the CCD during the FORT *off* periods, and the FORT would be turned back on to recapture

the atom. A simple estimate showed that a 500 ms integration period would probably be sufficient time to get an image of a single, trapped atom before the dark current of the present (uncooled) camera would be reached, although it is probable that with the present FORT lifetime the atom would be heated out of the trap long before this limit is reached.

Bibliography

[1] see C. H. Bennett and D. P. DiVincenzo, Nature **404**, 247 (2000) for the most recent review.

[2] P. W. Shor, [Conference Paper] 35th Symp. Found. Comp. Sci. (1994). D. P. DiVincenzo and P. W. Shor, Phys. Rev. Lett. **77**, 3260 (1996). L. K. Grover, Phys. Rev. Lett. **79**, 4709 (1997).

[3] J. Preskill, Phys. Today **52**, 24 (1999).

[4] C. H. Bennett, P. W. Shor, J. A. Smolin and A. V. Thapliyal, Phys. Rev. Lett. **83**, 3081 (1999).

[5] C. H. Bennett, G. Brassard and N. D. Mermin, Phys. Rev. Lett. **68,** 557 (1992).

[6] C. H. Bennett et al., Phys. Rev. Lett. **70**, 1895 (1993).

[7] D. Bouwmeester et al., Nature **390**, 575 (1997).

[8] A. Furusawa et al., Science **282**, 706 (1998).

[9] H.J. Kimble, in *Cavity Quantum Electrodynamics, Advances in Atomic, Molecular and Optical Physics, Supplement 2*, ed. P.R. Berman, (Academic, San Diego, 1994).

[10] S. Haroche and J. M. Raimond, Sci. Am. **268**, 26 (1993).

[11] C. Monroe et al., Phys. Rev. Lett. **75**, 4717 (1995).

[12] Ch. Roos et al., Phys. Rev. Lett., **83**, 4713 (1999).

[13] N. Gershenfeld and I. L. Chuang Sci. Am. **278**, 50 (1998).

[14] B. E. Kane, Nature **393**, 133 (1998).

[15] W. H. Zurek and J. P. Paz, Phys. Rev. Lett. **72**, 2508 (1994).

[16] B. T. H. Varcoe, S. Brattke, M. Weidinger and H. Walther, Nature **403**, 743 (2000).

[17] G. Nogues et al., Nature **400**, 239 (1999).

[18] C. A. Sackett et al., Nature **404**, 256 (2000).

[19] C. J. Myatt et al., Nature **403**, 269 (2000).

[20] C. Monroe et al., Phys. Rev. Lett. **75**, 4011 (1995).

[21] J. Ye, D. W. Vernooy and H. J. Kimble, Phys. Rev. Lett. **83**, 4987 (1999).

[22] C. J. Hood, T. Lynn, A. C. Doherty, A. S. Parkins and H. J. Kimble, Science **287** 1447, (2000).

[23] P. W. H. Pinske, T. Fischer, P. Maunz and G. Rempe, Nature **404**, 365 (2000).

[24] Q. A. Turchette et al., Phys. Rev. Lett. **75**, 4710 (1995).

[25] The identification of this term is due to Hideo Mabuchi.

[26] S. Haroche, M. Brune and J. M. Raimond, Europhys. Lett. **14**, 19 (1991).

[27] S. E. Hamann et al., Phys. Rev. Lett. **80**, 4149 (1998).

[28] M. Kasevich et al., Phys. Rev. Lett. **66**, 2297 (1991).

[29] M. H. Anderson et al., Science **269**, 198 (1995).

[30] K. B. Davis et al., Phys. Rev. Lett. **75**, 3969 (1995).

[31] Q. A. Turchette, R. J. Thompson and H. J. Kimble, Appl. Phys. B **60**, S1 (1995).

[32] D. W. Vernooy, V. S. Ilchenko, H. Mabuchi, E. W. Streed and H. J. Kimble, Opt. Lett. **23**, 247 (1998).

[33] D. W. Vernooy, A. Furusawa, N. Ph. Georgiades, V. S. Ilchenko and H. J. Kimble, Phys. Rev. A **57**, R2293 (1998).

[34] D. W. Vernooy and H. J. Kimble, Phys. Rev. A **55**, 1239 (1997).

[35] D. W. Vernooy and H. J. Kimble, Phys. Rev. A **56**, 4287 (1997).

[36] H. Mabuchi, J. Ye and H. J. Kimble, Appl. Phys. B **68**, 1095 (1999).

[37] G. Griffel, A. Serpengüzel and S. Arnold, *1995 IEEE Symposium on Frequency Control*, (IEEE, New York, 1995).

[38] A. Serpengüzel, S. Arnold and G. Griffel, Opt. Lett. **20**, 654 (1995).

[39] V.B. Braginsky and V.S. Ilchenko, Sov. Phys. Dokl., **32**, 307 (1987).

[40] H. Mabuchi and H.J. Kimble, Opt. Lett. **19**, 749 (1994).

[41] F. Treussart, J. Hare, L. Collot, V. Lefèvre, D.S. Weiss, V. Sandoghar, J.-M. Raimond and S. Haroche, Opt. Lett. **19**, 1651 (1994).

[42] C. E. Wieman and L. Hollberg, Rev. Sci. Instrum. **62**, 1 (1991). K. B. MacAdam, A. Steinbach and C. E. Wieman, Am. J. Phys. **60**, 1099 (1992). L. Ricci et al., Opt. Comm. **117**, 541 (1995). K. C. Harvey and C. J. Myatt, Opt. Lett. **16**, 911 (1991). K. G. Libbrecht et al., Am. J. Phys.**63**, 729 (1995).

[43] V. B. Braginsky, M.L. Gorodetsky, and V.S. Ilchenko, Physics Letters A, **137**, 393 (1989).

[44] L. Collot, V. Lefèvre-Sequin, M. Brune, J.-M. Raimond and S. Haroche, Europhys. Lett. **23**, 327 (1993).

[45] M. L. Gorodetsky, A. A. Savchenkov and V. S. Ilchenko, Opt. Lett. **21**, 453 (1995).

[46] J. A. Stratton, *Electromagnetic Theory* (McGraw-Hill, New York, 1941), p. 554.

[47] P. W. Barber and R. K. Chang eds., *Optical Effects Associated with Small Particles* (World Scientific, Singapore, 1988).

[48] V. S. Ilchenko and M. L. Gorodetsky, Laser Physics **2**, 1004 (1992).

[49] J.C. Swindal, D.H. Leach and R.K. Chang, Opt. Lett. **18**, 191 (1993).

[50] M. L. Gorodetsky and V. S. Ilchenko, Opt. Comm. **113**, 133 (1994).

[51] D.S. Weiss, V. Sandoghar, J. Hare, V. Lefèvre-Sequin, J.-M Raimond, and S. Haroche, Opt. Lett. **20**, 1835 (1995).

[52] R. W. P. Drever et al., Appl. Phys. B **31**, 145 (1983). G. C. Bjorklund et al., Appl. Phys. B **32**, 145 (1983).

[53] S.C. Hill and R.E. Benner, in *Optical Effects Associated with Small Particles*, P.W. Barber and R.K. Chang eds. (World Scientific,New Jersey, 1988).

[54] G. Rempe, R.J. Thompson, H.J. Kimble and R. Lalezari, Opt. Lett. **5**, 363 (1992).

[55] C. Lin, *Handbook of Microwave and Optical Components*, ed. K. Chang (Wiley: NewYork, 1991), p. 11.

[56] H. G. Unger, *Planar Optical Waveguides and Fibres* (Clarendon Press,Oxford, 1977), p. 130.

[57] P. K. Tien, Appl. Opt. **10**, 2395 (1970).

[58] D. Marcuse, *Light Transmission Optics* (Van Nostrand Reinhold Company: New York, 1972), 368 *ff.*

[59] J. Oudar, *The Physics and Chemistry of Surfaces* (Blackie: Glasgow, 1975), 85 *ff.*

[60] A. W. Adamson, *The Physical Chemistry of Surfaces* (Wiley, New York, 1982), 421 *ff.*

[61] G.M. Hale and M.R. Querry, Appl. Opt. **12**, 555 (1973).

[62] H. J. Kimble, Trans. R. Soc. London, Ser. A **355**, 2327 (1997).

[63] G. Rempe et al., Phys. Rev. Lett. **23**, 1727 (1991).

[64] H. Mabuchi, Q. A. Turchette, M. S. Chapman and H. J. Kimble, Opt. Lett. **21**, 1393 (1996).

[65] C. J. Hood, M. S. Chapman, T. Lynn, and H. J. Kimble, Phys. Rev. Lett. **80**, 4157 (1998).

[66] V. Sandoghdar, et al., Phys. Rev. A **54**, R1777 (1996).

[67] D. J. Norris, M. Kuwata-Gonokami and W.E. Moerner, Appl. Phys. Lett. **71**, 297 (1997).

[68] Q. A. Turchette, Ph.D. Thesis, California Institute of Technology, 1997.

[69] P. Simoneau et al., Opt. Comm. **59**, 103 (1986).

[70] S.N. Bagayev et al., Appl. Phys. B**48**, 31 (1989). Ch. Chardonnet et al., Appl. Phys. B**59**, 333 (1994). J. Ye, L.-S. Ma and J.L. Hall, IEEE Trans. Instr. Meas. **46**, 178 (1997).

[71] J.C. Knight et al., Opt. Lett. **20**, 1515 (1995).

[72] J.C. Knight et al., Opt. Lett. **21**, 698 (1996).

[73] E.A Hinds and V. Sandoghdar, Phys. Rev. A **43**, 398 (1991).

[74] D. Kleppner, Phys. Rev. Lett. **47**, 233 (1981).

[75] A.J. Campillo, J.D. Eversole and H.B. Lin, Phys. Rev. Lett. **67**, 437 (1991).

[76] X. Fan, H. Wang and M. Lonergan, [Conference Paper] Opt. Soc. Am. (1999).

[77] M. L. Gorodetsky and V. S. Ilchenko, J. Opt. Soc. Am. B **16**, 147 (1999).

[78] N. Dubreuil et al., Opt. Lett. **20**, 813 (1995).

[79] J. C. Knight, G. Cheung, F. Jacques and T. A. Birks, Opt. Lett. **22**, 1129 (1997).

[80] M. Cai, G. Hunziker and K. Vahala, IEEE Phot. Tech. Lett. **11**, 686 (1999).

[81] J.-P. Laine, B. E. Little and H. A. Haus, IEEE Phot. Tech. Lett. **11**, 1429 (1999).

[82] M. Cai and K. Vahala, Opt. Lett. **25**, 260 (2000).

[83] B. E. Little et al., Opt. Lett. **25**, 73 (2000).

[84] V. S. Ilchenko, X. S. Yao and L. Maleki, Opt. Lett. **24**, 723 (1999).

[85] V. S. Ilchenko, X. S. Yao and L. Maleki, [Conference Paper] Proceedings of SPIE, **3611**, 190 (1999).

[86] W. Von Klitzing et al., Elect. Lett. **35**, 1745 (1999). V. S. Ilchenko, private communication (1999). O. Painter, private communication (2000).

[87] B. G. Englert, J. Schwinger, A. O. Barut and M. O. Scully, Europhys. Lett. **14**, 25 (1991).

[88] B.W. Shore, P. Meystre and S. Stenholm, JOSA **B8**, 903 (1991).

[89] T. W. Mossberg, M. Lewenstein and D. J. Gauthier, Phys. Rev. Lett. **67**, 1723 (1991).

[90] A. C. Doherty, A. S. Parkins, S. M. Tan and D. F. Walls, Phys. Rev. A **56**, 833 (1997).

[91] H. Mabuchi, Quantum Semiclass. Opt. **8**, 1103 (1996).

[92] P. Storey, M. J. Collett and D. F. Walls, Phys. Rev. Lett. **68**, 472 (1992).

[93] A. M. Herkommer, H. J. Carmichael and W. P. Schleich, Quantum Semiclassic. Opt **8**, 189 (1996).

[94] A. M. Herkommer, V. M. Akulin and W. P. Schleich, Phys. Rev. Lett. **69**, 3298 (1992).

[95] M. J. Holland, D. F. Walls and P. Zoller, Phys. Rev. Lett. **67**, 1716 (1991).

[96] I. S. Averbukh, V. M. Akulin and W. P. Schleich, Phys. Rev. Lett. **72**, 437 (1994).

[97] A. B. Matsko, S. P. Vyatchinin, H. Mabuchi and H. J. Kimble, Phys. Lett. A **192**, 175 (1994).

[98] W. Ren and H. J. Carmichael, Phys. Rev. A **51**, 752 (1995).

[99] M. O. Scully, G. M. Meyer and H. Walther, Phys. Rev. Lett. **76**, 4144 (1996).

[100] T. Pellizzari, S. A. Gardiner, J. I. Cirac and P. Zoller, Phys. Rev. Lett. **75**, 3788 (1995).

[101] J. I. Cirac, P. Zoller, H. J. Kimble and H. Mabuchi, Phys. Rev. Lett. **78**, 3221 (1997).

[102] C. K. Law and H. J. Kimble, J. Mod. Opt. **44**, 2067 (1997). A. Kuhn, M. Hennrich, T. Bondo and G. Rempe, Appl. Phys. **B69**, 373 (1999).

[103] S. Haroche, in *Cavity Quantum Electrodynamics, Advances in Atomic, Molecular and Optical Physics, Supplement 2,* ed. P.R. Berman (Academic, San Diego, 1994).

[104] N. Davidson, H. J. Lee, M. Kasevich and S. Chu, Phys. Rev. Lett. **72**, 3158 (1994).

[105] C. K. Law and J. H. Eberly, Phys. Rev. Lett. **76**, 1055 (1996).

[106] Z. Byalnicka-Birula, P. Meystre, E. Schumaker and M. Wilkens, Opt. Comm. **85**, 315 (1991).

[107] P. Marte, R. Dum, R. Taïeb, P. D. Lett and P. Zoller, Phys. Rev. Lett. **71**, 1335 (1993).

[108] Y. Castin and J. Dalibard, Europhys. Lett. **14**, 761 (1994).

[109] M. Wilkens, E. Schumacher and P. Meystre, Phys. Rev. A **44**, 3130 (1991).

[110] M. BenDahan, E. Peik, J. Reichel, Y. Castin and C. Salomon, Phys. Rev. Lett. **76**, 4508 (1996).

[111] S. Wilkinson, C. Bharucha, K. Madison, Q. Niu and M. Raizen, Phys. Rev. Lett. **76**, 4512 (1996).

[112] J. I. Cirac, A. S. Parkins, R. Blatt and P. Zoller, Opt. Comm. **97**, 353 (1995).

[113] D. J. Wineland, J. Dalibard and C. Cohen-Tannoudji, J. Opt. Soc. Am. B **9**, 32 (1992).

[114] J. I. Cirac, R. Blatt, P. Zoller and W. D. Phillips, Phys. Rev. A **46**, 2668 (1992).

[115] R. J. C. Spreeuw, T. Pfau, U. Janicke and M. Wilkens, Europhys. Lett. **32**, 469 (1995).

[116] M. Holland, K. Burnett, C. Gardiner, J. I. Cirac and P. Zoller, Phys. Rev. A **54**, R1757 (1996).

[117] H. Wallis, J. Dalibard and C. Cohen-Tannoudji, Appl. Phys. B **54**, 407 (1992).

[118] M. Holland, S. Marksteiner, P. Marte and P. Zoller, Phys. Rev. Lett. **76**, 3683 (1996).

[119] J. Dalibard and C. Cohen-Tannoudji, J. Opt. Soc. Am. B **2**, 1707 (1985).

[120] A. S. Parkins, P. Marte, P. Zoller and H. J. Kimble, Phys. Rev. Lett. **71**, 3095 (1993).

[121] R. Kosloff, J. Phys. Chem. **92**, 2087 (1988).

[122] H. I. Yoo and J. H. Eberly, Phys. Rep. **118**, 239 (1985).

[123] M. W. Noel and C. R. Stroud, Phys. Rev. Lett. **77**, 1913 (1996).

[124] *Cavity Quantum Electrodynamics,* ed. P. Berman (Academic Press, San Diego, 1994).

[125] For a more recent review, see contributions in the Special Issue of Physica Scripta **T76** (1998).

[126] H. Walther et al., *Fourteenth International Conference on Laser Spectroscopy,* Innsbruck, June 1999.

[127] T. Pellizzari, et al., Phys. Rev. Lett. **75**, 3788 (1995).

[128] J.-I. Cirac, et al., Physica Scripta **T76**, 223 (1998).

[129] H. Mabuchi and H. Wiseman, Phys. Rev. Lett. **82**, 1798 (1999).

[130] W. Petrich, M.H. Anderson, J. R. Ensher and E. Cornell, Phys. Rev. Lett. **74**, 4157 (1995). J. D. Weinstein and K. G. Libbrecht, Phys. Rev. A **52**, 4004 (1995). V. Vuletic, T. W. Hansch and C. Zimmerman, Europhys. Lett. **36**, 349 (1996).

[131] J. D. Miller, R. A. Cline, and D. J. Heinzen, Phys. Rev. **A47**, R4567 (1993). R. J. C. Spreeuw et al., Phys. Rev. Lett. **72**, 3162 (1994). H. J. Lee, C. S. Adams, M. Kasevich, and S. Chu, Phys. Rev. Lett. **76**, 2658 (1996). For a recent review, see R. Grimm and M. Weidemuller, Quant. Ph. Preprint /9902072, 24 Feb. (1999).

[132] A. Hemmerich and T. W. Hansch, Phys. Rev. Lett. **70**, 411 (1993). G. Grynberg et al., Phys. Rev. Lett. **70**, 2249 (1993).

[133] W. Lange, private communication (1999). D. Leibfried, private communication (2000).

[134] G. M. Meyer, H. J. Briegel and H. Walther, Europhys. Lett. **37** 317 (1997).

[135] C. J. Hood, M. S. Chapman, T. W. Lynn, and H. J. Kimble, Phys. Rev. Lett. **80**, 4157 (1998).

[136] J. Ye et al., IEEE Trans. Instru. & Meas. **48**, 608 (1999).

[137] P. Münstermann, T. Fischer, P. W. H. Pinske and G. Rempe, Opt. Comm. **159**, 63 (1999).

[138] P. Münstermann et al., Phys. Rev. Lett. **82**, 3791 (1999).

[139] E. L. Raab et al., Phys. Rev. Lett. **59**, 2631 (1987).

[140] C. Monroe, W. Swann, H. Robinson and C. Wieman, Phys. Rev. Lett. **65**, 1571 (1990). F. Shimizu, K. Shimizu and H. Takuma, Opt. Lett. **16**, 339 (1991). K. E. Gibble, S. Kasapi and S. Chu, Opt. Lett. **17**, 526 (1992).

[141] Y. Castin, H. Wallis and J. Dalibard, J. Opt. Soc. Am. B **6**, 2046 (1989).

[142] D. Sesko et al., Phys. Rev. Lett. **63**, 961 (1989). T. Takekoshi and R. J. Knize, Opt. Lett. **21**, 77 (1996).

[143] see Z. Hu, Ph.D. Thesis California Institute of Technology, 1995 for a nice derivation.

[144] E. Riis, D. S. Weiss, K. Moler and S. Chu, Phys. Rev. Lett. **64**, 1658 (1990).

[145] Z. T. Lu et al., Phys. Rev. Lett. **77**, 3331 (1996).

[146] K. Gibble, S. Chang and R. Legere, Phys. Rev. Lett. **75**, 2666 (1995). C. J. Myatt et al., Opt. Lett. **21**, 290 (1996).

[147] Y. T. Sasaki, J. Vac. Sci. Technol. A **9**, 2025 (1991).

[148] P. Bouyer, T. Gustavson, K. G. Hanitos and M. A. Kasevich, Opt. Lett. **21**, 1502 (1996).

[149] K. G. Libbrecht and J. L. Hall, Rev. Sci. Instr. **64**, 2133, (1993).

205

[150] C. C. Bradley, J. Chen and R. Hulet, Rev. Sci. Instr. **61**, 2097, (1990).

[151] J. Dalibard and C. Cohen-Tannoudji, J. Opt. Soc. Am. B **6**, 2023, (1989). J. Lawall et al., Phys. Rev. Lett. **73**, 1915 (1994).

[152] J. H. Shirley, Opt. Lett. **7**, 537 (1982).

[153] P. D. Lett et al., J. Opt. Soc. Am. B **6**, 2084, (1989).

[154] J. S. Seeley, J. Opt. Soc. Am. **54**, 342 (1964).

[155] W. Lichten, J. Opt. Soc. Am. A **2**, 1869 (1985).

[156] R. G. Devoe et al., Phys. Rev. A **37**, R1802 (1988).

[157] A. Yariv, *Quantum Electronics* (Wiley: New York, 1967), 139 *ff.*

[158] R. J. Thompson, Ph.D. Thesis, University of Texas at Austin, 1994.

[159] H. Mabuchi, Ph.D. Thesis, California Institute of Technology, 1999.

[160] Ron Brady, Coherent Inc., Private Communication.

[161] J. Helmcke, S. A. Lee and J. L. Hall, Appl. Opt. **21**, 1686 (1982).

[162] J. J. Childs et al., Phys. Rev. Lett. **77**, 2901 (1996).

[163] D. W. Vernooy and H. J. Kimble, Phys. Rev. A **56**, 4287 (1997).

[164] C. Cohen-Tannoudji, *Fundamental Systems in Quantum Optics, Les Houches Summer School Session LIII*, J. Dalibard, J. M. Raimond and J. Zinn-Justin, eds. (Elsevier, Amsterdam, 1992) p. 41 *ff.*

[165] T. A. Savard, K. M. O'Hara, and J. E. Thomas, Phys. Rev. A **56**, R1095 (1997).

[166] C. Gardiner, J. Ye, H. C. Nagerl and H. J. Kimble [in press] (2000).

[167] A. C. Doherty, A. S. Parkins, S. M. Tan and D. F. Walls, Phys. Rev. A **56**, 833 (1997). A. C. Doherty, A. S. Parkins, S. M. Tan and D. F. Walls, Phys. Rev. A **57**, 4804 (1998).

[168] P. Horak, et al., Phys. Rev. Lett. **79**, 4974 (1997). G. Hechenblaikner, M. Gangl, P. Horak and H. Ritsch, Phys. Rev. A **58**, 3030 (1998).

[169] A. C. Doherty, unpublished.

[170] T. L. Boyd and H. J. Kimble, Opt. Lett. **16**, 809 (1990).

[171] Y. Yamamoto, T. Mukai and S. Saito, Electron. Lett. **17**, 327 (1981). S. Kobayashi, Y. Yamamoto, M. Ito and T. Kimura, IEEE J. Quantum Electron. **QE-18**, 582 (1982).

[172] C. S. Adams et al., Phys. Rev. Lett. **74**, 3577 (1995). H. J. Lee, C. S. Adams, M. Kasevich and S. Chu, Phys. Rev. Lett. **76**, 2658 (1996). H. Perrin, A. Kuhn, I. Bouchoule and C. Salomon, Europhys. Lett. **42**, 395 (1998). A. J. Kerman, V. Vuletic, C. Chin and S. Chu, Phys. Rev. Lett. **84**, 439 (2000).

[173] V. Vuletic and S. Chu, Phys. Rev. Lett. **84**, 3787 (2000).

[174] J. Ye, D. W. Vernooy, and H. J. Kimble, in preparation (2000).

[175] C. J. Hood and C. Wood, in preparation (2000).

[176] D. Leibfried et al., Phys. Rev. Lett. **77**, 4281 (1996).